UNIVERSITY OF BIRMINGHAM

EngD Thesis

An investigation of cracking in laser metal deposited nickel superalloy CM247LC

By

Philip Alexander McNutt

Supervisor: Professor Moataz Attallah

Department of Metallurgy and Materials
School of Engineering
University of Birmingham
Edgbaston
Birmingham B15 2TT
United Kingdom
1st February 2015

Acknowledgements

I would like to thank my supervisors Dr Moataz Attallah and Roger Fairclough for their support, advice and guidance over the course of this project. There were countless setbacks and problems over the years, and their advice was invaluable in helping me deliver this project.

I would also like to thank Dr Robert Scudamore and Dr Emma Ashcroft at TWI for giving me the opportunity to conduct this work using the laser deposition equipment at TWI Yorkshire. My time spent working in the lasers department was truly enjoyable, and I got to work with some fantastic people on a fascinating range of projects.

And of course I would also like to thank my parents and family, whose constant and unwavering love and support over the years have made me who I am today, and without which none of this would have been possible.

Thank you all

Contents

Chapter 1

Introduction and Abstract

1 Chapter 1 - Introduction and Abstract

The nickel superalloy CM247LC is a casting alloy developed in the 1970's as an evolution of the alloy Mar-M247, to address issues with cracking during casting of thin wall sections. This alloy has been used extensively throughout the aerospace industry for the production of static and rotating polycrystalline engine components, such as directionally solidified turbine blades, turbine disks, vanes, stators, and combustion chambers. The high aluminium and titanium content of the alloy results in a high γ' volume fraction, which improves performances at high temperatures, but makes it exceedingly difficult to repair via conventional fusion methods such as welding.

Laser metal deposition (LMD) is an additive manufacturing method that utilises a focused laser beam as a heat source for the weld addition of a metal powder to a substrate, which is used for the repair and manufacture of components by layer-wise material addition. This method has been proven capable of producing repairs onto difficult to weld materials, due to the ability to closely control the heat input, and by extension, the microstructure of the deposited part.

Using Design of Experiments (DOE) methodology, an experiment was constructed that evaluated the cracking response of laser deposited CM247LC against four critical processing variables; Laser power, scanning speed, laser spot diameter and deposit dilution. In order to carry out the test matrix, a series of processing rules were devised that relate the size and shape of an individual deposit track to the degree of track overlap and Z-increment between layers, reducing unnecessary variation between trials that may have obscured the intrinsic relationship between the four key processing variables and the crack response.

Through this process, it was determined that cracks form during solidification, due to the formation of a eutectic composition liquid with depressed melting temperature, which wets the grain boundaries and interdendritic regions, reducing their ability to withstand contraction

stresses. Interpretation of the DOE results showed that by increasing the laser power and laser spot diameter, and decreasing the scanning speed and deposit dilution, cracking could be reduced in deposited samples due to the increased heat input lowering the thermal gradient and decreasing the residual stresses generated during solidification.

Experiments conducted in chapter 5 were aimed at eliminating cracks through various methods, such as reducing the powder particle size range, changing the scanning pattern of the toolpath and preheating the material to 800°C. Through this work it was determined that finer particle sizes improve the deposition efficiency, but resulted in a greater cracking response. Cracks were found to be shorter in length compared to samples deposited using larger powder size ranges, which is believed to be due to accelerated solidification rates within the melt pool.

Comparison of various toolpath strategies showed that cracking response was heavily dependent on developed microstructures, with some toolpaths producing microstructures that consisted of large columnar grains, while a cross hatch toolpath produced a more random microstructure that was shown to produce the lowest crack response.

The greatest reduction in cracking was observed for samples produced using a high temperature pre-heat. Cracks were still observed within the material, but were of a much finer scale and not surface connected, meaning material deposited using this method may be suitable for post deposition Hot Isostatic Pressing (HIP) in order to consolidate the internal structure and remove cracks and voids.

While none of the approaches used in this work led to a successful, crack free repair strategy for CM247LC, it has shown that cracking can be reduced significantly by preheating, and it is believed that further work investigating this area would yield promising results.

Chapter 2

Literature review

2 Chapter 2 - Literature review

2.1 Introduction

In this chapter, a review of the literature surrounding the project shall be presented in order to provide some context for the work, illustrate how it is relevant to industry, and explore what work has been done in this field to date.

2.2 Aero industry overview and business context

International air traffic has seen a steady and continuous growth over the last 40 years, with over 400 new long haul routes expected to open up in the next 20 years, as well as emerging markets in Asia and the far-east. In order to meet the demands of international trade and travel, it is predicted that 25,951 new aircraft (100+ seats) worth USD $3.1 trillion will need to be commissioned [1], with some of the existing aircraft being decommissioned, refurbished or converted to freight aircraft, as illustrated in Figure 2-1.

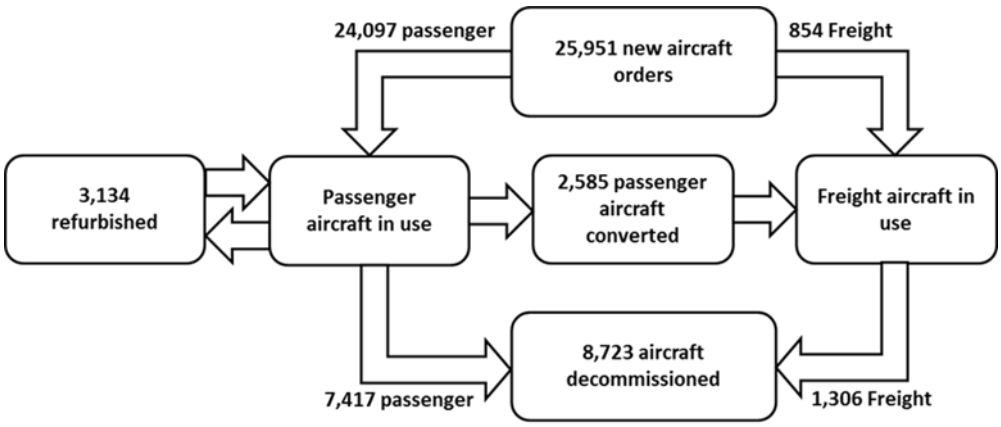

Figure 2-1 - Demand and allocation of aircraft projected up to 2025 [1]

In order to reduce fuel costs to the airline and comply with environmental legislation on emissions, the optimisation of the thermal and propulsive efficiencies of the modern aero-engine has become paramount. Even a small increase in efficiency and service interval of

these engines relates to tremendous savings in fuel and maintenance costs over the life of the engine [2-4].

Modern civil aero-engines are typically high bypass turbofan designs, where a portion of the air intake from the large fan blades at the front of the engine goes to burn the fuel and drive the turbine, while the rest is diverted backwards at high speed to produce additional thrust (Figure 2-2A). The high bypass ratio design allows greater propulsion efficiency from the engine, with modern engines deriving as much as 90% of their thrust from the bypassed air [5]. Military engines on the other hand have very low bypass ratio, generally being of the turbojet design, which deliver high thrust and performance from a more compact system, at the expense of reduced efficiency (Figure 2-2B).

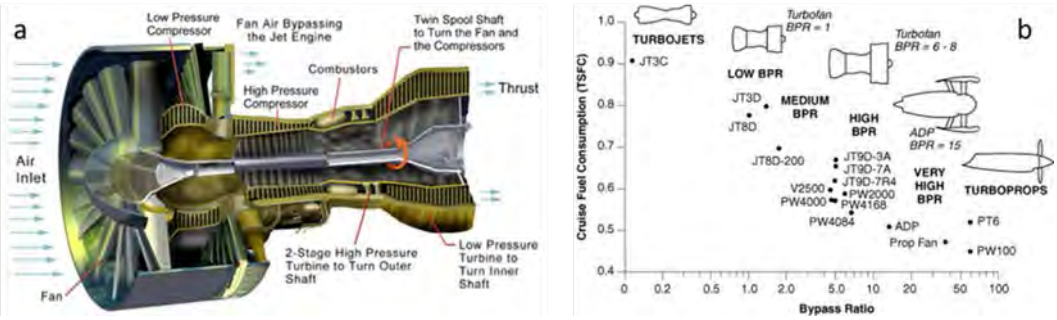

Figure 2-2 - A) Modern high bypass ratio jet engine schematic B) graph illustrating the propulsion efficiency of various engine designs as a function of the bypass ratio [2].

Improvements in thermal efficiency, as well as reductions in CO_2 and NOX emissions can both be achieved by increasing the compression ratio and turbine inlet temperature of the engine, ensuring that the fuel burns more cleanly and efficiently [3]. However, increasing the compression ratio and turbine inlet temperature means that the engine components are going to be exposed to higher temperatures, higher stresses and more aggressively corrosive and oxidising environments, which leads to a shorter service life of components, more frequent service intervals and increased cost [6].

The development of directionally solidified castings in the 1970s provided a step change in the creep resistance of components produced using nickel-base superalloys, due to the

elimination of grain boundaries transverse to the loading axis [7-10]. Developments in single crystal investment castings eliminated grain boundaries almost entirely, improving creep resistance further and allowing higher turbine inlet temperatures and greatly improved engine efficiency (Figure 2-3) [11,12]. The use of internal cooling channels and thermal barrier coatings has allowed nickel superalloy components to be used at temperatures that in some cases even exceed their own melting point [4,6,13].

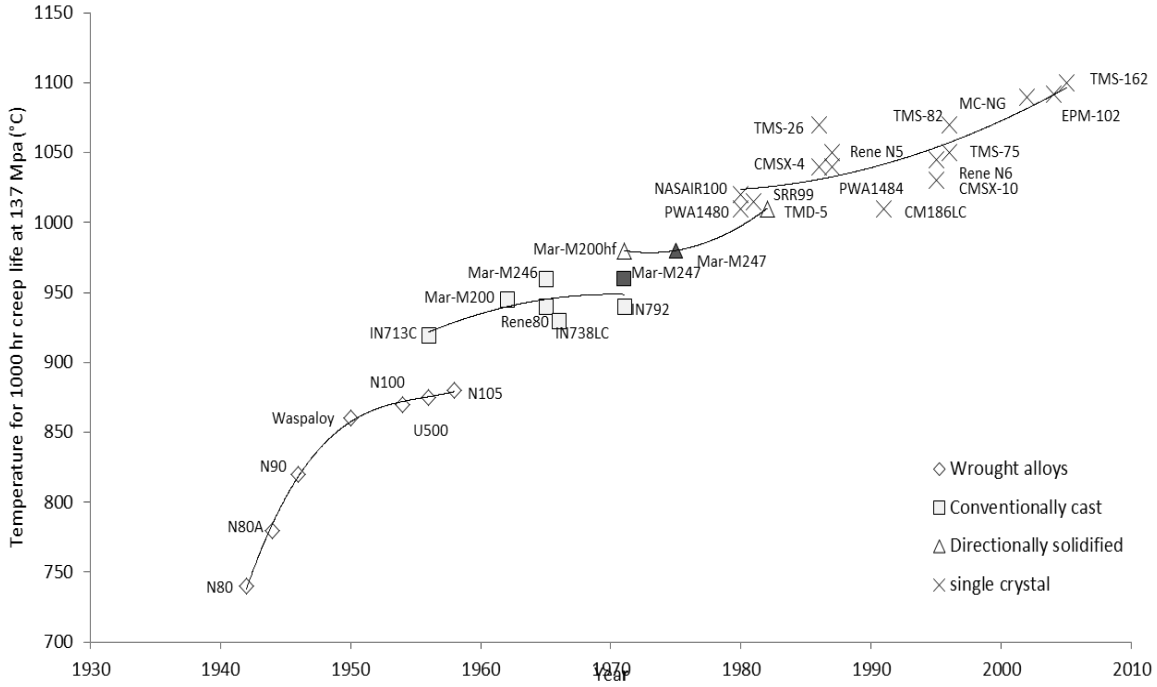

Figure 2-3 - The evolution of Nickel superalloy temperature tolerance [9]

While these methods have realised huge savings in maintenance costs and fuel consumption, these components will inevitably deteriorate to a point where they are considered no longer fit for service, and must be scrapped or recycled [9]. Due to the high cost of manufacture, repair and replacement, there is a clear financial incentive for more economical manufacturing routes [14,15], more cost effective and reliable repair procedures [16] and improved component performance and durability [9,13,17,18]. With these considerations in mind, additive manufacturing is emerging as a viable option for enabling the repair of materials that were previously difficult or impossible to repair via conventional routes.

2.3 Additive manufacture overview

Additive manufacturing refers to a group of processes that are capable of producing functional engineering components directly from CAD data by means of layer wise material addition. This allows components to be created, modified or repaired with the minimum amount of material wastage compared to conventional subtractive manufacturing routes, such as machining, in which material is removed from the feedstock until the desired shape is achieved [19-24].

There are numerous technologies that are capable of additively producing functional components from engineering alloys (Table 2-1), generally through the melting and consolidation of a suitable feedstock material such as powder or wire.

Table 2-1 – General classifications of commercially available additive manufacturing technologies, according to heat source and material form.

Heat source	Material form		
	Blown powder	**Pre-placed powder**	**Wire**
Laser	Laser Metal Deposition [25]	Selective Laser Melting [26]	Laser Wire Deposition [27]
Electron beam		Electron beam melting [28]	Electron Beam Freeform Fabrication [28]
Electric arc			Shaped Metal Deposition [29]

Some of the benefits of the additive manufacturing approach are listed below:

1. Reduced material costs – Very little scrap is generated through additive manufacturing, so the material efficiency is high.
2. Reduced energy costs – Powder feedstock for additive manufacture applications is produced directly from molten metal, and can be produced without the need for casting, forging, rolling etc.
3. Reduced time to manufacture – Products can go from the design stage to manufacture directly from the CAD data without the need for tooling modification or die manufacture
4. Integrated components – Parts that are normally manufactured from multiple parts can be produced as a single integrated component, removing the need for welding or mechanical fasteners, improving strength and reducing weight and costs.
5. Complex internal structures and features – By building up a component layer by layer using the appropriate methods, it is possible to produce complex internal features, such as strengthening ribs or baffles, that allow a component to be made with reduced weight and with fewer production steps.
6. Topologically optimised components – Through the use of finite element stress analysis, it is possible to design components that provide the required strength with the minimum of material. Additive manufacture allows these components to be produced quickly and economically.
7. Repair of un-repairable high value components – Highly alloyed and complex components that are considered un-weldable may be repaired using suitable AM processes, with very little distortion and microstructural defects compared to conventional fusion processes such as arc welding.

Consider for example a hinge bracket that is intended to go into some area of an aircraft (Figure 2-4 rear). Conventional manufacturing methods would take a billet of alloy material and machine away as much material as required to create the desired part. This method has a high cost to buy the material and also a high cost to machine, with the design engineer attempting to strike a balance between the performance of a part and the economy of its manufacture.

Figure 2-4 - Topologically optimised hinge bracket from an Airbus A380 manufactured using conventional machining (rear) and topologically optimised additive manufacture routes (front)

In comparison, a component manufactured using additive manufacturing only uses the amount of material needed to generate the component shape, with minimal post processing and machining required to produce the final shape and properties [15].

This gives design engineers greater freedom to explore alternative component designs, allowing components to be manufactured economically that are optimised to reduce weight and improve performance (Figure 2-4 front). This is particularly attractive for the manufacture of aerospace components, as weight reductions reduce annual fuel consumption by $55 dollars per lb, which equates to $1375 per lb increased revenue for an aircraft's service life [30].

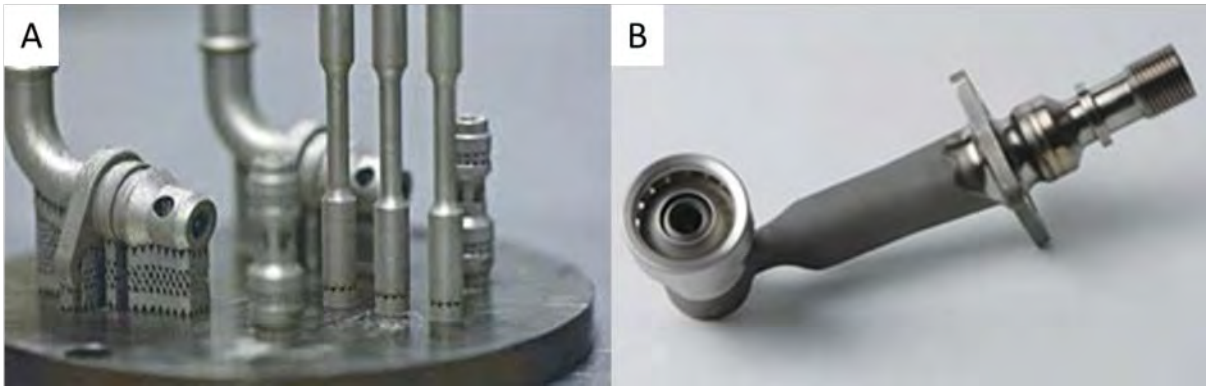

Figure 2-5 - A) Small engineering components manufactured using the Selective Laser Melting (SLM) additive manufacturing method B) Jet engine fuel injection nozzle, similar to those manufactured using additive methods [30].

In 2013, GE aviation announced that they had signed an Additive Manufacture co-operative agreement with Sigma labs, with the intention of producing over 100,000 additively manufactured aero-engine components by 2020, for their LEAP^{TM} and GE9X engines. These components are primarily fuel nozzles (Figure 2-5B), which are reportedly 25% lighter and 500% more durable than traditionally manufactured nozzles [31].

Work conducted by the US air force research laboratory has shown that by incorporating additive manufacturing into the production of aero-engine casings, it is possible to reduce the cost of manufacture by approximately 30% [32] while at the same time achieving a reduction in part size and weight. Similarly, Lockheed martin investigated the use of additive manufacture methods for the production of Ti-6Al-4V Bleed Air Leak Detector (BALD) brackets for the joint strike fighter platform, demonstrating that the buy-to-fly ratio could be reduced from 33:1 to just over 1:1, with a 50% decrease in manufacturing costs [33].

In 2006, the European Commission funded a large collaborative project known as "FANTASIA", which aimed to develop flexible and near net shape generative manufacturing chains and repair technologies for complex shaped aero-engine parts. This €6.5m project was led by Fraunhofer ILT in Germany, with the stated goal of reducing the repair costs and lead time by 40%.

This project demonstrated how additive manufacturing technologies may be used for the repair and manufacture of high value engine components, such as High Pressure Turbine (HPT) casings and shrouds, worn bearing races on the High Pressure Compressor (HPC) drum, and for the deposition of blades directly onto a powder metallurgy manufactured turbine disk, to produce a bladed disk (BLISK) at reduced cost [34].

2.4 Laser Metal Deposition (LMD) overview

Laser metal deposition is a "blown powder" additive manufacturing process (Table 2-1) that uses a laser beam to melt and deposit a metal powder onto the surface of an appropriate substrate material [Figure 2-6]. The metal powder is blown using an inert gas into the melt pool created by the laser, using a specially designed powder delivery nozzle, accurately aligned to the laser to ensure optimum powder capture. When the powder enters the melt pool, it is melted and assimilated into the liquid, causing the volume of melt to increase.

As the laser beam moves along its prescribed toolpath, the liquid solidifies proud of the surface, creating a raised track of material. By overlapping parallel tracks and layering tracks on top of each other, it is possible to create raised features on the surface of the substrate to a near net shape.

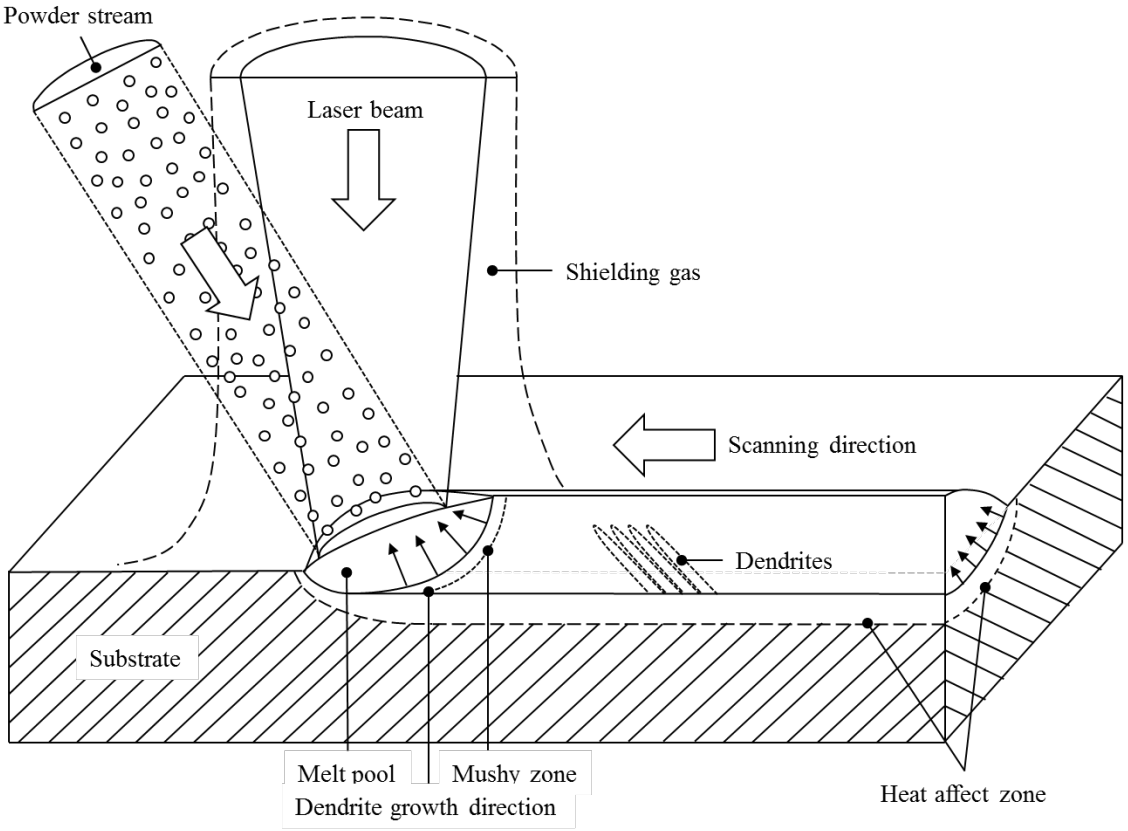

Figure 2-6 - Schematic illustration of the laser metal deposition process

2.4.1 Laser metal deposition applications

2.4.1.1 Deposition of simple freestanding solid components (original part manufacture)

Laser metal deposition of components onto a sacrificial substrate material is a potential manufacturing route for a range of materials and components that require the efficiency or properties produced by the process.

However, complex internal features and overhangs are difficult to produce through blown powder laser metal deposition, as there must be material to support the melt pool that is formed by the laser. If there is insufficient material to support the melt pool, then the deposition process will rapidly become unstable and the geometry of the deposit will deteriorate. However, simple solid parts with low angle side-walls are relatively easy to manufacture in a wide variety of materials using laser metal deposition and simple 3 axis manipulation [19].

More complex components, such as shown in Figure 2-7, can be deposited by changing the angle of the workpiece relative to the cladding head using a 5 axis manipulator. This ensures that the stream of powder is not being affected by gravity, and the melt pool is always supported.

Figure 2-7 - Laser metal deposition manufacture of helicopter engine combustor housing using 5-axis Trumpf DMD machine at TWI Yorkshire [20]

2.4.1.2 Deposition of functional coatings or features onto existing parts (Hybrid manufacture)

By using LMD as a supplemental process within a manufacturing route, it is possible to simplify the entire process and eliminate unnecessary and expensive steps. For example, landing gear struts for aircraft are conventionally manufactured by forging a billet of material through multiple stages, with each stage refining the shape and features of the part [24]. In order to produce the numerous bosses, flanges and extrusions that are part of the design, expensive closed die forging and machining steps are required.

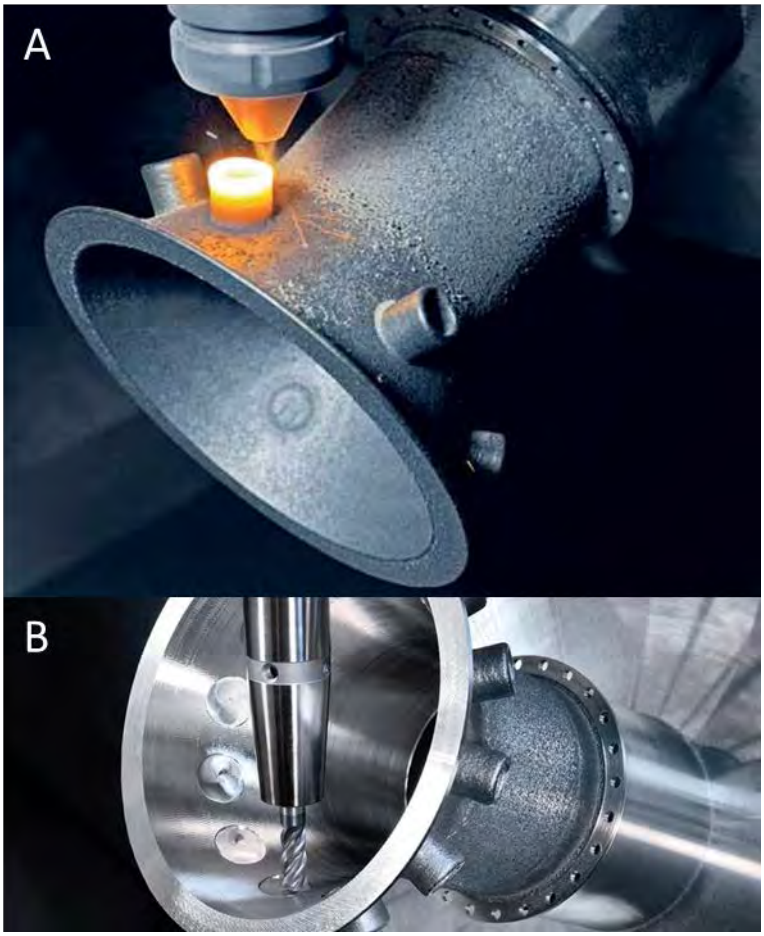

Figure 2-8 – A) LMD of features onto component as part of a hybrid manufacturing route B) Combined laser metal deposition and machining [35]

Alternatively, by taking a simply formed component, with none of the bosses, flanges and extrusions worked into it, and using LMD to build up the desired features to a near-net shape, then you have eliminated a number of expensive and time consuming steps from the manufacturing process. This process is known as hybrid manufacture, because it is a combination of conventional subtractive and additive manufacturing methodologies.

Although the laser deposition process is capable of producing near net shape deposits, the surface finish and geometrical accuracy of the deposited part generally requires that some degree of post processing is performed (milling, grinding, drilling, tapping, etc.) before they can be put into service.

Over the past several years, a number of systems have come onto the market that are combined 5-axis CNC machining centre and laser deposition cell (Figure 2-8), with one system manufactured by hybrid manufacturing technologies ltd being capable of retro-integration with existing CNC machining centres [35]. These systems allow components to be loaded into a fixture within the processing cell, and then a scanning probe measures the outer surfaces and generates a CAD file, from which a deposition and machining toolpath is generated based on the desired final geometry [36].

Component scanning and adaptive toolpath generation [37] correct for thermal distortion in the part, ensuring that the machining toolpaths are accurate and the final parts are of a repeatable quality.

The degree of automation and repeatability of these systems make it suitable for high volume repair and hybrid manufacturing processes of small components, such as aero-engine turbine blades, with the potential to generate large savings in materials and manufacturing costs.

2.4.1.3 Repair of damaged parts

Unlike conventional fusion processes, such as GTAW, laser metal deposition allows extremely tight control over the size of the fusion zone, and the amount of heat being introduced into the component. The result of this is that laser metal deposition is capable of tailoring the microstructure of the deposited part to meet the requirements of the repair, whilst avoiding the introduction of cracks or the disruption of the microstructure.

For example, single crystal turbine blades are manufactured using a complex investment casting process that eliminates all but one of the crystals, in order to eliminate grain boundaries and improve creep strength. Over time the tips of these blades will become worn, and must be repaired or replaced.

Laser metal deposition has been used extensively for single crystal and directionally solidified turbine blade repair (Figure 2-9), as it is possible to control the heat flow and crystallisation texture, so that there is epitaxial growth across the fusion boundary, and the <001> crystallographic microstructure is maintained [38,39]

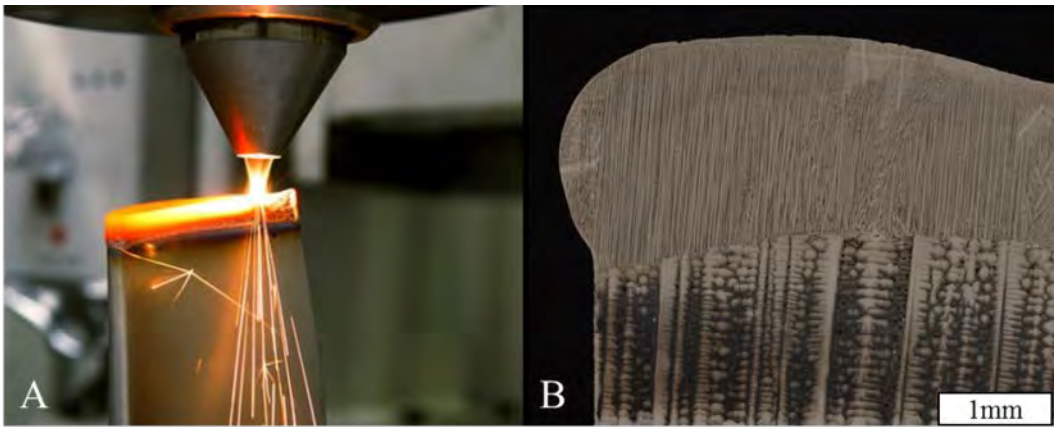

Figure 2-9 –A) Laser metal deposition repair of damaged turbine blade [39], B) Repair microstructure for directionally solidified turbine blade, showing epitaxy of deposited material [40]

2.4.1.4 Functionally graded layers

By using multiple powder sources of differing alloy content, it is possible to gradually vary the composition of the deposited material over multiple layers. This may be performed in order to reduce the interfacial stresses between a substrate and a coating, reduce the galvanic potential at the interface that may have led to accelerated corrosion, or it may be to provide different properties to different parts of a component, such as improved toughness, corrosion resistance, hardness or wear resistance.

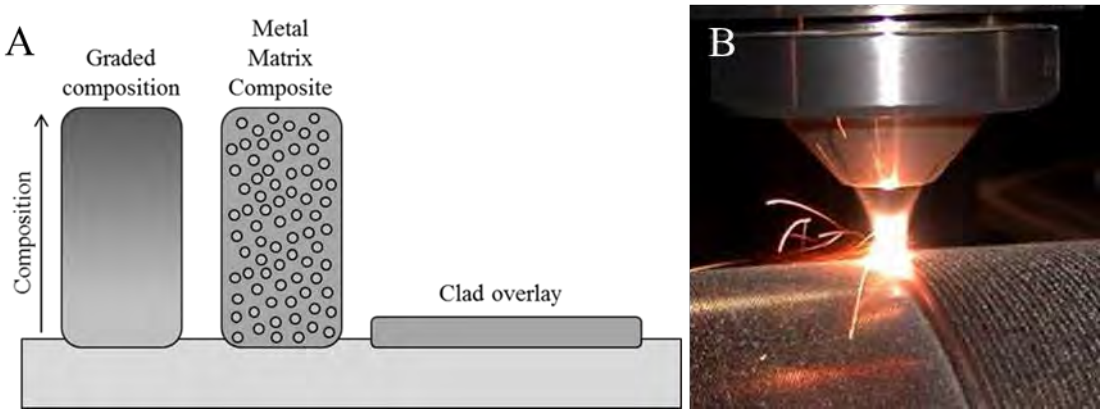

Figure 2-10 – A) examples of functionally graded layers produced using laser metal deposition B) Laser clad overlay being deposited onto rotating shaft using a coaxial nozzle [0]

Laser metal deposition is also a viable method for the manufacture of metal matrix composites (MMC), in which hard reinforcement phases, such as carbides or oxides, are held within the matrix of a lower melting point metal (Figure 2-10). By co-feeding the reinforcement phase with the matrix powder, the laser heating of the melt pool is sufficient to melt the matrix powder, but leave the reinforcement particles intact [41]. However, correct heat input from the laser is critical to ensure the reinforcement material is not melted and absorbed by the matrix.

This method can also be used to perform micro-alloying, in which different composition feedstock powders are fed to the nozzle, where they are melted by the laser to form a deposit with a composition that is equal to the sum of the individual powder feedstocks.

2.4.2 Laser Metal Deposition equipment

2.4.2.1 Powder delivery nozzles

In many systems, the powder delivery nozzle is mounted coaxially to the laser beam, so that the laser passes through an aperture in the centre of the nozzle (Figure 2-11A,B). This allows powder to enter the melt pool from multiple angles, giving the process the flexibility to move in virtually any direction. Side feed nozzles are more application specific, as they are only suitable for single direction deposition (Figure 2-11C) [19,25].

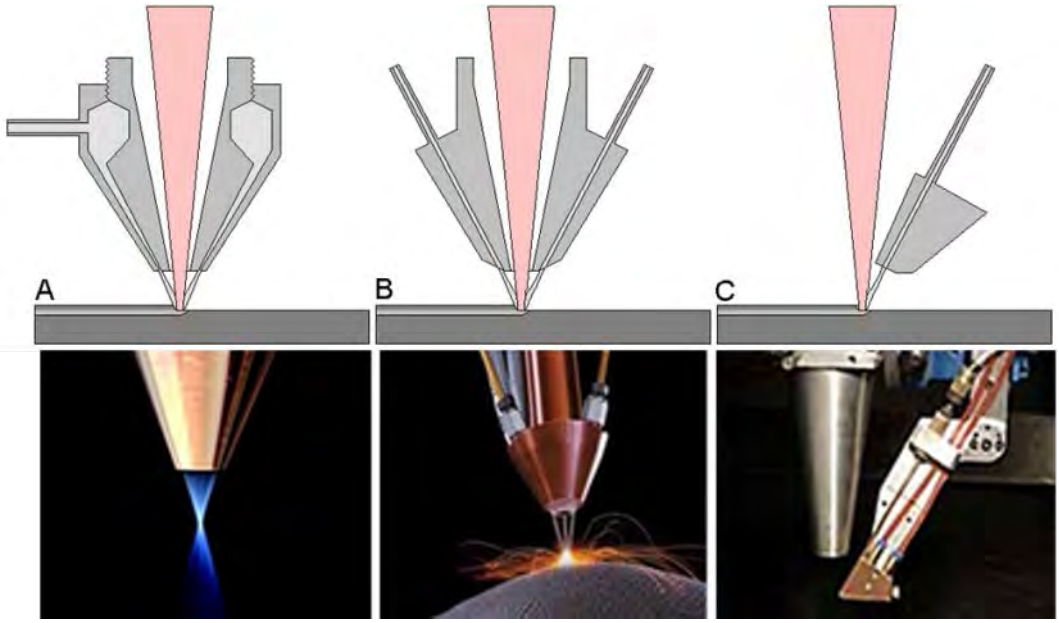

Figure 2-11 - A) Conical flow coaxial nozzle B) Multiple stream coaxial nozzle C) Side need nozzle [19,25]

2.4.2.1.1 Conical flow coaxial nozzles

These nozzles comprise of a pair of concentric cones with truncated tips, typically made from brass or copper (Figure 2-11A). These are placed concentrically to each other, so that a narrow annulus is formed between the inner and outer surfaces. Powder is injected into this annulus in several locations, whereupon the gas pressure forces the powder towards the ring shaped opening at the end. When the powder exits the nozzle, it forms a hollow cone of powder that comes to a focal point some distance from the nozzle tip.

The laser beam and shielding gas are fed coaxially through the central aperture of the nozzle, with the shielding gas serving to protect the melt pool from the atmosphere, as well as producing a positive pressure within the nozzle that prevents powder or fumes from settling on the internal optical elements.

Through correct selection of powder size and by adjusting the annulus gap, lateral cone position and gas flow rates, it is possible to achieve an extremely fine powder focus, enabling deposition of features down to 0.5mm in width.

While this type of nozzle can produce excellent results, it is fairly delicate and should not be used at laser powers greater than 1000W due to the danger of the thin conical sections overheating and melting. Similarly, if the nozzle collides with the workpiece the thin edges of the cones can become deformed, introducing turbulence that scatters the powder focus [25].

2.4.2.1.2 Multiple stream nozzles

These nozzles are generally fabricated from a single piece of copper or brass, with a central aperture for the laser, and powder delivery tubes drilled at a fixed angle so that when powder is blown through them, they converge at a fixed distance from the nozzle tip (Figure 2-11B). As this type of nozzle can be made from a single piece of material, there are no thin sections that can become melted or dented, and no adjustable parts that can become misaligned. This makes the multiple stream nozzle variant suitable for applications that require high laser powers and high build rates.

2.4.2.1.3 Side feed nozzles

These nozzles are commonly used in applications that require only a single deposition direction (Figure 2-11C), such as cladding of constantly rotating shafts. This has the advantage of allowing the powder stream to enter the melt pool at the optimum angle and position, to ensure peak deposition efficiency and deposit quality. This is illustrated schematically in Figure 2-6, which shows a single stream of powder entering the leading edge of a melt pool. If the powder was injected from the trailing edge, some of the powder would impact on the solidified track instead of the melt pool, decreasing the deposition efficiency and surface finish of the part.

2.4.2.2 Powder feeder

Modern powder feeders for laser metal deposition are typically based around the rotating disk design, in which a hopper doses out a stream of powder into a groove in a rotating disk (Figure 2-12**)**. The rate of powder mass delivery is adjusted by the speed of rotation of the disk, with faster rational speeds producing greater mass flow rates. Inert gas such as argon is used to keep the hopper at a positive pressure of approximately 1.5 bar, which both protects the powder oxidation, as well as providing the gas flow required to move the powder. Most powder feeders have the option of a heated jacket for the hopper, which prevents moisture pickup.

As the track of powder on the disk rotates, it passes beneath an outlet port (powder pick-up) and the positive pressure within the hopper causes the powder to be ejected. Flexible, anti-static polymer tubing carries the powder from the outlet port of the powder feeder to the deposition nozzle, where it is supplied to the process.

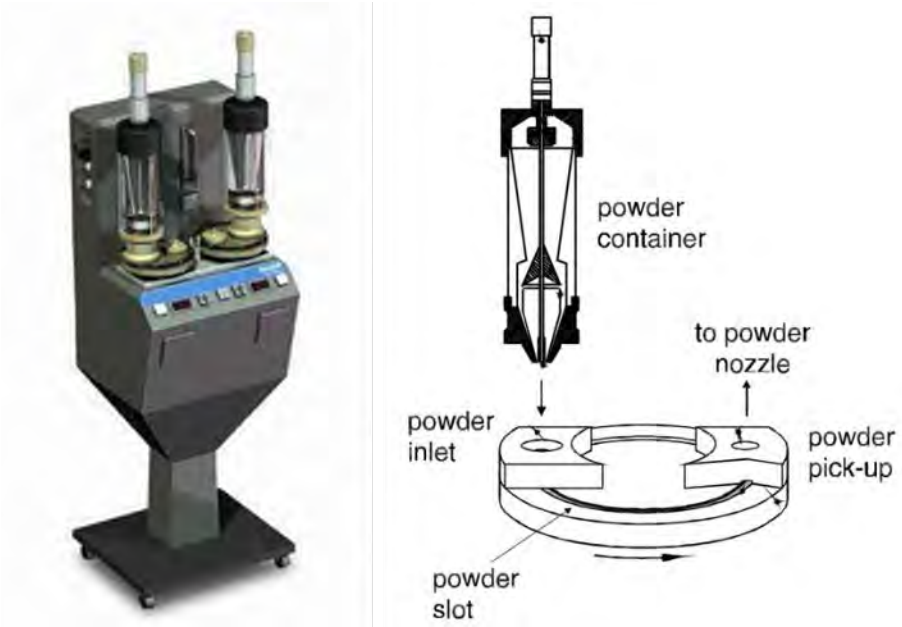

Figure 2-12 – Sultzer-metco twin-10C dual hopper powder feeder [25]

2.4.3 Metallurgical advantages and disadvantages of Laser Metal Deposition

Advantages

- The laser beam has a much higher energy density than other fusion processes such as arc, meaning it is capable of causing melting and fusion without adding excessive heat into the substrate or deposited material. This results in less disruption to the microstructure of the substrate material, a smaller heat affected zone and less distortion.
- The high focusability of the laser source means very fine and accurate features can be produced, with features of less than 0.5mm being possible.
- It is possible to accurately control the laser power, allowing close control over the heat flow characteristics. By controlling the heat flow, it is possible to control the microstructure, allowing deposition and repair of materials otherwise considered difficult or impossible, such as single crystal nickel superalloy turbine blades.
- The rapid heating and cooling of the melt pool in addition to its small melt volume, means that the size of the nucleated grains will be relatively small, and with less segregation of alloying elements when compared to casting and conventional arc welding processes.

Disadvantages

- High cost of capital equipment, which discourages more widespread adoption in industry.
- Poor repeatability in mechanical properties between different machines or powder batches when using identical processing parameters. This is due in part to variation in powder particle size distribution, morphology, chemical composition, atomisation method, etc. This poor repeatability decreases the confidence in the technology.
- Limited availability of materials in powder form, and high variation in powder quality and classification between manufacturers
- The link between deposition parameters and mechanical properties is not fully understood
- Difficult to deposit complex components with internal cavities or overhangs
- Relatively low deposition rate compared to conventional arc processes, which when combined with the high cost of capital equipment make the process very expensive.

2.4.4 Process variables and their influence on deposit quality

There are a great number of process variables that influence the quality of a deposited part, and accurate control of these variables is an important consideration if predictable and repeatable results are to be obtained. Figure 2-13 illustrates how these process variables contribute to the deposit quality, and Table 2-2 lists some of the values by which a laser deposit quality is determined.

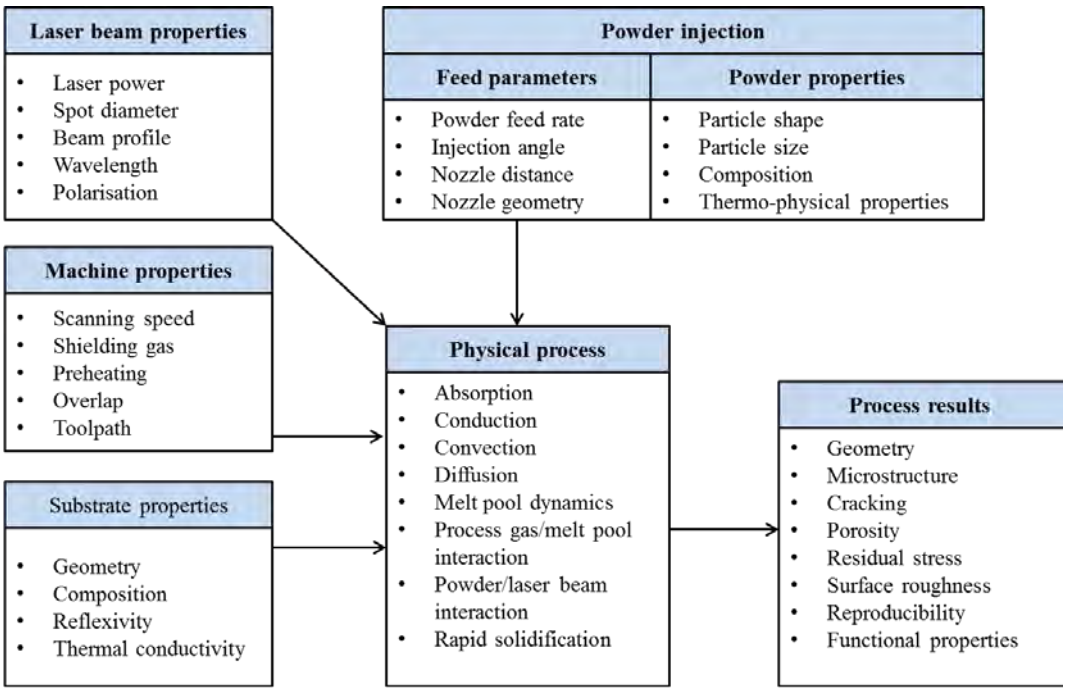

Figure 2-13 – Variables in laser metal deposition [42]

Table 2-2 - Factors by which the quality of a laser deposited part may be judged [25]

Geometrical properties	Mechanical properties	Metallurgical properties	Qualitative properties
Deposit dimensions	Hardness distribution	Microstructure	Porosity
Dilution	Residual stress	Dilution	Cracking
Surface roughness	Wear resistance	Grain size	
	Tensile strength	Homogeneity	
	Toughness	Corrosion resistance	

2.4.4.1 Laser power

Laser power has a significant effect on the deposition efficiency and surface finish, as well as the height and width of the deposited tracks. As laser power increases, so too does track width, improving the surface finish of the deposited part as there is more energy available for full melting of the incident powder particles [43,44]. This results in a limited increase in deposit height, when scanning speed, powder feed rate and laser spot size are kept constant, but causes a decrease in deposit height as the degree of melting of the substrate increases [45].

If excessive laser powers are used, this can lead to melt pool vaporisation, with a subsequent increase in laser power absorption and the formation of a keyhole (Figure 2-14), which is desirable for laser welding of thick sections, but extremely undesirable for laser metal deposition due to the turbulence and instability of the melt [46].

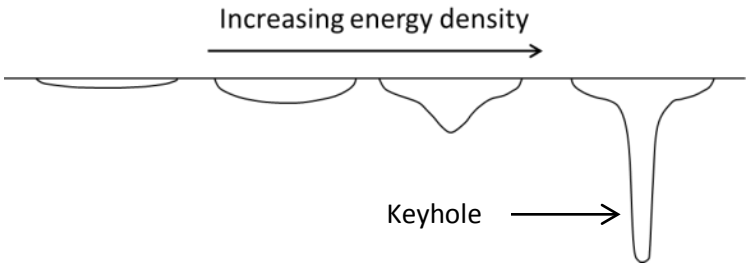

Figure 2-14 – Effect of energy density on the melt pool interface shape, with low energy density producing a shallow melt pool and high energy density producing keyholing

Conversely, if the laser power is not high enough, then there may be insufficient energy to cause melting and deposit fusion, which may lead to poor deposit density and adhesion to the substrate [45,46].

2.4.4.2 Laser spot size and beam profile

For a fixed laser power, small spot sizes produce a higher energy density that may lead to vaporisation of alloying elements and excessive penetration of the melt pool. The reduced size of the melt pool also decreases the capture area for powder particles, decreasing the process efficiency and build rate. Large laser spot sizes decrease the energy density for a fixed laser power and scanning speed. Matching a large spot size with a higher laser power results in a broad, shallow melt pool that has a higher capture area of powder particles, increasing the efficiency of the process

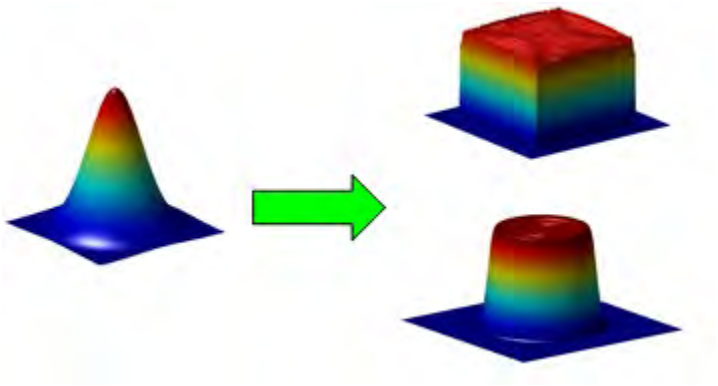

Figure 2-15 – Illustration of different laser beam profiles produced using diffractive optical lenses [49]

The distribution of energy over the width of the beam is also an important parameter, which can be tailored by using specialised laser optics that can shape the beam into a variety of profiles and energy distributions (Figure 2-15). This can be very advantageous in laser material processing applications, as it allows heating and cooling rates across the interaction area to be controlled, which can improve such parameters as build rate, deposit dilution and grain structure [46].

2.4.4.3 Scanning speed

High scanning speeds result in less laser/material interaction time and a decrease in the heat input, increasing the laser power required to cause melting and fusion as well as the powder mass delivery rate required to produce a deposit of a desired geometry. Fast scanning speeds also change the shape of the melt pool from circular to teardrop shaped, which can result in undesirable grain structure than forms a crack prone centreline grain boundary [58].

Slow scanning speed may lead to excessive heat build-up in the material due to the longer laser/material interaction, while fast scanning speeds also help contribute to melt pool convection effects, such as Marangoni currents, that decrease the stability of the process due to disruption of the melt pool surface.

2.4.4.4 Specific energy

Because the effect that the laser beam has on the substrate is dependent on the laser power, interaction time and interaction area, an expression has been developed that combines laser power, scanning speed and laser spot size into a single parameter, termed the specific energy.

The equation for calculating specific energy (E) is given below, where P is laser power (Watts), D is the diameter of the laser spot (mm) and V is the scanning velocity (mm/s) [47].

$$E = \frac{P}{D.V} = [J/mm^2]$$

This is a rather simplistic approximation of energy input, which has been used by various authors to relate deposit quality to processing parameters, to varying degrees of success. From the equation it can be seen that the same energy density can be obtained by different combinations of laser power, scanning speed and laser spot size, but the shape, size and quality of the deposited parts will be vastly different.

2.4.4.5 Powder mass feed rate

The cross section of a single deposited track can generally be described by a circle, bisected by a chord that is representative of the width of the melt pool (Figure 2-16). High powder mass flow rates will result in more powder entering the melt, causing the volume of molten material to increase. Since the melt pool width remains relatively constant, an increase in deposit volume will result in the contact angle (θ) between the deposits changing (Figure 2-17).

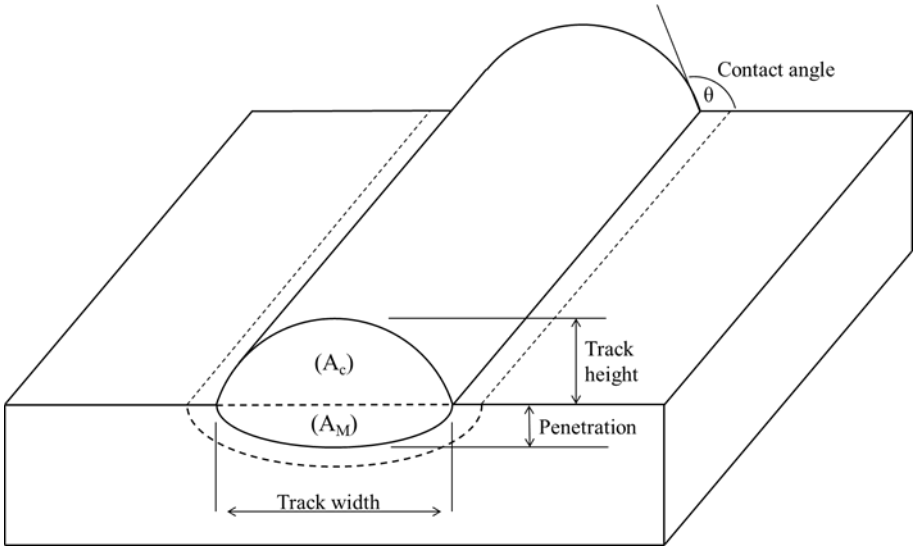

Figure 2-16 - Schematic illustration of a single deposited track

Increased powder feed rate also results in a decrease in effective laser energy, as the powder particles act to absorb a fraction of the incident laser light. Conversely, low powder feed rates would allow a greater fraction of the laser to interact with the substrate, increasing the depth of penetration, as illustrated in Figure 2-17 and Figure 2-18**.**

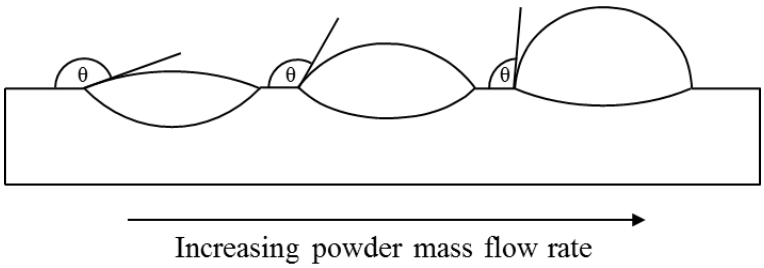

Figure 2-17 - Effect of powder feed rate on deposit geometry [25]

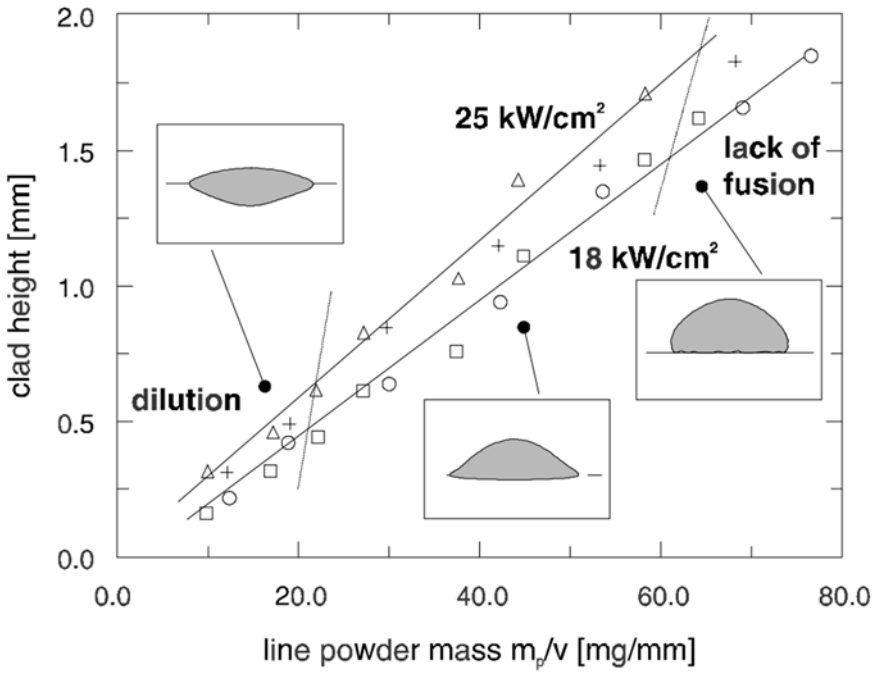

Figure 2-18 – Example of a process diagram produced by Kreutz (CITE) for the deposition of Stellite®, in which different powder feed rates produce different shapes tracks with different heights and penetrations [25]

2.4.4.6 Deposit dilution

Deposit dilution in a dimensionless measurement of the degree of mixing between the deposit and the substrate. During deposition, a melt pool is formed on the surface of the substrate, into which a metal powder is injected and melted. For laser cladding applications where a highly alloyed material is being overlaid onto a substrate of differing composition, the dilution between clad layer and substrate can produce undesirable results, including the formation of cracks, residual stresses, intermetallic phases, and accelerated corrosion. By

controlling the dilution, laser metal deposition has been demonstrated to allow deposition of dissimilar materials that would be very difficult using conventional fusion welding processes.

Various methods exist to measure the dilution of a deposit, one of which involves performing elemental composition measurements at different points within the deposit. Another relatively simple method is to simply cross section the deposit, and measure the area of deposit that lies above the substrate surface, and the area of melted material that lies below the substrate surface (Figure 2-19).

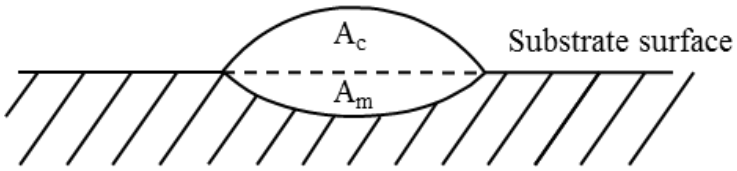

Figure 2- 19 - Illustration of deposit dilution

$$Dilution = \frac{A_c}{A_m}$$

The influence of various processing variables on the properties of the deposited part are summarised in Table 2-3, which illustrates the effect that increasing the processing variable has on the shape and properties of the deposit [19,25,29,34].

Table 2-3 – Influence of the increase in various process parameters on deposit properties (↑=increase, ↓ = decrease) [19,25,29,34]

Process variables	Properties				
	Clad height	Penetration	Dilution	Hardness	Deposit thickness
↑ Laser power	↓	↑	↑	↓	↑
↑ Scanning speed	↑	↓	↓	↑	↓
↑ Powder feed rate	↑	↓	↓	↑	↑
↑ Laser spot diameter	↑	↓	↓	↑	↓

2.4.5 Potential Processing defects

2.4.5.1 Cracking

Cracking can occur during laser deposition for a variety of reasons, and is covered in greater detail in section 2.5.3.

2.4.5.2 Porosity

Porosity can occur within the deposit for several reasons.

1) Gas bubbles can become entrapped in the melt pool during solidification, which may occur as a result of excessive melt pool agitation, porosity in the powder feedstock, or vaporisation of alloying elements, leading to the formation of gas pores [48].
2) Rapid melt pool solidification can lead to entrapped porosity, as the gas does not have sufficient time to escape the melt pool [48]
3) Contraction voids may form when isolated pockets of liquid are allowed to solidify separate from the remaining melt. The contraction stresses during solidification of the terminal liquid is sufficient to pull the semi-solid material apart, producing a contraction void [86].
4) Incorrect surface preparation can lead to contamination of the melt pool, which influences the surface tension and the bonding of the coating to the substrate
5) Overlapping tracks can lead to the formation of inter-run porosity if the deposit is excessively large, as this decreases the contact angle θ (Figure 2-20) and prevents full fusion of adjacent tracks (Figure 2-20) [46,48].

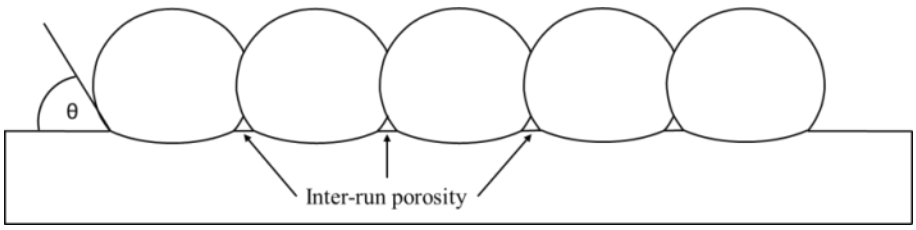

Figure 2-20 – Excessive build height leading to the formation of inter-run porosity

2.4.5.3 Distortion and residual stress

Although LMD is considered "low heat input", when compared to such processes as arc welding, the rapid melting of the substrate by the laser gives rise to very high thermal gradients, which when combined with dissimilar coating/substrate combinations, can give rise to thermal stresses. Since the yield stress (flow) of the material decreases with increasing temperature, plastic deformation can occur, leading to distortion. Once the heat source is removed, the residual stress remains in the material and can contribute to the formation of cracks [50,51,57].

An expression for the thermal stress (σ_{th}) is given below:

$$\sigma_{th} = \frac{E.\Delta\alpha.\Delta T}{1-v}$$

Where:

- σ_{th} = Thermal stress
- E = Elastic modulus of deposit material
- v = poisons ratio of deposit material
- $\Delta\alpha$ = Difference in linear thermal expansion between deposit and substrate
- ΔT = Difference in temperature between deposit and substrate

From this expression it can be see that if the temperature gradient is high, then the thermal stress will increase. Similarly, if the substrate and deposit materials have strongly differing linear thermal expansion coefficients, then the thermal stress will also increase.

For the cladding of dissimilar materials, this expression is a simple way of explaining the generation of stress fields that may lead to distortion or cracking. However, this explanation is rather simplistic and does not account for such factors as phase change due to melting, volumetric contraction during solidification or during solid state phase transformations, etc.

Much work has been conducted on the use of Finite Element Analysis (FEA) to model and predict the stresses and deformation that may be generated during laser metal deposition [50-56]. Studies into the stress distribution in simple shapes, such as those conducted by Kamara [50] showed that the deposited material experiences a residual *tensile* stress following deposition, while the substrate experiences a residual *compressive* stress.

2.5 The metallurgy of Nickel Base Superalloys

2.5.1 Nickel superalloy phases

The application of a superalloy component will determine what sort of microstructure it will have, for example, the microstructural requirements of a turbine disk and a turbine blade will be very different, as each component is exposed to different temperatures and stresses.

The turbine disk is subjected to low cycle fatigue from high loads during take-off and landing, which necessitates the use of a fine grained equiaxed microstructure [59,60]. This microstructure is well suited to fatigue resistance, but has poor resistance to creep at high temperatures, due to the large number of grain boundaries that act as diffusion pathways for mass transfer.

In comparison, turbine blades which are exposed to the hottest part of the gas stream, rotating at high speeds and experiencing high centrifugal stresses, require a microstructure that is strong enough to withstand the centrifugal stresses as well as withstanding creep. Directional solidification and single crystal casting development met these requirements by eliminating transverse grain boundaries, or eliminating grain boundaries entirely [61,62].

The primary constituent phases of most modern nickel superalloys are:

1) γ phase – Face Centre Cubic austenitic structure
2) γ' phase – Intermetallic precipitates with an ordered $L1_2$ structure
3) Carbides

2.5.1.1 The γ phase

The γ phase forms the matrix of the superalloy, consisting primarily of nickel, with the addition of alloying elements to improve strength. Pure nickel has a Face Centre Cubic (FCC) crystal structure, which can be represented as a cube with atoms on each corner, and the centre of each face (Figure 2-21) [9,57].

This phase can be strengthened to an extent by the random substitution of nickel atoms with other solute elements, such as Co, Cr, Fe, Mo, W, Ta and Re. Due to the difference in size between these solute atoms and the nickel atoms, they will cause the lattice to deform elastically around the solute, creating a tensile or compressive strain field which impedes dislocation motion and improves strength [67].

This strengthening mechanism is known as solid solution strengthening, as the solute atoms that contribute to the lattice distortion increase the strength without precipitating out to form a secondary phase.

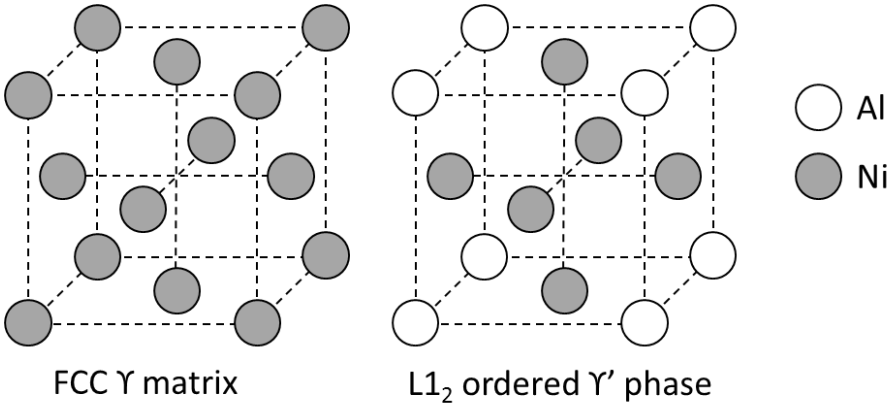

Figure 2-21 – lattice structure of the FCC γ and L1$_2$ γ' phase [9]

Nickel superalloys that are strengthened predominantly by solid solution are generally easier to weld and fabricate, as there are far fewer secondary phases being precipitated that may decrease the strength and integrity of the weld.

2.5.1.2 The γ' phase

The largest strengthening effect for nickel alloys occurs due to the precipitation of the intermetallic phase γ', with the stoichiometry A_3B (where A may be nickel or cobalt, and B may be aluminium, titanium or tantalum)

$$\gamma' = (Ni,Co)_3(Al,Ti,Ta)$$

As illustrated in Figure 2-21, the γ' phase has an order $L1_2$ structure, with nickel occupying the face centres and Al or Ti occupying the corner points.

This phase precipitates coherently in the γ matrix phase in a cube-cube relationship, with low lattice misfit (δ). Lattice misfit is calculated using the equation below, where a_γ and $a_{\gamma'}$ are the lattice parameters for the γ and γ' phases respectively [67-73].

$$\delta = 2\,x\,\frac{a_\gamma - a_{\gamma'}}{a_\gamma + a_{\gamma'}}$$

As alloying elements such as Al and Ti partition to the γ' phase, the γ' precipitates grow larger. As γ' size increases, so too does the δ value, which influences the morphology of the precipitate [63]. Hagel and Beattie [56] identified that for δ between 0 and 0.05%, the precipitates are spherical, but between 0.5 and 1.0% the precipitates are cuboidal. For δ greater than 1.25%, the precipitates form plates [64], which can be very harmful to the creep strength of the material [66].

Segregation of alloying elements during solidification gives rise to regions of the microstructure of differing composition, as the dendrites reject alloying elements such as aluminium and titanium into the remaining liquid. This creates interdendritic regions and grain boundaries that are enriched in elements that contribute to the formation of γ'. The result of this is that γ' will precipitate within the grain boundaries and interdenritic regions first (Primary γ'), followed by the formation of secondary γ'[9,66,67]. This effect is illustrated in Figure 2-22, which shows a bi-modal distribution of primary and secondary γ'.

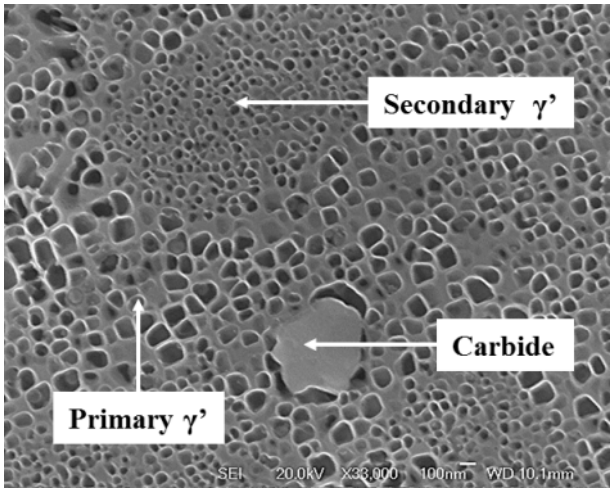

Figure 2-22 – SEM micrograph of CM247LC in the as- laser deposited condition, showing presence of primary and secondary γ' and MC type carbide (Micrograph produced by the author)

In precipitation strengthened nickel superalloys such as CM247LC, the high strength properties are due to the interactions between the dislocations and the γ' precipitates. In order dislocations to cleave a γ' particle, they must travel in partial-pairs due to the high energy penalty incurred by travelling through an ordered phase. These partial-pairs of dislocations are coupled by an anti-phase boundary, creating what is known as a super-dislocation [9,67].

The strength of a nickel superalloy and its ability to impede dislocation motion, is influenced by the size and volume fraction of the γ' precipitates. If the γ' precipitates are large, and spaced far apart, the dislocations find it easier to loop around them or bow past them. For small precipitates spaced close together, the dislocations find it easier to climb and bypass them rather than cut through. Modern superalloys aim to maximise the γ' volume fraction as much as is feasible, with some alloys containing approximate 70% γ' by volume [69]. By comparison, CM247LC contains approximately 62 vol% in its solution treated and aged condition [70].

2.5.1.3 Carbides

Carbides are important constituents of polycrystalline nickel superalloys, as they form within the grain boundaries and cause pinning, which reduces grain coarsening and boundary migration (sliding) at high temperatures (This is only relevant for polycrystalline and directionally solidified alloys, as single crystal castings do not have grain boundaries, hence do not require grain boundary pinning carbides) Different carbide types are observed depending on the composition of the alloy and the processing route taken. The most common carbides observed in nickel superalloys are listed in Table 2-4:

Table 2-4 - Common carbide phases present in superalloys

Carbide	Description
MC	High temperature carbide that is formed from the molten state, which has a course, random globular, blocky or script shaped microstructure. At elevated temperatures, the MC carbides decompose, releasing carbon that forms other carbide morphologies.
M_6C	Intermediate temperature carbide, with a complex cubic structure. They form when the Mo and W content is greater than 6-8 at%.
$M_{23}C_6$	Forms during lower temperature heat treatment, especially in alloys with moderate to large Cr content. Can form during decomposition of MC type carbides or by reacting with residual carbon in the matrix. Tendency to form along grain boundaries.

Carbides are formed in the molten stage during solidification due to the strong segregation of Carbon, which reacts with active elements such as Ti, Ta and Hf to form MC type carbides[71], where M stands for one or more metal atoms. During heat treatment and service, these MC carbides decompose to form other carbide phases such as $M_{23}C_6$ at 760-980°C and M_6C at 815-980°C [9].

Common reactions are:

1. $MC + Y \rightarrow M_{23}C_6 + Y'$
2. $MC + Y \rightarrow M_6C + Y'$

Carbides provide the best improvement to properties when they form discrete equiaxed phase at the grain boundaries, as this improves pinning. Depending on the chemistry, processing route and service history of the alloy, carbides can form continuous films at grain boundaries, which can be problematic, as they act as crack propagation pathways and reduce the ductility of the alloy [72,73].

During welding of superalloys, constitutional liquation cracking can occur within the grain boundaries of the heat affected zone. This can be attributed to the liquation of titanium rich MC carbide phases, which melt prematurely and wet the grain boundary, causing it to separate and form a crack [74].

The typical morphology of these carbides is illustrated in Figure 2-23, which shows how the microstructure of a cast nickel base superalloy has evolved over the years.

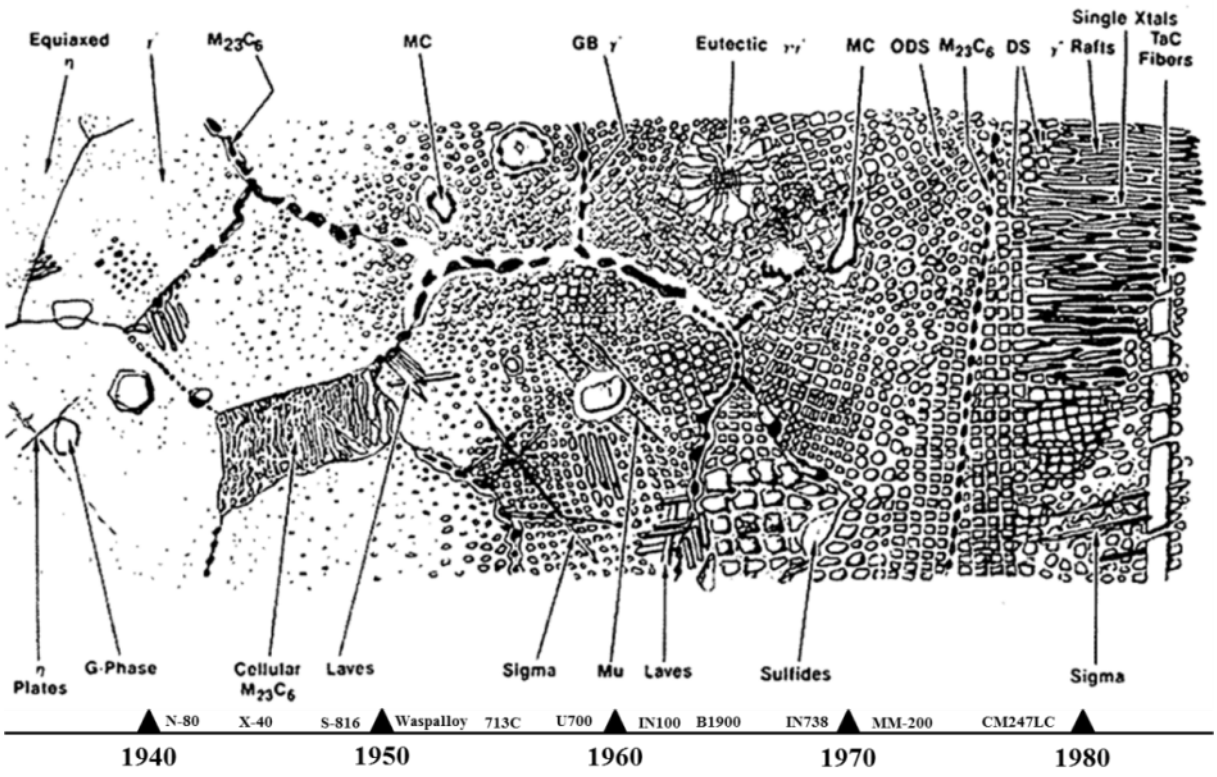

Figure 2-23 - Illustration of the microstructure of different generations of superalloys, including the phases that are to be found [67]

2.5.1.4 Undesirable TCP phases

As the demands for fuel efficiency and performance increase, the alloying of the high temperature parts becomes more complex. As the composition becomes more complex, it becomes more difficult to control and predict the formation of Topologically Close Packed (TCP) phases, such as σ, μ, and laves [9,75,76].

TCP phases are undesirable, as they decrease the strength and service life of the component by acting as crack initiation site, as well as tying up solid solution strengthening elements. Generally the short term (tensile) strength of TCP susceptible material are not influenced too greatly, but TCP phases have been shown to have a serious negative effect on long term creep strength [58,75,76].

Refractory elements such as W, Mo, Re, and Ta are added to superalloys as solid solution strengthens of both the γ and γ' phases, but high levels of these additions can lead to the formation of TCP phases during heat treatment or in-service. Other elements such as Cr, Fe, Nb, Co are known to form TCP phases [9]

TCP phases consist of close packed planes of atoms separated by layers of much larger atoms. These normally form as plates (appearing as needles in section), but can also appear as irregular or elongated globules

Table 2-5 lists several TCP phases, along with their crystal structure and chemical compositions.

2.5.1.5 Additional phases in superalloys

Table 2-5 - The chemistry and crystal structure of various phases present in a range of superalloy materials [9,67].

Phase	Structure	Formula	Description
M_3B_2	Tetragonal	(Ta, V, Nb, Mo, Ti, Cr, Ni, Fe)$_3B_2$ Mo_2FeB_2	Appears in NBS with greater than 0.03% B. Borides appear similar to carbides but are not attacked by preferential carbide etchants.
σ (TCP)	Tetragonal	Cr(Fe, Co) FeCrMo CrFeMoNi CrCo CrNiMo	Most commonly observed in iron-base and cobalt-base superalloys, but less commonly in nickel base superalloys. Forms after extended exposure to temperatures between 540-980^{o}C. Appears as irregular, and often elongated, globules.
MN	Cubic	(Ti, Nb, Zr)N (Ti, Nb, Zr)(C, N)	Observed in alloys containing Ti, Ni or Zr. Insoluble at temperatures less than melting point. Easily recognised as-polished, with square to rectangular shapes and yellowish colour.
γ''	BCT	Ni_3Nb	Principle strengthening phase in IN718, form as coherant disk shaped precipitates on the (100) plane. Too small to resolve using SEM, but observable using dark field TEM.
Laves (TCP)	Hexagonal	Fe_2(Nb, Ti, Mo) Co_2(Ta, Ti)	Common in iron-base and cobalt-base superalloys, appearing as irregular shaped globules, which appear elongated or in the form of platelets after periods of high temperature exposure.
η	HCP	Ni_3Ti	Found in alloys with high Ti/Al ratios. May form intergranuluarly in cellular form or intergranularly as acicular platelets in a widmanstatten pattern.
μ (TCP)	Rhombohedral	Co_2W_6	Observed in alloys with large quantities of Mo or W. Appears as course irregular widmanstatten platelets at high temperatures

2.5.2 The effect of alloying elements on the microstructure

Nickel superalloys tend to have a rather complex alloying chemistry, with some alloys containing over 10 different alloying elements. These are added to improve such properties as high temperature strength, ductility, creep resistance, corrosion resistance, oxidation resistance, castability and formability. Table 2-6 explains the role of different alloying elements on the performance of various superalloys, while Table 2-5 describes various other phases that may be present in nickel and nickel/iron based superalloys.

Table 2-6 - Condensed list of the role of various alloying elements on the properties of nickel superalloy [9,67]

Element	Contribution
Ni	Forms the austenitic FCC matrix, γ (Gamma)
Cr	Improves corrosion resistance and promotes topologically close packed phases, along with providing moderate matrix strengthening and a moderate increase in γ' volume fraction. Also creates the grain boundary carbides $M_{23}C_6$ and M_7C_3. Although it improves oxidation resistance, excessive amounts may lead to the formation of TCP phases σ and μ so its use should be limited.
Co	Decreases the solubility limit of Aluminium and Titanium in the matrix, encouraging higher volume fractions of γ' precipitation, raises the γ' solvus temperature, improves sulphidation resistance and contributes to solid solution strengthening of the γ matrix. Lowers the stacking fault energy, which reduces dislocation motion and creep at high temperatures. May also aid forgeability
Mo	Strong Contribution to solid solution strengthening of the γ matrix, as well as helping to lower diffusivity of precipitation hardening elements such as Ti, which lowers the tendency for γ' particles to coarsen over time at high temperatures. Can also form $M_{23}C_6$ and M_6C carbides.
W	Strong contribution to solid solution strengthening of the γ matrix, and a moderate increase to γ' volume fraction. In addition, W helps to reduce diffusivity of precipitation strengthening elements in a similar way to Mo. Also forms MC, $M_{23}C_6$ and M_6C carbides. Promotes topologically close packed phases σ (Tetragonal) and μ (Rhombohedral).
Ta	Strong contribution to solid solution strengthening, as well as providing strengthening through formation of high melting point TaC carbides. Approximately 75% of the Ta preferentially segregates to the γ' phase and interdendritic region reducing the tendency to hot tearing in directionally solidified alloys.
Al	Forms the ordered $L1_2$ phase γ', which provides the primary strengthening mechanism for nickel superalloys. Also improves oxidation resistance.
Ti	Also forms γ', taking the place of Al in the $L1_2$ unit cell
C	When added in quantities between 0.05-0.2% combines with refractory and reactive elements to form MC type carbide, that decompose during service or heat treatment to form lower carbides such as $M_{23}C_6$ and M_6C.
B	Typically added in small quantities (<1 wt%) in order to improve the creep rupture strength of a nickel superalloy by the formation of tetragonal M_3B_2 borides at grain boundaries, impeding grain boundary migration. Can be harmful to solidification crack formation, as it aggressively partitions to the solidification boundary, reducing the surface energy of the liquid and promotes wetting of the grain boundaries with a low melting point liquid film.
Zr	Improves creep properties and refines grain boundaries
Hf	Added as a grain boundary modifier, which refines and redistributes grain boundary carbides, as well as promoting grain boundary Y-Y' eutectic formation, which is thought to improve alloy ductility when present in low quantities. Hafnium also acts to scavenge up spare Oxygen and Nitrogen.
Re	Added to DS and SX nickel casting alloys to improve creep rupture properties by reducing the Υ' coursening rate at high temperatures. Quantities exceeding 6wt% are known to contribute to the formation of high rhenium content σ (sigma) phases in the nickel matrix through long exposure at high temperatures

2.5.3 Cracking in nickel superalloys

During manufacture, heat treatment and service, defects may be introduced into the structure of the component. These defects may be in the form of hard, refractory inclusions, undesirable phases, porosity, and cracks. Cracks are particularly hazardous because of the high stress concentration at the crack tip, which will cause the crack to grow under an applied load until the component fails catastrophically. As engine requirements become more demanding and alloy design becomes more complex, it has become increasing difficult to process these alloys without introducing cracks of one type or another. These cracks can be broadly classed into 4 main mechanisms:

- Solidification cracking,
- Grain boundary liquation,
- Ductility dip and
- Strain age cracking.

2.5.3.1 Solidification cracking

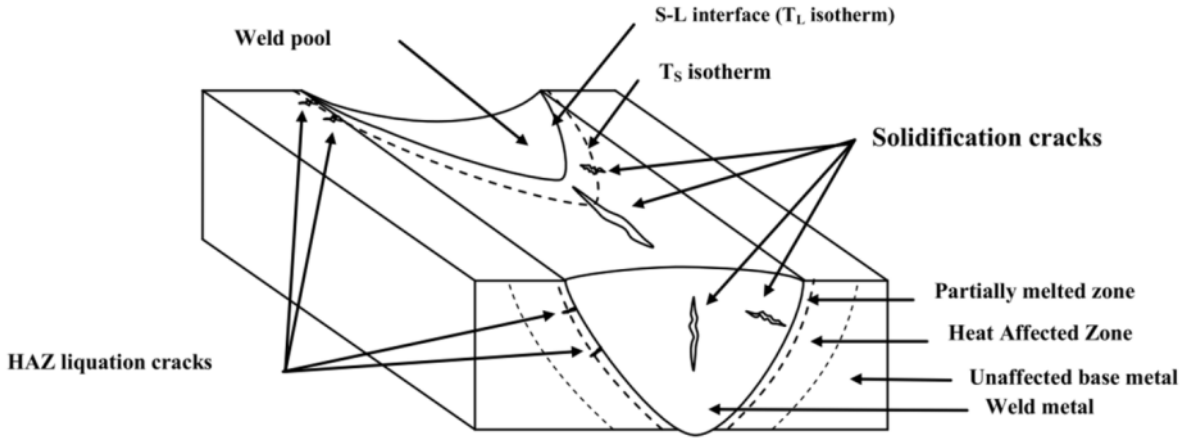

Figure 2-24 - Schematic illustration of various cracks that may form during welding [88]

In the early 1950s Pellini proposed the "strain theory" for solidification cracking [78], which stated that the solidifying metal grains are separated by a continuous liquid film. As the cooling material approaches the solidus temperature, the solidification stresses generated by localised thermal expansion and contraction surrounding the melt pool are appreciably higher, and the relatively weak solid/liquid boundaries separate to form an intergranular rupture.

The Shrinkage-brittleness theory [79] presented in 1948 proposed that the newly formed dendrites are incapable of accommodating the strain during solidification. Whereas Pelini proposed that the stresses are uniformly distributed, the shrinkage-brittleness theory suggested that the temperature range at which solidification cracking occurs is between the solidus temperature and the coherence temperature (the temperature at which the dendrites meet) and that if a critical strain is exceeded within this temperature range, and no liquid was available to in-fill, then a solidification crack would form. This suggested that alloys having a wide solidification temperature range being more prone to solidification cracking.

Work conducted by Borland [80] in the early 1960s proposed a generalised theory that was based around some of the previous work. In this theory he divided the solidification sequence into four stages [81]:

1. Primary dendrite formation, where movement of both solid and liquid phases is significant
2. Dendrite interlocking at the coherence temperature, involves the development of continuous formation of both solid and liquid phases, but motion is limited to the liquid only.
3. Grain boundary development at the critical temperature, where the semi-continuous network of dendrites restricts movement of the liquid, forming isolated pockets of liquid.
4. Solidification of the terminal liquid.

From this sequence, Borland suggested that cracks may form when the temperature drops below the coherence temperature, and is related to the critical solidification range of the alloy in stage 3, where the dendrites isolate pockets of liquid that are separated from the remaining melt and cannot be in-filled (Figure 2-25). This meant that as the critical solidification range increases, which is a function of the alloy chemistry, so too does the tendency of the material to form solidification cracks.

Other solidification cracking theories [85-91], with the factors identified that are known to affect solidification cracking susceptibility listed below:

- The solidification temperature range
- The distribution and quantity of liquid during the final stages of solidification
- The primary solidification mode (equiaxed, dendritic, etc.)
- The surface tension of the grain boundary liquid
- The grain structure

Elemental segregation during solidification was identified as a critical factor for solidification cracking, which occurs due to the rejection of solute elements from the solid phase into the liquid phase due to limited solid solubility. As segregation occurs during solidification, the melting temperature of the remaining interdendritic liquid becomes suppressed, and can form eutectic compositions that act to wet the grain boundaries and weaken the material.

It is generally accepted that a fine equiaxed grain structure is less susceptible to solidification cracking than a columnar microstructure[89], which is due to the better accommodation of strain, ease of liquid in-fill for crack healing, and reduced scale of segregation [58].

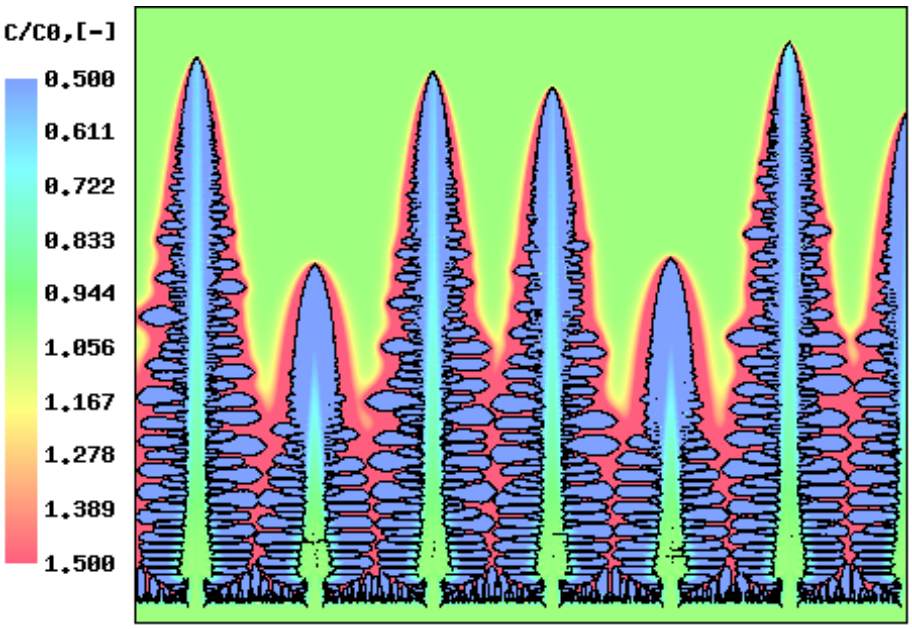

Figure 2-25 - Computer simulation of cooperative dendrite growth [81], illustrating elemental segregation during growth, and formation of interdendritic regions of different composition to the dendrite trunk

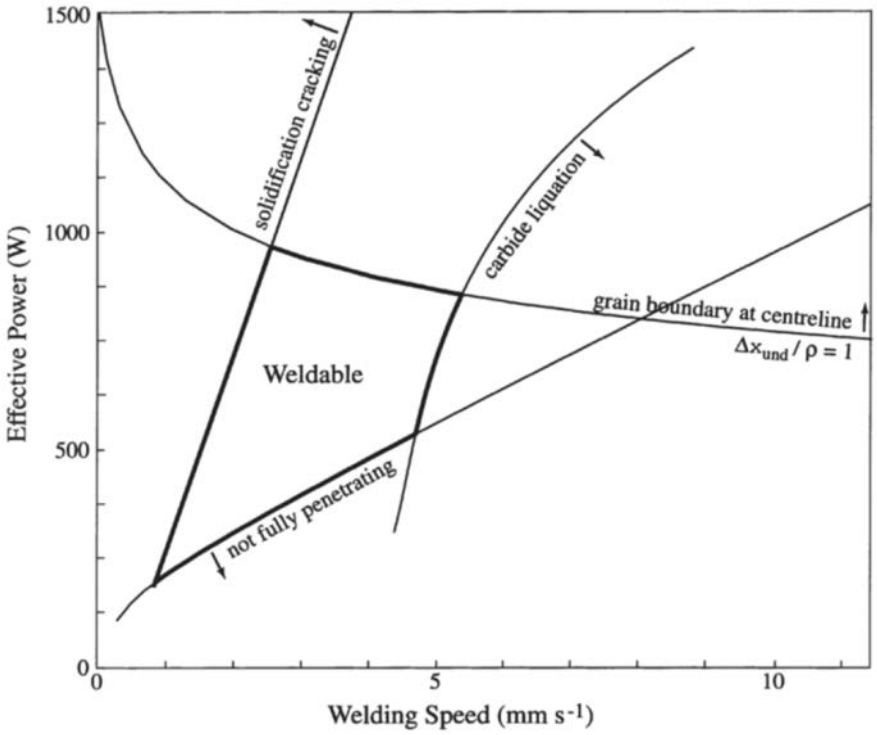

Figure 2-26 - Weldability map illustrating the weldable regime formed by excluding regions where 1) full penetration of the weld bead does not occur 2) A centreline grain boundary is predicted 3) Liquation occurs around carbides in the heat affected zone 4) solidification cracking is predicted [58]

2.5.3.2 Liquation cracking

This typically originates in the HAZ adjacent to deposits, due to the dissolution of grain boundary phases under rapid heating. The dissolution of the grain boundary phases occurs at too high a rate to allow full dissolution into the surrounding matrix, forming a low melting point eutectic along the grain boundary that fails under applied tensile stress (Figure 2-27) [82,89].

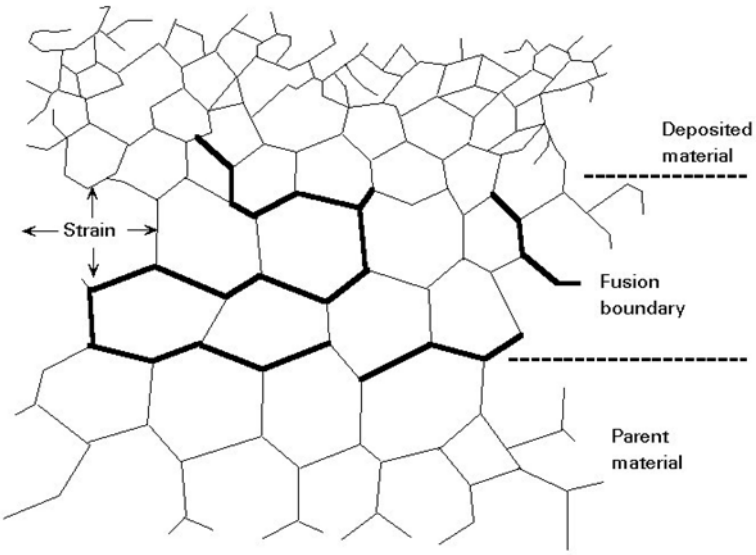

Figure 2-27 - Schematic illustration of liquation cracking

A solution treatment to anneal the material and reduce the hardness, combined with fine grains are preferred to materials with large grains in an aged condition, with fine grains being better able to accommodate the strains developed during welding or deposition [89], and the larger surface area of grain boundaries reduces the stress intensity on the grain boundary triple points, which are the most susceptible sites for crack nucleation [77]. Finer grains also reduce the scale of elemental segregation during solidification, which results in thinner liquid films on the grain boundaries [90]

Reduction in impurity levels and refinement of the microstructure lead to improved liquation resistance, but for investment cast components, the grain size tends to are generally much larger than for wrought or PM produced components.

2.5.3.3 Strain age cracking

Also known as reheat cracking, this mainly occurs in γ' precipitate strengthened alloys during post weld heat treatment or high temperature service [83]. Defects appear as intergranular micro-cracking either in the HAZ or the deposit itself with carbides acting as crack initiation sites [84]. In some alloys, as γ' precipitates within the γ matrix, the negative lattice mismatch causes a volumetric contraction of the grain, putting the grain boundaries under tensile stress, leading to cracking. The susceptibility of an alloy to strain age hardening can be qualitatively assessed by using a weldability assessment diagram, which plots the Al and Ti content of an alloy (Figure 2-28) [9,67]. These two elements contribute to forming the strengthening γ' strengthening phase, which is essential for high temperature performance. Alloys with an Al + Ti content greater than 4wt% are considered difficult to weld, due to these elements causing a higher volume fraction of γ' to precipitate, however this does not take into account variations in the microstructure that may arise from different thermo-mechanical processing or heat treatments.

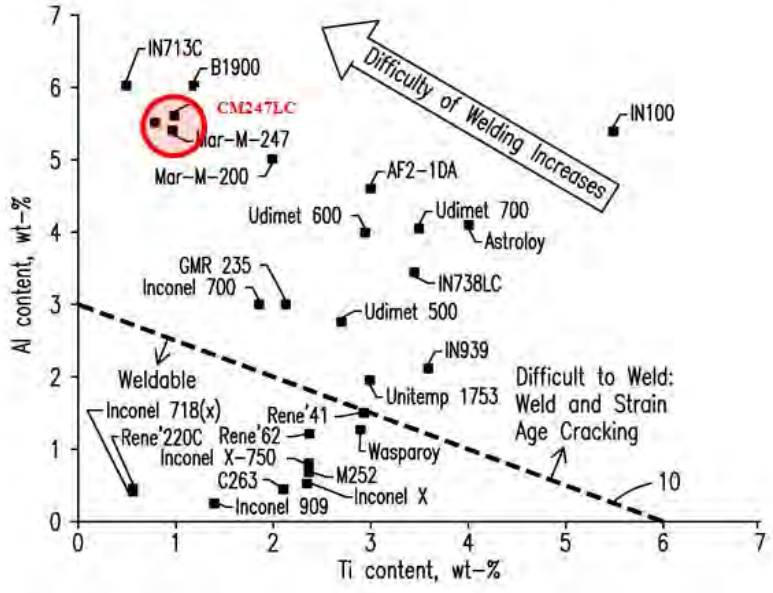

Figure 2-28 - Weldability assessment diagram for various precipitation strengthened Nickel based superalloys [9]

2.5.3.4 Ductility dip cracking

Ductility Dip Cracking (DDC) is an intergranular, solid-state cracking mechanism that occurs due to loss of ductility within a certain temperature range below the alloy's solidus temperature (Figure 2-29). This cracking mechanism has been reported in various alloy systems including stainless steels [91,92] , Ni-base alloys [93-95], aluminium alloys, copper alloys and titanium alloys [96]. This is believed to be due to a combination of the macroscopic thermal and solidification stresses generated at elevated temperatures, and the microscopic stresses generated within the grain boundaries due to the precipitation of partially coherent carbide phases. High chromium nickel superalloys, while resistant to corrosion and stress corrosion cracking, are known to be particularly susceptible to DDC.

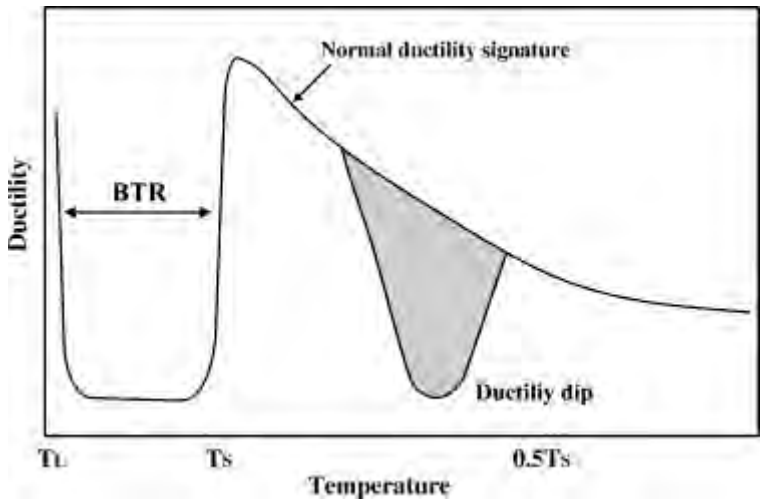

Figure 2-29 - Schematic illustration of ductility profile for an austenitic alloy, showing the intermediate temperature region where ductility dip occurs, the higher temperature Brittle Temperature Range (BTR) that is due to segregation cracking [92]

Susceptible alloys have a tendency to form a semi-continuous $M_{23}C_6$ carbide phase along the grain boundary, which is partially coherent with one side of the grain boundary, which Lim et al. [97] proved showed a cube on cube (100) $M_{23}C_6$ II (100) FCC alloy orientation, with low angle grain boundaries forming densely distributed fine and faceted carbides, with high angle grain boundaries forming courser carbides.

DDC could be considered as a grain boundary sliding, creep like process, occurring at intermediate temperatures where the grain boundary sliding process is activated. Sliding occurs until reaching high temperature, whereupon dynamic recrystallization occurs, which inhibits DDC.

Work done by Young et al [98] showed that the onset of DDC corresponds with the precipitation of $M_{23}C_6$ carbides, and is relatively insensitive to the segregation of sulphur and other impurity elements to the grain boundaries. Carbide misfit stresses were found to be a maximum in the early stages of carbide precipitation and decrease with time as the carbide increases in size. This is due to a reduction in the local chromium content immediately surrounding the carbide, generation of dislocations to accommodate the generated stresses, and the carbide interface moving away from the plane of the grain boundary. Short cooling times also lead to an increase in carbide misfit, as there is less time for the chromium content at the grain boundary to become depleted.

2.5.4 CM247-LC

2.5.4.1 History, development and application

CM-247LC was developed in 1978 by the Cannon-Muskegon group to address the problems with grain boundary cracking that Mar-M247 experienced during casting of complex cored, thin wall aerofoils. The reduced carbon composition was tailored towards the casting of directionally solidified blade and vane applications [99], meaning that some carbide forming elements could be reduced as there is less carbon with which to react. This results in improved strength and ductility (Figure 2-30 - Figure 2-32).

Although designed for directionally solidified casting, CM247LC is also used in the fine equiaxed polycrystalline form, for applications such as combustor housing, and turbine disks [100-103].

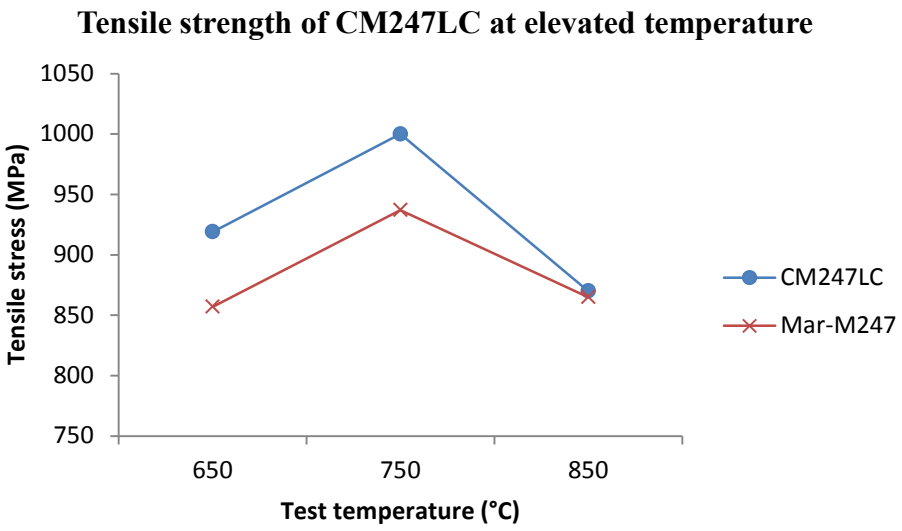

Figure 2-30 - Graph illustrating difference in tensile stress between Mar-M247 and CM247LC at different test temperatures [104]

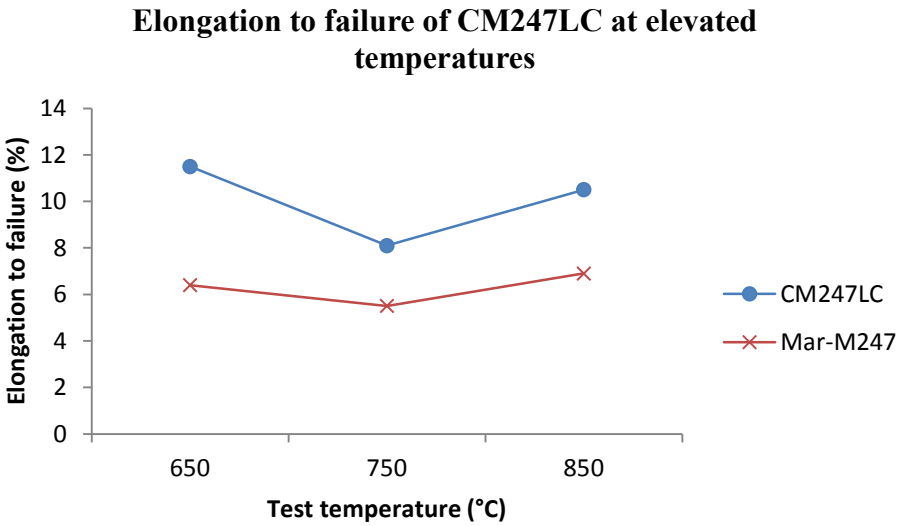

Figure 2-31 - Graph illustrating difference in elongation to failure between Mar-M247 and CM247LC at different test temperatures [104]

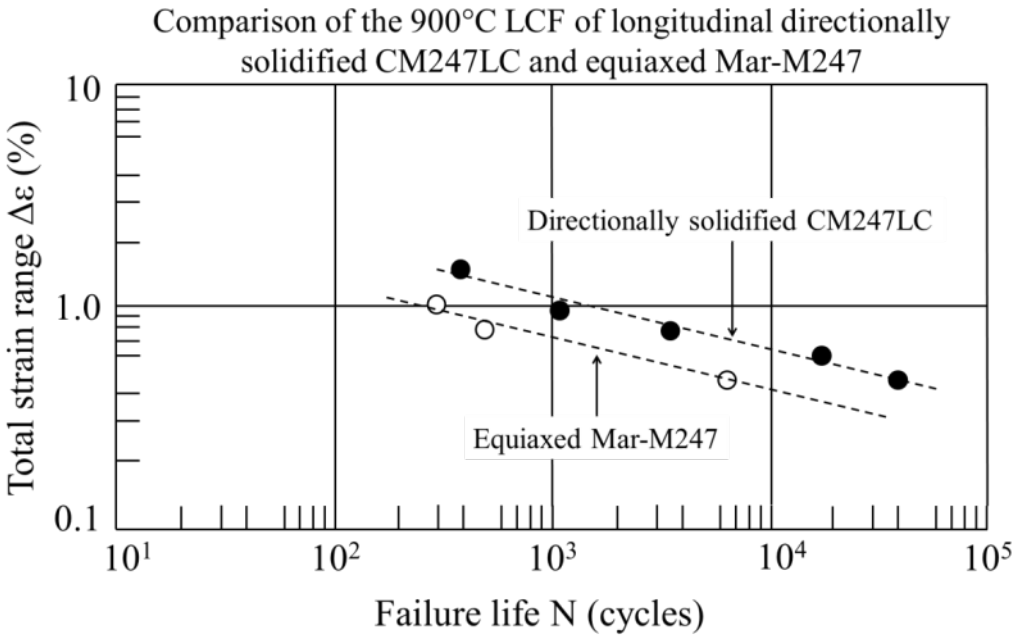

Figure 2-292 - Comparison of LCF behaviour for CM247LC and Mar-M247 [104]

2.5.4.2 Chemistry and microstructure

Table 2-7 – Comparison between Nickel superalloy Mar-M247 and its low carbon derivative CM247LC

Alloy	Composition (Wt %)											
	Ni	**Cr**	**Co**	**Mo**	**W**	**Ta**	**Al**	**Ti**	**C**	**B**	**Zr**	**Hf**
Mar-M247	Bal	8.4	10	0.7	10	3	5.5	1	0.15	0.015	0.05	1.5
CM247LC	Bal	8	9	0.5	9.5	3.2	5.6	0.7	0.07	0.015	0.01	1.4

The reduction in Zr and Ti, and the tighter control over Si (0.1 wt% max) and S (150 ppm max) in CM247LC, was designed to eliminate grain boundary cracking during directional solidification casting of thin walled components, while the lowered carbon content was designed to improve the carbide microstructure, stability and ductility at low to intermediate temperatures (Table 2-7) [105].

The reduction in tungsten from 10wt% in Mar-M247 to 9.5wt% in CM247LC was designed to minimise the formation of M_6C carbide platelets during high temperature solution treatment and in service exposure.

The reduction of carbon content in CM247LC also allowed for the reduction of carbide forming elements Ti, W, Mo and Cr. The benefit of this is that CM247LC is far less likely to develop the undesirable brittle TCP phase σ during extended periods at elevated temperatures.

Titanium reduction in CM247LC has the effect of reducing the size of the γ/γ' eutectic nodules, and reduce the total eutectic content from approximately 4% in Mar-M247 to 3% in CM247LC, which was reported to lead to a decrease in the grain boundary cracking during DS casting [106].

2.6 State of the art for CM247LC deposition and repair

One of the key difficulties in processing CM247LC is its high tendency to crack during casting or fusion welding.

A review of the literature shows that there is a distinct lack of work published regarding the laser metal deposition of CM247LC for repair and manufacture applications, with much of the published work being focused on defects that arise during DS casting and heat treatment [100-103]

Some authors have attributed the high crack susceptibility of Mar-M247 and CM247LC to the relatively high aluminium and titanium contents, which are identified as key contributors to weld cracking, by the formation of high volume fractions of the γ' phase and excessive strain generation due to its precipitation. This would suggest that the cracking is due to strain age hardening, whereas casting literature suggests that cracks form during solidification due to the separation of partially liquid grain boundaries.

Work presented by Hagedorn [107] conducted SLM processing of Mar-M247, using high temperature preheats in order to reduce the thermal gradients and residual stress. Samples processed at room temperature and 1200°C substrate preheat temperature. Samples deposited at room temperature exhibited a high degree of cracking, whereas preheated samples were crack free. Cracking was linked to strong epitaxy of grain growth, with the cracks following the columnar grain boundaries. Samples deposited at high preheat were crack free, and the density was less sensitive to changes in processing parameters, although the high preheat temperature essentially placed the material in the solution treatment range, which caused excessive grain coarsening and a decrease in the epitaxial growth, resulting in quasi-equiaxed grains instead of columnar grains, as the heat flux was no longer directly down into the substrate. Also the gamma prime was excessively coarsened, with cube sizes of 1μm being typical, compared to 0.5μm which is normal for a cast alloy.

Work conducted by Luke Carter [108] investigating the selective laser metal deposition of CM247LC showed that even with the very low heat inputs associated with the SLM process, cracks forming along the grain boundaries and interdendritic regions. As part of his investigation, the role of scan pattern was investigated for the SLM processing, in which he found that when using the island scan toolpath, the rapid laser scanning could be considered as a planar heating front, which produces a bimodal microstructure of fine and coarse grains as a result of the different heating and cooling rates at the centre of the front, and at the ends where conduction is faster and the grain structure is more randomised. From this he found that cracking was more severe in the regions with the random grain structure. Micro-CT analysis identified that cracks were located mainly in the fine grained regions, which he attributed to ductility dip cracking through high angle grain boundaries. Post deposition HIP was used to consolidate the samples, which proved to be an effective, if costly, method of producing fully dense parts.

Novel methods have been developed for the repair of damaged CM247LC components, which include the use of intermediate composition brazing material [109], in which a near eutectic composition foil is sandwiched between two components, then heated up to cause melting of the eutectic phase and brazing both parts together, this method is a form of liquid phase sintering

The Liburdi method has been developed (and patented) by R. Sparling and J. Liburdi [110], and proven to be capable of repairing surface damage in Mar-M247. This liquid phase sintering process involves filling the damaged area with a putty containing a high volume fraction of a high melting point powder particles, then covering the surface with a second putty containing a low melting point powder. Heating the entire part results in the low melting point powder melting and wetting the high melting point powder beneath. Continued heating allows diffusion of alloying elements between the liquid phase and the solid phase, resulting in a composition that is close to that of Mar-M247 that is fully dense and free of cracks,

without introducing any distortion to the damaged part. One benefit of this process is that it can be used to create metal matrix composites, by blending in hard particles to improve the wear resistance. Transient liquid phase bonding was also investigated by Cheng, et al, [111].

Work conducted by Chiang [112] in laser welding with powder filler of another crack susceptible alloy IN-738 involved using an induction heater to preheat the substrate to 800°C prior to welding. This work showed that sound welds could be performed on material that had been preheated, with no evidence of solidification cracks in the weld material, or liquation cracks in the HAZ, although strain age cracking did occur after post weld heat treatment. This work agrees with that of other authors [113] who investigated the use of high temperature preheats in the electron beam welding process, and found that cracking was reduced due to the lower thermal gradient

Work conducted by Mousavizade et al [114] attempted to improve the liquation cracking susceptibility of IN738 laser welds, by friction stir processing the surface layer. This resulted in a refinement of the grain structure and the dispersion of the grain boundary phases that give rise to HAZ liquation cracking. While this is an interesting approach to help reduce cracking within the HAZ, it does not address the issue of hot cracking, which occurs during solidification of the melt pool.

One reported method of preventing cracking during welding and repair of CM-247 and Mar-M247 is to subject the alloy to an overage pre-weld heat treatment in order to grow the γ' to a high volume fraction [106]. This is done in order to increase the ductility of the material, which will permit ambient temperature weld repair without cracking. This method involves a slow heating cycle to a high temperature inside a vacuum furnace, followed by a soak period and slow cool to around 300°C and then a rapid quench.

While this process may produce adequate repair welds, the pre-weld heat treatment required is slow and costly and the effects of the heat treatment on the microstructure of polycrystalline Mar-M247 and CM-247 has not been examined.

2.7 Introduction to Design of Experiments (DOE) methodology

2.7.1 Design of Experiments overview

Design of Experiments (DOE) is a statistical method of experiment design that allows the maximum amount of information to be obtained from a given amount of experimental effort. The statistical theory behind DOE can be described using the concept of a "black box" process model (Figure 2-33), with several discrete or continuous inputs (factors) that can be controlled by the operator, and one or more measurable outputs (Responses), where the outputs are generally considered continuous [117]

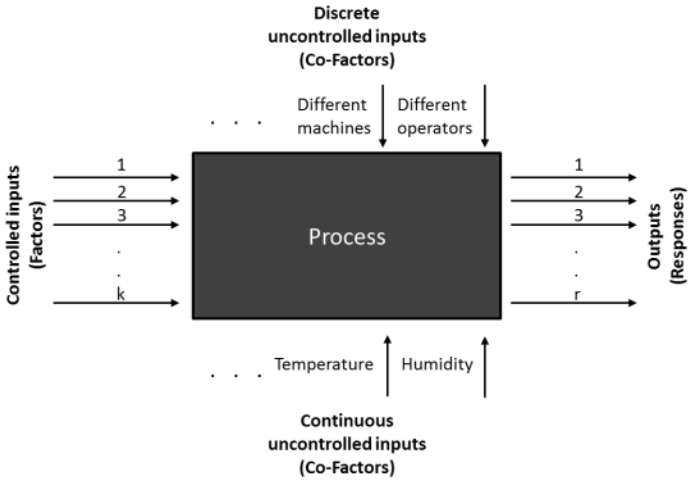

Figure 2-33 – Black box process model schematic [121]

Experimental data is used to derive an approximate empirical model linking the inputs and outputs, so that the relationships between them can be better understood, predicted, and trends observed that may indicate a process optimisation path.

However, before embarking on an in-depth experiment using DOE methodology, it is worth considering the following [118,119]

1. Are the measurement systems capable for all of the responses? The tools and methods used to measure the responses generated by the experiment must be capable of measuring the changes and differentiating between the results accurately.
2. Is the process stable? Control runs should be included that are made at the "standard" process condition (centre points). The experiment should generally start and end with such runs, and these should not be executed sequentially. A plot of the outcome of the control runs will indicate the intrinsic scatter of the process.
3. Are the responses likely to be approximated well by simple polynomial models? Over the range of the experiment, the outputs must be continuous and reasonably smooth. Any sharp falloff in response value is likely to be missed by the approximating polynomials that are fitting to the data, as they assume a smoothly curving response surface.

   If the response is known to be piecewise smooth (Figure 2-34), then the experiment should be split into two separate experiments, each looking at the shape of the different sections. A jagged surface will not successfully be approximated by a smooth polynomial.

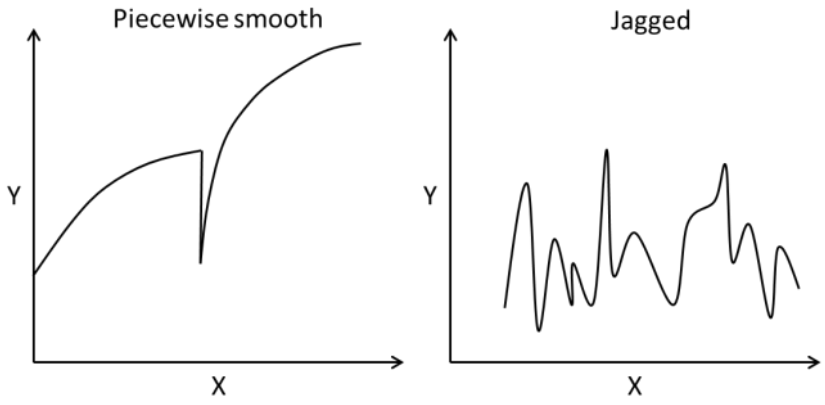

Figure 2-34 – Examples of piecewise smooth and jagged results set

4. Are the residuals well behaved? The amount of deviation from the measured results and the predicted responses is described as a "residual". The predicted response is calculated from the chosen model, once all of the unknown model parameters have been estimated from the experimental data [120].

Residuals could be considered an element of variation that is not explained by the fitting model. As these are considered a type of error, assumptions can be made that the group of residuals should be roughly normal and independently distributed with a mean of 0 and some constant variance.

If the residuals are not normally distributed, then it may mean that the residuals contain "structure" that is not accounted for in the residuals. Residuals may be plotted graphically using histograms, normal probability plots or dot plots, such as shown in Figure 2-35 below.

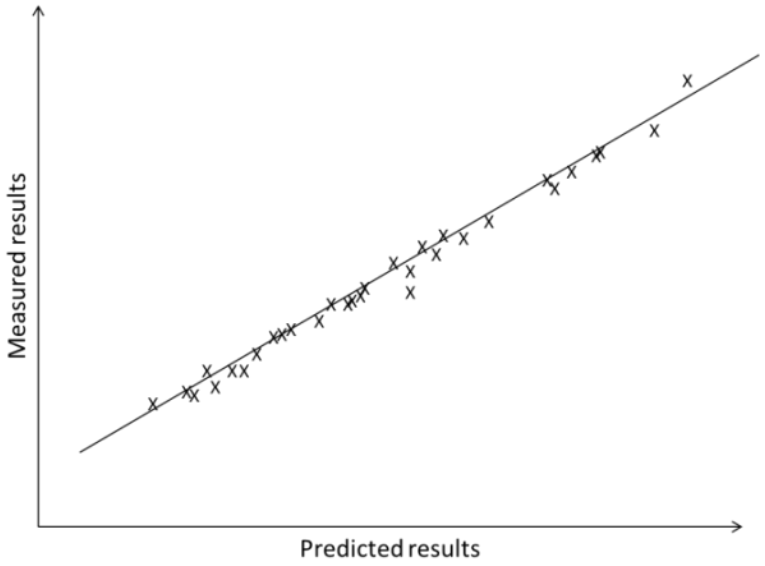

Figure 2-35 – Example studentised plot of residuals

If the points form an S shaped curve, then the residuals would have a bimodal distribution of residuals, while a break in the middle of the graph would be an indication of abnormalities in the residual distribution.

Studentised residuals (Figure 2-35) are the quotient resulting from the division of a residual by an estimate of its standard deviation. Generally the standard deviations of residuals in a sample vary greatly from one data point to another, despite the errors all having the same standard deviation, so studentising is a good way of comparing residuals at different data points.

2.7.2 DOE planning and execution

The DOE process, from the planning stage through to completion, generally consists of the following 5 steps [120]:

1. Set objectives
2. Select process variables
3. Select and experimental design
4. Execute the design
5. Analyse and interpret the results

This section describes some of the considerations for each step of the experiment, how they relate to the subject of this thesis, and some of the theory behind the experiment structure and interpretation of the results.

2.7.2.1 Setting the objective

Careful consideration of the objective of the experiment is important, as it will affect the selection of the factors, response and experiment design. The objective of this experiment is to better understand how the LMD processing parameters affect the cracking response in laser deposited CM247LC. Objectives can be broadly classified into four groups

1. Comparative design - For choosing between alternatives with narrow or broad scope, either for initial comparison or confirmatory comparison
2. Screening designs - To identify which factors are important to the responses. This may be used to examine a large number of factors in a fractional factorial experiment
3. Response surface - Response surface modelling is used to hit a specific target, maximise or minimise a response, reduce process variation or make a process more robust.
4. Regression modelling - This is used to estimate a precise model, quantifying the dependence of response variables on process inputs.

The objective of this work is to understand how the laser metal deposition process variables affect the crack formation in laser deposited CM247LC. Response surface methodology was chosen as the method of analysing this data for two reasons:

1. It would allow the interactions between process variables to be examined with respect to the number of cracks that form
2. The topography of the response surface may indicate if there is a process optimisation path that results in crack free deposits, or reduced crack density.

2.7.2.2 Select process variables

Process variables include both the factors and responses, and the selection of these should be considered carefully. This may include some degree of judgement on the part of the designer, and so an understanding of the process is important:

Care must also be taken in defining the range for the factors, i.e. how high and how low they will go. Some parameter combinations will be impractical or even dangerous, and so it is important to have an understanding of the process in order to select realistic process factor ranges.

2.7.2.3 Select an experimental design

As described in section 3.4.1, the choice of experiment design will be influenced by the objectives of the experiment. In this work, the objective is to find a combination of processing parameters that reduce or eliminate cracks in laser deposited CM247LC, and so a response surface methodology was chosen, using a full factorial central composite design.

Central composite design (Figure 2-36, Figure 2-37) is a method used in response surface methodology for building second order quadratic models for the response variable, without needing to complete a full three-level factorial experiment.

Central composite designs generally consist of the following [117-121]

- 2^k factorial runs, where k is the number of process factors. For example, an experiment with 4 factors, there will be 16 factorial runs, with each run varied over 2 levels. This gives 8 points that form the corners of a cube.
- A set of centre point runs, the values of which are the median of the values used in the factorial set. As described in section 3.4.1, these are performed to test the stability and improve the precision of the experiment. The number of centre points is variable and not rigidly determined by the number of factors.
- 2*k axial points (α). These are identical to the centre points except for one variable, which will be varied above and below the median of the factorial levels. For k = 4, then there will be 8 α points. α points may be "spherical" or "rotatable".
    - Spherical – Both the α and factorial points lie on the surface of a sphere, with the centre points aligned to the centre of the sphere.
    - Rotatable – The α points are shifted or placed such that the variance of predicted values of the response are all equal, for x's that are an equal distance from the centre

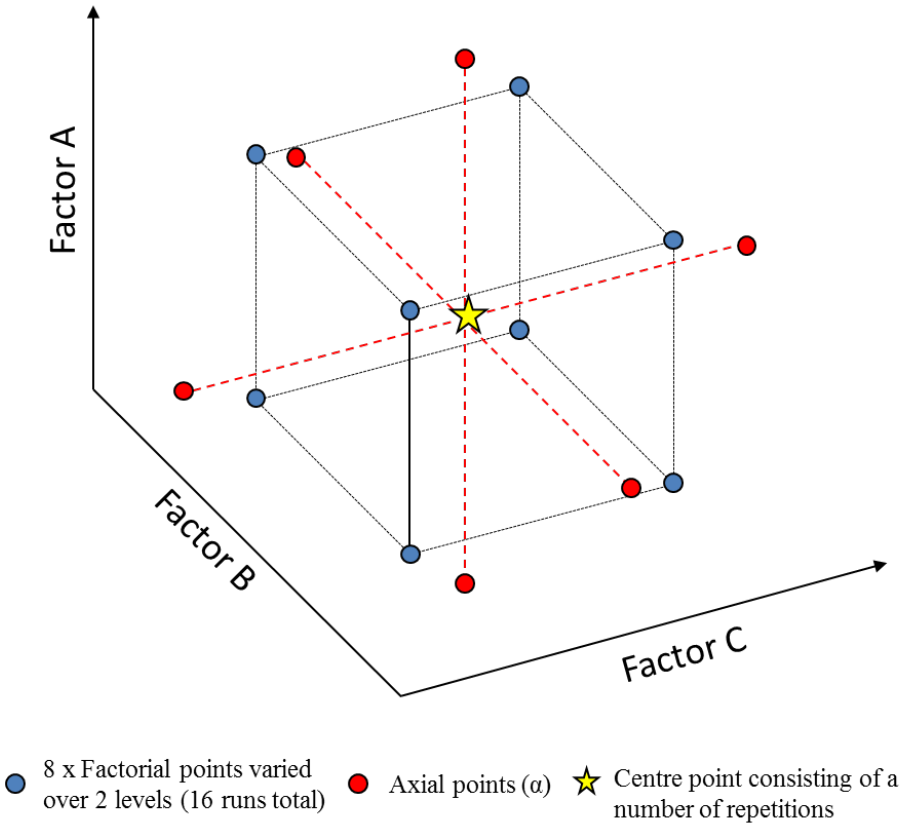

Figure 2-36 – Schematic illustration of a central composite design [120]

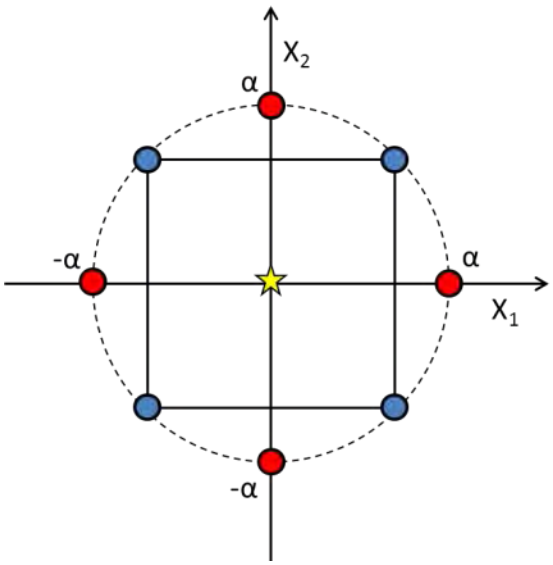

Figure 2-37 – Schematic illustration of spherical central composite design for 2 factors (X_1, X_2) [120]

2.7.2.4 Execute the DOE

The DOE should be executed according to run number generated by the DOE software. The software automatically randomises the run numbers, so that the influence of equipment setup on process repeatability can be examined.

2.7.2.5 Analyse and interpret the results

The basic steps in DOE data analysis are listed below (Figure 2-38):

1. Look at the data
2. Create the theoretical model
3. Create a model from the data
4. Test the model assumptions using residual graphs
5. Use the results to answer the questions in the experimental objectives

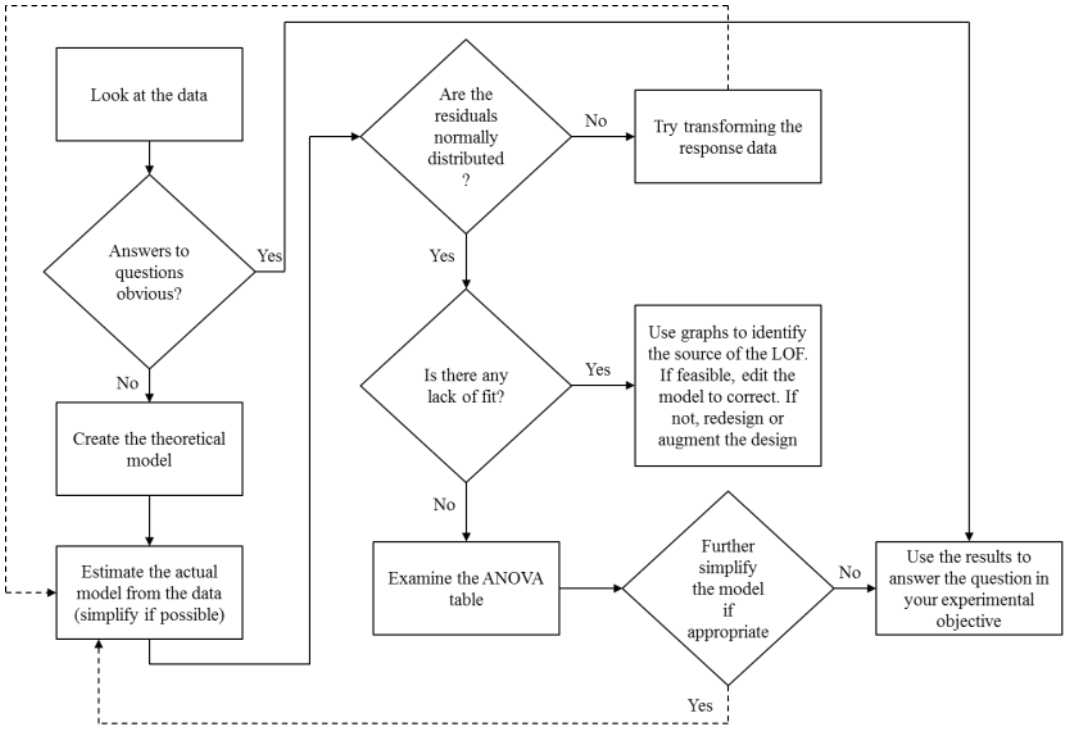

Figure 2-38 – Flowchart illustrating the process steps used to analyse and interpret the DOE data [120]

2.7 Literature review summary

Based on a review of the literature, it would appear that there is a lack of published work concerning the laser metal deposition of CM247LC for repair or manufacture applications. To date there has been a significant amount of work concerned with the repair of single crystal turbine blades of the newer grades of alloy, but there is a lack of work published on the laser repair of polycrystalline Mar-M247 components such as powder metallurgy HIP'd components. Many older engines that are currently in use contain Mar-M247, and repair strategies that may be developed through the course of this work may also be applicable to other superalloy grades.

The closest study conducted so far was performed by Carter [108,116] and Hagedorn [107], who investigated CM247LC and Mar-M247 alloys respectively in the SLM process. Their findings showed that the heating and cooling rate are critical parameters for the deposition of crack susceptible alloys such as CM-247LC, with pre-heating and post deposition HIP being advisable in order to achieve fully dense components.

However the SLM processes are not well suited to the repair of existing polycrystalline components, due to their size and shape, and so laser metal deposition is being considered as a suitable repair route.

Work conducted in the deposition of crack susceptible weld filler material by using combined induction preheating and laser metal deposition showed that cracking could be eliminated for single pass welds, due to the reduction in thermal gradient between the melt pool and the surrounding material [113], and so this is being considered as a possible processing route.

The use of Design of Experiments methods is a good approach to use for evaluating a process with as many process variables as Laser Metal Deposition, as it allows multiple variables to be examined at once in order to investigate how they affect an outcome [117-121].

2.8 Chapter 2 - List of figures

2.9 Chapter 2 – List of table

2.10 Chapter 2 References

1. The UK aerospace industry. 2004-05: House of commons trade and industry committee.

2. Unified propulsion 3 - Efficiencies of A/C engines. Available from: http://ocw.mit.edu/ans7870/16/16.unified/propulsionS04/UnifiedPropulsion3/UnifiedPropulsion3.htm.

3. MHI Achieves 1,600 degrees C Turbine Inlet Temperature in Test. Available from:http://www.bloomberg.com/apps/news?pid=conewsstory&tkr=MHVYF:US&sid=ahc_P974AiD8.

4. Rao, J.S., B. Kishore, and V. Kumar Weight optimization of turbine blades. 2011.

5. Cervenka, M., The Rolls Royce Trent engine. 2000.

6. Shepherd, D.P., et al., Life extension methods in aero-engines. OMMI, 2004. 3(1).

7. Wlodawer, R., Directional solidification of steel castings. 1966: Pergamon press.

8. Quested, P. and M. McLean, Solidification morphologies in directionally solidified superalloys. Materials Science and Engineering, 1984. 65(1): p. 171-180.

9. Donachie, M.J. and S.J. Donachie, Superalloys - A technical guide. second edition ed. 2002: ASM international.

10. Maldini, M., et al. Creep and fatigue properties of a directionally solidified nickel base superalloy at elevated temperature. in Proceedings of the Eighth Internal Symposium on Superalloys. 1996.

11. Busquet, F. and F. Forrat, method for the manufacture of single crystals. 1971, US Patent 3,584,676.

12. Higginbotham, G.J.S., J.R. Marjoram, and F.J. Horrocks, Method of and mould for making a cast single crystal. 1984, Google Patents.

13. Schneibel, J.H., Beyond Nickel-Base superalloys, in TMS. 2004: Charlotte, NC.

14. Schmitz, A. Unconventional (advanced) manufacturing processes for gas-engine turbine components. 2013; Available from: http://www.transport-research.info/web/projects/project_details.cfm?ID=41686.

15. Voice, W. Net-shape processing applied to aero-engine components. 2006; 1-12].

16. Tillack, D.J., Welding superalloys for aerospace applications. WELDING JOURNAL-NEW YORK-, 2007. 86(1): p. 28.

17. Zhu, Y., et al., The development and long-time structural stability of a low segregation HF free superalloy - DZ125L. TMS, 2000.

18. Gabb, T., The next generation of high temperature alloys. JOM, 2010. 62(1): p. 47-47.

19. Associates, W. and T.T. Wohlers, Wohlers Report 2013: Additive Manufacturing and 3D Printing State of the Industry : Annual Worldwide Progress Report. 2013: Wohlers Associates.

20. TWI-Global. 2014. Revolutionary development cuts manufacturing times using Laser Metal Deposition. [ONLINE] Available at: http://www.twi-global.com/news-events/case-studies/revolutionary-development-cuts-manufacturing-times-using-laser-metal-deposition-583/. [Accessed 01 January 15].

21. Bourell, D., et al. A brief history of additive manufacturing and the 2009 roadmap for additive manufacturing: looking back and looking ahead. in US-Turkey Workshop on Rapid Technologies. 2009.

22. Lyons, B. Additive manufacturing in aerospace; Examples and research outlook. in Frontiers of Engineering 2011, Additive Manufacturing. 2011.

23. Additive manufacturing: Pursuing the promise, U.D.o. energy, Editor. 2012.

24. Allen, J., The business case for additive manufacture, in Laser materials processing in aerospace and precision manufacturing. 2005: Rolls Royce, Derby.

25. Schneider, M.F., Laser cladding with powder, effect of some machining parameters on clad properties. 1998: Universiteit Twente.

26. Bremen, S., W. Meiners, and A. Diatlov, Selective Laser Melting. Laser Technik Journal, 2012. 9(2): p. 33-38.

27. Tellez, A.G.M., Fibre laser metal deposition with wire: Parameters study and temperature control. 2010, University of Nottingham.

28. Taminger, K. Electron beam additive manufacturing: State-of-the-Technology, challenges & opportunities. in Direct digital manufacturing workshop. 2010. Solomons, MD.

29. Baufeld, B., et al. Manufacturing Ti-6Al-4V components by shaped metal deposition: microstructure and mechanical properties. in IOP Conference Series: Materials Science and Engineering. 2011. IOP Publishing.

30. American airlines "Fuel smart" program literature. Available from: http://hub.aa.com/en/nr/media-kit/operations/fuelsmart.

31. GE aviation signs addititve manufacturing cooperative agreement with Sigma Labs.2013;Availablefrom:http://www.geaviation.com/press/other/other_20130524.html.

32. Kinsella, M.E., Additive manufacturing of superalloys for aerospace applications, M. Metals branch, ceramics and NDE division, Editor. 2008.

33. Dehoff, R., et al. Case study: Additive manufacturing of aerospace brackets.

34. Gasser, A., et al., Laser Additive Manufacturing. Laser Technik Journal, 2010. 7(2): p. 58-63.

35. Jones, J.B., et al., Remanufacture of turbine blades by laser cladding, machining and in-process scanning in a single machine. 2012.

36. Ruan, J. and F.W. Liou. Automatic toolpath generation for multi-axis surface machining in a hybrid manufacturing system. in ASME 2003 International Design Engineering Technical Conferences and Computers and Information in Engineering Conference. 2003. American Society of Mechanical Engineers.

37. Qi, H., M. Azer, and P. Singh, Adaptive toolpath deposition method for laser net shape manufacturing and repair of turbine compressor airfoils. The International Journal of Advanced Manufacturing Technology, 2010. 48(1-4): p. 121-131.

38. Gregori, A. and D. Bertaso, Welding and Deposition of Nickel Superalloys 718, Waspaloy and Single Crystal Alloy CMSX-10. Welding in the World, 2007. 51(11-12): p. 34-47.

39. Gäumann, M., et al., Single-crystal laser deposition of superalloys: processing–microstructure maps. Acta Materialia, 2001. 49(6): p. 1051-1062.

40. Bansal, R., Acharya, R., Gambone, J. J., Das, D., 2011. Experimental and theoretical analysis of scanning laser epitaxy applied to Nickel-based superalloys. Solid Freeform fabrication proceedings; 496-503

41. Theiler, C., T. Seefeld, and G. Sepold. Deposition of graded metal matrix composites by laser beam cladding.

42. Lepski, D. and H. Eichler, Software zur Prozess-Simulation des Laser-Pulver-Auftragschweißens. JOT Journal für Oberflächentechnik, 2003. 43(1): p. VI-IX.

43. R. M. Mahamood, E.T.A. Effect of laser power on surface finish during laser metal deposition process. in World congress on Engineering and Computer science. 2014. San Francisco.

44. Shukla, M., et al., Effect of Laser Power and Powder Flow Rate on Properties of Laser Metal Deposited Ti6Al4V.

45. Mahamood, R.M., et al., Effect of Laser Power on Material Efficiency, Layer Height and Width of Laser Metal Deposited Ti6Al4V. 2012.

46. Steen, W.M., Laser Material Processing. 1996.

47. Santo, L. and Davim, J. (2014). Surface engineering techniques and applications: Research advancements. IGI Global. Page 154.

48. Ashan, M. N. 2011. Modelling and analysis of Laser Direct Metal deposition of Ti-6Al-4V. PhD Thesis. University of Manchester.

49. HOLO/OR. 2015. Design and manufacture of diffraction optical elements. [ONLINE] Available at:http://www.holoor.com/. [Accessed 02 February 15].

50. Kamara, A. M., S. Marimuthu, and L. Li. "A numerical investigation into residual stress characteristics in laser deposited multiple layer waspaloy parts." Journal of Manufacturing Science and Engineering 133.3 (2011): 031013.

51. Lawrence, J. R., Waugh, D. 2014. "Laser surface engineering: processes and Applications". Woodhead publishing series in electronic and optical materials. Elsevier science. SN: 9781782420798.

52. Rangaswamy, P., et al. "Residual stresses in components formed by the laserengineered net shaping (LENS®) process." The Journal of strain analysis for engineering design 38.6 (2003): 519-527.

53. Labudovic, M., D. Hu, and R. Kovacevic. "A three dimensional model for direct laser metal powder deposition and rapid prototyping." Journal of materials science 38.1 (2003): 35-49

54. Moat, R. J., et al. "Stress distributions in multilayer laser deposited Waspaloy parts measured using neutron diffraction." (2007).

55. Pratt, P., et al. "Residual stress measurement of laser-engineered net shaping AISI 410 thin plates using neutron diffraction." Metallurgical and Materials Transactions A 39.13 (2008): 3155-3163.

56. Wang, Liang, Sergio D. Felicelli, and Phillip Pratt. "Residual stresses in LENS-deposited AISI 410 stainless steel plates." Materials Science and Engineering: A 496.1 (2008): 234-241.

57. Kobelco welding worldwide. 2015. The ABC's of Arc Welding. [ONLINE] Available at: http://www.kobelco-welding.jp/education-center/abc/ABC_2006-03.html. [Accessed 02 September 15].

58. Dye, D., O. Hunziker, and R. Reed, Numerical analysis of the weldability of superalloys. Acta materialia, 2001. 49(4): p. 683-697.

59. Helmink, R.C., et al., Advanced superalloys and tailored microstructures for integrally cast turbine wheels. 2000: Superalloys 2000 (Ninth international symposium). p. 171-179.

60. Winstone, M. and J. Brooks, Advanced high temperature materials: Aeroengine fatigue. Ciência & Tecnologia dos Materiais, 2008. 20(1-2): p. 15-24.

61. Segersäll, M., Nickel-Based Single-Crystal Superalloys: the crystal orientation influence on high temperature properties. 2013.

62. Das, N., Advances in nickel-based cast superalloys. Transactions of the Indian Institute of Metals, 2010. 63(2-3): p. 265-274.

63. Coakley, J. and D. Dye, Lattice strain evolution in a high volume fraction polycrystal nickel superalloy. Scripta Materialia, 2012. 67(5): p. 435-438.

64. Maniar, G.N., et al., Correlation of gamma-gamma prime mismatch and strengthening in Ni/Fe-Ni base alloys containing aluminum and titanium as hardeners. Metallurgical Transactions, 1970. 1(1): p. 31-42.

65. H.J. Beattie Jr. and W.C. Hagel: Trans. TMS-AIME, 221, 28 (1961).

66. Lavakumar, A., et al., Gamma Prime Coarsening Behavior of Nickel Super alloy Super cast 247A after Prolonged Thermal Exposures.

67. Reed, R.C., The superalloys - fundamentals and applications. 2006: Cambridge university press.

68. Antariksh Rao Pratap Singh. 2011. Mechanisms of ordered Gamma Prime Precipitation In Nickel Base Superalloys. PhD Thesis. University of North Texas.

69. Kattus, J.R., Aerospace structural metals handbook. 1999.

70. Huang, H.-E. and C.-H. Koo, Effect of solution-treatment on microstructure and mechanical properties of cast fine-grain CM 247 LC superalloy. Materials Transactions, 2004. 45(4): p. 1360-1366.

71. Chen, J., et al., MC carbide formation in directionally solidified MAR-M247 LC superalloy. Materials Science and Engineering: A, 1998. 247(1–2): p. 113-125.

72. C.T. Sims, N.S. Stoloff, W.C. Hagel, Superalloys 2, High-Temperature Materials ForAerospace and Industrial Power, John Wiley and Sons, 1987.

73. Singh Handa, Sukhdeep. "Precipitation of Carbides in a Ni-based Superalloy." (2014).

74. Rush, M.T., et al., An investigation into cracking in nickel-base superalloy repair welds. Advanced Materials Research, 2010. 89: p. 467-472.

75. Darolia, R., Lahrman, D, F., Field, R, D,. Superalloys 1988. Formation of topologically close packed phases in nickel base single crystal superalloys. Proceedings from the TMS sixth international symposium.

76. Sugui, Tian, et al. "Influence of TCP phase and its morphology on creep properties of single crystal nickel-based superalloys." Materials Science and Engineering: A 527.21 (2010): 5444-5451.

77. Lippold, J.C., S.D. Kiser, and K.N. Dupont, Welding metallurgy and weldability of nickel-base alloys. 2009.

78. Pellini, W.S., Strain theory of hot tearing Foundry, 1952. 80: p. 125.

79. W. I. Pumphrey and P.H. Jennings, A consideration of the nature of brittleness at temperatures above the solidus in castings and welds in aluminium alloys. J. Inst. Metals, 1948. 75: p. 235.

80. Borland, J.C., Generalised theory of super-solidus cracking in welds (and castings). British welding journal, 1960. 7: p. 508-512.

81. Andersson, J., Weldability of precipitation hardening superalloys–influence of microstructure. 2011: Chalmers University of Technology.

82. BAESLACK III, W. A., WP LATA, and SL WEST. 1998. "A study of heat-affected zone and weld metal liquation cracking in alloy 903." Supplement to the welding journal 1988

83. Henderson, M., et al., Nickel based superalloy welding practices for industrial gas turbine applications. Science and Technology of Welding & Joining, 2004. 9(1): p. 13-21

84. Copley, S, M,. Kear, B, H,. VerSnyder, F, L,. 1968. The Role of interfaces in Ni-base superalloys. Surfaces and Interfaces. Pp 353-369. ISBN: 978-1-4757-0180-7

85. Eskin, D.G. and L. Katgerman, A Quest for a New Hot Tearing Criterion. Metallurgical and Materials Transactions A, 2007. 38(7): p. 1511-1519.

86. Cross, C.E., On the Origin of Weld Solidification Cracking, in Hot Cracking Phenomena in Welds, T. Böllinghaus and H. Herold, Editors. 2005, Springer Berlin Heidelberg. p. 3-18.

87. Cross, C. and N. Coniglio, Weld solidification cracking: Critical conditions for crack initiation and growth, in Hot cracking phenomena in welds II. 2008, Springer. p. 47-66.

88. Yushchenko, K.A. and V.S. Savchenko, Classification and Mechanisms of Cracking in Welding High-Alloy Steels and Nickel Alloys in Brittle Temperature Ranges, in Hot Cracking Phenomena in Welds II, T. Böllinghaus, et al., Editors. 2008, Springer Berlin Heidelberg. p. 95-114.

89. Kou, S., Welding metallurgy. 2nd ed. 2003: John Wiley and sons.

90. Thompson, R.G., Microfissuring of Alloy 718 in the Weld Heat-Affected Zone. JOM, 1988. 40(7): p. 44-48.

91. ARATA, Y., F. MATSUDA, and S. Katayama, Solidification Crack Susceptibility in Weld Metals of Fully Austenitic Stainless Steels (Report I): Fundamental Investigation on Solidification Behavior of Fully Austenitic and Duplex Microstructures and Effect of Ferrite on Microsegregation. Transactions of JWRI, 1976. 5(2): p. 135-151.

92. Nissley, N. and J. Lippold. Ductility-dip cracking susceptibility of austenitic alloys. in 6 th International Conference: Trends in Welding Research. 2002.

93. Lippold, J. and N. Nissley, Ductility-dip cracking in high chromium, Ni-base filler metals, in Hot cracking phenomena in welds II. 2008, Springer. p. 409-425.

94. Nissley, N. and J. Lippold, Ductility-dip cracking susceptibility of nickel-based weld metals part 1: strain-to-fracture testing. Welding Journal, 2008. 87(10): p. 257s-264s.

95. Ramirez, A.J., J.W. Sowards, and J.C. Lippold, Improving the ductility-dip cracking resistance of Ni-base alloys. Journal of Materials Processing Technology, 2006. 179(1–3): p. 212-218.

96. Damkroger, B.K., B. Rath, and G. Edwards, Investigation of High Temperature Ductility Losses in Alpha-Beta Titanium Alloys. 1988, DTIC Document.

97. Lim, Y.S., et al., The effect of grain boundary misorientation on the intergranular M23C6 carbide precipitation in thermally treated Alloy 690. Journal of Nuclear Materials, 2004. 335(1): p. 108-114.

98. Young, G., et al., The mechanism of ductility dip cracking in nickel-chromium alloys. WELDING JOURNAL-NEW YORK-, 2008. 87(2): p. 31.

99. CM-247LC for turbine blades and vanes. Available from: http://www.c-mgroup.com/spec_sheets/CM_247.htm.

100. Huang, H.-E. and C.-H. Koo, Characteristics and mechanical properties of polycrystalline CM 247 LC superalloy casting. Materials Transactions, 2004. 45(2): p. 562-568.

101. Pollock, T.M. and S. Tin, Nickel-based superalloys for advanced turbine engines: chemistry, microstructure and properties. Journal of propulsion and power, 2006. 22(2): p. 361-374.

102. Kaufman, M., Properties of Cast Mar-M-247 for Turbine Blisk Applications. Superalloys 1984, 1984: p. 43-52.

103. Kim, I.S., et al., Influence of heat treatment on microstructure and tensile properties of conventionally cast and directionally solidified superalloy CM247LC. Materials Letters, 2008. 62(6–7): p. 1110-1113.

104. Harris, K., G. Erickson, and R. Schwer. MAR M 247 Derivations—CM 247 LC DS Alloy, CMSX® Single Crystal Alloys, Properties and Performance. in 5th Int. Symp. 1984.

105. Huang, H.-E. and C.-H. Koo, Effect of zirconium on microstructure and mechanical properties of cast fine-grain CM 247 LC superalloy. Materials Transactions, 2004. 45(2): p. 554-561.

106. Ramirez, A.J., W. Sowards, and J.C. Lippold, C. The Effect of Nb and Ti Additions on Intergranular Cracking of Ni-base alloys.

107. da Silva Bartolo, P.J., et al., High Value Manufacturing: Advanced Research in Virtual and Rapid Prototyping: Proceedings of the 6th International Conference on Advanced Research in Virtual and Rapid Prototyping, Leiria, Portugal, 1-5 October, 2013. 2013: Taylor & Francis.

108. Carter, L.N., et al., The influence of the laser scan strategy on grain structure and cracking behaviour in SLM powder-bed fabricated nickel superalloy. Journal of Alloys and Compounds, 2014. 615(0): p. 338-347.

109. Ozbaysal, K. and A. Kamel, Near eutectic composition nickel base sandwich braze foil. 2014, Google Patents.

110. Sparling, R., Liburdi powder metallurgy, applications for manufacture and repair of gas turbine components. BOOK-INSTITUTE OF MATERIALS, 2003. 800: p. 987-1005.

111. Cheng, J.M.-L., Transient liquid phase bonding in the nickel base superalloy CM 247 LC. 2005, University of British Columbia.

112. Chiang, M. F., and C. Chen. "Induction-assisted laser welding of IN-738 nickel–base superalloy." Materials Chemistry and Physics 114.1 (2009): 415-419.

113. Kim, D.-Y., et al., A study on fusion repair process for a precipitation hardened IN738 Ni-based superalloy. Journal of engineering for gas turbines and power, 2000. 122(3): p. 457-461.

114. Mousavizade, M.S. and M.F. Ghaini, Effect of preweld surface modification using friction stir processing of IN738 superalloy on the liquation cracking of autogenous laser welds. Metallurgical and Materials Engineering, 2012. 18(1): p. 43-52.

115. Morin, J.A., Weld repair of superalloy materials. 2010, Google Patents.

116. Carter, L.N., M.M. Attallah, and R.C. Reed, Laser Powder Bed Fabrication of Nickel-Base Superalloys: Influence of Parameters; Characterisation, Quantification and Mitigation of Cracking. Superalloys 2012, 2012: p. 577-586.

117. Onlinecourses.science.psu.edu, (2015). Lesson 1: Introduction to Design of Experiments STAT 503. [online] Available at: https://onlinecourses.science.psu.edu/stat503/node/5 [Accessed 4 Feb. 2015].

118. Park, Gyung-Jin. "Design of experiments." Analytic Methods for Design Practice (2007): 309-391.

119. Montgomery, Douglas C., and Douglas C. Montgomery. Design and analysis of experiments. Vol. 7. New York: Wiley, 1984.

120. Anderson, Mark J., and Patrick J. Whitcomb. "Design of experiments." Kirk-Othmer encyclopedia of chemical technology (2000).

121. Engineering statistics handbook. 2015. Process improvement. [ONLINE] Available at: http://www.itl.nist.gov/div898/handbook/pri/section1/pri1.htm. [Accessed 16 September 15].

Chapter 3

General methodology and equipment setup

3 Chapter 3 - General methodology and equipment setup

3.1 Laser metal deposition equipment

Laser metal deposition (LMD) trials were conducted at TWI Sheffield, using the robotic laser processing cell shown in Figure 3-1. This cell consisted of a sealed and safety interlocked room, designed to protect personnel from accidental exposure of laser light. Laser focusing optics and powder delivery nozzles are manipulated relative to the workpiece using a Kuka KR30HA 6-axis robot.

Figure 3-1 - TWI Yorkshire robotic laser processing cell used for deposition trials. A) 7KW IPG fibre laser B) KUKA KR30HA robot C) Coaxial powder delivery nozzle D) Powder feeder E) Laser focusing optics F) Steel welding table

3.1.1 IPG YLR-7000 laser

The laser used for this work was constructed from 36 multi-mode laser modules, each contributing up to 200W at 1.064µm. The fibres from each module are spliced together to produce a single high power beam.

One characteristic of this design is that the laser does not produce a stable beam when powers less than 10% of max output are requested, with laser power scaling in a non-linear fashion at low powers. This was corrected to a degree by isolating half of the laser modules, so that only 17 were active, which then allowed stable laser powers down to 200W. This is illustrated in section 3.2.1.

The output fibre from the laser is delivered to a beam switching device, which is used to re-direct into one of three processing fibres for the two robotic laser processing cells at TWI Sheffield.

3.1.2 Powder feeder

All deposition trials were conducted using a seltzer-metco twin-10C powder feeder, as described in section 2.4.2.2.

Gas pressure and flow rate were set to 1.5 bar and 6 l/min respectively. A dosing disk with a small 3mm x 0.6mm groove was used, which allowed faster rotation speeds to be used in order to minimise the clumping effect that can occur during powder pick up. Powder was maintained at 80°C using a heated jacket, to prevent moisture ingress.

3.1.3 Laser cladding head

The assembled cladding head is illustrated schematically in Figure 3-2, with the critical components labelled A-N.

Laser light is delivered from the IPG-YLR7000 laser generator to the cladding head via a 20m long 300μm/0.2 NA optical fibre (D). The laser light is divergent as it exits the fibre, so a beam collimator (F) expands and straightens the beam to 40mm diameter, minimising the energy intensity on the optical surfaces.

The collimated beam is reflected through 90° by a beam bending mirror, consisting of a flat quartz mirror with a 1064 nm reflective coating applied. As this mirror only reflects light of the specified wavelength, a coaxial camera system (I) was able to view down through the mirror and observe the process.

Laser light was focused using a 160mm FL lens (J), comprising of a doublet lens assembly on an adjustable carriage, which allows the focal point to be moved +/= 5mm. To protect the delicate anti-reflective coating on the focusing lens, a replaceable glass window (K) was inserted between the lens and the nozzle, preventing any powder or fumes from contaminating the optical surfaces.

To allow lateral adjustment of the powder delivery nozzle (N) to the laser beam for alignment purposes, the powder delivery nozzle was attached to a bespoke X-Y adjustment carriage (M). This carriage was designed to allow up to +/- 20mm of vertical adjustment of nozzle position, by moving the nozzle up or down inside a collar.

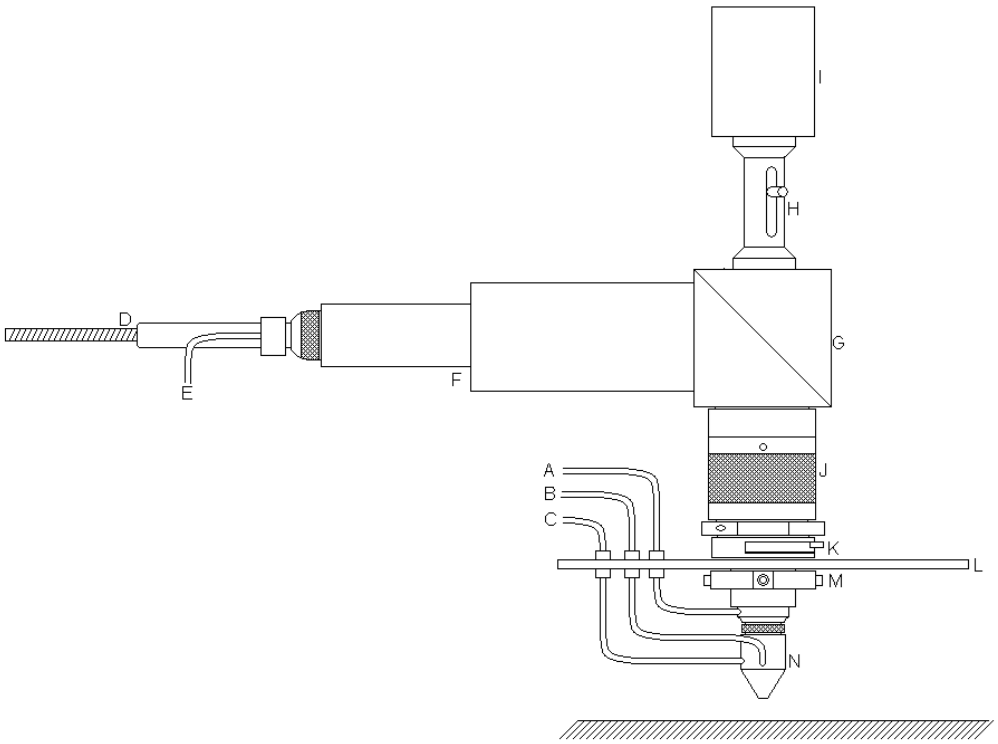

Figure 3-2 - Schematic illustration of laser deposition head used for experimental trials

A. Shielding gas delivery tube (*6/4mm PTFE tubing*)
B. Powder delivery tube (*6/4mm Anti-static PTFE tubing*)
C. Cooling water for nozzle (*6/4mm PTFE tubing*)
D. Beam delivery fibre (*Optoskand - QB3315 - 300µm - 0.2 NA*)
E. Cooling water for fibre coupling (*6/4mm PTFE tubing*)
F. Laser beam collimator (*Optoskand - 1-9382x1 - FL 120mm*)
G. Beam bending cube (*Optoskand - 9439x1*)
H. Coaxial camera focusing lens (*Optoskand - 9441x2 – C mount*)
I. Coaxial video camera (*Siemens - CCBS1225-LP – Manual focus*)
J. Focusing optics (*Optoskand - 1-9229x2 – F160mm – Ø50mm*)
K. Protective window (*Optoskand 1-9354x1*)
L. Process shielding chamber upper plate (Purpose built)
M. Nozzle lateral adjustment screw (purpose built)
N. Coaxial laser deposition nozzle (ILT Fraunhofer)

3.1.4 Laser deposition nozzles

Two variations of laser deposition nozzle were used for this work, supplied to TWI by ILT Fraunhofer GmbH. A comparison of the merits and drawbacks of these nozzle types may be found in section 2.4.2.1.

For deposition work requiring laser powers less than 1000W, or when the heat input is relatively low and a concentrated powder spot is required, a conical flow coaxial nozzle was used (Figure 3-3A). For high heat input deposition work at laser powers above 1000W, a three-stream coaxial nozzle was used (Figure 3-3B) as it of a more robust design and less sensitive to spatter build-up.

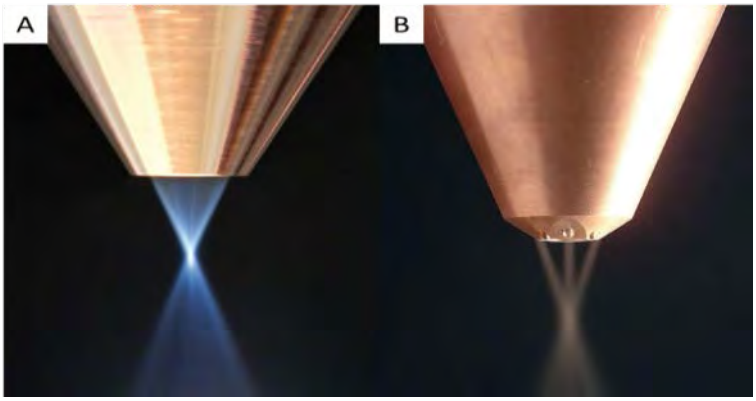

Figure 3-3 - Laser deposition nozzles used for this work, produced by ILT Fraunhofer GmbH A) conical flow coaxial B) three stream coaxial.

These nozzles allow coaxial gas flow, both to protect the melt pool and to prevent dust and fumes from entering the central aperture and contaminating the optical surfaces. Since deposition was performed under an inert atmosphere inside a sealed chamber, melt pool shielding by coaxial nozzle gas was not necessary.

3.1.5 Process shielding chamber

To prevent contamination of the melt pool during deposition, the deposition process was shielded using a purpose built deposition chamber (Figure 3-4). This comprised of a circular aluminium plate attached to the laser optics, a circular steel plate attached to the work bench with a drill vice firmly affixed in the centre, and a 500 gauge polythene membrane attached to the upper and lower plates using steel compression bands.

An inert atmosphere was produced within the chamber by back purging the bag with a 20l/min flow of argon (*BOC pureshield - 99.998% purity*). A one-way valve in the upper plate allowed a continuous slow of argon to pass through the chamber and out into the atmosphere, and allowed pressure relief to prevent the membrane from rupturing during robot movement.

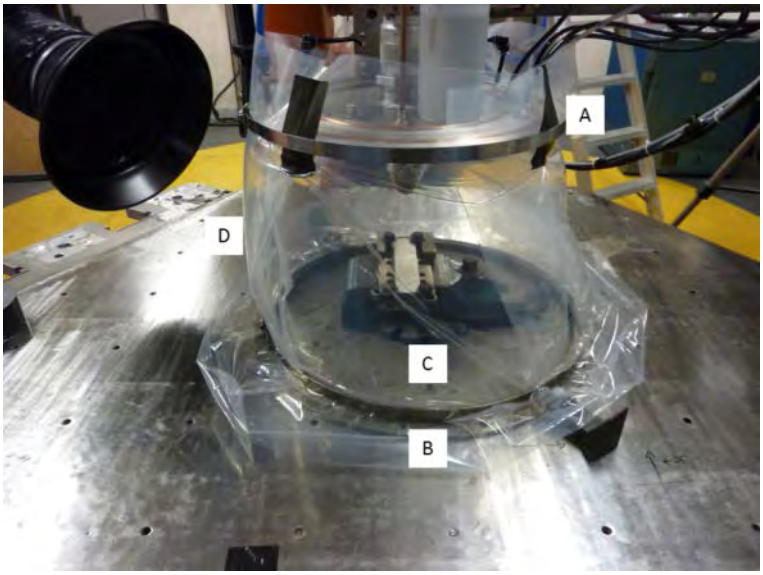

Figure 3-4 - Laser deposition chamber, consisting of: A) top plate B) bottom plate C) Clamping system D) polymer bag

This arrangement allowed oxygen content within the chamber to reach as low as 10 parts per million (ppm), with continuous process monitoring performed using a Systech® 810 oxygen meter, with a sampling rate of 1 l/min.

3.1.6 Substrate clamping fixture

A 200x100x10mm mild steel plate was fabricated with M6 drilled and tapped holes arranged in a 20x20mm square grid. This steel plate provided the clamping points for affixing the CM247LC substrates, which were then held in the jaws of the drill vice within the deposition chamber, as shown in Figure 3-4.

3.1.7 Induction heater

Deposit pre-heating trials conducted in chapter 5 were performed with the assistance of a 1kW Cheltenham induction TR1 induction heater, comprising of a power supply and water cooled portable ballast unit (Figure 3-5), onto which different induction coils could be attached.

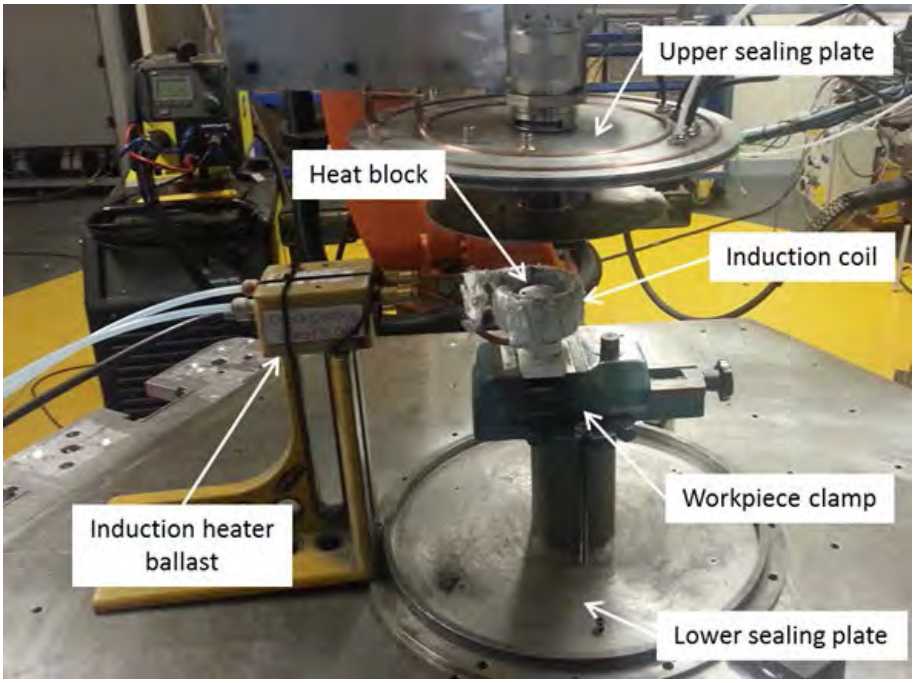

Figure 3-5 - Induction heating deposition apparatus without the sealing bag fitted.

The induction coil used for this work was fabricated from 8mm copper micro-bore tubing, formed from 5 turns, 80mm internal diameter and 10mm turn spacing, which was then wound with glass fibre insulation to reduce the radiative heat losses (Figure 3-6).

The induction coil and ballast assembly was raised approximately 300mm from the worktop in order to maximise the internal volume of the sealing chamber, and reduce intensity of the radiated heat onto the polyethene membrane. This also helped to prevent any creases in the bag from forming, which have a tendency to soften and rupture during deposition.

Figure 3-6 - Induction coil with glass fibre insulation in place.

To protect the PTFE tubing that delivers the powder, gas and water to the nozzle and optics, an Ø300x1.5 mm steel heat shield was fabricated that fits closely around the nozzle. This was found to be very effective at preventing radiated heat from melting the tubing.

The deposition chamber was sealed with 3 layers of 500 gauge polyethene, and purged with argon down to <100ppm O_2 to prevent oxidation of the deposit during or after deposition.

Due to the relatively low coupling efficiency between the magnetic fields produced by the induction coil and the non-magnetic CM247LC substrate material, it was necessary to heat the substrate indirectly by means of thermal conduction, rather than induction.

In order to achieve the maximum heating effect, a Ø50mm mild steel bar (heat block) mounted to ceramic insulation was placed concentrically within the coil and held in place using the workpiece clamp (Figure 3-7), The flat face of one end of the mild steel bar was drilled and tapped to accept M6 screws, which were used to securely clamp the CM247LC

substrate to the heat block. This allowed the induction coil to heat up the mild steel bar, and transfer the heat into the substrate. Contact surfaces were ground flat on a surface plate using SiC paper to ensure optimum contact and thermal coupling.

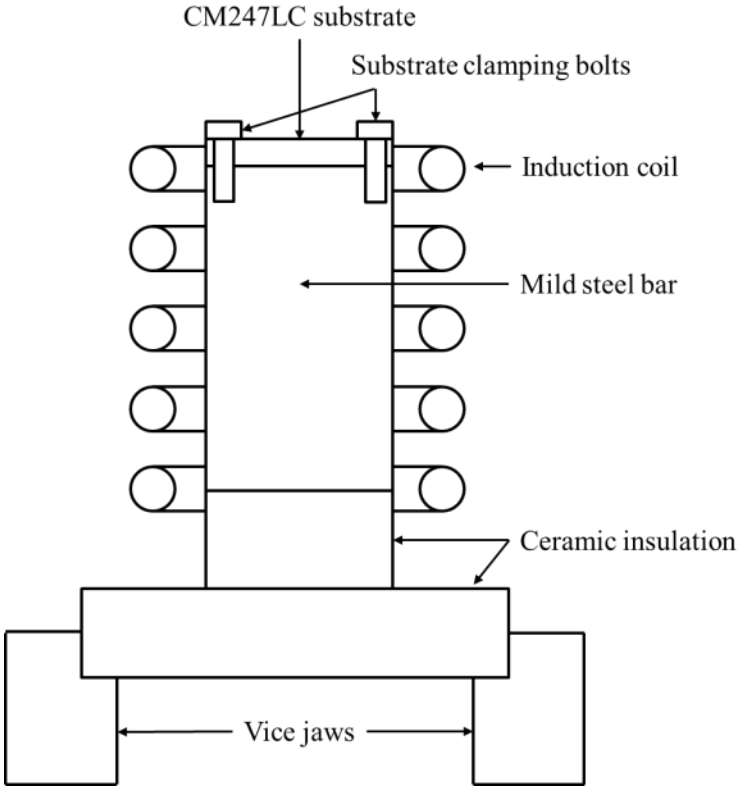

Figure 3-7 – Schematic illustration of the induction heating setup used for substrate pre-heating trials in chapter 5

3.2 Calibration methods

3.2.1 Laser power calibration

To correct for optical losses that occur along the path of the beam and ensure the correct power is reaching the workpiece, the laser must be calibrated. This can be performed by measuring the power output using a suitable laser power meter, and comparing the recorded power to the power requested.

Laser power calibration was performed at the start of each day, using a water cooled OPHIR thermal power sensor (Figure 3-8A) and OPHIR NOVA remote meter (Figure 3-8B). As discussed in section 3.1.1, the YLR-7000 laser was not capable of producing a stable beam at power requests below 10% of maximum, and so half of the laser modules were isolated to improve the stability. The effect of this can be seen in Figure 3-9.

Laser power was recorded in 25W increments at powers between 250 and 500W and 500W increments at powers between 500W and 3000W. For each measurement the laser was emitted for approximately 1 minute to allow the measurement to stabilise. The results are presented in Figure 3-9 and Table 3-1.

Figure 3-8 - A) Laser thermal power sensor (0.1-10kW) B) NOVA power meter

Table 3-1 - Laser power measurements for IPG YLR-7000 fibre laser, with half the modules active as well as with all modules active.

Laser power requested (W)	Laser power measure (W)	
	Half modules active	All modules active
250	45	85
275	70	133
300	96	192
325	128	246
350	140	303
375	166	327
400	177	349
425	189	372
450	200	393
475	212	415
500	226	438
1000	457	892
1500	690	1350
2000	921	1800
2500	1150	2260
3000	1390	2710

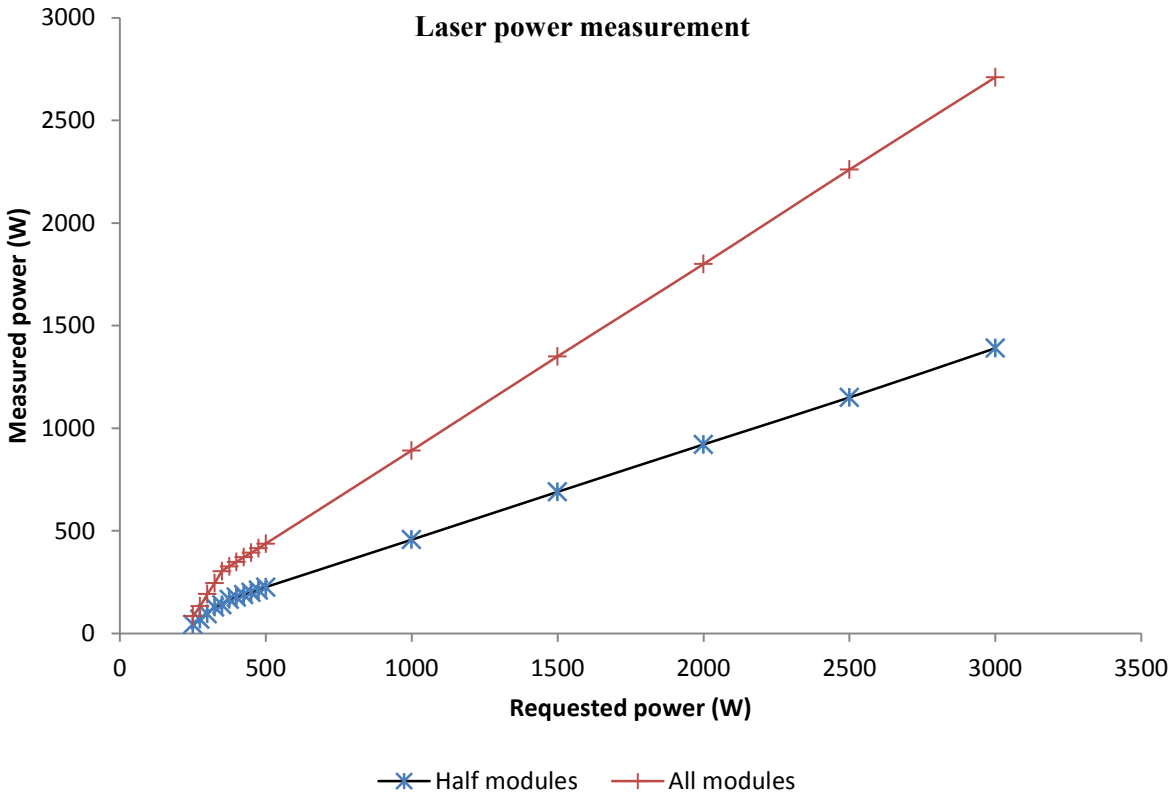

Figure 3-9 - Laser power measurements for IPG YLR-7000 fibre laser, taken with half the modules active as well as with all modules active.

Laser power scales linearly above 200W, and so a linear equation of the line of best fits through these points can be used to accurately predict the power that must be requested in order to produce the desired laser power at the workpiece.

3.2.2 Laser spot diameter and energy profile measurement

The size, shape and energy distribution of a laser beam are critical parameters that directly influence the quality of virtually all laser material processing operations, and for this reason it is important that these characteristics are measured to ensure they are consistent and accurate.

Using an Ophir Spiricon® digital beam profiler and BeamGage® software, measurements were taken of beam diameter and energy distribution at 15 point along the path of the laser beam, starting from the beam waist (focal point = 160mm) and working towards the focusing lens in 1mm increments.

The results of these measurements can be found in Figure 3-9 and Figure 3-10. This shows that the laser beam has a Gaussian profile, with the peak energy intensity located at the centre of the beam, and a minimum measured spot size of Ø0.6mm.

The results of the laser beam diameter measurements were used to extrapolate the distance from the optics to the workpiece in order to produce a spot of the required diameter.

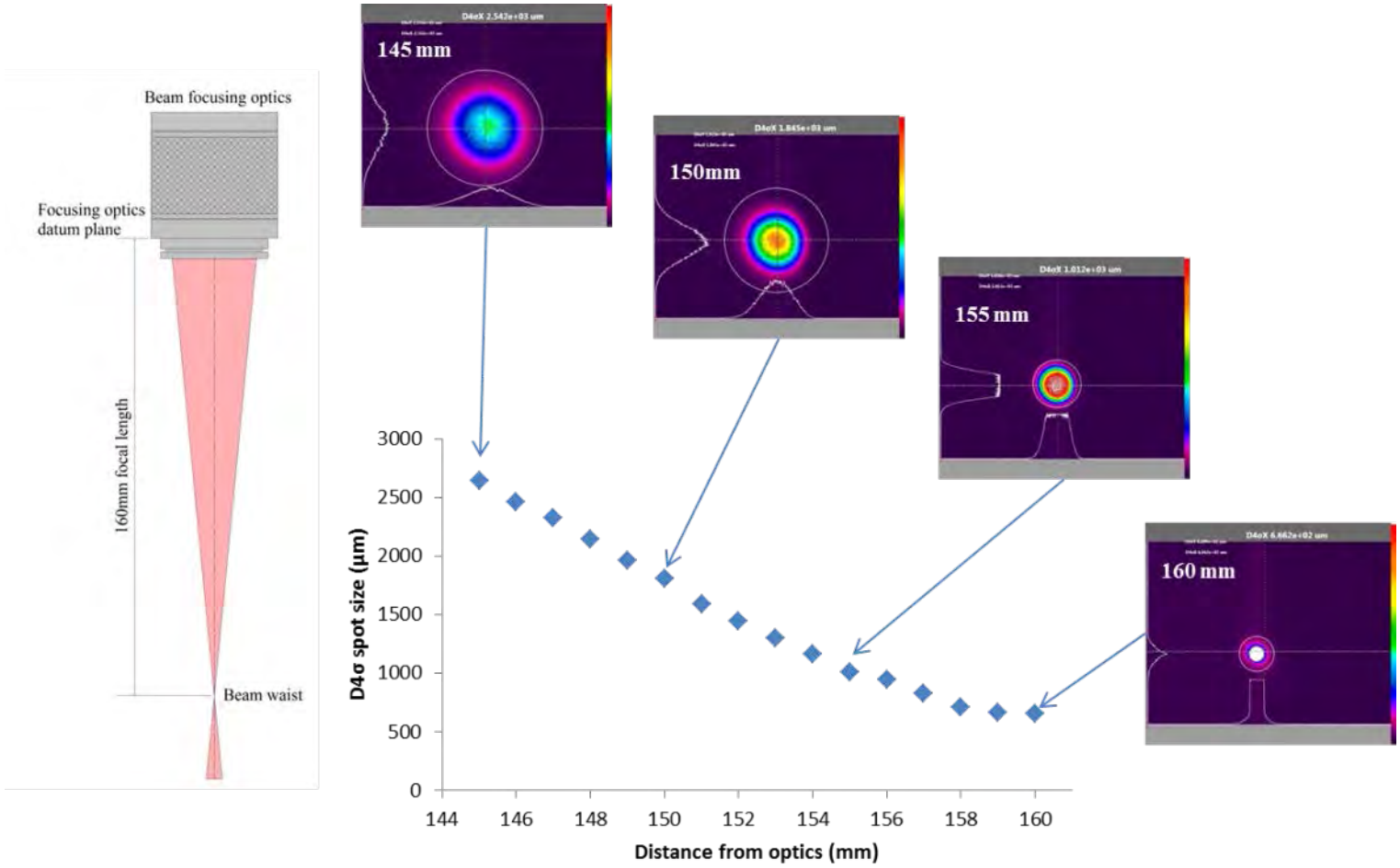

Figure 3-10 - Laser beam caustic generated using Ophir Spiricon® beam profiler for Optoskand F160 focusing optics, showing energy intensity profiles produced for 4 of these measurements

3.2.3 Nozzle setup and calibration

Correct setup of the laser deposition nozzle is a critical step in order to produce optimum results. The nozzle is aligned laterally and vertically to the coaxial laser beam to ensure the correct laser spot size is obtained and the highest powder capture efficiency is achieved.

3.2.3.1 Method for setting the laser spot size

3 Using the beam caustic graph generated during laser beam profilometry (Figure 3-10), the distance from the focusing optics that produces the desired spot size is calculated.

4 The robot moves the cladding head vertically, until the datum mark of the focusing optics are at the correct distance from the bench top. This is checked using a calibrated vernier height gauge.

5 The nozzle is retracted or extended within its clamping collar so that the focal point of the powder stream is precisely focused on the bench top. The powder focal length is a known distance (12mm for the nozzles used in this work), so a gauge block can be used to quickly set the distance (Figure 3-11).

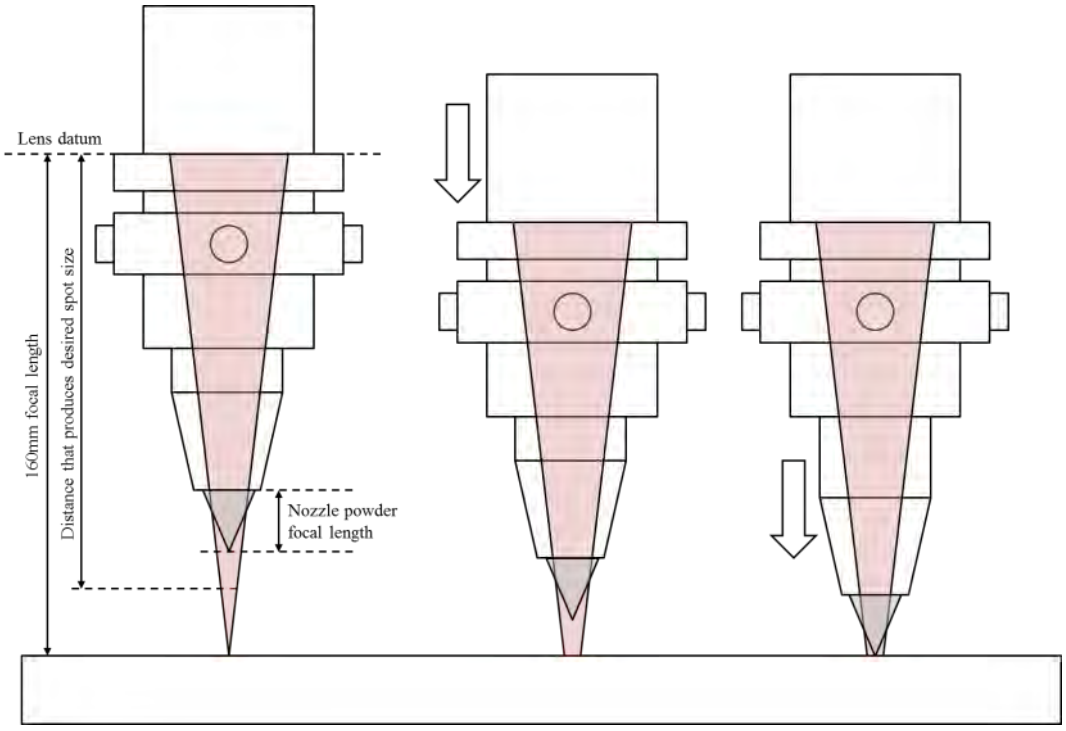

Figure 3-11 – Laser spot size adjustment

3.2.3.2 Method for aligning the deposition nozzle to the laser beam

1. A piece of 6mm thick mild steel plate, coated with engineers blue ink is securely clamped to the bench (Figure 3-12).
2. The cladding head is positioned so that the focal point of the powder delivery nozzle is exactly on the surface of the steel plate
3. The powder feeder is turned on for several seconds, causing a small patch of the ink to become abraded under the nozzle.
4. Using a sharp scribe and steel rule, a cross is inscribed through the centre of the abraded patch.
5. The laser beam is briefly emitted at low power (200W) to create a melted spot.
6. The distance from the centre of the scribed cross to the centre of the melted spot gives an indication of how well the nozzle is aligned. If adjustments are needed, the lateral adjustment screws for the nozzle are tightened or loosened, and the process is repeated until perfect alignment is achieved.

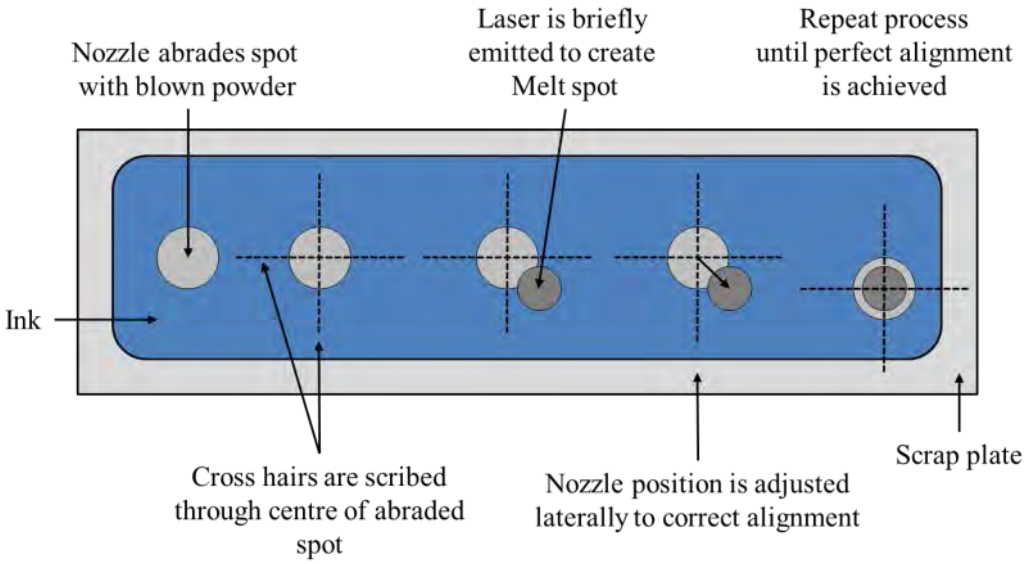

Figure 3-12 - Procedure for the alignment of nozzle to laser

3.2.4 Powder feed rate calibration

Powder mass flow rate measurements for powders CM247LC (20-40µm) and CM247LC (40-100µm) were conducted using a Sultzer-Metco twin-10C powder feeder, fitted with a grooved dosing disk (groove dimensions = 3mm wide x 0.6mm deep). Argon carrier gas was delivered at 1.5 bar / 6l/min throughout.

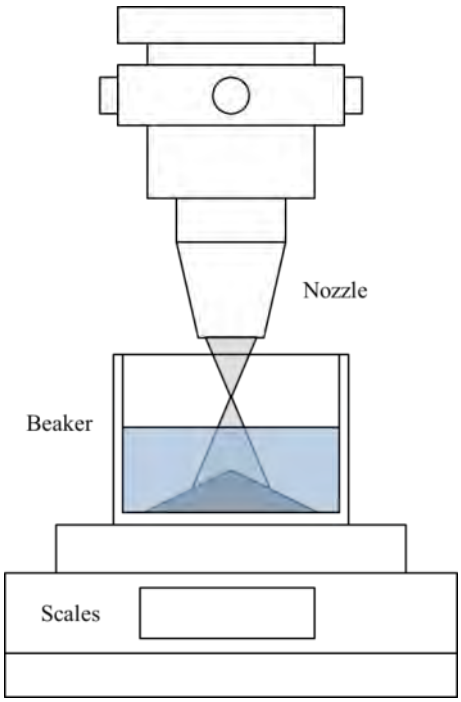

Figure 3-13 – Schematic illustration of the powder mass flow rate measurement process

A beaker half filled with water was placed on a set of accurate digital scales underneath the laser deposition nozzle (Figure 3-13). When the powder feeder is turned on, powder exits the nozzle and is effectively captured by the liquid and weighed.

Powder dosing speeds between 5 rpm and 50 rpm were used for each powder particle size, the results of which are presented in Table 3-2 and Figure 3-14. Plotting a graph of mass flow (g/min) rate vs dosing speed (rpm) allows a dosing speed to be calculated that delivers the desired mass flow rate.

Table 3-2 - Mass flow rate measurements for CM247LC powder

Dosing disk rpm	Powder mass flow rate (g/min)	
	20-40µm	40-100µm
5	1.50	1.23
10	2.61	2.14
15	3.72	3.05
20	4.67	3.83
25	5.80	4.76
30	6.98	5.72
35	7.93	6.50
40	9.01	7.39
45	10.18	8.35
50	11.28	9.25

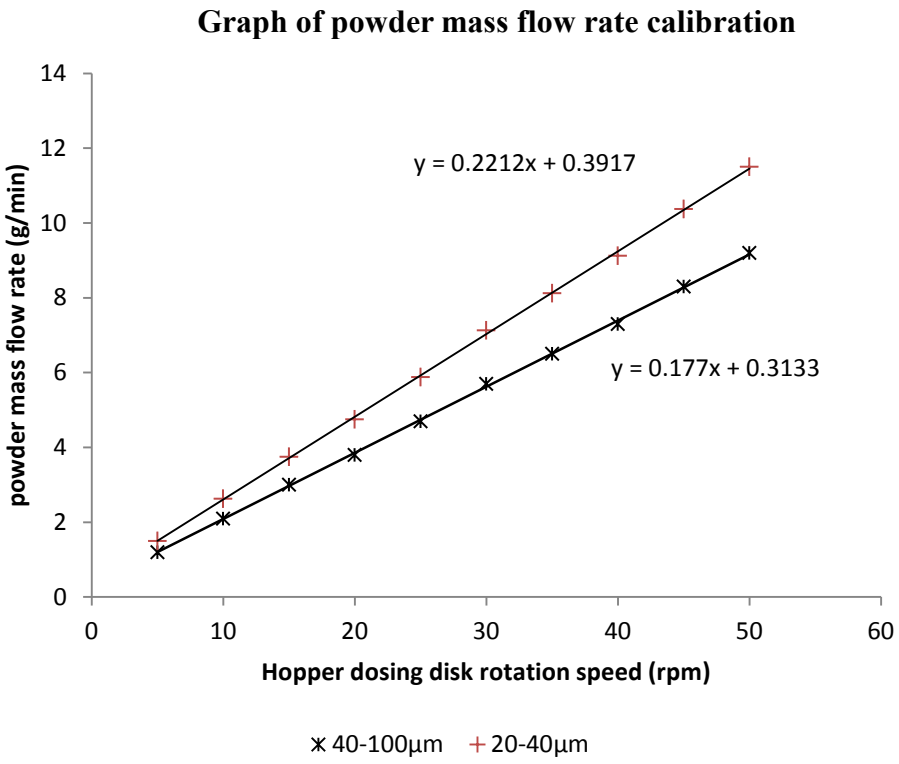

Figure 3-14 - Powder feed rate calibration chart for CM247LC powders

3.2.5 Induction heater calibration

Calibration of substrate temperature vs input voltage was conducted using a pair of thermocouples welded to a CM247LC substrate, which was securely clamped to the heating block within the induction coil (Figure 3-15). Temperature measurements were recorded using a National Instruments NI-DAQ data logger and Signal-Express software.

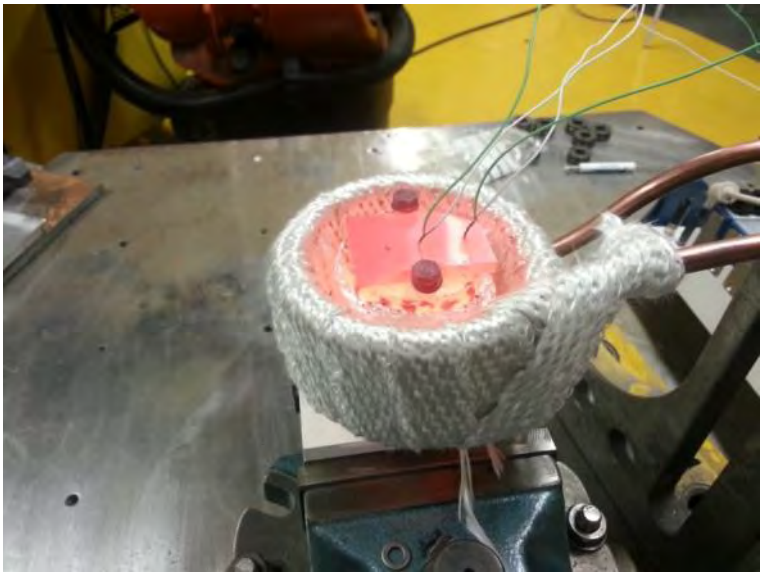

Figure 3-15 - Induction heater temperature calibration using thermocouples

A voltage was set on the heater controller, and the substrate was allowed to reach its equilibrium temperature, where the thermal losses due to conduction, convection and radiation are balanced by the heat input from the coil.

10 voltages were set for the induction heater, and the equilibrium temperature recorded for each. It was found that the induction heater could not output voltages greater than 300V before the thermal overload switch would cut out. A maximum temperature of 800°C was recorded for the substrate using this approach (Table 3-3, Figure 3-16) although due to the low power of the unit, voltages above 175V resulted in random power failures due to the thermal overload switch.

Table 3-3 - Induction heater calibration results

Voltage	Temperature (°C)
50	85
75	260
100	396
125	505
150	595
175	650
200	705*
225	752*
250	775*
275	796*

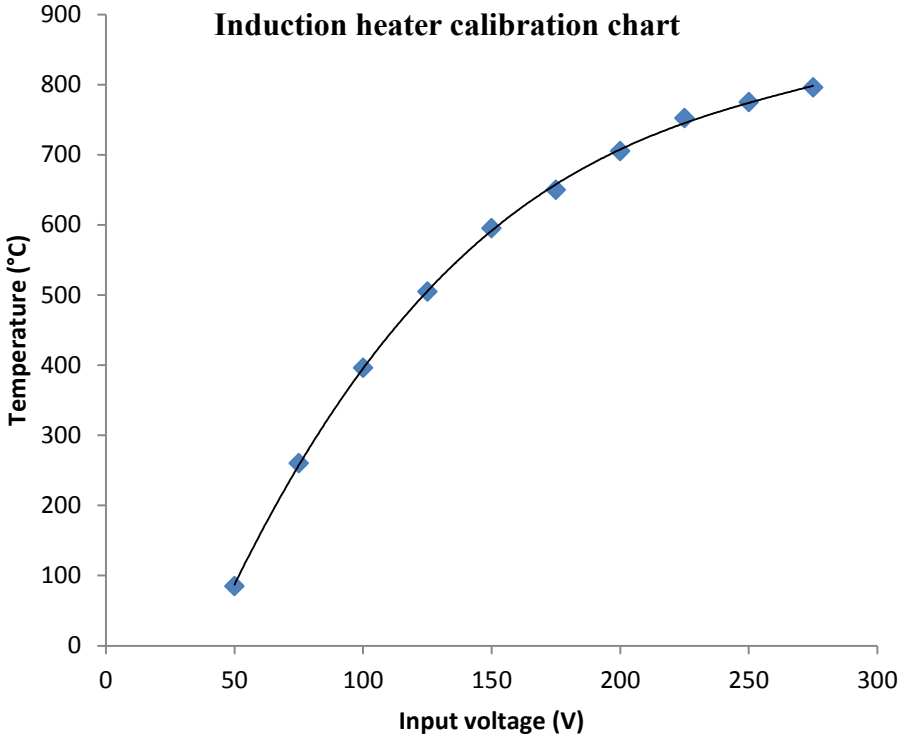

Figure 3-16 - Thermocouple temperature measurements for induction heater voltage calibration

3.3 Sample characterisation methods

Sample characterisation was performed using equipment at TWI Sheffield, TWI Cambridge and the University of Birmingham.

3.3.1 Metallographic sample preparation

Metallographic preparation of samples was conducted at TWI Sheffield, using the following equipment:

- Struers labotom® metallographic sectioning saw (Figure 3-17A)
- Struers labopress® hot mounting press with Ø40mm die (Figure 3-17B)
- Buehler twin disk manual sample grinder (Figure 3-17C)
- Struers tegrapol® semi-automatic sample polisher with tegradose® media dosing system (Figure 3-17D)

Figure 3-17 - Metallographic preparation equipment based at TWI Sheffield

3.3.2 Sample preparation routes

Depending on the nature of the material and the type of analysis to be conducted, different metallographic preparation methods were used (Figure 3-18, Table 3-4).

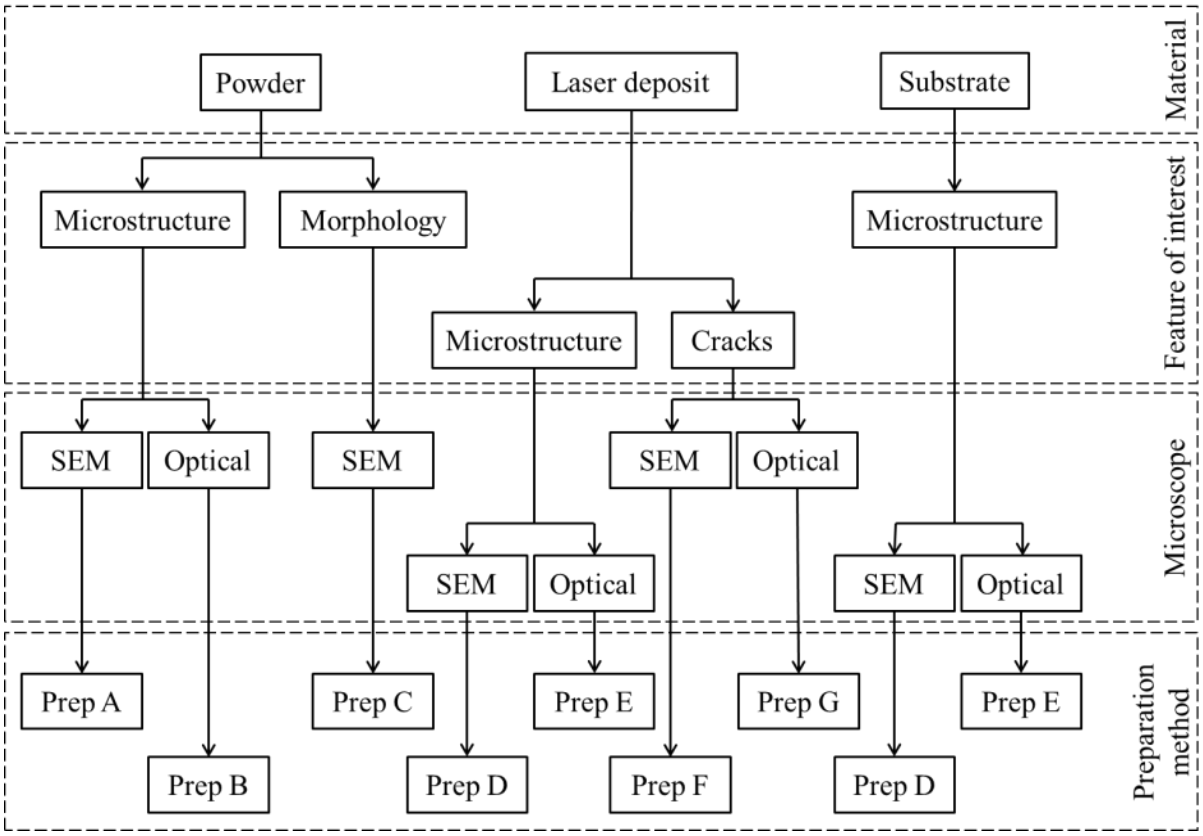

Figure 3-18 - Flowchart illustrating selection of metallographic preparation methods.

A. Microstructural characterisation of CM247LC powder using SEM

B. Microstructural characterisation of CM247LC powder using optical microscopy

C. Characterisation of powder morphology and surface features using SEM

D. Microstructural characterisation of laser deposited samples using SEM

E. Microstructural characterisation of laser deposited samples using optical microscopy

F. Quantification of cracks in laser deposited samples using optical microscopy

G. Characterisation of crack surface morphology in laser deposited samples using SEM

Table 3-4 - Metallographic preparation methods used for sample analysis (Etchant compositions may be found in Table 3-5)

Method	Sectioning	Encapsulation		Grinding			Polishing				Etching			
		Media	Method	Grit	RPM	Time	Media	Pad	RPM	Time	Etchant	Method	Time	Notes
A	Section by grinding	Conductive phenolic	Hot mount, 50kN, 180°C, 5 min	1200	100	2 min	OPS	Neoprene	150	5 min	Electrolytic	soaked cotton electrode	30 sec	12V/1A DC power supply
				2400	80	1 min								
				4000	80	1 min								
B		Epoxy	Cold mount	1200	100	2 min	OPS	Neoprene	150	5 min	Kallings	Swab	10 sec	
				2400	80	1 min								
				4000	80	1 min								
C	Powder sample is sprinkled onto conductive carbon sticky tab affixed to aluminium stub for morphology analysis in SEM													
D	Abrasive saw	Conductive phenolic	Hot mount, 50kN, 180°C, 5 min	120	200	5 min	OPS	Neoprene	150	5 min	Electrolytic	Immersion	10 sec or when edge turns brown	12V/1A DC power supply
				320	180	2 min								
				600	180	2 min								
				1200	150	2 min								
				2400	100	1 min								
				4000	80	1 min								
E	Abrasive saw	Non-conductive phenolic	Hot mount, 50kN, 180°C, 5 min	120	200	5 min	OPS	Neoprene	150	5 min	Kallings	Swab	10 seconds	
				320	180	2 min								
				600	180	2 min								
				1200	150	2 min								
				2400	100	1 min								
				4000	80	1 min								
F	Abrasive saw	Non-conductive phenolic	Hot mount, 50kN, 180°C, 5 min	120	200	5 min	OPS	Neoprene	150	5 min	Kallings	Swab	10 seconds	Samples are ground, polished, etched and then re-polished to reveal cracks
				320	180	2 min								
				600	180	2 min								
				1200	150	2 min								
				2400	100	1 min								
				4000	80	1 min								
G	Samples are sectioned and cut near to visible crack, then forced apart using a vice to reveal crack surface. Sample is mounted on conductive carbon sticky tab affixed to aluminium stub for SEM analysis													

Table 3-5 - Metallographic etchants used for the preparation of CM247LC samples

Etchant	Composition	Application	Comments
Waterless Kalling's	5 grams Cupric Chloride 100cc Hydrochloric acid 100cc Ethanol	Swab or immersion	Good macro-etch. General structure, grain boundary, grain size, carbides
Electrolytic etch	5ml Hydrofluoric acid 5ml Nitric acid 100ml ethanol	12V/1A DC. Immersion with W/Pt electrodes or swab with cotton pad connected to electrode.	Good micro-etch. Reveals γ' and γ/γ' eutectic phases under SEM

3.3.2 Microscopy methods

3.3.2.1 Optical microscopy

Optical microscopy of samples was conducted at TWI Sheffield using the Olympus BX60 optical microscope and Leica DFC450 5 megapixel digital camera.

Samples were ground, polished and macro-etched using waterless Kalling's solution (Table 3-5) to reveal the general microstructure and carbide phases. Etching the polished sample with waterless Kalling's turns carbide phases darker, but does not reveal the γ' phase, which is unresolvable under optical microscopy. Unlike electrolytic etching, Kalling's produces an uniform etch across the sample surface, making it suitable for macroscopic imaging and general optical microscopy.

3.3.2.2 Scanning Electron Microscopy (SEM)

Scanning Electron Microscopy was performed at TWI Cambridge, using a LEO 1550 FEG-SEM, equipped with QBSD, EPMA and in-lens secondary electron detector.

Cross- sectioned samples were ground, polished and electrolytically etched (Table 3-5) to reveal the microstructure, carbides, γ' and other phases not resolvable under optical microscopy.

3.3.3 Crack quantification method

Deposited blocks were cross- sectioned into four equal pieces transverse to the long axis of the block, as shown in Figure 3-19B. Three of these sections were hot mounted in non-conductive phenolic resin in order to present regions from ¼, ½ and ¾ of the deposit length. These mounted samples were metallographically prepared for optical microscopy as described in Table 3-4 (method F), and the remaining section retained for future reference.

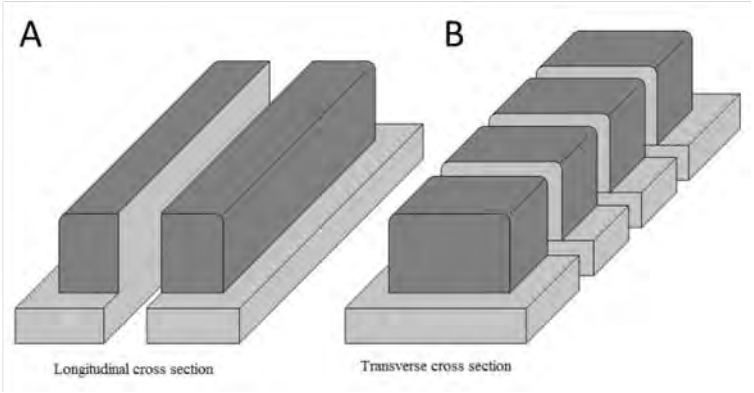

Figure 3-19 - Cross section methods used for analysis of deposited blocks A) Longitudinal B) Transverse

In order to reveal the fine scale cracks in the laser deposited blocks that were obscured during the grinding and polishing steps, polished samples were swab etched using a waterless Kalling's solution, then re-polished to produce a fine optical finish. The effect of this two-step polishing procedure on the number of observable cracks can be seen in Figure 3-20.

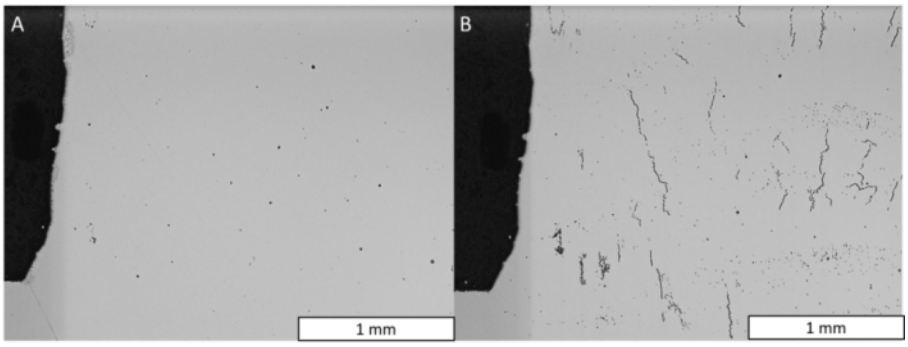

Figure 3-20 - Optical micrographs illustrating difference in observable cracks between (A) polished sample (B) sample that was polished, etched and re-polished. Both micrographs were taken from the same region of the same sample.

3.3.3.1 Crack measurement using optical microscopy

Polished samples were imaged using an Olympus BX60 optical microscope at 50x magnification. Non-overlapping optical micrographs were taken across the whole sample surface, starting in the bottom left hand corner at the interface between the deposit and the substrate, and moving towards the upper surface in a raster pattern (Figure 3-21).

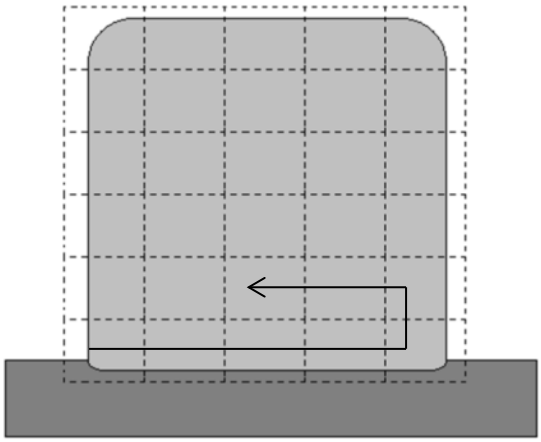

Figure 3-21 - Diagram illustrating position of optical micrographs for crack measurement analysis

Optical micrographs were analysed using ImageJ® open source image analysis software (http://imagej.nih.gov/ij/), calibrated to 720 pixels per mm length using a traceable calibration graticule slide (TWI R1011-1596).

Crack measurements for each sample were performed manually using the segmented line tool in ImageJ®, with each crack being individually measured and recorded (Figure 3-22). The sums of the total measured crack lengths for all of the micrographs in each sample were divided by the sum of the observed image area, to produce a value of crack length per unit area for each sample.

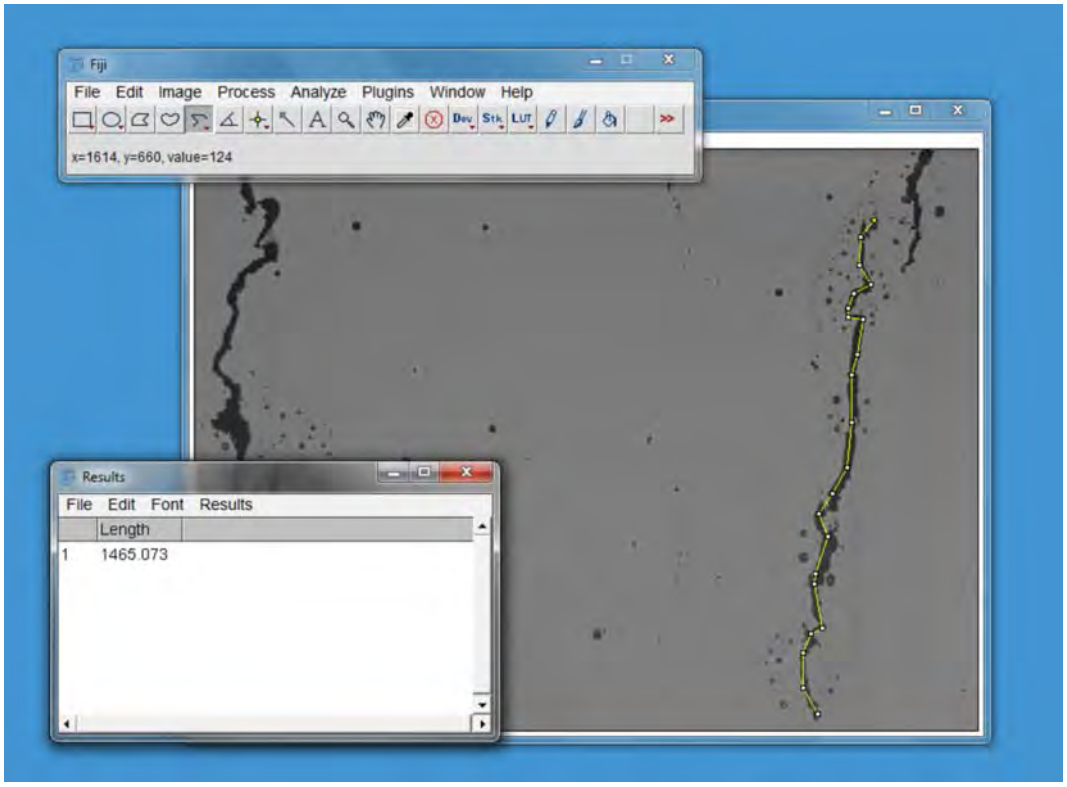

Figure 3-22 - Crack measurement method using ImageJ® software

3.4 Chapter 3 - List of figures

3.5 Chapter 3 – List of tables

Chapter 4

Investigation of cracking in laser deposited CM247LC through Design of Experiments methodology

4 Chapter 4 - Investigation of cracking in laser deposited CM247LC through Design of Experiments methodology

4.1 Introduction

In this chapter, Design of Experiments (DOE) methodology was used to create an experiment matrix for the laser deposition of CM247LC test blocks, so that the relationship between key process parameters and the cracking response could be evaluated and better understood.

As discussed in chapter 2, CM247LC is a polycrystalline casting alloy that was developed for use in the hot sections of aero-engines, where it is subjected to extreme temperatures and stress. A review of the literature surrounding this material revealed that there are very few economical repair and re-manufacture routes available to this material, due to its high tendency to form cracks.

Laser metal deposition is being examined as a potential repair and manufacture process, due to the ability to accurately control the size and shape of the material addition, as well as the heat input to the material, which allows some degree of microstructural control.

4.2 Experimental approach

4.2.1 Equipment and materials

4.2.1.1 Laser metal deposition equipment

Deposition trials were conducted at TWI Sheffield, using the equipment described in section 3.1. All deposition work was performed under an inert argon atmosphere to limit the formation of undesirable oxide phases that may affect the cracking response of the process [1].

4.2.1.2 CM247LC Powder

Gas atomised CM247LC was supplied by the University of Birmingham, in the size range 0-150μm. This size range is typically used for Hot Isostatic Pressing (HIP), as it has a wide range of particle sizes that allow efficient packing and rapid consolidation. However, this range is not so suitable for laser metal deposition in the as-received condition, and must be sieved into a more desirable size range. For laser metal deposition, a more appropriate size range is in the region of 40-100 μm.

Larger particles (>100μm) generally include a greater degree of porosity compared to fine powder, and generally have more irregular particle morphologies due to the slower cooling rate of the larger droplets during atomisation [2]. Smaller powder particles (<20μm) tend to have poor flowability, which may impede powder flow inside the hopper and delivery tubing to the process [3], leading to irregular mass flow rates.

Samples of each powder size range were sent to London & Scandinavian metallurgical Ltd for elemental analysis, Malvern oxygen measurement and particle size distribution measurement. Samples of powder were also sectioned and metallographically prepared for optical and

electron microscopy using the methods outlined in section 3.3.1, in order to evaluate the microstructure, chemical homogeneity and morphology of the particles.

4.2.1.3 CM247LC Substrate

CM247LC substrate was provided by TWI Ltd as an Ø150x100mm cylindrical bar, produced by Hot Isostatic Pressing (HIP) of CM247LC powder using the parameters listed in Table 4-1.

Table 4-1 - HIP parameters used for production of substrate material

Material	Powder size (µm)	Temp (°C)	Pressure (Mpa)	Time (hrs)
CM247LC	0-150	1160	150	4

The consolidated bar was sliced into 5mm thick disks (Figure 4-1) by Wire Electric Discharge Machining (WEDM), which were then surface ground to a 120 grit finish using a belt linisher to remove the recast layer. The recast layer is produced during WEDM, and is made up of heavily carbonised molten metal particles that have re-deposited onto the surface of the workpiece during cutting, and may act as initiation sites for cracks and other defects [4,5].

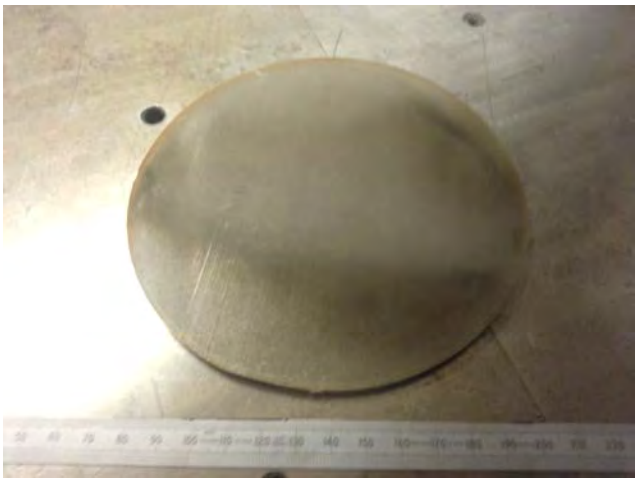

Figure 4-1 - 5mm thick CM247LC substrate in the as-cut condition, cut using the Wire EDM process

4.2.1.4 Definition of process variables and creation of experiment design

The objective of this work is to understand how the laser metal deposition process variables affect the crack formation in laser deposited CM247LC. Response surface methodology was chosen as the method of analysing this data for two reasons:

1. It would allow the interactions between process variables to be examined with respect to the number of cracks that form
2. The topography of the response surface may indicate if there is a process optimisation path that results in crack free deposits, or reduced crack density.

In order to design an experiment matrix using DOE methodology, it was necessary to first define three aspects of the experiment:

- The DOE factors - What are the process variables that are to be examined?
- The range - What are the minimum and maximum values for these factors?
- The response - How is the outcome of the experiment to be judged?

4.2.1.5 DOE process factors (inputs)

Using Design of Experiments (DOE) software Design Expert® 7, a full factorial central composite design experiment was constructed based around four processing variables (Table 4-2): laser power, scanning speed, laser spot diameter and deposit dilution.

To prevent unachievable parameters from being defined by the software (such as a laser spot diameter that was smaller than was physically possible) or parameters that may cause damage to the laser deposition equipment, a parameter range was chosen in terms of its alpha values. Defining the process limits by the alpha values allowed an absolute value of the experiment parameter range to be set rather than have maximum and minimum values generated by the software, which may otherwise be outside of the safe range of the equipment.

Table 4-2 - Parameter range defined for the DOE

Factor	Alpha minus	Alpha Plus
Laser power (Watts)	200	1000
Scanning speed (mm/s)	2.5	15
Laser spot diameter (mm)	1	2.5
Deposit dilution	1	2

In this work, laser power, scanning speed and laser spot diameter are considered *independent* variables, meaning their values are predefined and are not greatly influenced by changes in other process variables. For example, the laser power does not vary depending on the scanning speed, or vice versa.

As discussed in section 2.3.3.5.6, deposit dilution is a *dependant* variable, which in this case means that the geometry of the deposit (penetration, width, height, etc.) is strongly influenced by the other process variables. This means that for each distinct laser power, scanning speed and laser spot size combination generated by the DOE software, a powder mass flow rate must be determined experimentally that will produce the dilution specified by the DOE.

For the purposes of this work, the deposit dilution is defined as the ratio between the clad area (A_c) and the melted area (A_m) of a deposited track when viewed in cross section [6-8], as illustrated in Figure 4-2.

$$Dilution\ (D) = {}^{A_c}/_{A_m}$$

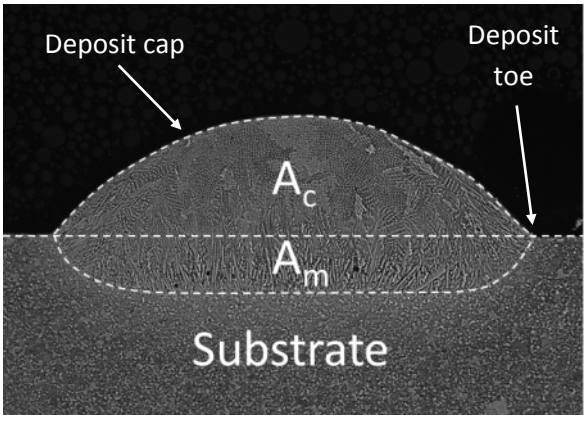

Figure 4-2 - Cross section of laser deposited track, showing the clad area (A_c) and the melted area (A_m)

Deposit dilution was chosen as the fourth factor for several reasons:

1. The deposit shape directly influences the build rate and quality of the deposited part, and so it is important to understand and control it [6].

2. As the deposition nozzle becomes worn, or deteriorates over time due to tip contamination, the efficiency of the process decreases, meaning fewer powder particles enter the melt pool to form the deposit. Checking the deposit dilution against those done previously using the same parameters is a quick and easy way of ensuring that the correct powder mass delivery rate is being used [6,9,10].

3. Changing the powder mass delivery rate changes the dilution in a linear relationship (for a fixed laser power, scanning speed and laser spot size) and so the delivery rate required to produce a deposit of a desired shape is easily calculated [7,10-13].

4.2.1.6 DOE Process response (output)

The single response output defined for the experiment is the *crack density*, which is defined as crack length per unit area ($\mu m/\mu m^2$). The methodology used to quantify crack length is detailed in section 3.2.3.

While this is not a definitive measurement of the total crack content (as this procedure uses a two dimensional analysis to measure a three dimensional defect), it was felt that it was sufficient for a *comparative* study of the effect of process variables on the cracking response of laser deposited CM247LC.

4.2.1.7 Generating the DOE test matrix

Using the parameter ranges listed in Table 4-2, a test matrix comprising of 30 experimental runs was generated using the central composite design factorial method (Figure 4-3). This test matrix is illustrated graphically in Figure 4-3, as a cube with corner points (pink), a central point (red) and alpha points (blue) that project in positive and negative directions from the centre point along all three axes. Each axis represents a process factor, with the forth factor (dilution) represented by varying each point over 2 levels, a high dilution (+) and a low dilution (-).

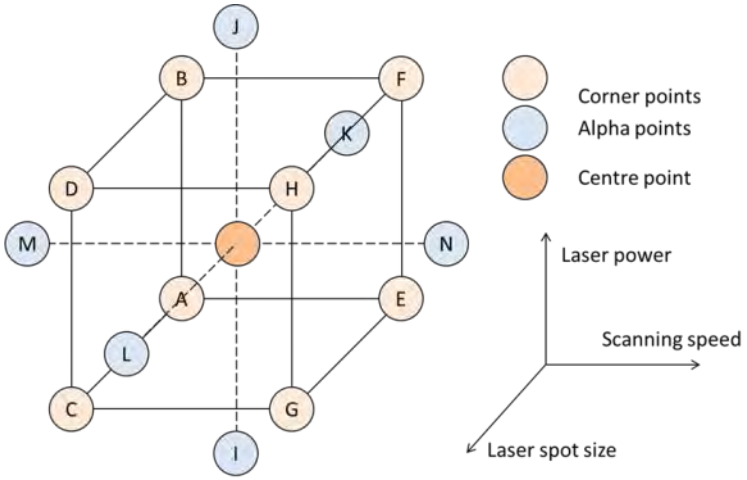

Figure 4-3 - Graphical illustration of central composite experiment design from Table 3.

The centre point of the projected cube represents a set of 6 identical experimental runs (duplicates), which are inserted to test the intrinsic variability of the process. If the variation in the results for the duplicates is greater than the variation in results across the other runs, then it would be very difficult for the software to identify and correlate any underlying relationships.

Table 4-3 - DOE experiment plan generated by Design Expert 7 ® software, for the deposition of CM247LC blocks for crack measurement analysis, listed by standard order.

Standard order (Std)	Run	Laser power (W)	Laser spot diameter (mm)	Scanning speed (mm/s)	Dilution
1 (Corner A-)	4	400	1.375	5.625	1.25
2 (Corner B-)	9	800	1.375	5.625	1.25
3 (Corner C-)	13	400	2.125	5.625	1.25
4 (Corner D-)	7	800	2.125	5.625	1.25
5 (Corner E-)	30	400	1.375	11.875	1.25
6 (Corner (F-)	27	800	1.375	11.875	1.25
7 (Corner G-)	17	400	2.125	11.875	1.25
8 (Corner (H-)	18	800	2.125	11.875	1.25
9 (Corner A+)	16	400	1.375	5.625	1.75
10 (Corner B+)	19	800	1.375	5.625	1.75
11 (Corner C+)	12	400	2.125	5.625	1.75
12 (Corner D+)	20	800	2.125	5.625	1.75
13 (Corner E+)	2	400	1.375	11.875	1.75
14 (Corner F+)	26	800	1.375	11.875	1.75
15 (Corner G+)	11	400	2.125	11.875	1.75
16 (Corner H+)	8	800	2.125	11.875	1.75
17 (Point I)	22	200	1.75	8.75	1.5
18 (Point J)	15	1000	1.75	8.75	1.5
19 (Point K)	5	600	1	8.75	1.5
20 (Point L)	6	600	2.5	8.75	1.5
21 (Point M)	28	600	1.75	2.5	1.5
22 (Point N)	1	600	1.75	15	1.5
23 (Centre -)	23	600	1.75	8.75	1
24 (Centre +)	24	600	1.75	8.75	2
25 (Centre dup)	29*	600	1.75	8.75	1.5
26 (Centre dup)	14*	600	1.75	8.75	1.5
27 (Centre dup)	25*	600	1.75	8.75	1.5
28 (Centre dup)	3*	600	1.75	8.75	1.5
29 (Centre dup)	21*	600	1.75	8.75	1.5
30 (Centre dup)	10*	600	1.75	8.75	1.5

4.2.2 Process rule development

As mentioned in section 4.2.2.1, the process variables defined in the DOE test matrix are not sufficient by themselves to allow the deposition of blocks that would be suitable for analysis. In order to deposit blocks of acceptable quality, the following variables must be fully defined:

- Laser power (W) - Defined by DOE
- Scanning speed (mm/s) - Defined by DOE
- Laser spot diameter (mm) - Defined by DOE
- Powder feed rate (g/min) - ?
- Track separation distance (ΔX) - ?
- Vertical movement distance between layer (ΔZ). - ?

Each of the 30 DOE runs are defined by the laser power, scanning speed, laser spot diameter and deposit dilution, but order to obtain a specific deposit dilution for a given laser power, scanning speed and laser spot diameter, an experiment must be conducted in which a powder feed rate is determined that will produce the desired dilution. Low powder feed rates produce a low clad area value (A_c), high powder feed rates produce a high A_c value, and by adjusting the rate at which powder enters the melt pool, it is possible to obtain the desired dilution value.

Similarly, the values of ΔX and ΔZ will need to be experimentally determined for each DOE run. Because each DOE run will produce a deposit track of different shape and size, it is not possible to use the same value of ΔX and ΔZ for each block, as the degree of overlap between tracks and the layer thicknesses would be different in each case. This would lead to poor deposit shape and quality, which may introduce additional scatter to the results that would obscure any inherent relationships.

The approach used for this work was to define the ΔX and ΔZ values as *percentages* of the known track width and layer thickness, as it makes them independent of deposit geometry. To this end, a set of experiments were devised that established *processing rules*, in which a powder feed rate is determined for each DOE run to produce the desired dilution, defines ΔX as a percentage of the individual track width which can be applied across all DOE runs, and similarly defines the ΔZ as a percentage of the thickness of a single layer of tracks deposited using the ΔX value established.

It was hoped that these rules would help to reduce the variability between DOE runs, so that underlying relationships may be more easily evaluated without the introduction of additional scatter.

This process is illustrated by the flow chart in Figure 4-4, which details the experiments that were to be conducted before the full DOE test matrix of blocks could be deposited. While the actual parameters are not transferable between DOE tests, the rule that was used to determine that parameter should be.

By depositing the DOE test blocks, quantifying the cracking response for each and then inputting the responses back into the DOE software, a 3D response surface can be generated that shows how the different factors influence the cracking. The software also allows an "*optimisation"* of the process, which predicts a set of parameters that would produce the best response. The experiment plan illustrated in Figure 4-4 also includes the deposition of this "optimised" block, which is used to validate the model produced by the DOE software. As mentioned previously, in this case the term optimised refers purely to the reduction in cracking, and does not consider deposit shape, surface finish or external quality.

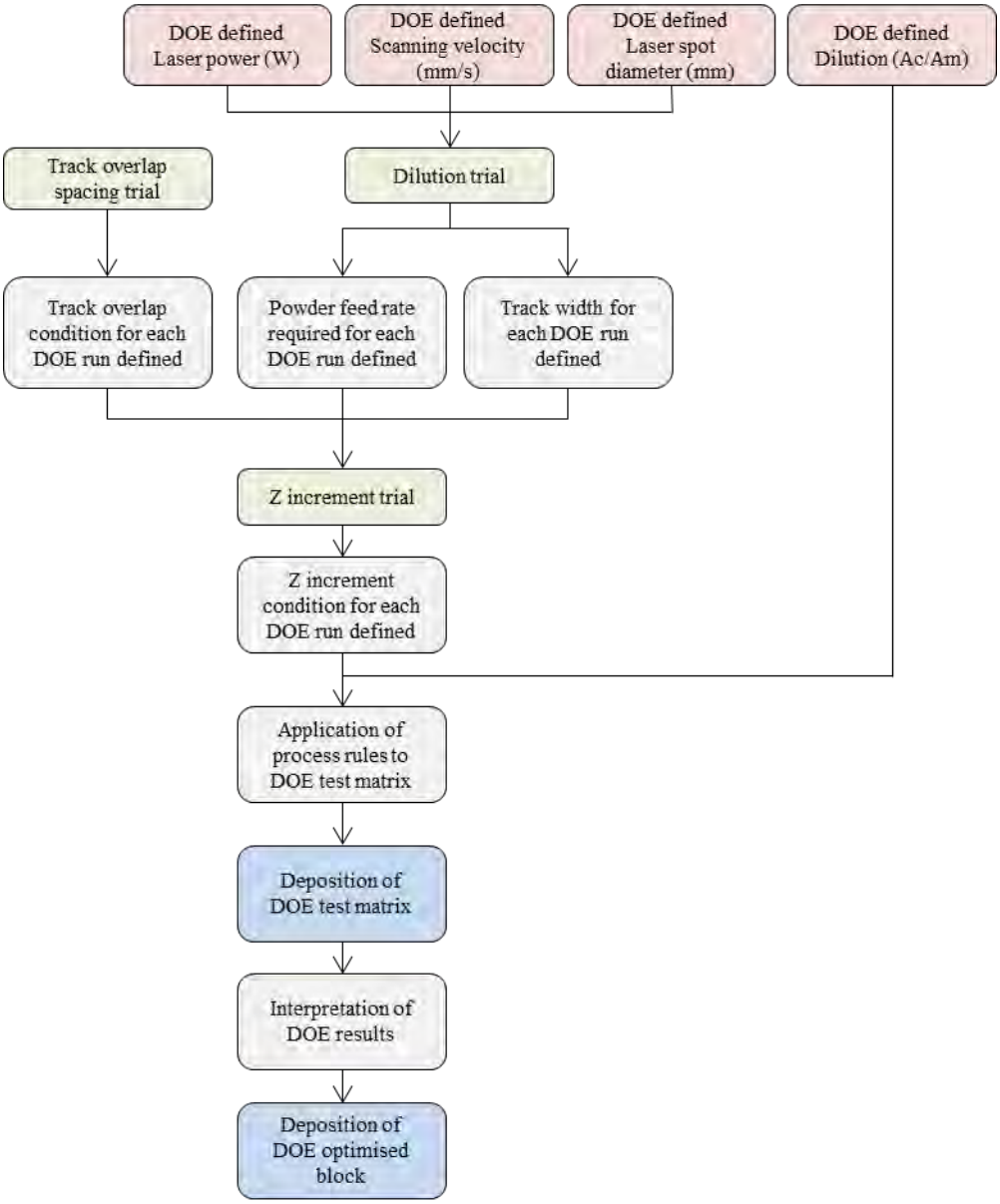

Figure 4-4 - Schematic showing experiment plan, including trials used to establish the deposition parameters needed for the deposition of DOE test blocks.

4.2.2.1 Determining powder feed rate required to produce desired dilution for each DOE run

When a metal powder is projected into the melt pool created by the laser, the volume of molten material in the pool increases, creating a raised profile that solidifies proud of the substrate surface as the laser moves along its prescribed path. It was found through previous experience, that the dilution of a deposited track generally varies linearly with an increase or decrease in powder mass feed rate (for a fixed power, speed and spot size) [6,7-14].

Of course, there is a limit to how much powder the melt pool can accommodate before the shape and size of the deposit becomes unstable, but for the purposes of this experiment, deposit dilution and powder mass flow rate can be considered to have a linear relationship.

With this understanding, it is possible to achieve a deposit of the desired shape and dilution with the minimum of experimental trials. This is achieved by depositing 2 tracks, each at different powder mass flow rates. Metallographic analysis of the track cross section produces a value of dilution for each track, the result of which is plotted on a graph against the powder feed rate and an equation generated that describes a straight line connecting them.

From the DOE experiment plan, 15 *distinct* parameter combinations of laser power, scanning velocity and laser spot diameter were identified (Table 4-4). For each of these parameter combinations, 2 tracks were deposited onto 5mm thick CM247LC substrate at 1.7 and 2.5 g/min, measuring 30mm in length using the laser power, scanning speed and laser spot diameter specified by the DOE.

Each track was sectioned perpendicular to the deposition direction to produce three equal pieces, which were then metallographically prepared for optical microscopy, using procedure E set out in section 3.3.1.

Optical micrographs of each cross section were analysed using ImageJ® image analysis software, using the polygon tool to measure the clad area (A_c) and melted area (A_m), and the straight line tool to measure the track width. An average value of deposit dilution and track width were calculated for each run in order to take into account irregular deposit height along the length, and the results recorded. From these results, graphs were plotted that allowed the powder feed rate for all 30 DOE runs to be calculated.

Table 4-4 - Deposition parameters used for deposit dilution experiment.

Sample ID	DOE run	Laser power (W)	Laser spot diameter (mm)	Scanning speed (mm/s)	Required dilution Ac/Am
PM-EngD-019/020	1	600	1.75	15	1.5
PM-EngD-003/004	2	400	1.38	11.88	1.75
PM-EngD-021/022	3	600	1.75	8.75	1.5
PM-EngD-005/006	4	400	1.38	5.63	1.25
PM-EngD-001/002	5	600	1	8.75	1.5
PM-EngD-039/040	6	600	2.5	5.63	1.5
PM-EngD-029/030	7	800	2.13	5.63	1.25
PM-EngD-007/008	9	800	1.38	5.63	1.25
PM-EngD-031/032	11	400	2.13	11.88	1.75
PM-EngD-033/034	13	400	2.13	5.63	1.25
PM-EngD-023/024	15	1000	1.75	8.75	1.5
PM-EngD-037/038	18	800	2.13	11.88	1.25
PM-EngD-025/026	22	200	1.75	8.75	1.5
PM-EngD-013/014	26	800	1.38	11.88	1.75
PM-EngD-015/016	28	600	1.75	2.5	1.5

4.2.2.2 Establishing a standard track overlap spacing condition (ΔX)

In order to produce deposited blocks of acceptable shape and integrity, a track overlap rule needed to be defined that could be applied across all runs to minimise variation. For the purposes of this work, the track spacing is defined as the distance between track centrelines (measured in mm) whereas track overlap (Figure 4-5) is the degree that one track overlaps an adjacent track, and can be measured as a percentage of the individual track width (W).

It is important that the degree of track overlap is correct, as incorrect overlap can have a negative impact on the quality of the deposited part:

- If the track spacing is too low, the tracks will pile up on top of one another, creating a deposited layer that is thicker at one end than the other. In some cases this may lead to excessive re-melting of adjacent track and excessive heat input into the substrate [15].

- If the track spacing is too large, then the surface of the deposited layer will be very uneven, consisting of parallel grooves and ridges, which may lead to the introduction of lack-of-fusion defects and inter-run porosity.

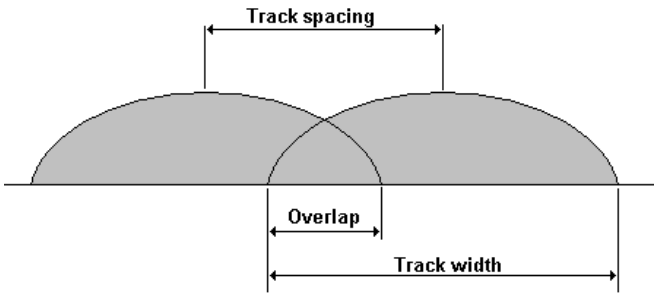

Figure 4-5 - Schematic illustration of two laser deposited tracks viewed in cross section overlapping each other

In order to investigate the influence of track overlap spacing on deposit regularity and crack density, 8 samples were deposited using different dilutions and track overlaps (Table 4-5), calculated as a percentage of measured single track width for a given laser power, scanning speed and laser spot diameter.

Samples were cross sectioned for metallographic analysis perpendicular to the deposition direction, and layer thickness measurements taken using optical microscopy. Choice of the most appropriate overlap condition was based both the regularity and evenness of the surface, as well as the degree of cracking that was observed.

For samples that displayed a high degree of cracking, micro-hardness measurements of the crack regions were also conducted, in order to investigate if there is any localised hardening or softening that may be influencing crack formation. This work was conducted at TWI Cambridge, using a Struers Duramin micro-indenter with 100g load.

Table 4-5 - deposit plan for the production of laser deposited patches to investigate effect of overlap conditions on clad layer quality

Deposit ID	Laser power (W)	Scanning speed (mm/s)	Laser spot size (mm)	Dilution	Powder feed rate (g/min)	Track spacing (mm)	Overlap %
PM-EngD-041	400	5	1	1.0	1.7	1.06	50%
PM-EngD-042	400	5	1	1.0	1.7		40%
PM-EngD-043	400	5	1	1.0	1.7		30%
PM-EngD-044	400	5	1	1.0	1.7		20%
PM-EngD-045	400	5	1	1.5	2.5	1.06	50%
PM-EngD-046	400	5	1	1.5	2.5		40%
PM-EngD-047	400	5	1	1.5	2.5		30%
PM-EngD-048	400	5	1	1.5	2.5		20%

4.2.2.3 Establishing a standard z-increment condition (ΔZ)

The Z-increment is the vertical distance that the laser deposition apparatus moves between layers. For open loop systems, such as the LMD equipment used for this work where there is no feedback control, it is important that this parameter is correctly configured [6,11,16-20] otherwise the deposit shape and quality will rapidly deteriorate with each subsequent layer.

- Setting the Z increment too high means that the nozzle will pull away from the deposit faster than the deposit can grow. This results in the powder focal point getting further and further away from the melt pool, leading to poor powder capture efficiency, surface finish and internal quality. This effect tends to get worse with each layer, until the nozzle gap is so large that the deposition process cannot continue.
- Setting the Z-increment too low means that the nozzle gap will gradually decrease, leading to poor powder capture and low build rate, excessive heating and poor surface finish.

During toolpath programming, the Z-increment is expressed in millimetres, but in order to create a rule that is applicable across all DOE parameter combinations, this must instead be expressed as a percentage of the measured individual layer thickness.

Using the layer thickness measurements from section 4.2.3.2 (for patches deposited using the 30% overlap condition and dilutions of 1.0 and 1.5), a number of blocks were deposited using Z-increments that were 100%, 90%, 80% and 70% of the measured layer thickness (Table 4-6).

Blocks measuring 30mm x 15mm x 10 layers thick were deposited using the cross hatch toolpath (Figure 4-6), in which alternating layers (A + B) are rotated 90° to each other. This toolpath was designed so that the end point of the first layer is directly below the start point of the second layer, and the endpoint of the second layer is directly above the start point of the first layer.

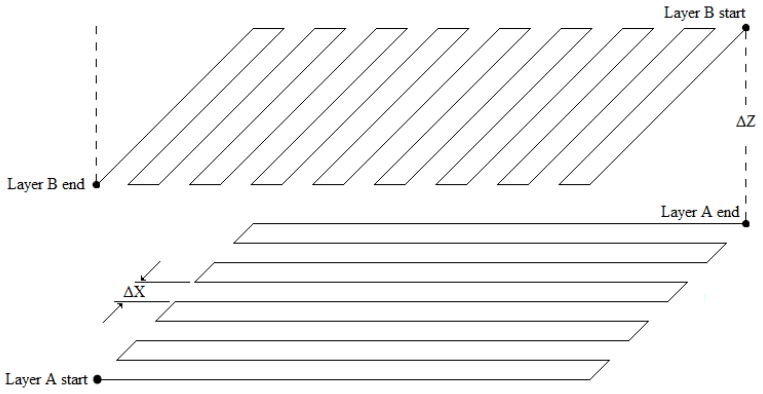

Figure 4-6 - Schematic illustration of cross hatch toolpath, where layers are at 90° to each other.

Table 4-6 - deposit plan for the production of laser deposited blocks to investigate the effect of Z increment on deposit shape and quality

Sample ID	Laser power (W)	Scanning speed (mm/s)	Laser spot Ø (mm)	Dilution	Powder feed rate (g/min)	Track spacing (mm)	Z increment (%)	Z increment (mm)	Layers
PM-EngD-049	400	5	1	1	1.7	1.06	100	0.278	20
PM-EngD-050	400	5	1	1	1.7	1.06	90	0.250	20
PM-EngD-051	400	5	1	1	1.7	1.06	80	0.222	20
PM-EngD-052	400	5	1	1	1.7	1.06	70	0.195	20
PM-EngD-053	400	5	1	1	1.7	1.06	85	0.234	60
PM-EngD-054	400	5	1	1.5	2.5	1.06	85	0.326	60

Deposited blocks were cross sectioned and metallographically prepared according to method E in section 3.3.1, and the distance from the substrate to the middle of the deposit surface measured by optical microscopy. The measured block height was compared against the theoretical block height (number of layers times the Z-increment), and a measurement of

height agreement (%) was obtained. For example, a block that is measured to be exactly the predicted height will have an agreement of 100%.

From this data, a graph of agreement (%) vs Z increment (%) was plotted, which allowed the optimum Z increment to be calculated at which the agreement is 100%.

Validation blocks at the calculated optimum Z-increment were also deposited for two dilution conditions, measuring 30 layers thick. These blocks were similarly sectioned and measured, and the results recorded.

4.2.2.4 Application of process rules to DOE test matrix

During section 4.2.3.1, each distinct DOE run was deposited as a single track at various powder feed rates, in order to investigate the relationship between the powder feed rate and the deposit dilution. Using this information, a powder feed rate was calculated for each DOE run that would produce the dilution specified by the DOE.

During section 4.2.3.2, the track overlap condition was defined, which suggested that an overlap equal to 30% of the measured single track width would provide the best results. Using the measured track widths from section 4.2.3.1, the overlap condition for each DOE run was then calculated.

In order to define the last process variable (ΔZ) required for the deposition of the DOE test blocks, 25 distinct DOE runs were deposited as a single overlapping layer, 10 tracks wide, using the calculated parameters for track spacing and powder feed rate (Table 4-7) These samples were then sectioned and the layer thickness measured using optical microscopy in order to define the ΔZ values required for the DOE block deposition.

Table 4-7 - Table showing distinct processing parameters for calculating DOE block Z increment from single layer thickness. Overlapping tracks deposited using a 30% track width overlap. Run 3 is DOE centre point, duplicated over runs 10, 14, 21, 25 and 29

Run	Laser power (W)	Laser spot diameter (mm)	Scanning velocity (mm/s)	Dilution (Ac/Am)	Powder mass flow rate (g/min)	ΔX (mm)
1	600	1.75	15	1.5	5.51	1.15
2	400	1.38	11.88	1.75	2.52	0.90
3*	600	1.75	8.75	1.5	3.05	1.26
4	400	1.38	5.63	1.25	1.75	1.09
5	600	1	8.75	1.5	7.33	1.33
6	600	2.5	8.75	1.5	2.22	1.26
7	800	2.13	5.63	1.25	2.59	1.59
8	800	2.13	11.88	1.75	3.27	1.59
9	800	1.38	5.63	1.25	2.22	1.60
11	400	2.13	11.88	1.75	2.55	0.87
12	400	2.13	5.63	1.75	2.79	0.87
13	400	2.13	5.63	1.25	1.47	1.04
15	1000	1.75	8.75	1.5	5.29	1.63
16	400	1.38	5.63	1.75	1.72	1.09
17	400	2.13	11.88	1.25	2.28	0.90
18	800	2.13	11.88	1.25	4.57	1.29
19	800	1.38	5.63	1.75	2.86	1.60
20	800	2.13	5.63	1.75	3.27	1.59
22	200	1.75	8.75	1.5	1.13	0.52
23	600	1.75	8.75	1	2.12	1.26
24	600	1.75	8.75	2	3.83	1.26
26	800	1.38	11.88	1.75	4.41	1.40
27	800	1.38	11.88	1.25	3.96	1.40
28	600	1.75	2.5	1.5	1.12	1.56
30	400	1.38	11.88	1.25	2.3	0.99

4.2.3 Block deposition

The majority of the preceding work has focused on developing the process rules that would be applied to the DOE factors in order to produce blocks of equivalent shape, size, and surface finish. This was an important process to go through, as it will ensure that there is the minimum amount of variability between DOE runs that may otherwise influence the cracking response, and mask any underlying trends.

As part of the DOE investigation, 30 test blocks were deposited and analysed, and the DOE software used to interpret the results in a way that highlights any underlying trends and relationships. Based on the interpretation of the results, a block was then deposited using the "optimised" parameters. It should be noted that in this case the term optimised simply means that it is using the best parameters from the limited range of the DOE parameters listed in Table 4-2, based on the interpretation of the DOE analysis.

4.2.3.1 Deposition of DOE test matrix

Substrates measuring 50mm x 30mm were cut from the 5mm thick CM247LC plates, using a metallographic sectioning saw. These were then securely clamped to the jig within the deposition chamber described in section 3.1.4, with the long and short edges of the substrate align to the X and Y axis of the robot respectively.

Substrates were thoroughly cleaned with scotchbrite®, acetone and paper towels to remove any surface contamination, and the deposition chamber sealed with polyethene membrane and purged with argon, reducing the oxygen content to <100ppm O_2.

Using the parameters developed in section 4.2.3, the DOE test matrix (Table 4-8) was deposited in full. Blocks measuring 30x15x10mm were deposited centrally onto the CM247LC substrate, using the cross-hatch toolpath. Deposited blocks were allowed to cool naturally to ambient temperature under argon shielding, before being removed for metallographic examination and crack quantification, as described in section 3.3.3.

Table 4-8 - Full processing parameters used for deposition of DOE test matrix

Run	Laser power (W)	Laser spot diameter (mm)	Scanning velocity (mm/s)	Dilution (Ac/Am)	Powder mass flow rate (g/min)	ΔZ (mm)	ΔX (mm)
1	600	1.75	15	1.5	5.51	0.39	1.15
2	400	1.38	11.88	1.75	2.52	0.26	0.90
3	600	1.75	8.75	1.5	3.05	0.40	1.26
4	400	1.38	5.63	1.25	1.75	0.33	1.09
5	600	1	8.75	1.5	7.33	0.52	1.33
6	600	2.5	8.75	1.5	2.22	0.45	1.26
7	800	2.13	5.63	1.25	2.59	0.46	1.59
8	800	2.13	11.88	1.75	3.27	0.65	1.59
9	800	1.38	5.63	1.25	2.22	0.38	1.60
10	600	1.75	8.75	1.5	2.97	0.40	1.26
11	400	2.13	11.88	1.75	2.55	0.30	0.87
12	400	2.13	5.63	1.75	2.79	0.30	0.87
13	400	2.13	5.63	1.25	1.47	0.28	1.04
14	600	1.75	8.75	1.5	2.98	0.40	1.26
15	1000	1.75	8.75	1.5	5.29	0.52	1.63
16	400	1.38	5.63	1.75	1.72	0.31	1.09
17	400	2.13	11.88	1.25	2.28	0.23	0.90
18	800	2.13	11.88	1.25	4.57	0.41	1.29
19	800	1.38	5.63	1.75	2.86	0.49	1.60
20	800	2.13	5.63	1.75	3.27	0.65	1.59
21	600	1.75	8.75	1.5	2.98	0.55	1.26
22	200	1.75	8.75	1.5	1.13	0.14	0.52
23	600	1.75	8.75	1	2.12	0.28	1.26
24	600	1.75	8.75	2	3.83	0.52	1.26
25	600	1.75	8.75	1.5	2.97	0.40	1.26
26	800	1.38	11.88	1.75	4.41	0.40	1.40
27	800	1.38	11.88	1.25	3.96	0.33	1.40
28	600	1.75	2.5	1.5	1.12	0.48	1.56
29	600	1.75	8.75	1.5	2.97	0.48	1.26
30	400	1.38	11.88	1.25	2.3	0.25	0.99

4.2.3.2 Deposition of test block using DOE optimised parameters

Using the crack measurement results for the DOE test matrix, a 3D response surface graph was generated that related the crack density response to the process variables. This response surface was used to generate an "optimised" set of parameters, by which the crack density should be the lowest.

However before a block can be deposited, trials must first be conducted to establish the powder feed rate required to produce the desired dilution specified by the DOE software. Track spacing and z-increment also still needed to be determined experimentally using the methods established in sections 4.2.3.

Due to the high laser power and slow scanning speeds used, there was a greater chance of causing damage to the delicate fast flow coaxial nozzle, due to reflected laser light or radiated heat. For this reason, the fast flow coaxial nozzle was exchanged for the 3-beam coaxial nozzle described in section 3.1.3, as it is more rugged in design, and more suitable for the conditions. The change of powder delivery nozzle was accompanied by re-validation trials, to correct for the reduced deposition efficiency in order to ensure the same deposit shape and dilution was obtained.

The parameters used for the deposition of the DOE optimised block are listed in Table 4-9.

Table 4-9 - DOE "optimal" parameters

Process parameter	Value	Units
Laser Power	1000	W
Scanning speed	5	mm/s
Laser spot diameter	3	mm
Deposit dilution	2	
Powder dosing speed	35	rpm
Powder feed rate	6.5	g/min
Track spacing	1.8	mm
Z increment	0.8	mm

4.3 Results

4.3.1 Powder and substrate characterisation

4.3.1.1 Powder analysis

Chemical analysis of the supplied powder and substrate material (Table 4-10), showed that the elemental composition is consistent with the nominal composition found in the literature [21-23], although the tungsten content of the supplied powder was measured to be 0.9wt% lower than nominal.

Table 4-10 - Chemical composition of supplied powder and substrate materials, including nominal composition for CM247LC alloy

	Composition (Wt %)											
Alloy	**Ni**	**Cr**	**Co**	**Mo**	**W**	**Ta**	**Al**	**Ti**	**C**	**B**	**Zr**	**Hf**
CM247LC (nominal)	Bal	8	9	0.5	10	3.2	5.6	0.7	0.07	0.015	0.01	1.4
CM247LC (supplied)	Bal	8.1	9	0.43	9.1	3.2	5.4	0.88	0.077	0.012	0.01	1.3
CM247LC (substrate)	Bal	8.17	9.14	0.51	9.71	2.97	5.32	0.83	0.08	0.015	0.05	1.37

Particle size distribution measurements were conducted by London & Scandinavian metallurgical Co, using a mastersizer® 2000 particle size analyser, the results of which are shown in Table 4-11 and Figure 4-7.

Particle analysis data for the three size ranges measured, showed that the as-received powder possessed the largest specific surface area (0.16 m^3/g) and the lowest uniformity (0.583). Powder sieved to the 20-40µm range had the best uniformity (0.204) and a specific surface area that is nearly as high as for the as received powder. The 40-100µm powder exhibited the lowest specific surface area (0.0692 m^3/g) and uniformity close to that of the 20-40µm powder (0.215).

Table 4-11 - Particle analysis data for the three powder size ranges measured

Powder size range	Mean particle size (by vol)	Specific surface area (m^2/g)	Uniformity
0-150	69.72	0.16	0.583
20-40	41.08	0.155	0.204
40-100	92.97	0.0692	0.215

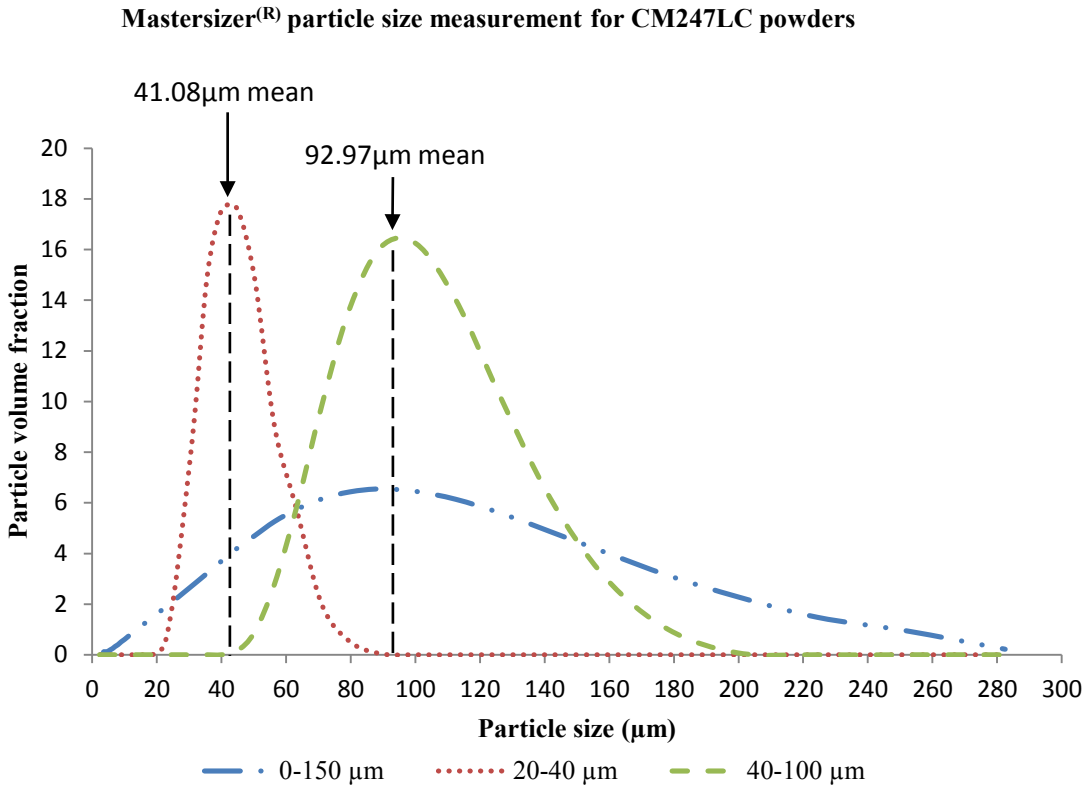

Figure 4-7 - Mastersizer® particle size distribution measurements for CM247LC powder in the size ranges 0-150µm (as received), 20-40µm and 40-100µm (Test certificates may be found in Appendix A)

Topographical analysis of the 0-150µm powder using Secondary Electron Imaging (SEI) SEM showed that the powder was predominantly spherical, with a moderate number of conjoined and elongated particles (Figure 4-8).

Satellite particles were found to be adherent to the larger particles, with the smaller particles appearing more uniform in shape and with fewer satellites due to the faster cooling rates (Figure 4-9). Also observable using backscattered SEM were a number of sub-micron scale precipitates on the powder surface, located at, or near to, the surface connected cellular boundaries (Figure 4-10).

Cross sections of the 20-40µm (Figure 4-11) and 40-100µm (Figure 4-12) powder particles were prepared using method A outlined in section 3.3.1, and subjected to QBSD SEM analysis. Comparison of the two sizes showed that both batches contained particles that were near fully dense, with a large number of conjoined and elongated particles, particularly in the 40-100µm size range.

Differential scanning calorimetry (DSC) of supplied powder showed that the material has a solidus temperature of 1331°C and a liquidus temperature of 1373.5°C during heating at 10°C/min, with γ' precipitation starting upon cooling at 1269°C (Figure 4-14).

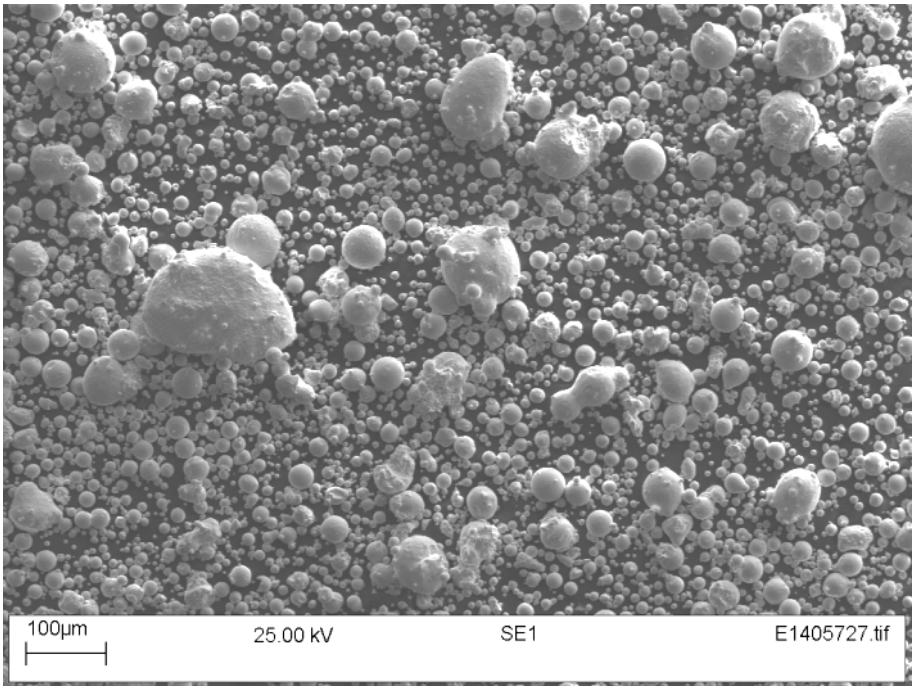

Figure 4-8 - SEI SEM image of as-received CM247LC powder in the size range 0-150µm

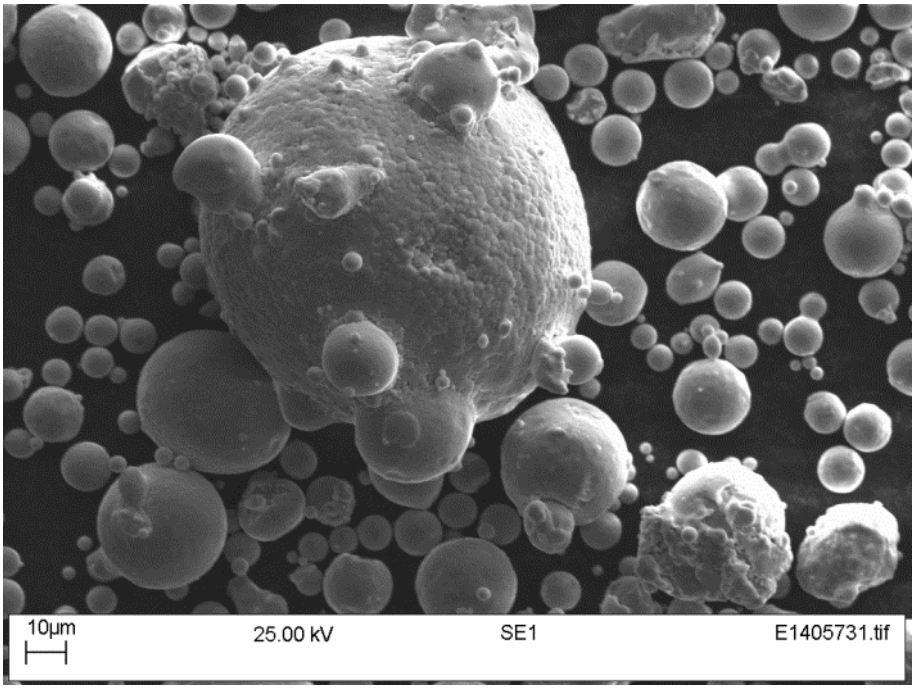

Figure 4-9 - SEI SEM micrograph of as-received CM247LC powder particles

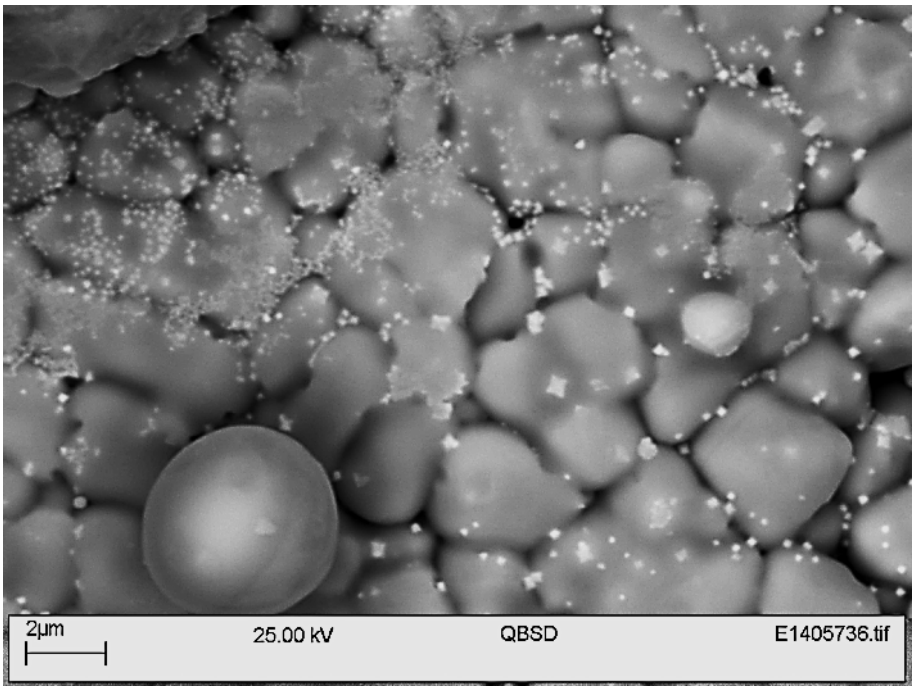

Figure 4-10 - QBSD SEM micrograph showing cellular particle topography and presence of sub-micron precipitates on the powder surface.

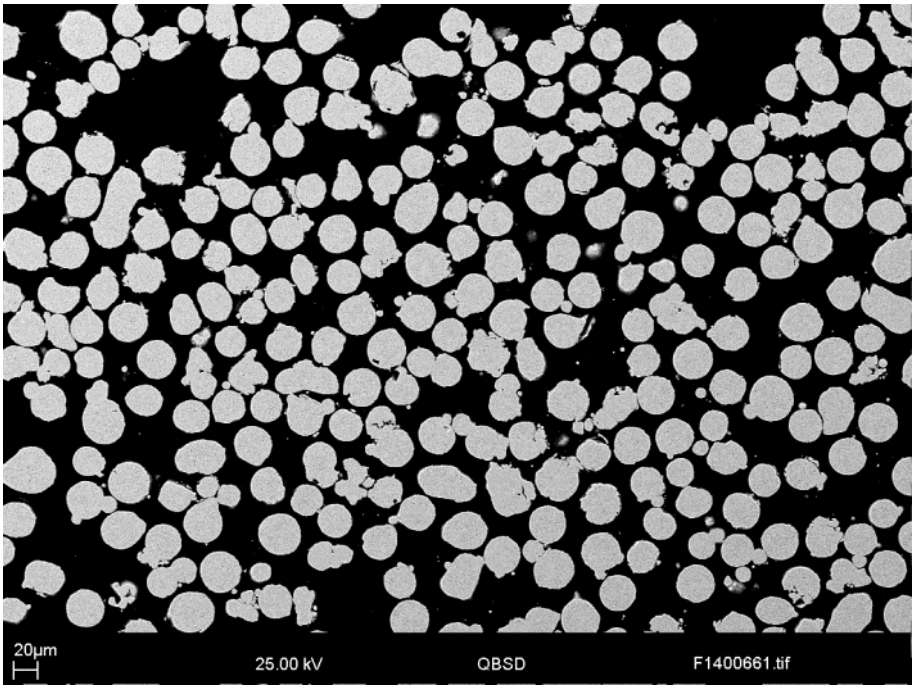

Figure 4-11 - QBSD SEM micrographs of 20-40µm CM247LC powder

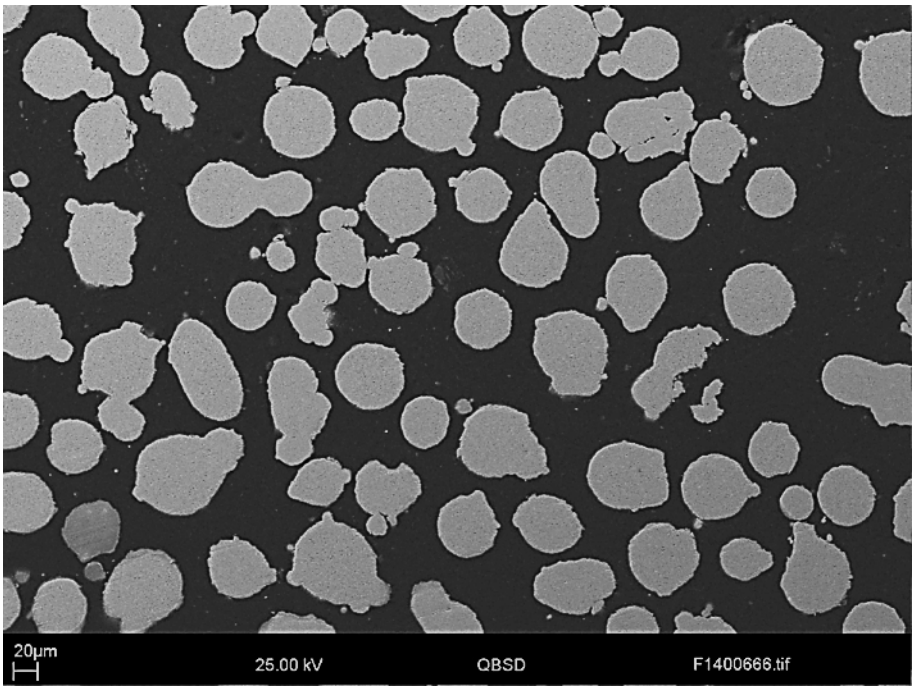

Figure 4-12 - QBSD SEM micrographs of 40-100µm CM247LC powder

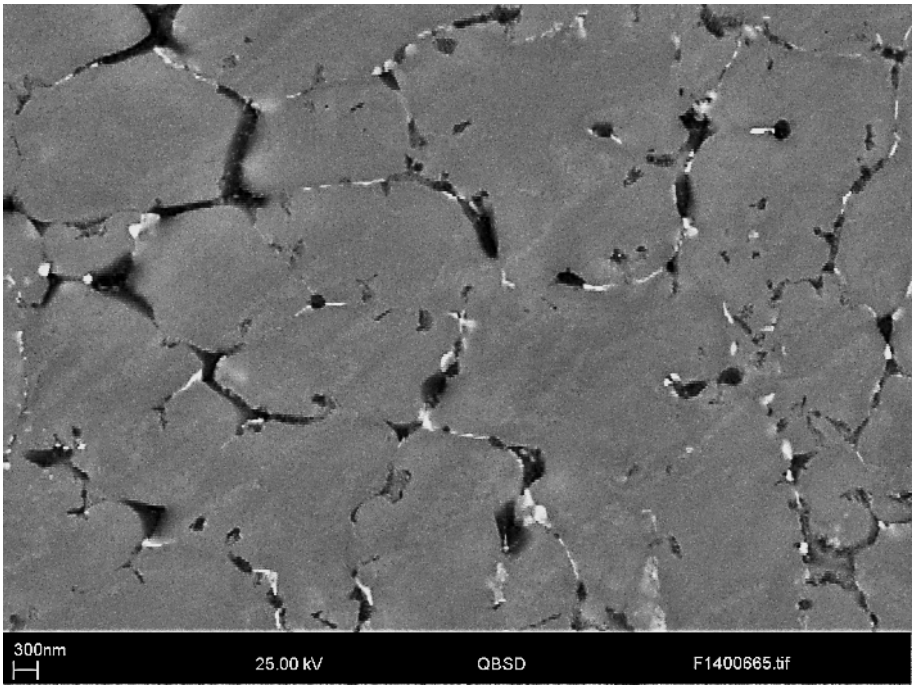

Figure 4-13 - QBSD SEM micrograph of CM247LC cross sectioned powder particle, showing fine cellular grain structure and evidence of carbide formation at the cell boundaries

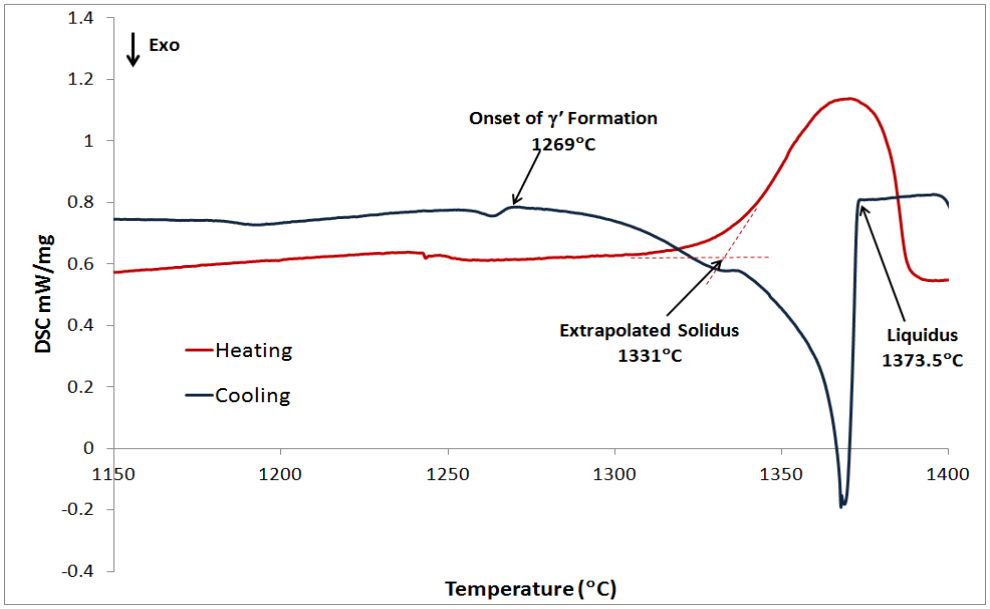

Figure 4-14 - DSC results for the heating (red) and cooling (blue) of CM247LC powder, annotated with solidus, liquidus and onset of γ' formation (Heating/Cooling = 10°C/min).

4.3.1.2 Substrate analysis

Microstructural analysis of a section of HIP'd CM247LC substrate, prepared using method D in section 3.3.1.1, revealed a microstructure consisting of blocky γ' (Figure 4-15, Figure 4-16) measuring between 0.5-3μm in width, within a γ matrix containing fine scale unidentified carbides.

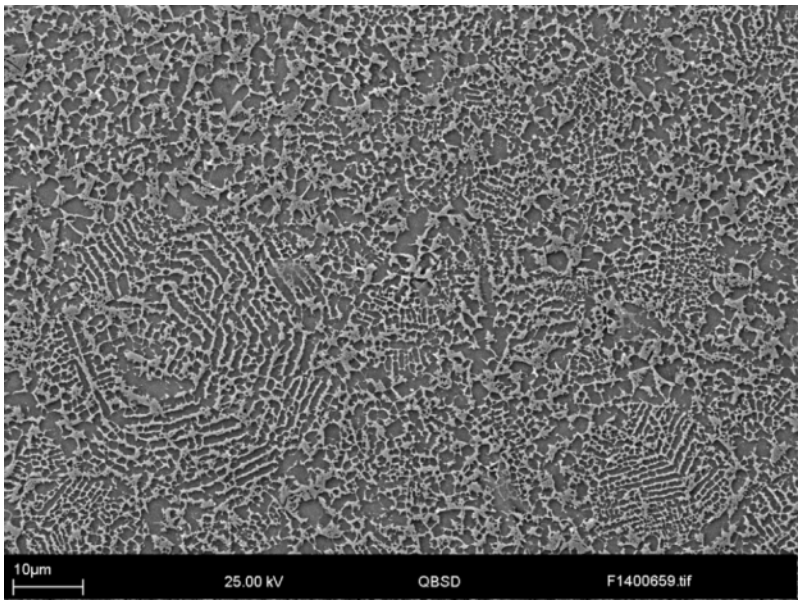

Figure 4-15 - QBSD SEM micrograph of CM247LC HIP consolidated substrate. Dark phases are γ'.

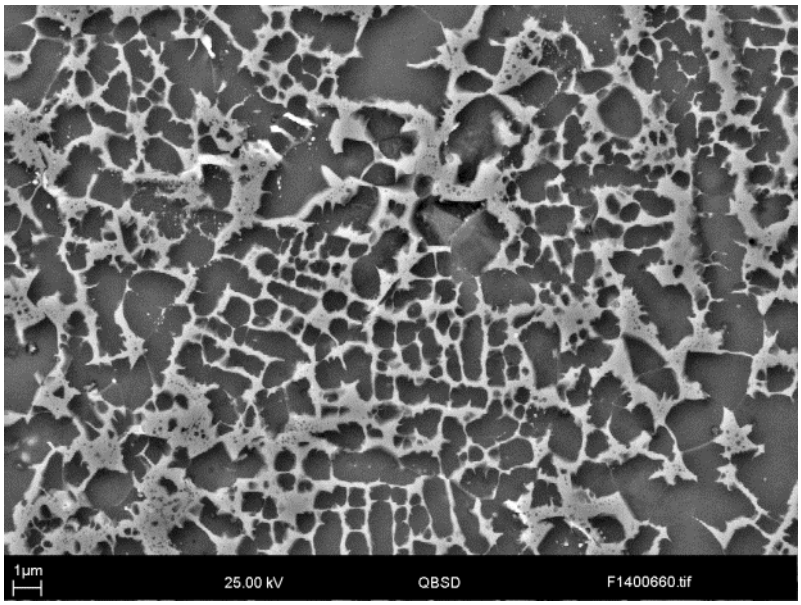

Figure 4-16 - QBSD SEM micrograph of CM247LC HIP consolidated substrate - dark phases are γ',

4.3.2 Process parameter development trials

4.3.2.1 Quantifying deposit shape as a function of powder mass flow rate

Using the parameters listed in Table 4-12, single tracks measuring 30mm in length were deposited at two different powder feed rates (1.2 and 2.1 g/min) using the 40-100µm CM247LC powder. Deposited tracks were metallographically cross sectioned, polished and etched using Method E described in section 3.3.1 to reveal the fusion boundary with the substrate.

Optical micrographs were taken for each track (Figure 4-17 - Figure 4-19) and image analysis software used to measure the clad area (A_c), melted area (A_m) and track width for each (Table 4-13).

Table 4-12 - Deposition parameters for deposit dilution experiment.

Sample ID	DOE run	Laser power (W)	Laser spot diameter (mm)	Scanning speed (mm/s)	Required dilution Ac/Am
PM-EngD-019/020	1	600	1.75	15	1.5
PM-EngD-003/004	2	400	1.38	11.88	1.75
PM-EngD-021/022	3	600	1.75	8.75	1.5
PM-EngD-005/006	4	400	1.38	5.63	1.25
PM-EngD-001/002	5	600	1	8.75	1.5
PM-EngD-039/040	6	600	2.5	5.63	1.5
PM-EngD-029/030	7	800	2.13	5.63	1.25
PM-EngD-007/008	9	800	1.38	5.63	1.25
PM-EngD-031/032	11	400	2.13	11.88	1.75
PM-EngD-033/034	13	400	2.13	5.63	1.25
PM-EngD-023/024	15	1000	1.75	8.75	1.5
PM-EngD-037/038	18	800	2.13	11.88	1.25
PM-EngD-025/026	22	200	1.75	8.75	1.5
PM-EngD-013/014	26	800	1.38	11.88	1.75
PM-EngD-015/016	28	600	1.75	2.5	1.5

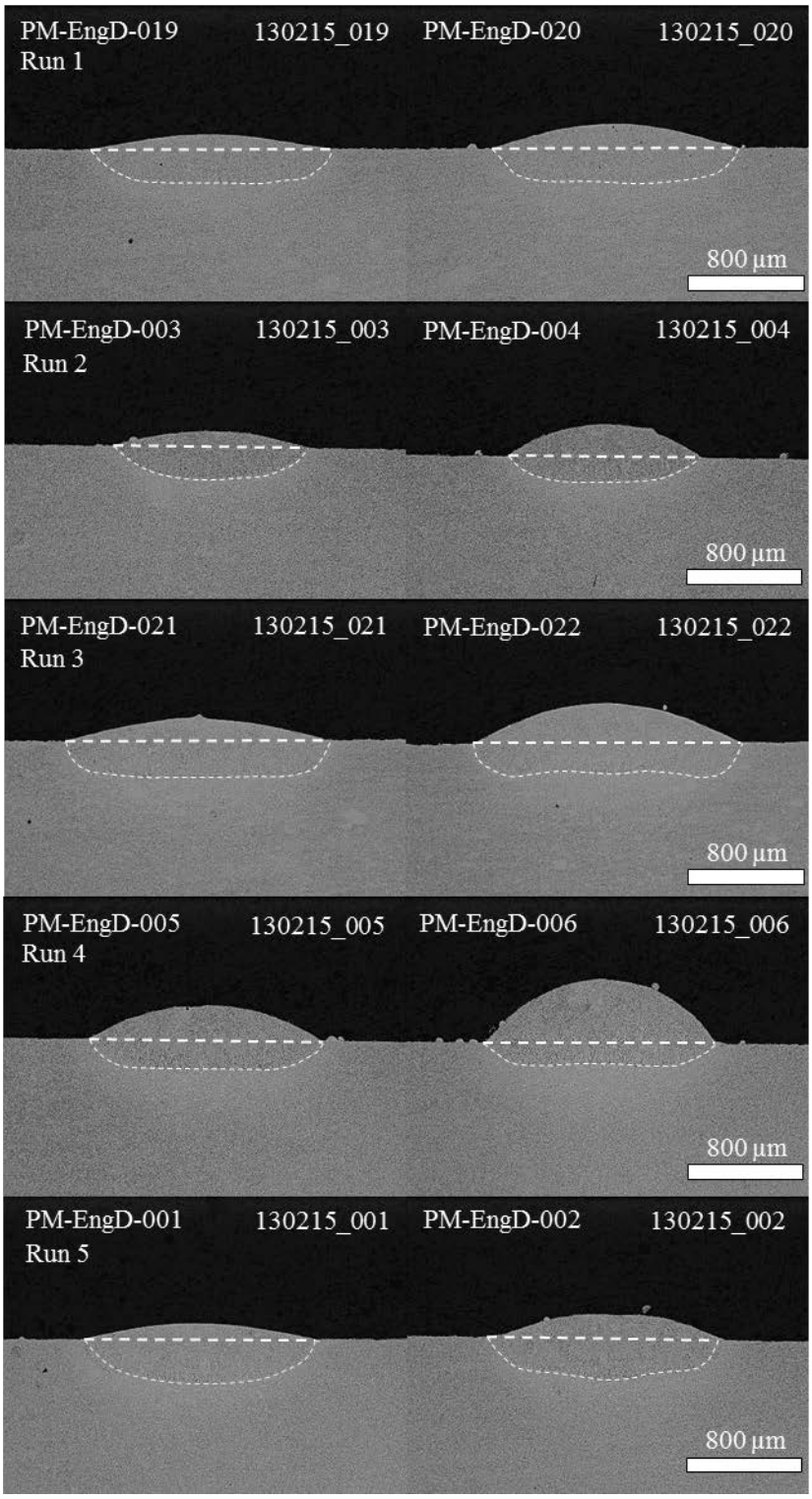

Figure 4-17 - Single track dilution measurements for distinct DOE runs 1-5

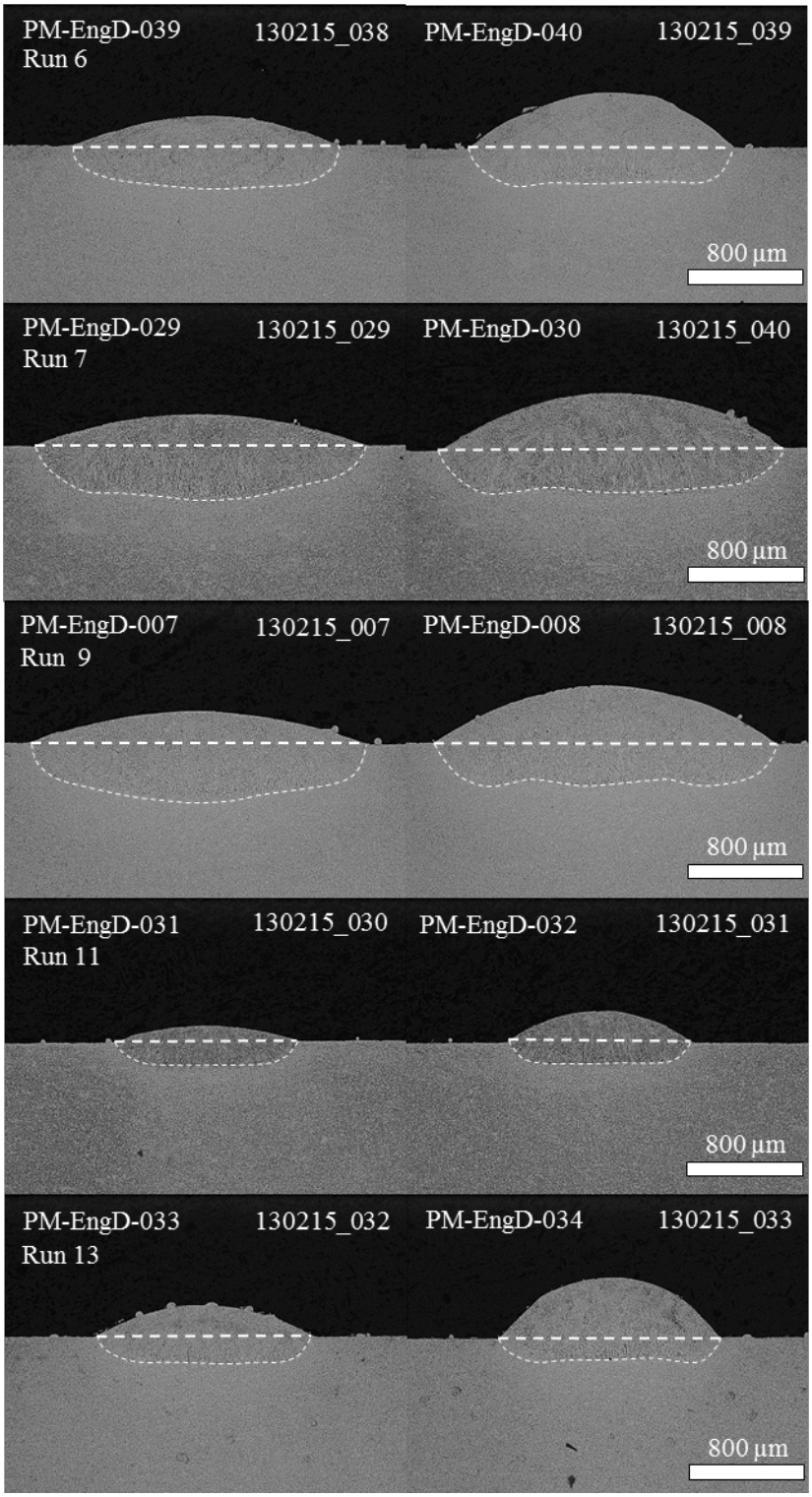

Figure 4-18 - Single track dilution measurements for distinct DOE runs 6, 7, 9, 11 and 13

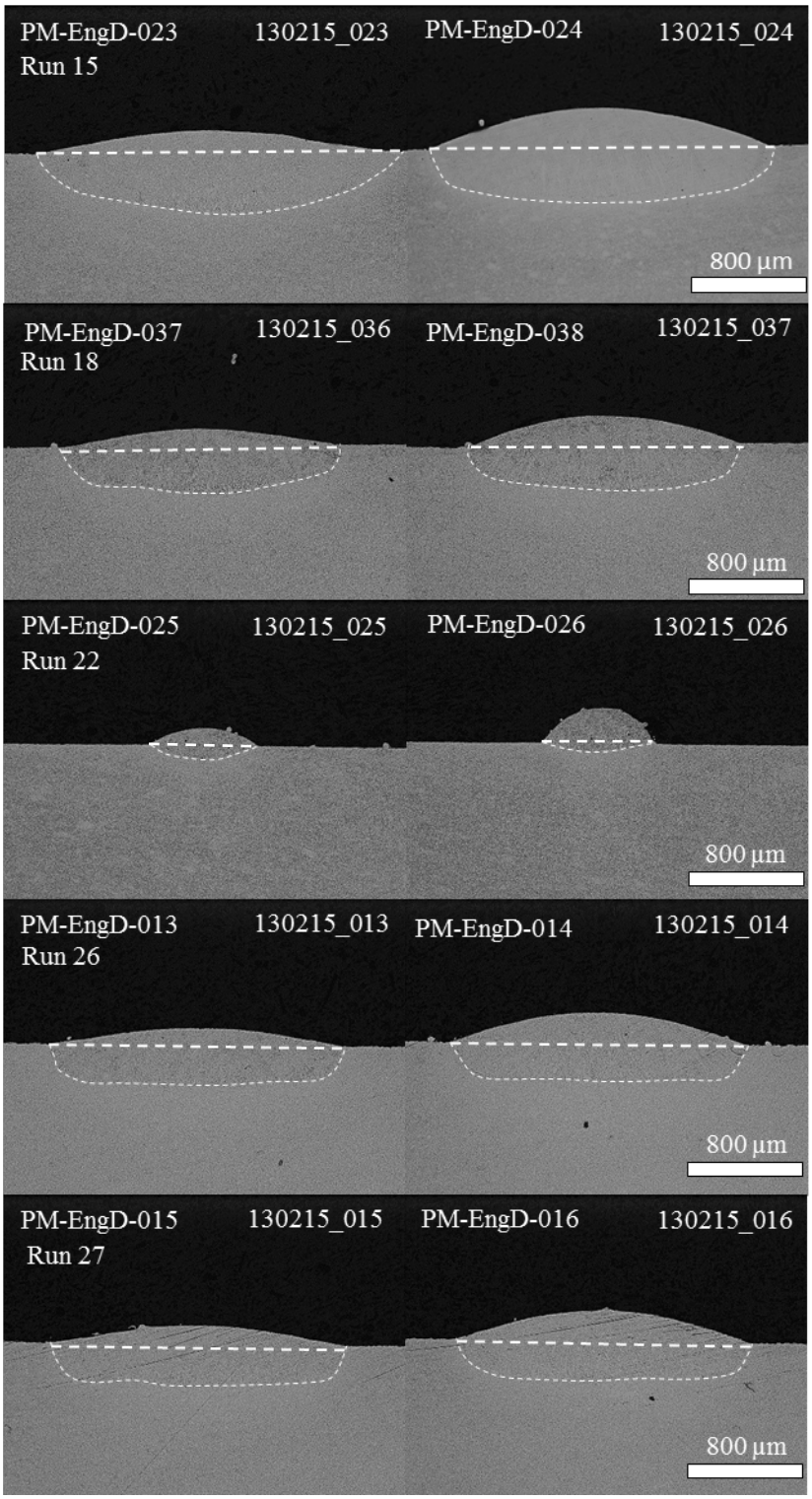

Figure 4-19 - Single track dilution measurements for distinct DOE runs 15, 18, 22, 26 and 27

Table 4-13 - Results from single track dilution experiment

Run #	Sample #	Image #	Power	Laser spot diameter	Speed	Required dilution	Powder feed rate	Ac	Am	Measured dilution A_c/A_m	Track width	Calculated powder feed rate (g/min)
			(W)	(mm)	(mm/s)		(g/min)	(µm^2)	(µm^2)		(mm)	
1	PM-EngD-019	130215-019	600	1.75	15	1.5	1.19	119755	360910	0.332	1.71	5.51
	PM-EngD020	130215-020					2.08	197519	341895	0.578	1.74	
2	PM-EngD-003	130215-003	400	1.375	11.875	1.75	1.19	101775	224804	0.453	1.362	2.52
	PM-EngD-004	130215-004					2.08	214756	185324	1.159	1.357	
3	PM-EngD-021	130215-021	600	1.75	8.75	1.5	1.19	192306	446067	0.431	1.879	3.05
	PM-EngD-022	130215-022					2.08	349610	392379	0.891	1.887	
4	PM-EngD-005	130215-032	400	1.375	5.625	1.25	1.19	273556	283450	0.965	1.543	1.75
	PM-EngD-006	130215-033					2.08	299252	222404	1.346	1.579	
5	PM-EngD-001	130215-001	600	1	8.75	1.5	1.19	125304	382016	0.328	1.607	7.33
	PM-EngD-002	130215-002					2.08	204448	394235	0.519	1.615	
6	PM-EngD-039	130215-038	600	2.5	8.75	1.5	1.19	265272	473222	0.561	1.887	2.22
	PM-EngD-040	130215-039					2.08	517098	414032	1.249	1.879	
7	PM-EngD-029	130215-029	800	2.125	5.625	1.25	1.19	356564	692159	0.515	2.351	2.59
	PM-EngD-030	130215-040					2.08	658724	678351	0.971	2.431	
9	PM-EngD-007	130215-011	800	1.375	5.625	1.25	1.19	356607	772727	0.461	2.409	2.22
	PM-EngD-008	130215-012					2.08	664522	641879	1.035	2.392	
11	PM-EngD-031	130215-031	400	2.125	11.875	1.75	1.19	100329	192281	0.522	1.318	2.55
	PM-EngD-032	130215-032					2.08	200727	165595	1.212	1.310	
13	PM-EngD-033	130215-033	400	2.125	5.625	1.25	1.19	238236	277560	0.858	1.651	1.47
	PM-EngD-034	130215-034					2.08	468703	222760	2.104	1.626	
15	PM-EngD-023	130215-023	1000	1.75	8.75	1.5	1.19	244637	864527	0.283	2.469	5.29
	PM-EngD-024	130215-024					2.08	457006	776108	0.589	2.431	
18	PM-EngD-037	130215-036	800	2.125	11.875	1.25	1.19	144574	546004	0.265	1.939	4.57
	PM-EngD-038	130215-037					2.08	265935	520286	0.511	1.917	
22	PM-EngD-025	130215-025	200	1.75	8.75	1.5	1.19	60282	44366	1.359	0.75	1.13
	PM-EngD-026	130215-026					2.08	121983	35642	3.423	0.802	
26	PM-EngD-013	130215-013	800	1.38	11.875	1.75	1.19	162363	631565	0.257	2.096	4.41
	PM-EngD-014	130215-014					2.08	302125	507073	0.596	2.129	
27	PM-EngD-015	130215-015	800	1.375	11.875	1.25	1.19	168662	544653	0.31	2.077	3.96
	PM-EngD-016	130215-016					2.08	289961	496519	0.584	2.082	
28	PM-EngD-027	130215-027	600	1.75	2.5	1.5	1.19	760235	559339	1.359	2.29	1.12
	PM-EngD-028	130215-028					2.08	1E+06	540542	2.581	2.384	
30	PM-EngD-017	130215-017	400	1.375	11.875	1.25	1.19	131888	338420	0.39	1.514	2.3
	PM-EngD-018	130215-018					2.08	213344	245991	0.867	1.489	

4.3.2.2 Establishing optimum track separation (ΔX)

Using the parameters listed in Table 4-14, 8 single-layer overlap patches were deposited, measuring 30mm in length and 10 tracks in width. For the deposition of these patches, a rectangular raster pattern was used with a scanning speed of 5mm/s and a laser spot diameter of 1mm.

Cross sections of the deposited patches were taken transverse to the deposition direction. These cross sections were then metallographically polished and etched to reveal the fusion boundary, using method D described in section 3.3.1.1. Overlapping optical micrographs were taken at 50x magnification, which were then stiched together using ImageJ® to form a composite image covering the entire patch width, as shown in Figure 4-20 and Figure 4-21.

Using ImageJ® software, calibrated against a known source, the height of the deposit was measured at ten points corresponding to the position of the individual tracks. The quantity and location of the cracks visible in each patch were also recorded (Table 4-14).

Graphs were plotted for each overlap condition, which show how the overlap percentage affects the overall flatness of the layer (Figure 4-22). By plotting the line of best fit through these points, it can be seen that a high degree of overlap has the effect of making the deposit thicker at one end than the other, as well as introducing a greater number of cracks.

Table 4-14 - Track overlap trials conducted using 400W laser power, 5mm/s scanning speed, 1mm laser spot diameter and powder feed rates of 1.7 and 2.5 g/min

Powder mass flow rate	Overlap %	Sample	Height measurement (µm)										Observed cracks
			1	2	3	4	5	6	7	8	9	10	
1.7 g/min	50	PM-EngD-041	260	301	336	360	358	383	377	413	389	407	9
	40	PM-EngD-042	273	361	343	372	360	354	366	378	355	395	6
	30	PM-EngD-043	299	332	310	321	325	315	298	315	321	322	6
	20	PM-EngD-044	313	304	311	304	328	296	304	296	330	300	3
2.5 g/min	50	PM-EngD-045	466	518	580	574	614	608	620	670	687	653	5
	40	PM-EngD-046	480	551	561	505	511	545	591	499	545	580	6
	30	PM-EngD-047	414	431	410	435	430	418	439	405	445	405	3
	20	PM-EngD-048	481	480	467	480	467	488	495	481	474	490	3

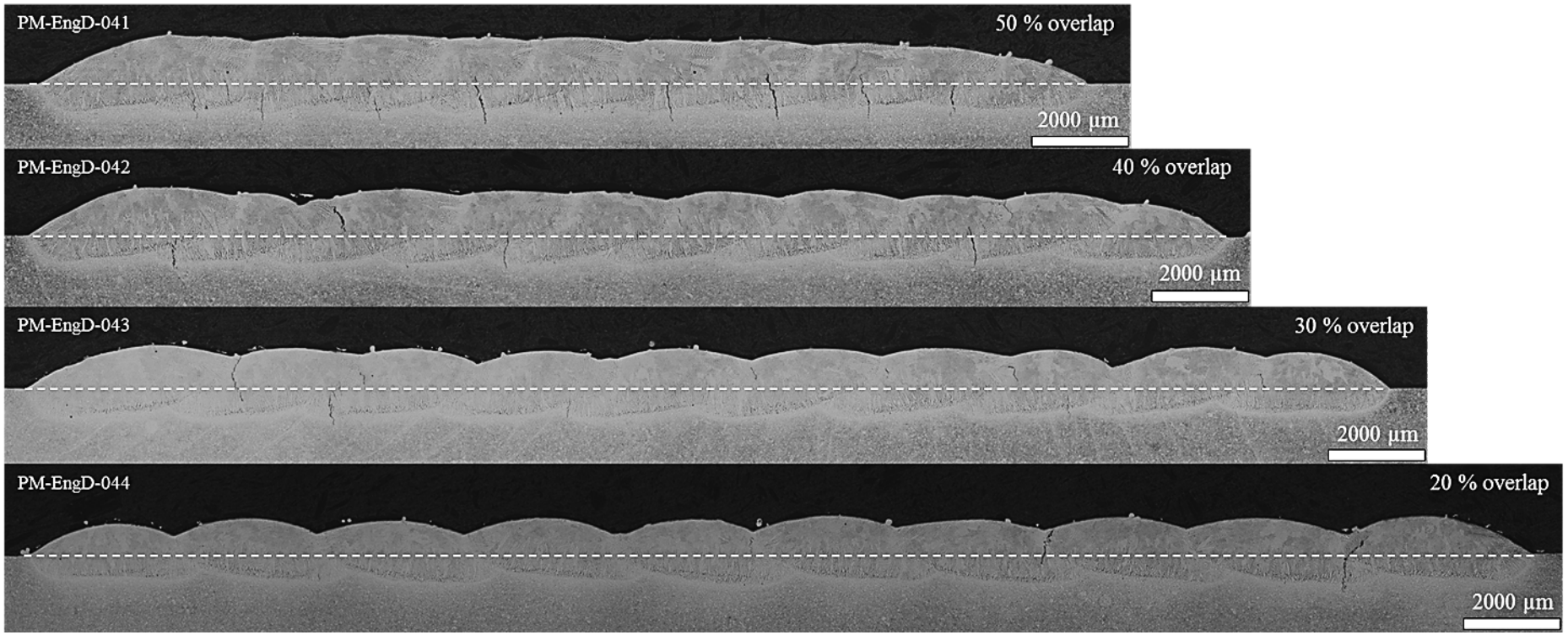

Figure 4-20 - Overlap trials conducted using 400W laser power, 5mm/s, 1mm laser spot diameter, 5 g/min

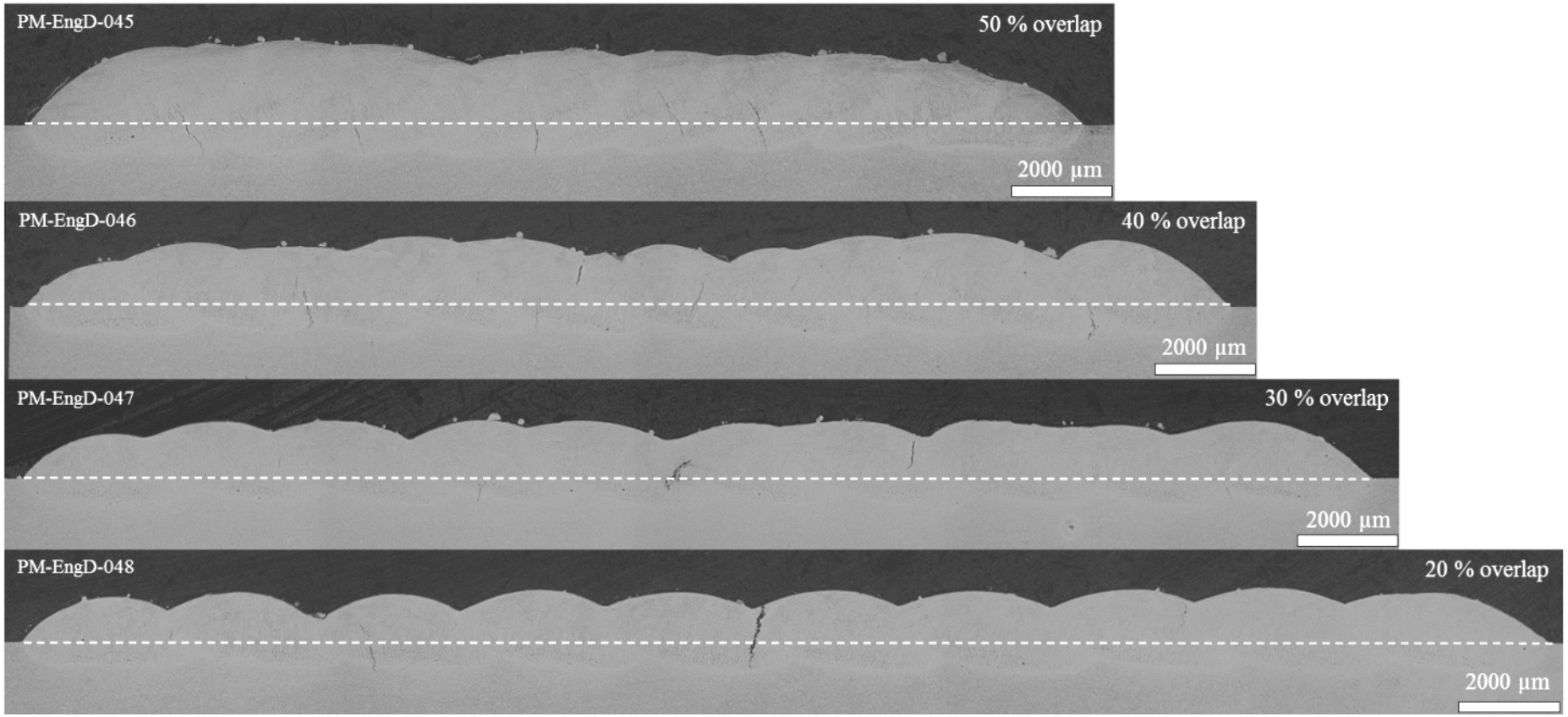

Figure 4-21 - Overlap trials conducted using 400W laser power, 5mm/s, 1mm laser spot diameter, 7 g/min

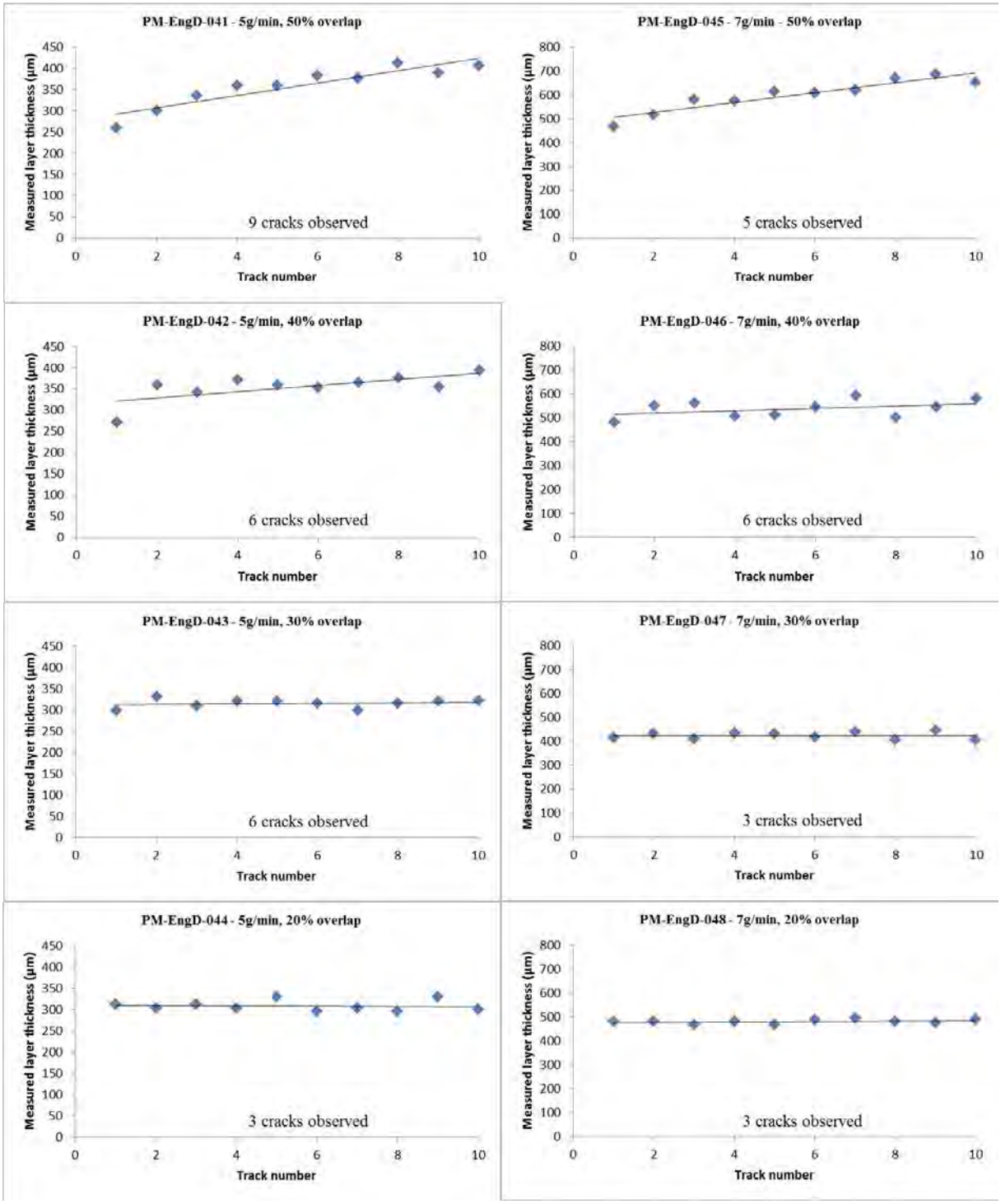

Figure 4-22 - Graphs illustrating the results presented in Table 4-13, showing how the degree of overlap affects deposit pile-up and surface flatness.

4.3.2.2.1 Hardness measurement results for overlap trials

Vickers micro-hardness measurements were performed on sample PM-EngD-041 (Figure 4-20), using a Struers Duramin-20, with 100g load. Measurements were taken beneath the fusion zone of an overlapping deposit trial that exhibited the highest number of cracks penetrating into the HAZ region of the substrate. 41 measurements were taken at approximately 0.2mm increments at the points highlighted in Figure 4-23.

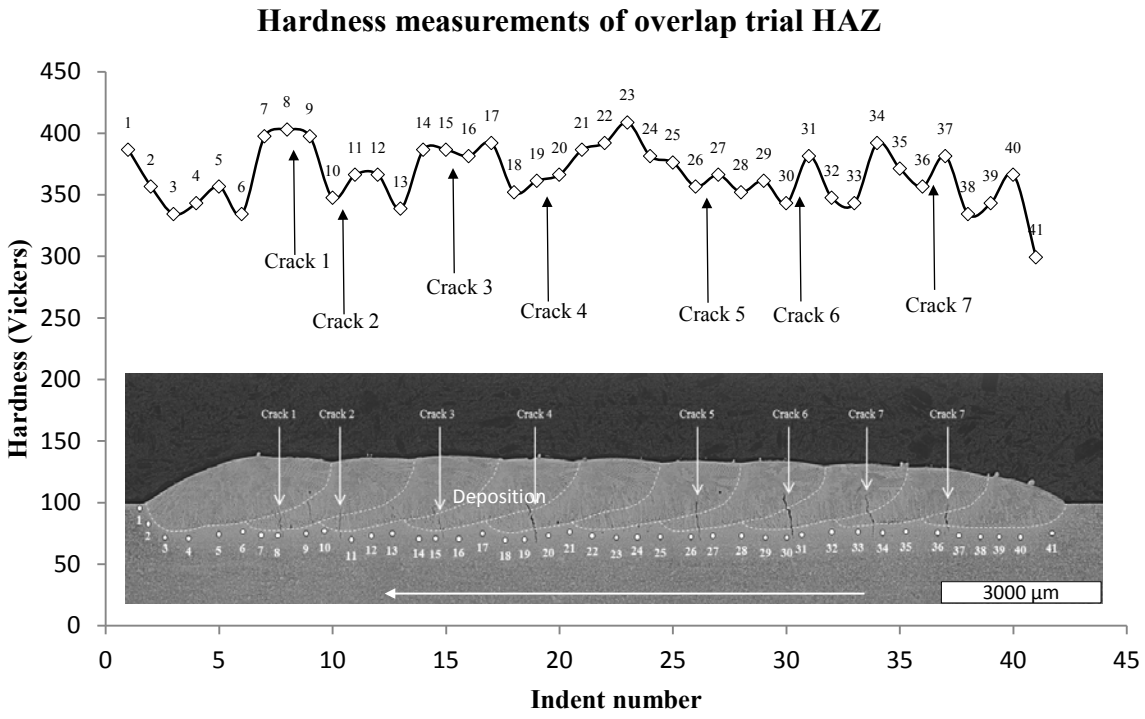

Figure 4-23 - Hardness measurements taken within the HAZ, along fusion boundary of sample PM-EngD-041

Results show that the hardness of the HAZ varies widely across the deposit width, with hardness measurements ranging from 299 Hv near the start of the deposit, to 408 Hv near the middle. Hardness measurement of the substrate, taken some distance away from the HAZ showed that HIP'd CM247LC has a base hardness of 420 Hv

4.3.2.2 Establishing optimum Z-increment condition (ΔZ)

A single layer of overlapping tracks were deposited, measuring 30mm in length and 10 tracks in width. The height of this layer was measured using the methods described in section 4.3.2.1, and 4 Z-increment ratios calculated, based on percentage of the measured layer thickness (Table 4-15).

From the results of the 4 deposited blocks (Figure 4-24), a Z-increment that is 85% of the measured single layer thickness was calculated to produce the best result (Figure 4-25), as it showed the least deviation from the calculated build height.

This 85% Z-increment condition was tested for two different dilution values (1.0 and 1.5) by depositing blocks to a thickness of 30 layers (Figure 4-26). These two blocks were then cross sectioned and measured using the established method. Both blocks were measured to be within 1% of the calculated build height (Table 4-15).

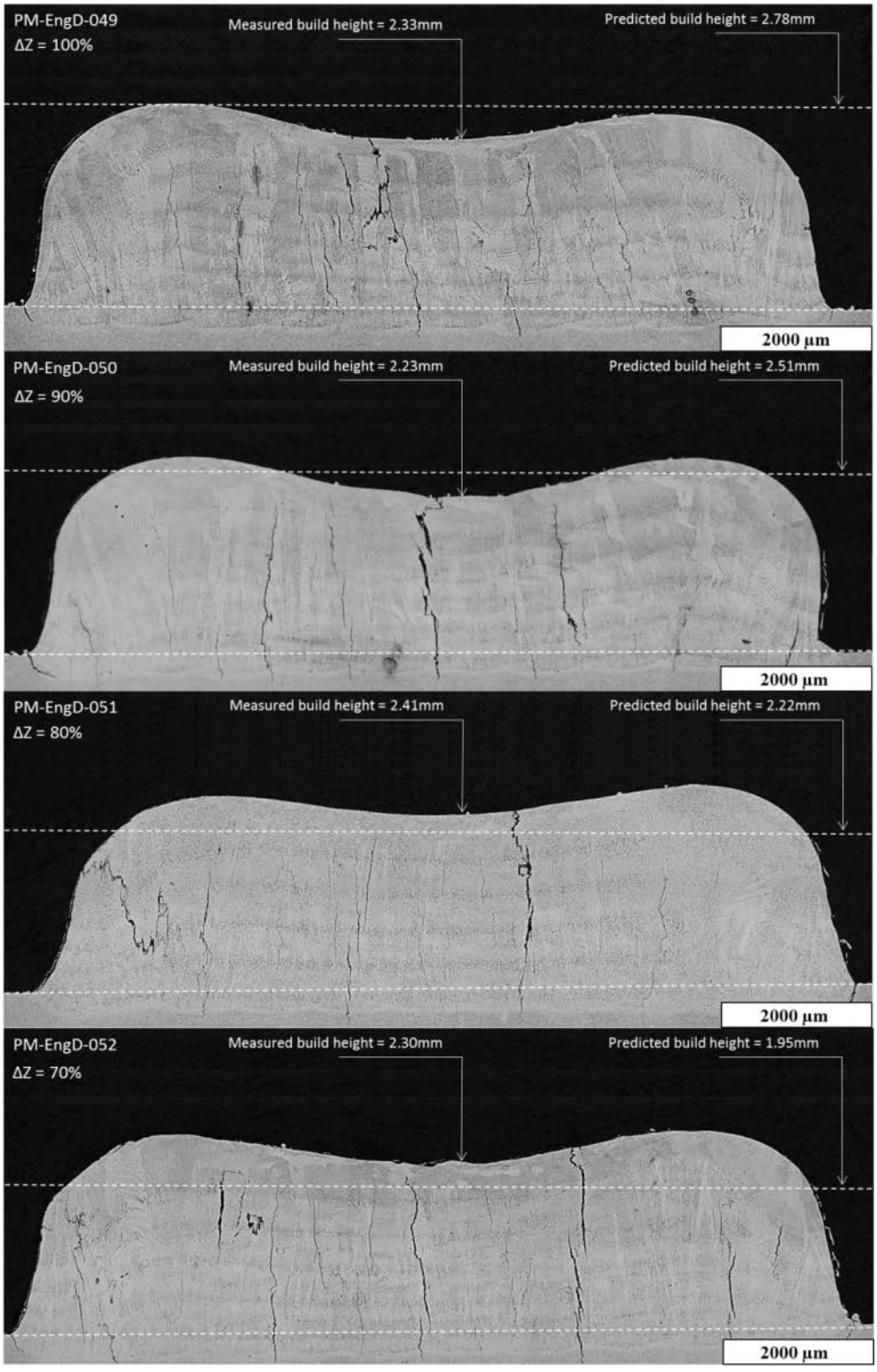

Figure 4-24 - Blocks deposited using different Z increments, where the Z increment is given by a percentage of the measured single layer thickness.

Table 4-15 - Table showing deposition parameters and measured build height for Z increment trial blocks.

Sample ID	Laser power	Scanning speed	Powder feed rate	Dilution	Laser spot diameter	Measured layer thickness	Overlap spacing		Z increment		Number of layers	Predicted height	Measured height	Disparity
	W	mm/s	g/min	Ac/Am	mm		(%)	ΔX (mm)	%	ΔZ (mm)		mm	mm	%
PM-EngD-49	400	5	1.7	1.0	1	0.278	30	1.059	100	0.278	10	2.780	2.334	83.96
PM-EngD-50									90	0.250		2.502	2.231	89.17
PM-EngD-51									80	0.222		2.224	2.413	108.50
PM-EngD-52									70	0.195		1.946	2.297	118.04
PM-EngD-53									85	0.234	30	7.013	6.980	99.54
PM-EngD-54			2.5	1.5		0.383		1.063	85	0.326	30	9.767	9.752	99.85

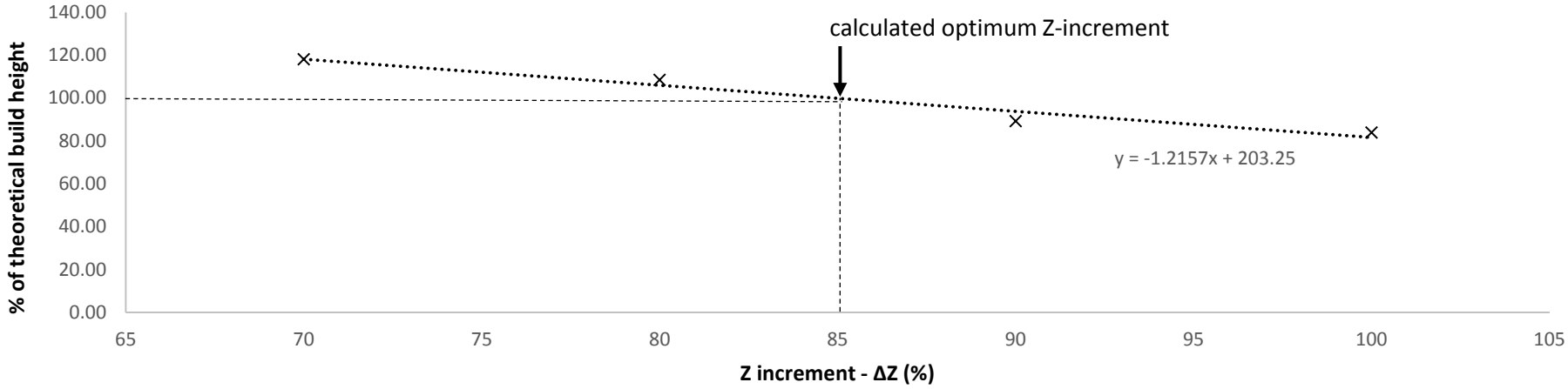

Figure 4-25 - Graph illustrating results listed in Table 4-15, showing that a Z increment of approximately 85% of the single layer thickness should allow a block to be deposited that maintains a consistent build rate.

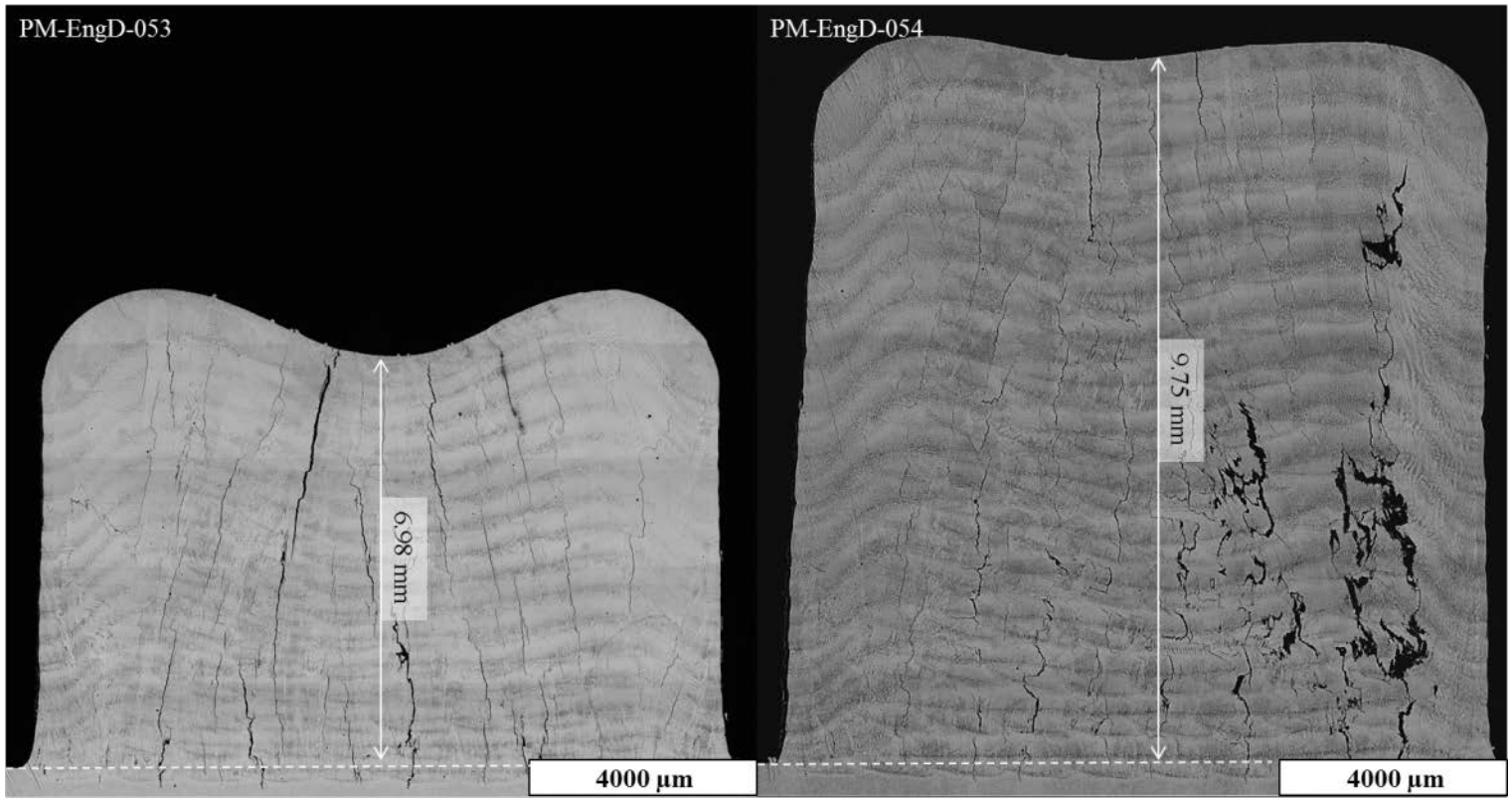

Figure 4-26 - Z increment trials using 85% ΔZ condition, 30 layers. PM-EngD-053 used a dilution of 1.0, PM-EngD-054 used a dilution of 1.5.

4.3.2.3 Application of process rules to the deposition of DOE test matrix

Using the parameter relationships established in previous trials, a single layer of overlapping tracks were deposited for each 25 distinct DOE run, using the calculated powder feed rate required to produce the DOE specified dilution, and using a track overlap of 30% of the measured single track width.

Each of these overlapping samples were cross sectioned and metallographically prepared (Figure 4-27 - Figure 4-29), and then optical microscopy and image analysis software was used to measure the layer thickness, from which the Z increment is calculated using the condition established in section 4.3.2.2.

The complete list of processing parameters that has been developed for the deposition of the DOE test block matrix is shown in Table 4-8. Using these parameters, 30 blocks were deposited (Figure 4-30, Figure 4-31) measuring 30x15x10mm nominal.

It was noted that nozzle performance decreased continuously throughout the deposition of the 30 test blocks, which necessitated that for each block, the powder flow rate had to be re-checked and calibrated against deposit shape, so that the decreased nozzle efficiency could be taken into account.

This nozzle degradation is caused by the build-up of particulates on the annulus of the nozzle tip, which creates a turbulence effect in the otherwise lamellar powder stream, leading to a loss of powder focus and less powder entering the melt pool.

Table 4-16 - Layer thickness measurements and calculated Z increments for distinct DOE runs

Sample ID	DOE run	Laser power	Scanning speed	Powder feed rate	Dilution	Laser spot diameter	ΔX	Measured layer thickness	Calculated ΔZ	Image number
		W	mm/s	g/min	Ac/Am	mm	mm	mm	mm	
PM-EngD-69	1	600	15	4.86	1.5	1.75	1.146	0.458	0.389	130219-056-058
PM-EngD-77	2	400	11.88	2.59	1.75	1.38	0.895	0.309	0.263	130219-088-090
PM-EngD-68	3	600	8.75	2.97	1.5	1.75	1.255	0.467	0.397	130219-052-055
PM-EngD-76	4	400	5.63	1.42	1.25	1.38	1.094	0.385	0.327	130219-084-087
PM-EngD-78	5	600	8.75	2.69	1.5	1	1.33	0.609	0.518	130219-091-094
PM-EngD-55	6	600	8.75	2.22	1.5	2.5	1.257	0.532	0.452	130219-001-004
PM-EngD-61	7	800	5.63	2.42	1.25	2.13	1.589	0.538	0.457	130219-023-027
PM-EngD-60	8	800	11.88	3.27	1.75	2.13	1.589	0.763	0.649	130219-018-022
PM-EngD-75	9	800	5.63	2.23	1.25	1.38	1.599	0.451	0.383	130219-079-083
PM-EngD-59	11	400	11.8	2.55	1.75	2.13	0.868	0.351	0.298	130219-015-017
PM-EngD-58	13	400	5.63	1.56	1.25	2.13	1.04	0.329	0.280	130219-012-014
PM-EngD-67	15	1000	8.75	4.27	1.5	1.75	1.631	0.61	0.519	130219-047-051
PM-EngD-74	16	400	5.63	1.72	1.75	1.38	1.094	0.361	0.307	130219-075-078
PM-EngD-57	17	400	11.88	2.28	1.25	2.13	0.904	0.273	0.232	130219-009-011
PM-EngD-56	18	800	11.88	4.08	1.25	2.13	1.289	0.487	0.414	130219-005-008
PM-EngD-73	19	800	5.63	2.86	1.75	1.38	1.602	0.571	0.485	130219-070-074
PM-EngD-66	21	600	8.75	2.22	1.5	1.75	1.255	0.645	0.548	130219-043-046
PM-EngD-65	22	200	8.75	1.18	1.5	1.75	0.517	0.167	0.142	130219-041-042
PM-EngD-64	23	600	8.75	2.12	1	1.75	1.255	0.328	0.279	130219-037-040
PM-EngD-63	24	600	8.75	3.83	2	1.75	1.255	0.615	0.523	130219-033-036
PM-EngD-72	26	800	11.88	4.61	1.75	1.38	1.399	0.471	0.400	130219-066-069
PM-EngD-71	27	800	11.88	3.83	1.25	1.38	1.399	0.391	0.332	130219-062-065
PM-EngD-62	28	600	2.5	1.25	1.5	1.75	1.563	0.567	0.482	130219-028-032
PM-EngD-70	30	400	11.88	2.56	1.25	1.38	0.988	0.298	0.253	130219-059-061

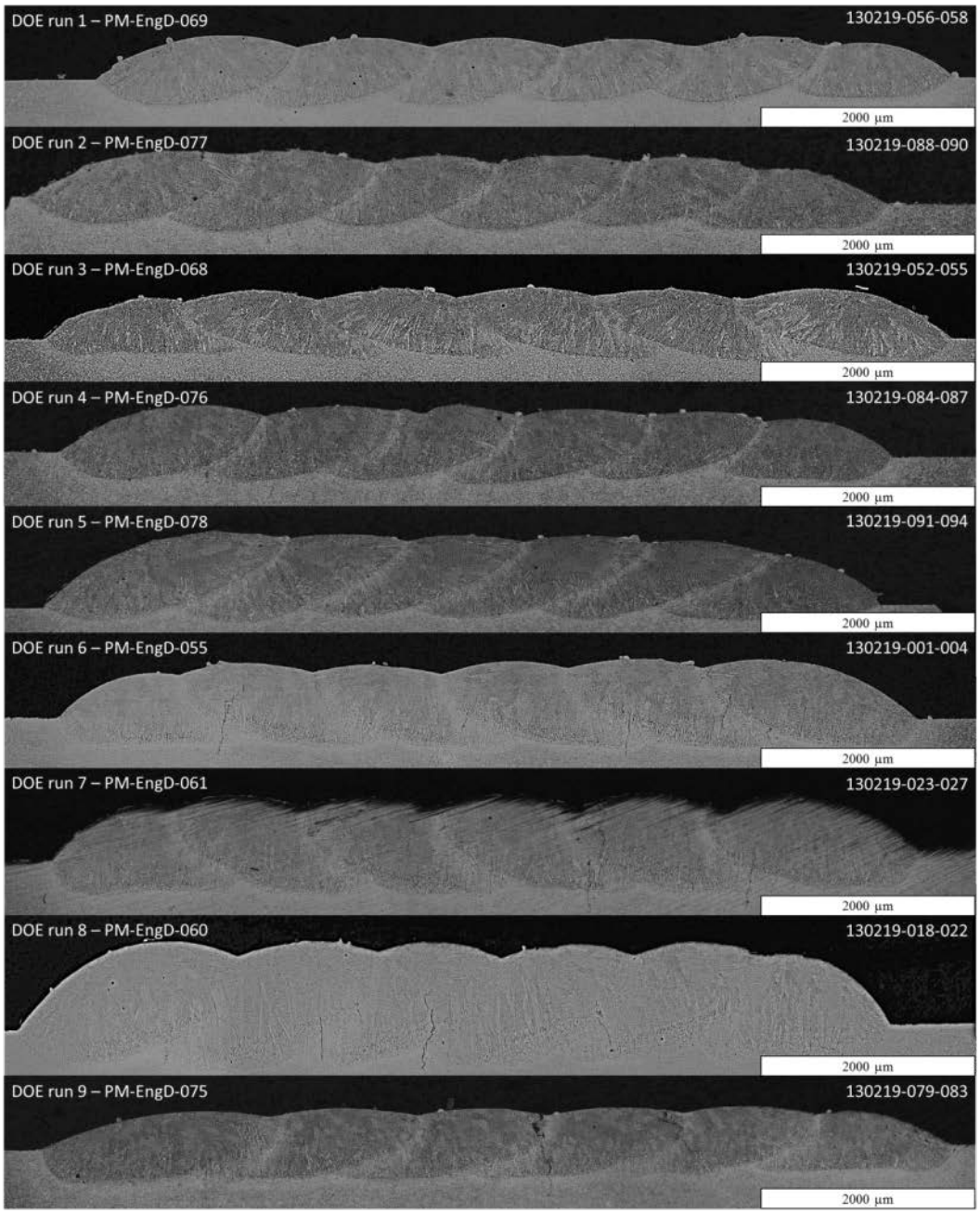

Figure 4-27 - Overlap patches used to establish DOE block Z increment – Deposited using 30% overlap condition – runs 1-9

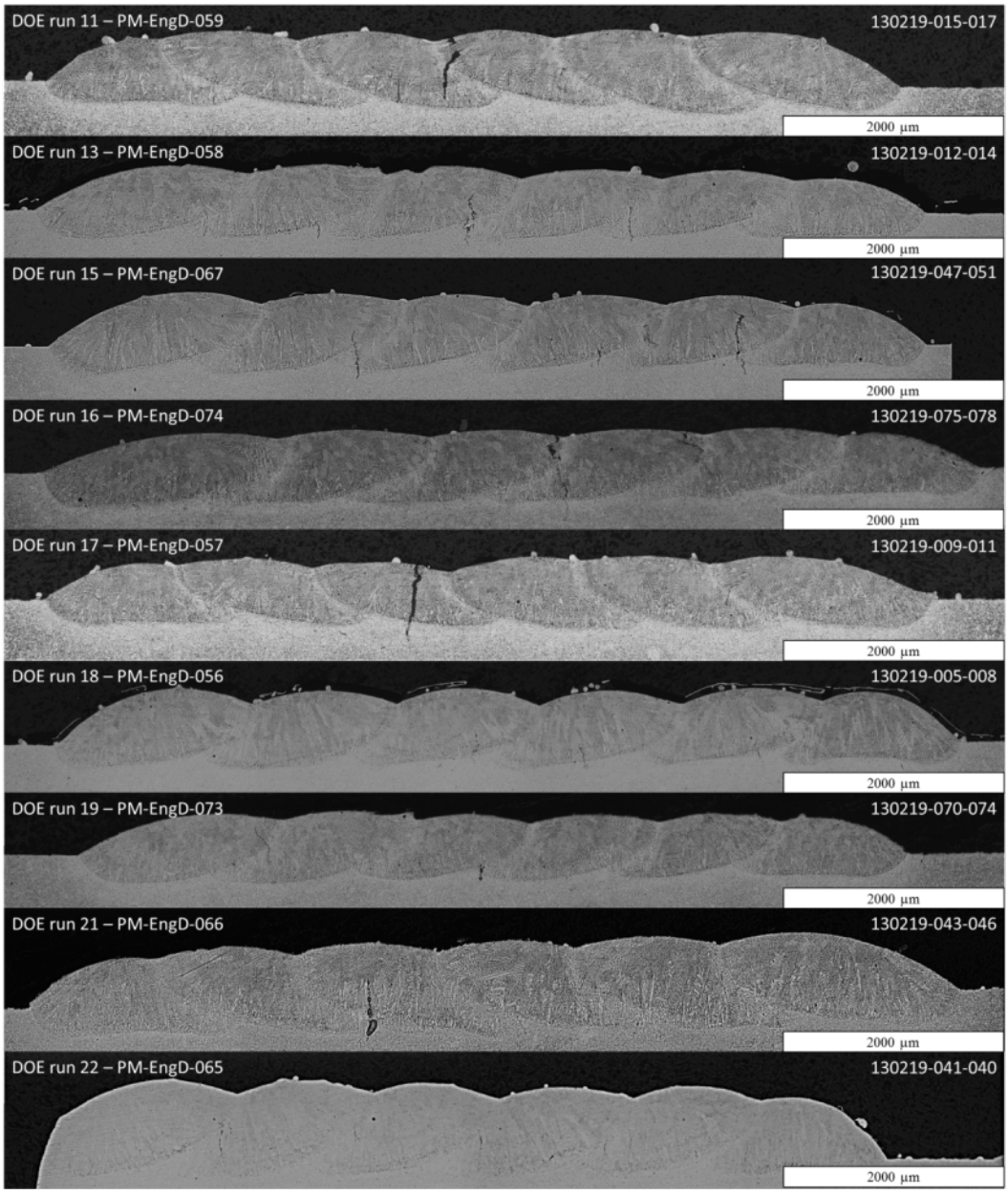

Figure 4-28 - Overlap patches used to establish DOE block Z increment – Deposited using 30% overlap condition – runs 11-22 (excluding duplicate runs 12 and 20)

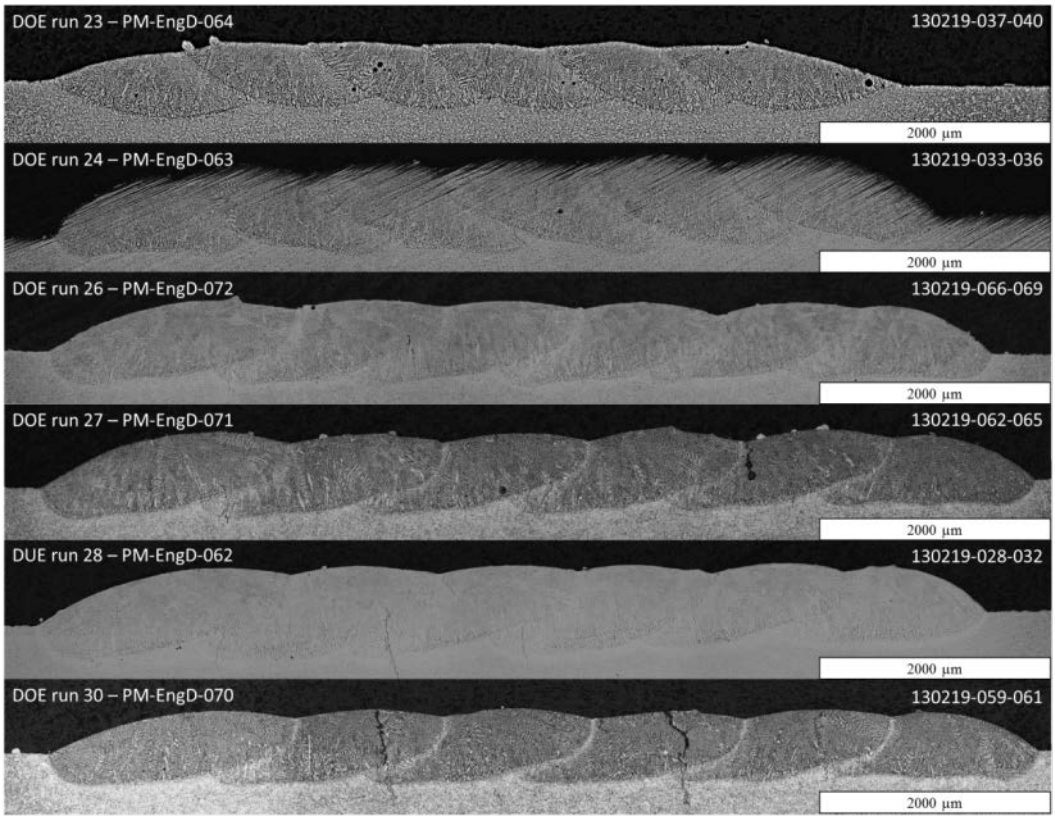

Figure 4-29 - Overlap patches used to establish DOE block Z increment – Deposited using 30% overlap condition – runs 23-30 (excluding duplicate runs 25 and 29)

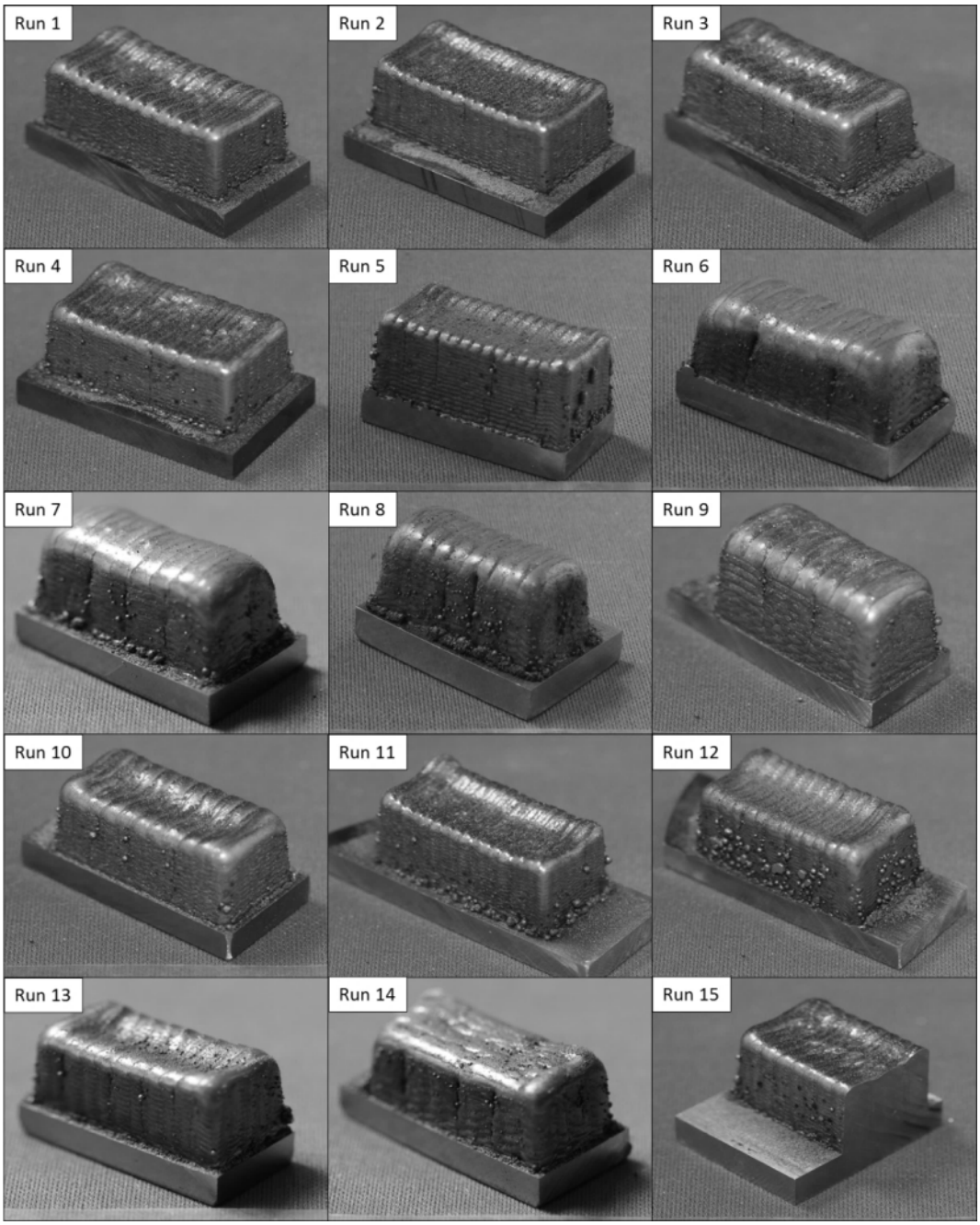

Figure 4-30 - DOE test blocks run 1-15

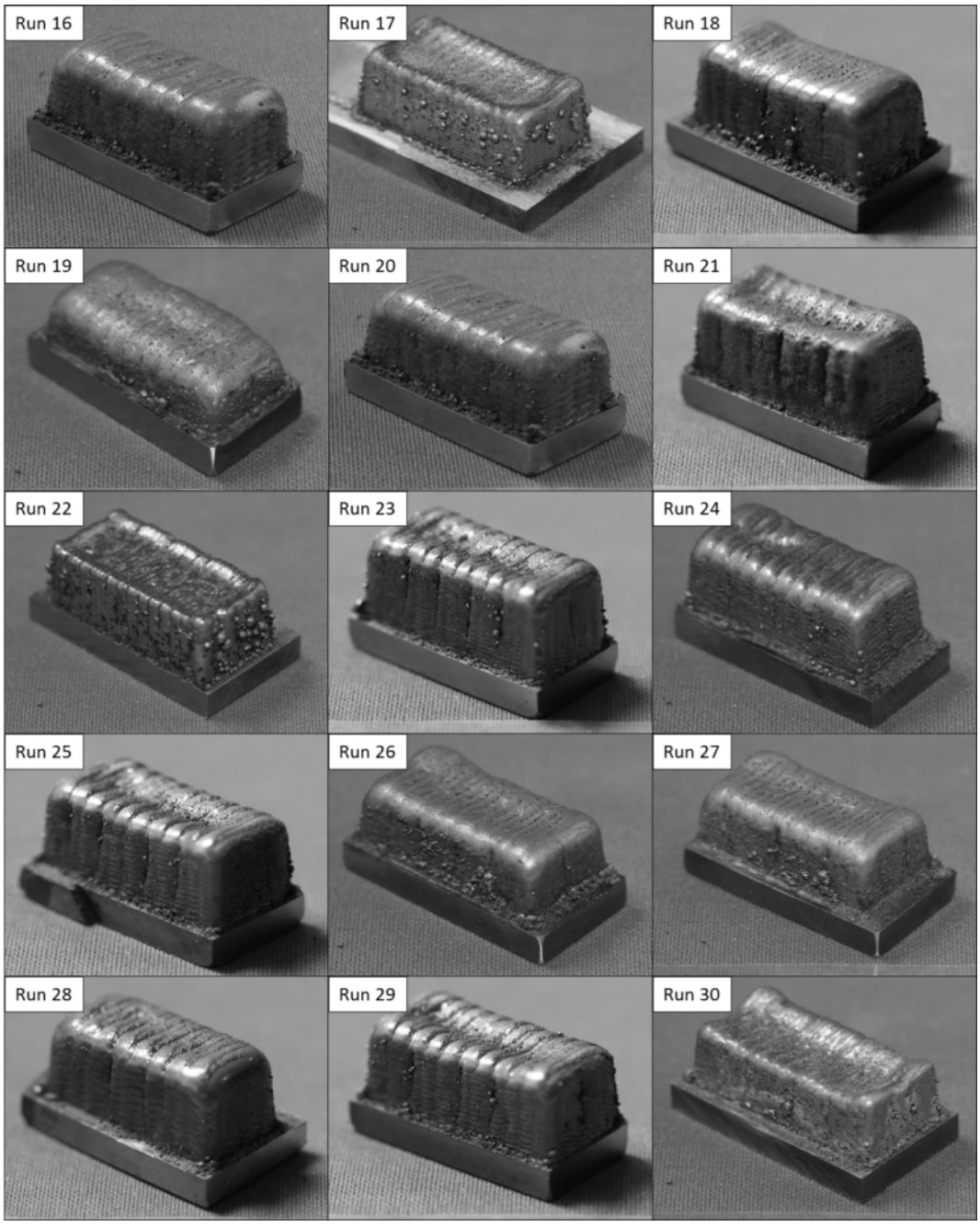

Figure 4-31 - DOE test blocks run 16-30

Visual inspection of the deposited blocks showed that all samples exhibited some degree of surface connected cracking, with cracks running vertically, perpendicular to the substrate surface. All samples exhibited satellite particles adhered to the sidewalls and deposit bases, the most noticeable of which was DOE run 22.

Blocks were metallographically sectioned as described in section 3.3.3 and polished, using method E described in section 3.3.1. Crack measurements were recorded for three samples from each block in order to produce a more reliable measurement.

4.3.3 Crack quantification and interpretation of DOE response

Crack measurement results for the DOE test blocks were compiled from over 3200 individual micrographs (Table 4-17, Table 4-18), with crack density results plotted by run number (Figure 4-32) and calculated energy density (Figure 4-33) and entered into the DOE software. Results were interpreted using the software (Figure 4-34 - Figure 4-37) and a response surface generated for crack density (Figure 4-38) and process desirability (Figure 4-39).

These response surfaces indicated that cracking was reduced for blocks that were deposited with high laser power, slow scanning speed, large laser spot diameter and low dilution.

Table 4-17 - Measurement of crack density for DOE test blocks (ordered by DOE run number)

Run	Laser power (W)	Laser spot diameter (mm)	Scanning speed (mm/s)	Dilution	Energy density (J/mm2)	crack density (µm/µm^2)
30	400	1.38	11.88	1.25	24.40	0.001748725
29	600	1.75	8.75	1.5	39.18	0.001539024
28	600	1.75	2.5	1.5	137.14	0.001421065
27	800	1.38	11.88	1.25	48.80	0.001523107
26	800	1.38	11.88	1.75	48.80	0.001362048
25	600	1.75	8.75	1.5	39.18	0.001536952
24	600	1.75	8.75	2	39.18	0.00144701
23	600	1.75	8.75	1	39.18	0.001481374
22	200	1.75	8.75	1.5	13.06	0.00219571
21	600	1.75	8.75	1.5	39.18	0.001423929
20	800	2.13	5.63	1.75	66.71	0.001285128
19	800	1.38	5.63	1.75	102.97	0.001481374
18	800	2.13	11.88	1.25	31.62	0.001488507
17	400	2.13	11.88	1.25	15.81	0.001591938
16	400	1.38	5.63	1.75	51.48	0.001369582
15	1000	1.75	8.75	1.5	65.31	0.001188662
14	600	1.75	8.75	1.5	39.18	0.001400425
13	400	2.13	5.63	1.25	33.36	0.001367651
12	400	2.13	5.63	1.75	33.36	0.001301179
11	400	2.13	11.88	1.75	15.81	0.001524705
10	600	1.75	8.75	1.5	39.18	0.001360578
9	800	1.38	5.63	1.25	102.97	0.001260089
8	800	2.13	11.88	1.75	31.62	0.001296582
7	800	2.13	5.63	1.25	66.71	0.001297756
6	600	2.5	8.75	1.5	27.43	0.001248434
5	600	1	8.75	1.5	68.57	0.001481374
4	400	1.38	5.63	1.25	51.48	0.001533545
3	600	1.75	8.75	1.5	39.18	0.001454782
2	400	1.38	11.88	1.75	24.40	0.001700638
1	600	1.75	15	1.5	22.86	0.001388637

Table 4-18 - Measurement of crack density for DOE test blocks (ordered by calculated energy density)

Run	Laser power (W)	Laser spot diameter (mm)	Scanning speed (mm/s)	Dilution	Energy density (J/mm2)	crack density (µm/µm^2)
22	200	1.75	8.75	1.5	13.06	0.00219571
11	400	2.13	11.88	1.75	15.81	0.001524705
17	400	2.13	11.88	1.25	15.81	0.001591938
1	600	1.75	15	1.5	22.86	0.001388637
2	400	1.38	11.88	1.75	24.40	0.001700638
30	400	1.38	11.88	1.25	24.40	0.001748725
6	600	2.5	8.75	1.5	27.43	0.001248434
8	800	2.13	11.88	1.75	31.62	0.001296582
18	800	2.13	11.88	1.25	31.62	0.001488507
12	400	2.13	5.63	1.75	33.36	0.001301179
13	400	2.13	5.63	1.25	33.36	0.001367651
3	600	1.75	8.75	1.5	39.18	0.001454782
10	600	1.75	8.75	1.5	39.18	0.001360578
14	600	1.75	8.75	1.5	39.18	0.001400425
21	600	1.75	8.75	1.5	39.18	0.001423929
23	600	1.75	8.75	1	39.18	0.001481374
24	600	1.75	8.75	2	39.18	0.00144701
25	600	1.75	8.75	1.5	39.18	0.001536952
29	600	1.75	8.75	1.5	39.18	0.001539024
26	800	1.38	11.88	1.75	48.80	0.001362048
27	800	1.38	11.88	1.25	48.80	0.001523107
4	400	1.38	5.63	1.25	51.48	0.001533545
16	400	1.38	5.63	1.75	51.48	0.001369582
15	1000	1.75	8.75	1.5	65.31	0.001188662
7	800	2.13	5.63	1.25	66.71	0.001297756
20	800	2.13	5.63	1.75	66.71	0.001285128
5	600	1	8.75	1.5	68.57	0.001481374
9	800	1.38	5.63	1.25	102.97	0.001260089
19	800	1.38	5.63	1.75	102.97	0.001481374
28	600	1.75	2.5	1.5	137.14	0.001421065

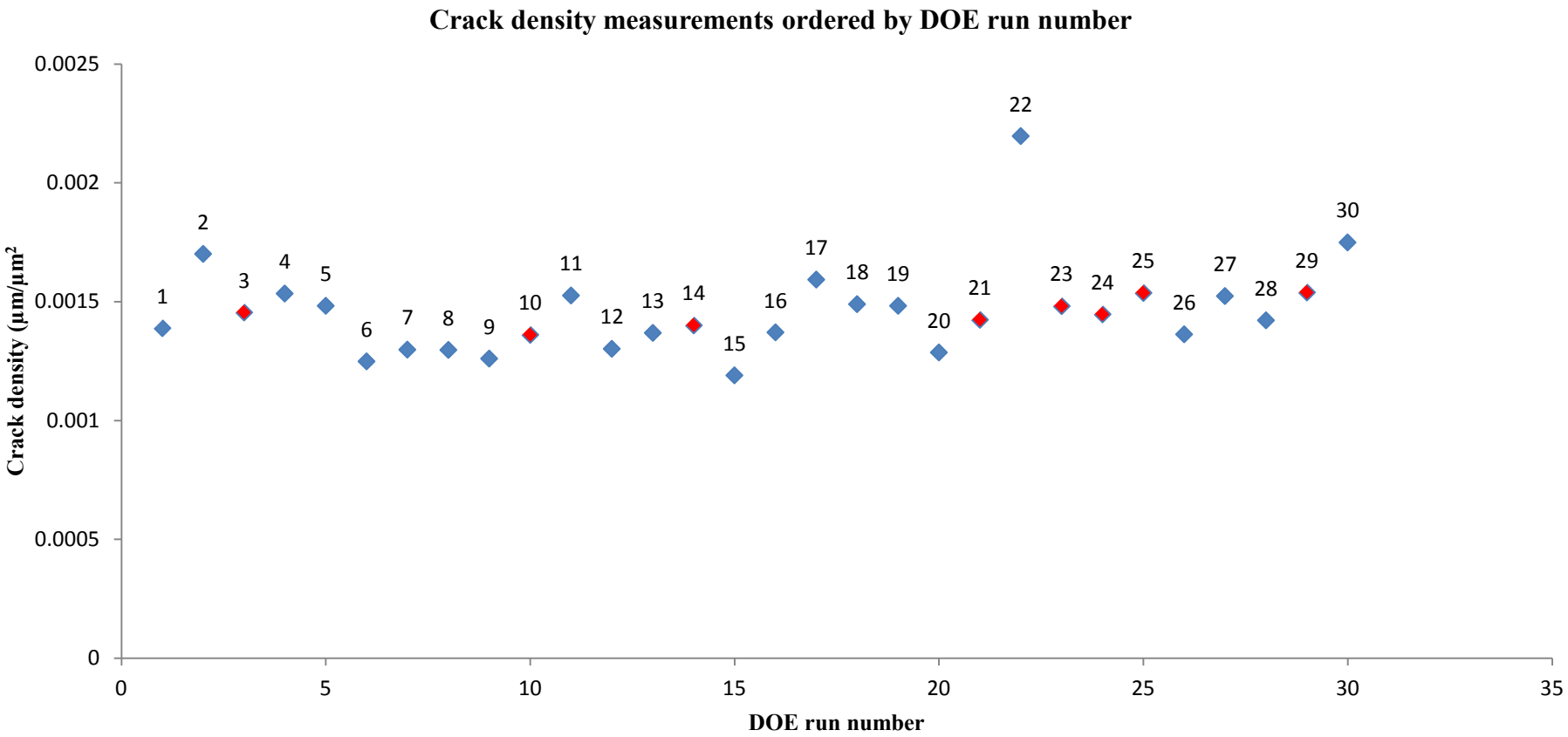

Figure 4-32 - Graph of measured crack density, plotted by DOE run number (as per Table 4-17). Red points indicate DOE centre point repetitions

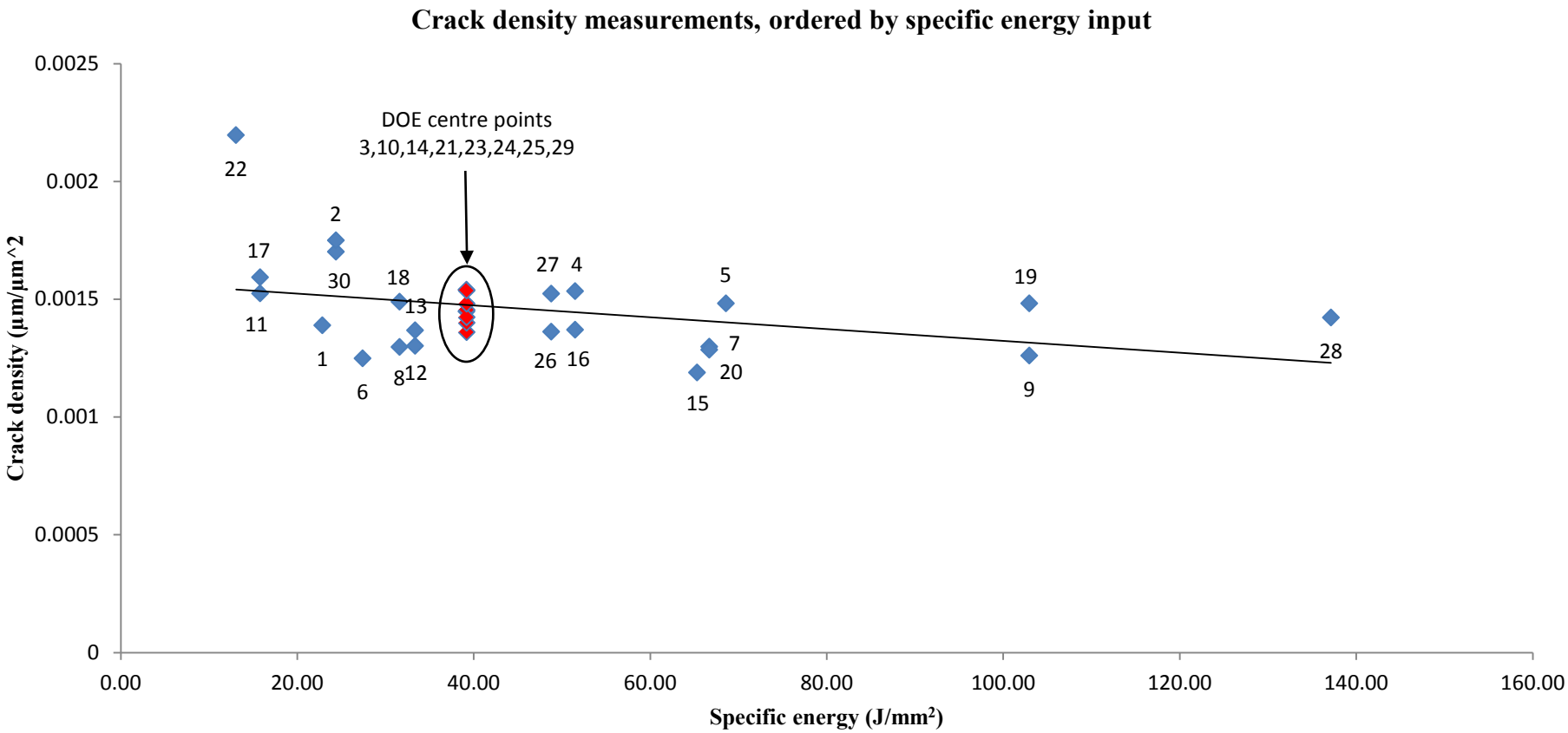

Figure 4-33 - Graph of measured crack density, ordered by calculated specific energy for each DOE run (as per Table 4-18). Red points indicate DOE centre point repetitions

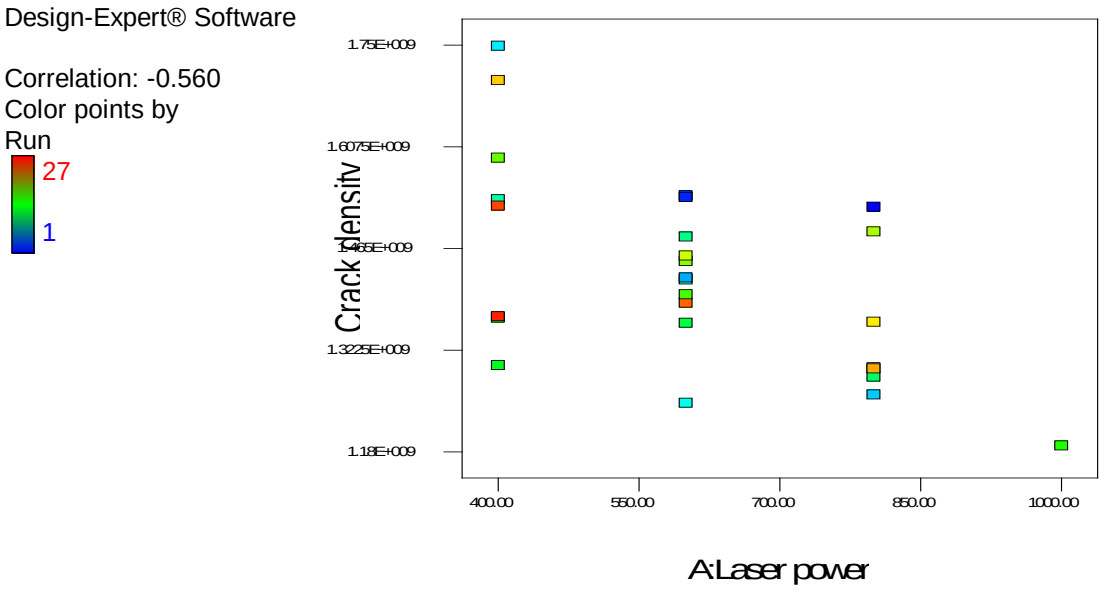

Figure 4-34 - Crack density results ordered by laser power levels using the DOE software

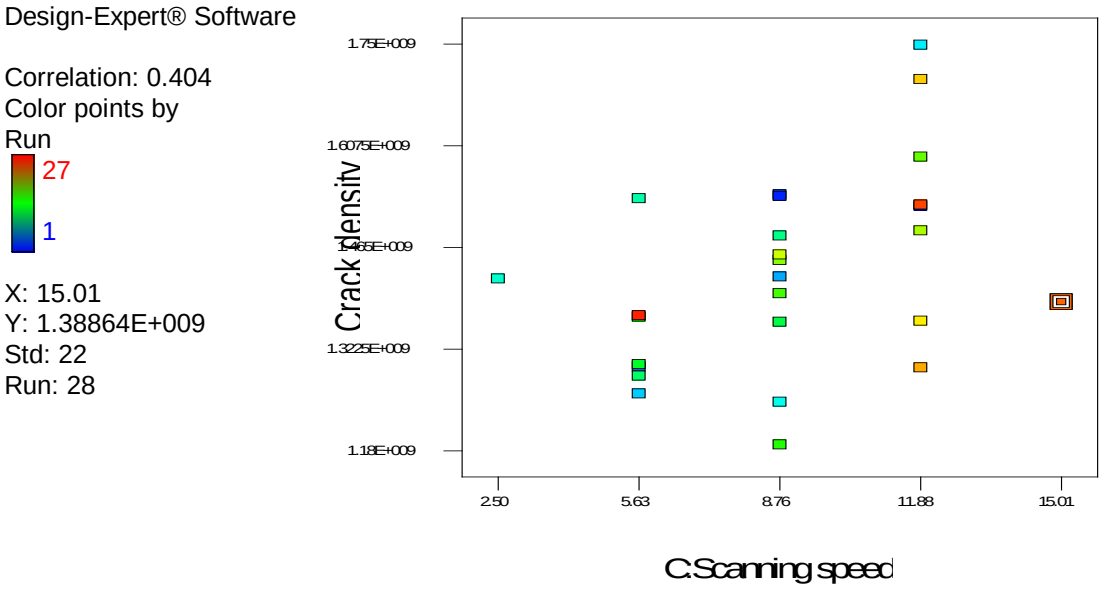

Figure 4-35 - Crack density results as ordered by laser scanning speed using the DOE software

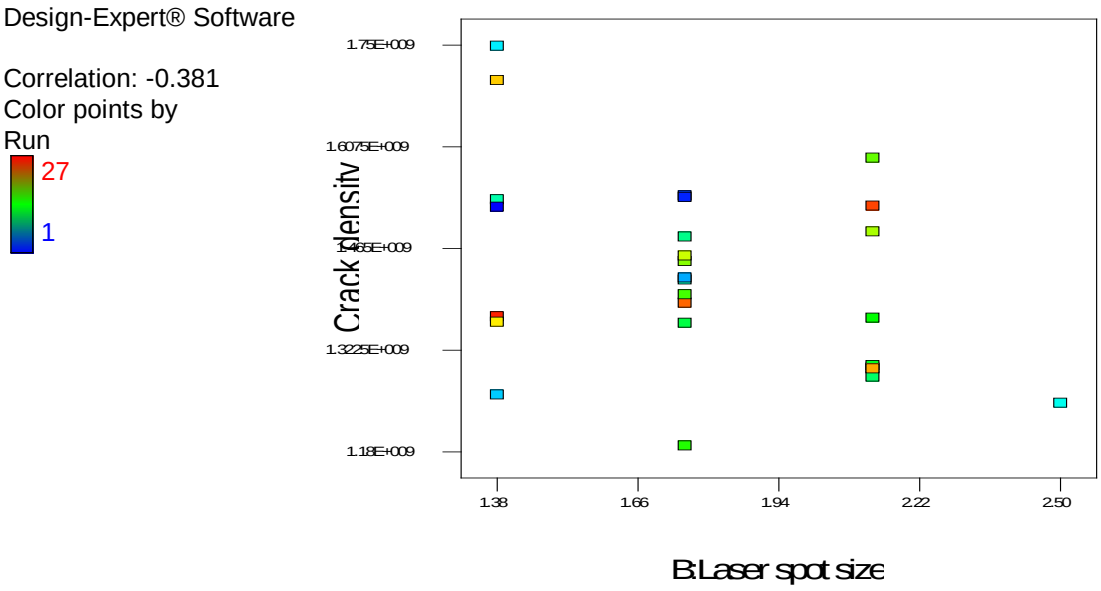

Figure 4-36 - Crack density results as ordered by laser spot size using the DOE software

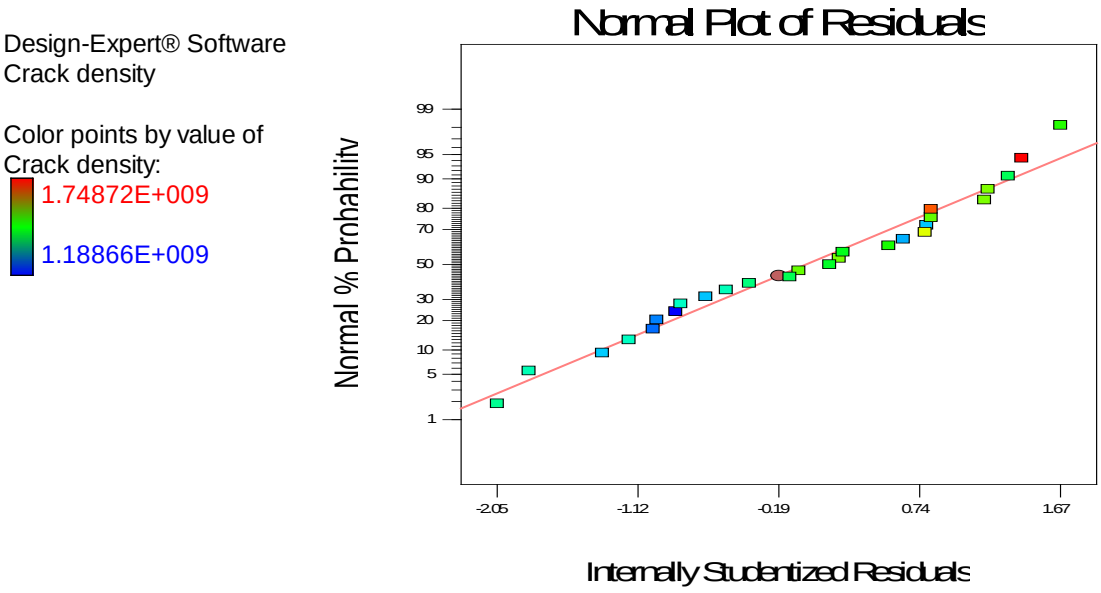

Figure 4-37 - Normal plot of residuals, showing that the results are normally distributed. (Studentised results are a quotient resulting from the division of a residual by an estimate of its standard deviation)

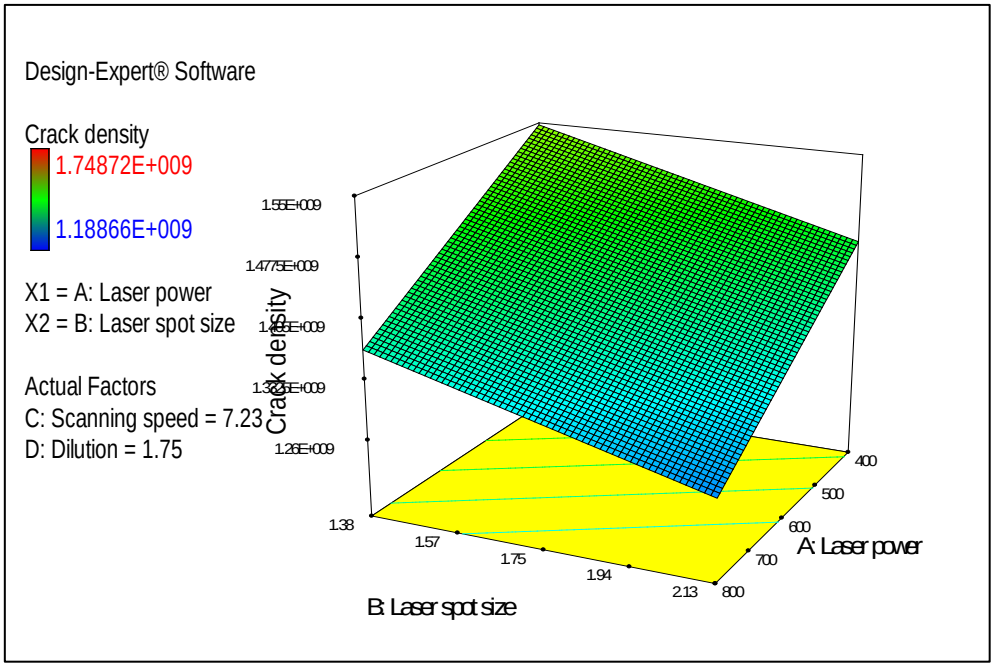

Figure 4-38 - DOE response surface generated from crack measurements, showing how crack density varies with spot size and laser power.

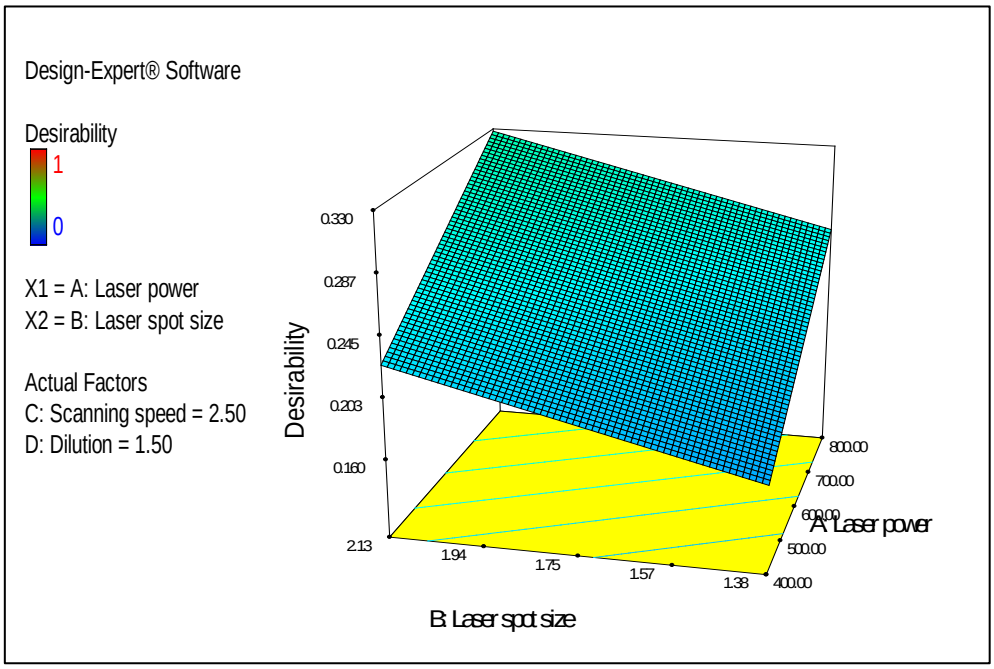

Figure 4-39 - DOE response surface plotted for desirability of outcome, showing desirability as a function of laser spot size and laser power.

4.3.4 Microstructural analysis and characterisation of crack morphologies

Optical microscopy of DOE deposited blocks revealed a microstructure of coarse columnar grains of dendritic composition, which appear to propagate epitaxially through multiple deposit layers (Figure 4-42). Cracks are of varying length and size, appearing to follow the grain boundaries and inter-dendritic pathways (Figure 4-40 - Figure 4-43).

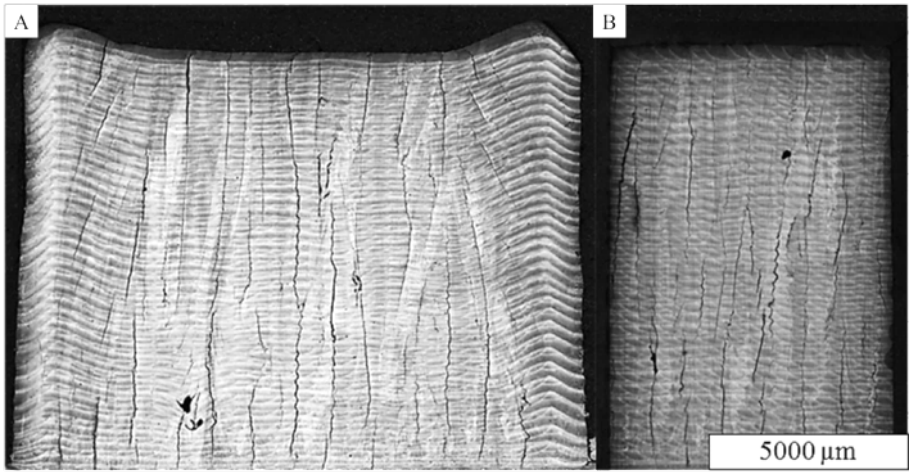

Figure 4-40 - DOE run 22 deposited at low (200W) heat input. A) Cross section transverse to long axis B) Cross sectioned along long axis

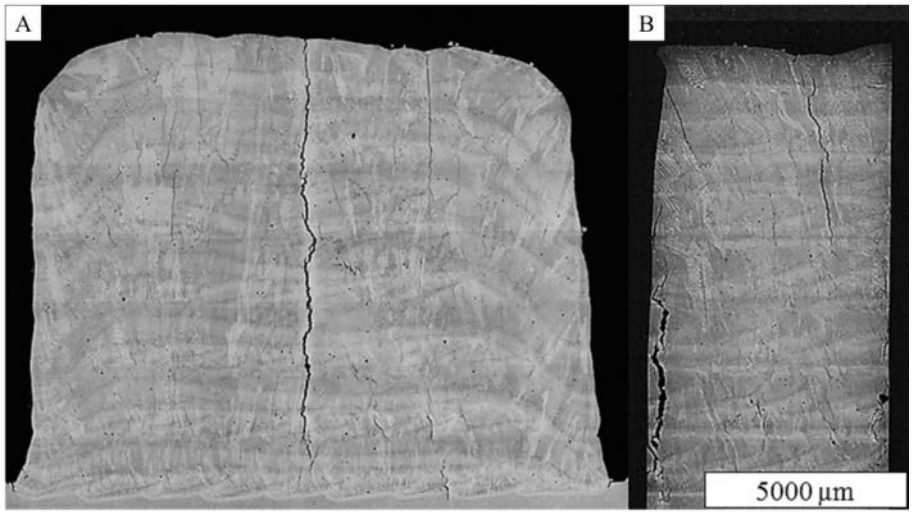

Figure 4-41 - DOE run 15 deposited at high (1000W) laser power A) Cross section transverse to long axis B) cross sectioned along long axis

Comparison of blocks deposited at low laser power (Figure 4-40 – DOE run 22) and high laser power (Figure 4-41 – DOE run 15) that the latter produced blocks with fewer cracks, but at the expense of deposit shape and accuracy. Blocks that are deposited at higher laser powers and slower scanning speeds tend to produce wider tracks, and the microstructure appears coarser, with larger columnar grains, a deeper heat affected zone and greater distortion in the substrate.

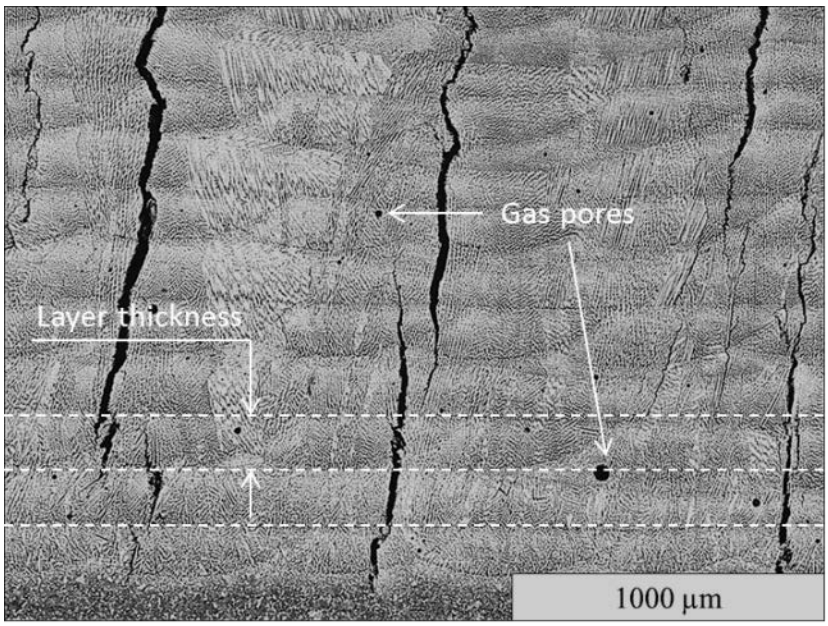

Figure 4-42 - 50x optical micrograph of DOE block 22 (200W laser power), showing epitaxial columnar grain growth, presence of cracks and gas porosity.

Examination of the fusion boundary between the deposit and the substrate showed several distinct zones, as illustrated in Figure 4-43. From the fusion boundary, there is a region of cellular solidification (B) measuring between 20-100µm in thickness (depending on heat input), above which dendritic grain solidification (A) is dominant. The HAZ of the deposit (C) was observed to a depth of between 100µm and 500µm from the fusion boundary, depending on the laser power and scanning speed of the DOE run.

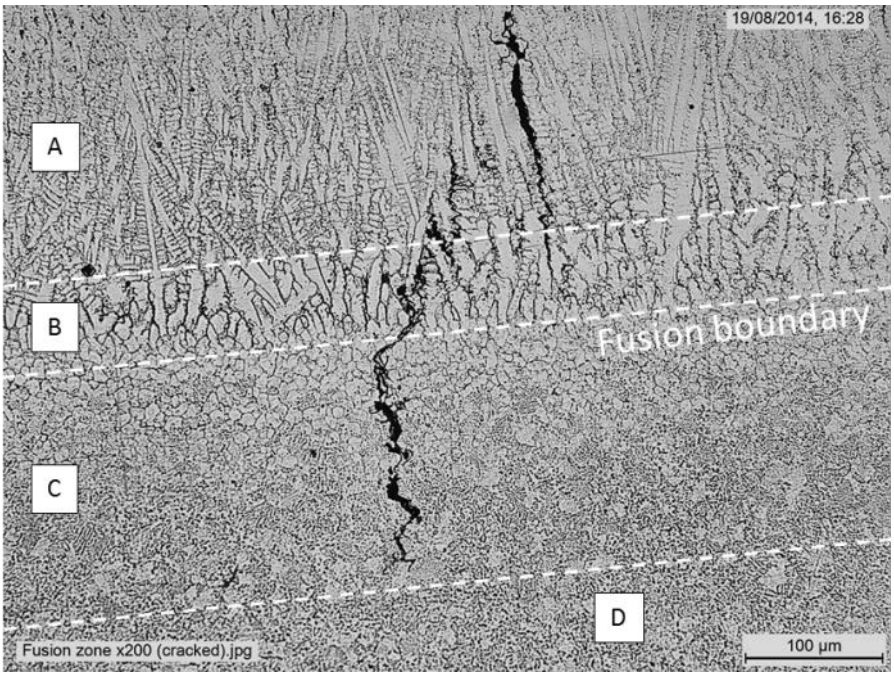

Figure 4-43 - 200X optical micrograph of DOE block 15 (1000W laser power). Areas of interest include the fusion boundary, Dendritic growth region (A), Cellular growth region (B), heat affected zone of substrate (C) and underlying unaffected substrate (D).

In many of the blocks deposited, cracks were observed penetrating into the substrate at the junction between the edge of the block and the substrate (Figure 4-44A). This "toe" crack was more pronounced for some blocks than others, with blocks deposited at specific energies greater than 39 J/mm^2 showing a greater tendency to form cracks in this area. SEM analysis of the cracks within the HAZ (Figure 4-45-Figure 4-47) shows that cracks appear to be propagating along the inter-particle boundaries (IPB), but the fine grain size of the HIP'd material makes it difficult to say conclusively what cracking mechanism is at play. No evidence of carbide or grain boundary liquation within the IPB was observed under SEI or QBSD SEM. Similarly, in many blocks, cracks were also penetrating downwards from the first deposit layer into the HAZ of the substrate (Figure 4-43, Figure 4-44B) in the same way observed in section 4.3.2.2.

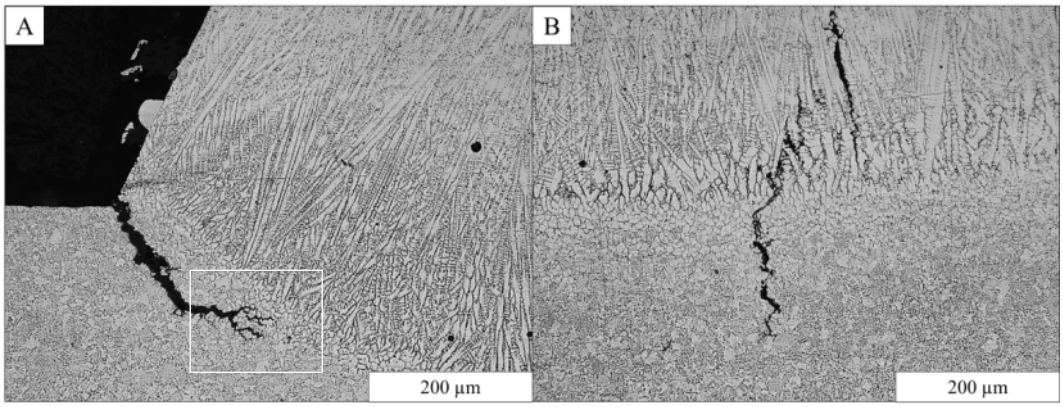

Figure 4-44 - A) Toe crack penetrating into substrate formed at the junction between the block edge and the substrate B) Crack penetrating into the substrate from the block interior

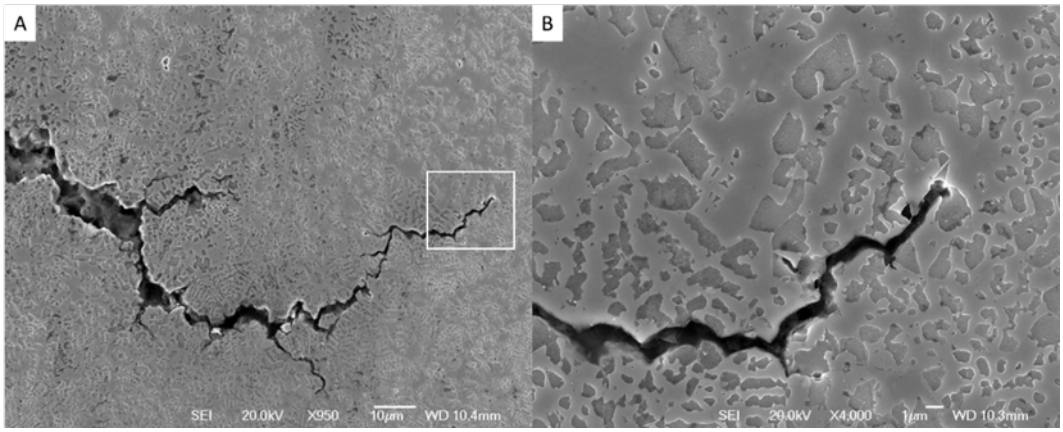

Figure 4-45 - SEI SEM micrographs of crack penetrating through the substrate as per Figure 4-44A

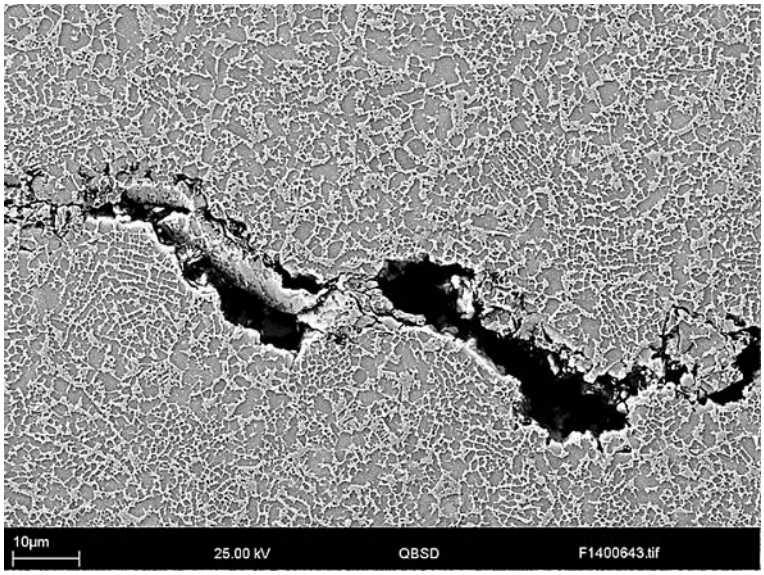

Figure 4-46 - QBSD SEM micrograph of toe crack within the HAZ

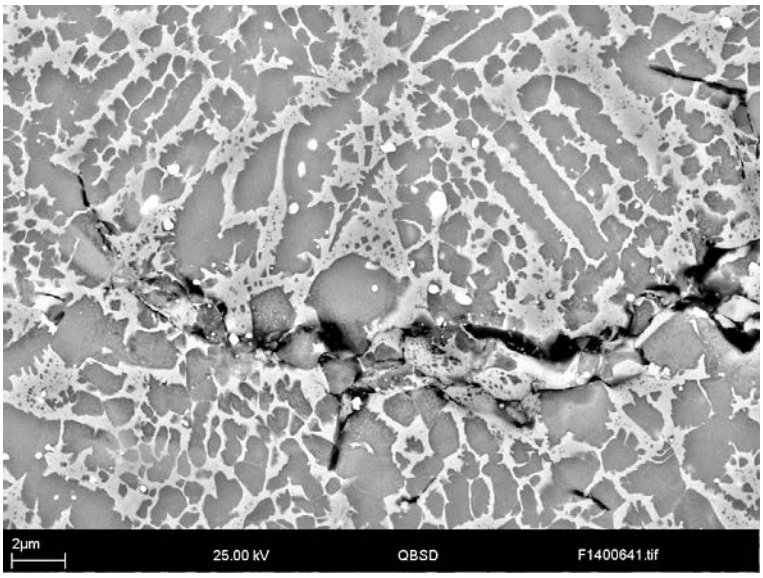

Figure 4-47 - QBSD SEM micrograph of toe crack tip within HAZ

Spherical gas porosity was observed in all of the deposited blocks to some degree, which appear to form randomly across the deposit. The size and distribution of these pores did not appear to be related to the propagation pathways of the cracks.

SEM analysis of the deposited blocks showed a dendritic microstructure (Figure 4-48), with γ/γ' eutectic phase and discrete particles observed along grain boundaries, inter-dendritic regions and the edges of cracks (Figure 4-49, Figure 4-50). Within the interdendritic region, there is evidence of fine scale (<150nm) primary and secondary γ' precipitation (Figure 4-51).

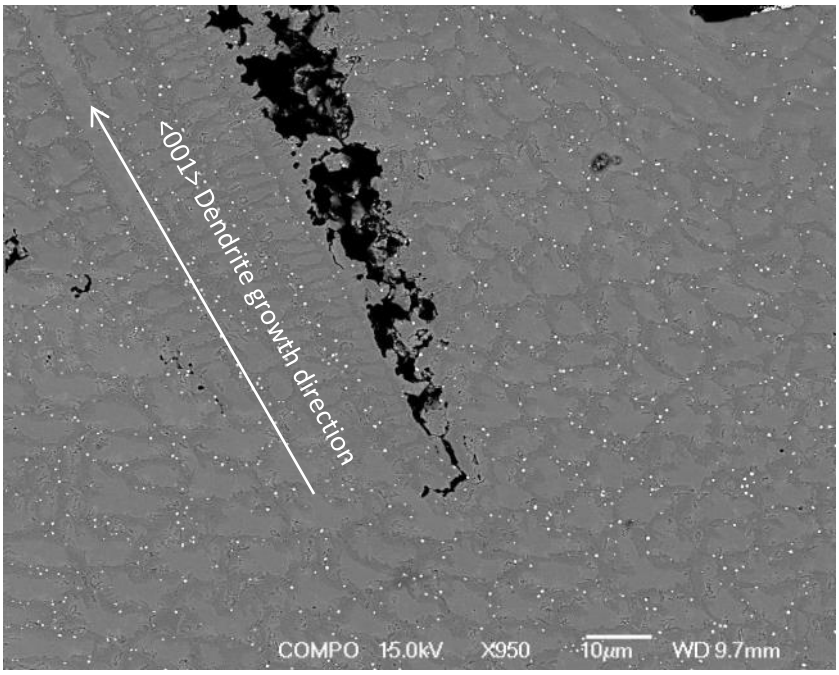

Figure 4-48 - QBSD SEM micrograph of deposit microstructure, showing crack tip, dendritic microstructure and location of discrete carbide phases (white dots)

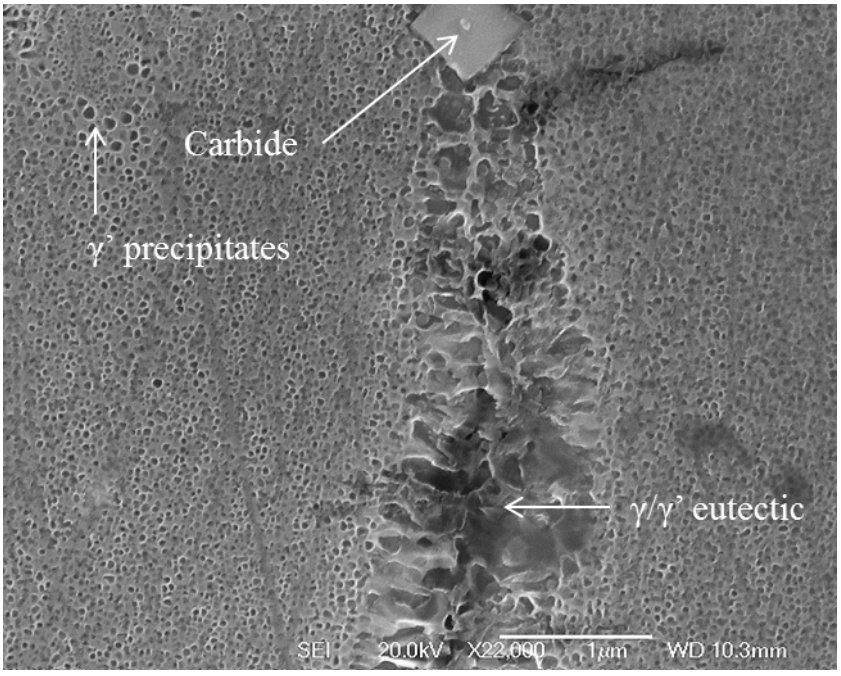

Figure 4-49 - SEI SEM micrograph showing intergranular γ/γ' eutectic along solidification boundary, MC type carbide and presence of nano-scale γ'

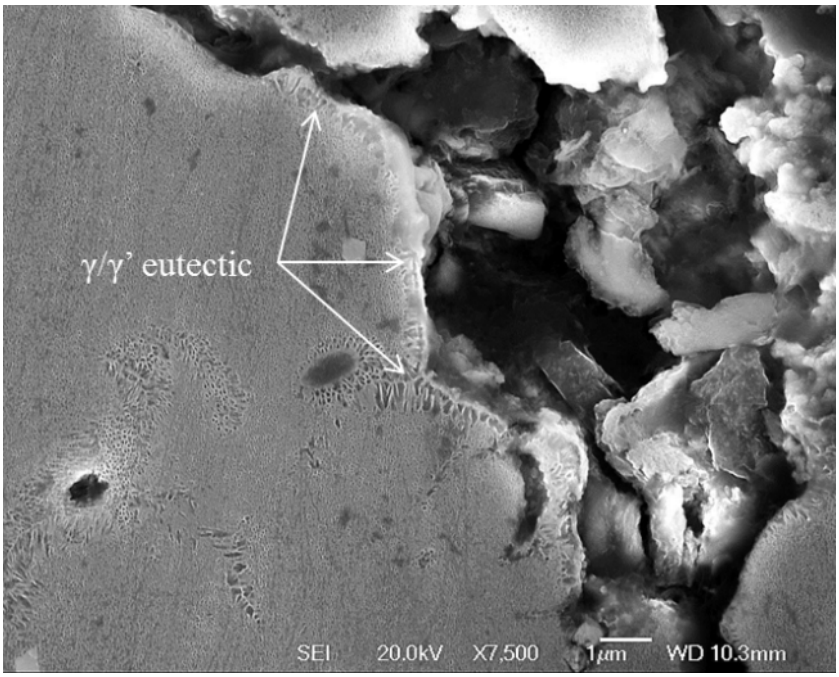

Figure 4-50 - SEI SEM micrograph of crack within the deposit, showing presence of retained γ/γ' eutectic along crack edge

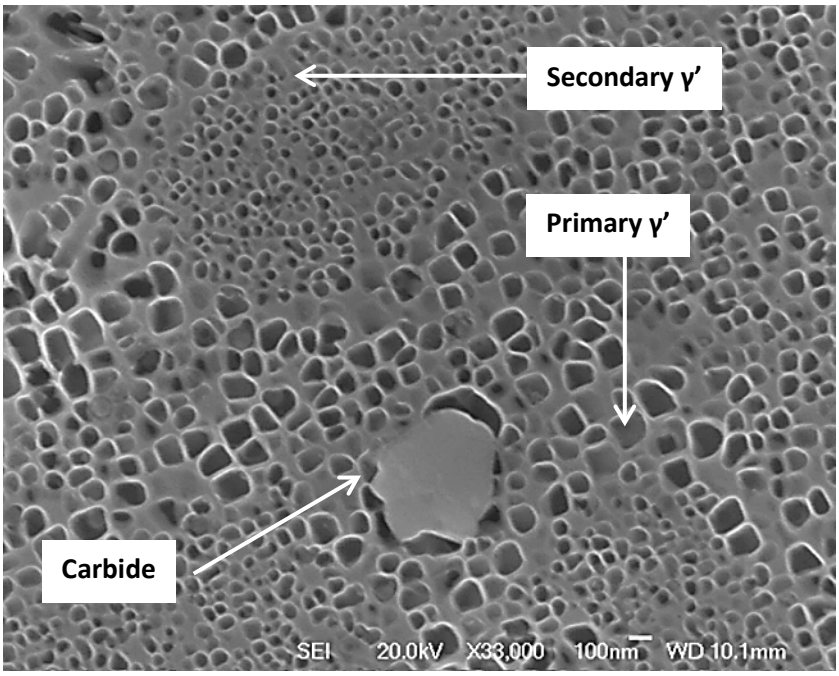

Figure 4-51 - SEI SEM micrograph of inter-dendritic region near grain boundary, showing carbide, primary γ' and secondary γ'

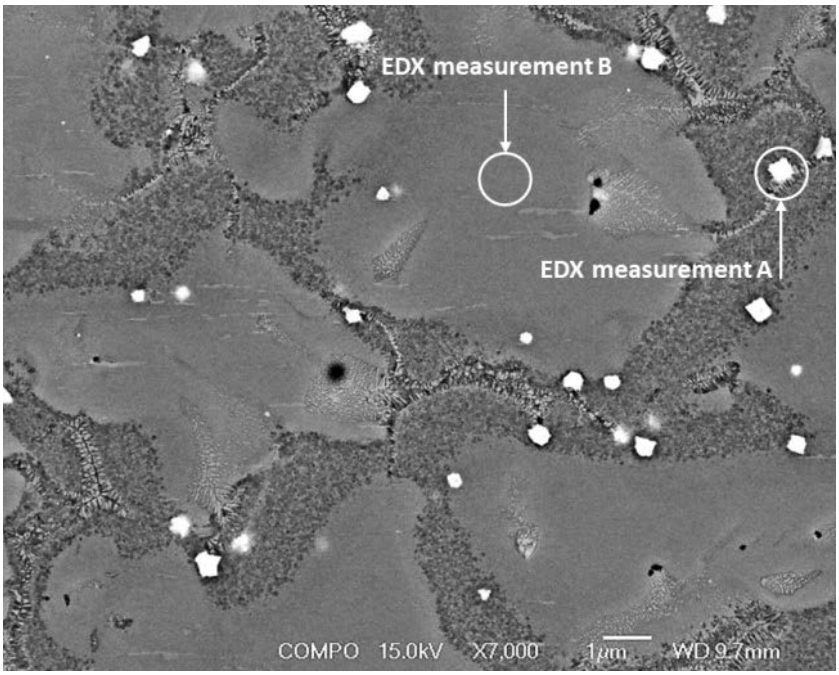

Figure 4-52 - Backscattered SEM micrograph taken from the deposit material, showing presence of discrete carbide phases, dendrite cores and inter-dendritic eutectic phases.

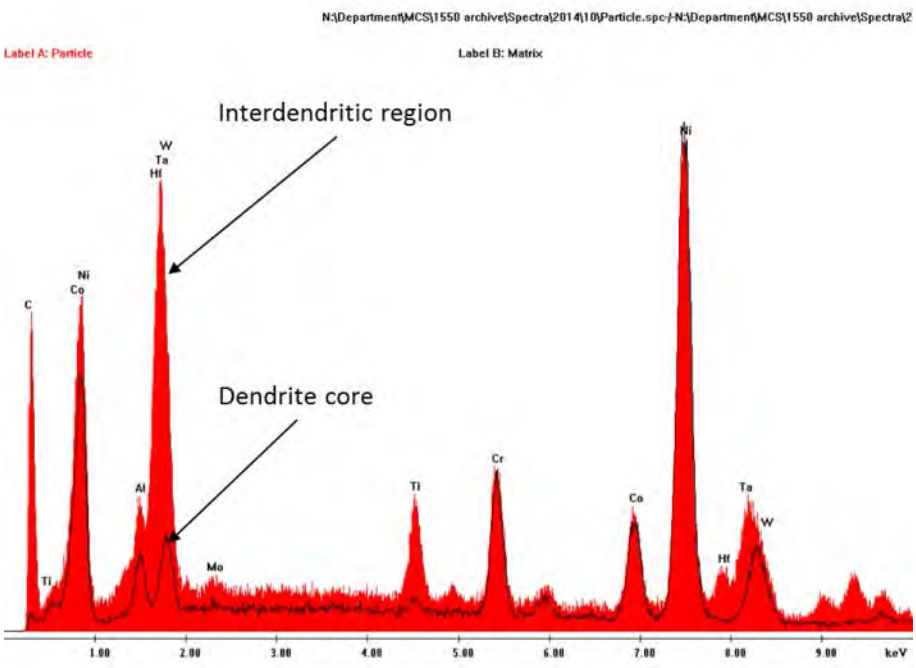

Figure 4-53 - EDX spectra for spot measurement points A and B in Figure 4-52. The red trace represents the measurement taken of the precipitate in the inter-dendritic region; the black trace overlaid onto it represents a measurement taken from the dendrite core.

Energy Dispersive X-ray spectroscopy (EDX) measurements were taken from the region surrounding a carbide particle within the interdendritic region (Figure 4-52 - measurement A) as well as from a dendrite core (Figure 4-52– measurement B). Interpretation of the EDX spectra (Figure 4-53) showed the interdendritic region surrounding the carbide particle to be rich in carbon, titanium, aluminium, tungsten, tantalum and hafnium.

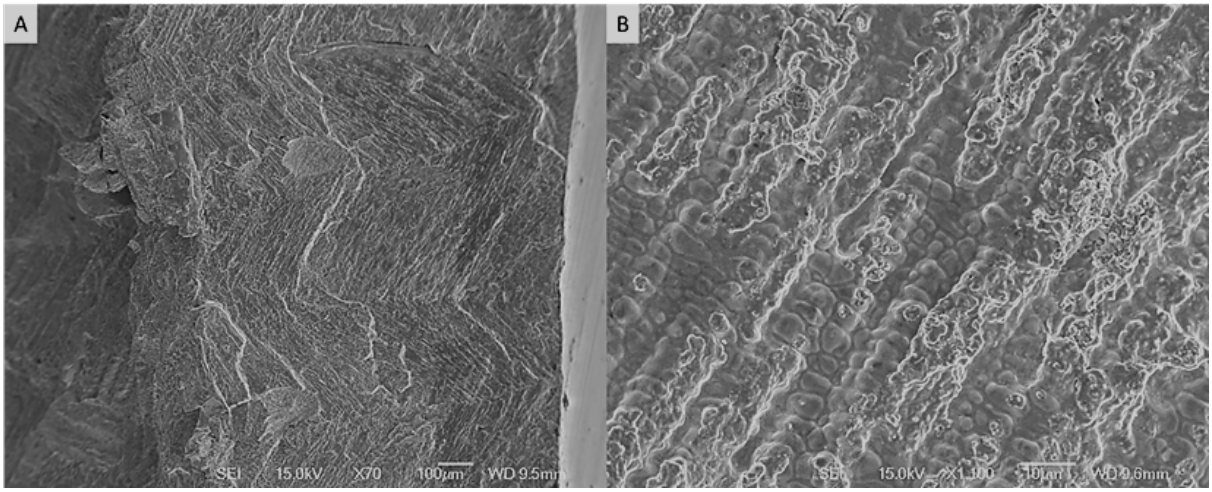

Figure 4-54 - SEM micrograph of crack surface morphology A) changes in dendrite growth orientation with alternating layers are observed B) Crack surface comprises a residual dendritic morphology, showing primary and secondary dendrite arms.

SEM characterisation of an exposed crack surfaces, showed a striated topography that appears to change direction in a zig-zag fashion (Figure 4-54A). The distance between the direction changes are consistent with the layer thickness of the toolpath, suggesting that the different scanning directions are causing the dendrites to re-align to the different direction of heat flow from the melt pool.

Closer examination of the crack surface revealed a dendritic morphology consisting of what appears to be long thin primary dendrite arms approximately 10µm in width, with short stubby secondary dendrites at approximately 2µm spacing (Figure 4-54B).The surfaces of these dendrites are covered in a relatively uniform dispersion of sub-micron sized particles (Figure 4-55) that appear spherical in shape, and are believed to be primary γ' that formed in the interdendritic regions during the terminal stages of solidification.

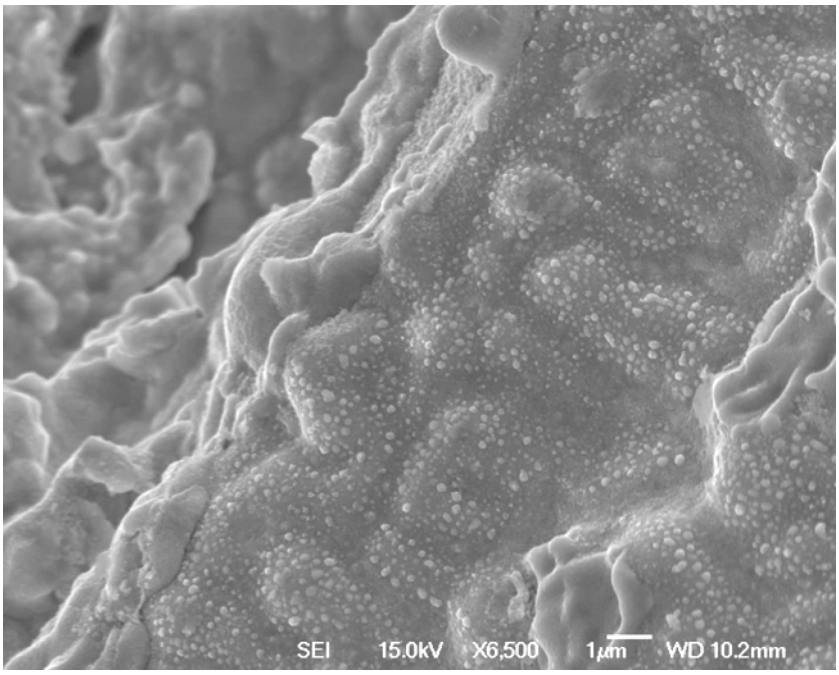

Figure 4-55 – SEI SEM micrograph of crack surface, showing residual dendritic morphology and the presence of a large number of sub-micron precipitates studding the surface

4.3.5 Deposition of block using “optimised” DOE parameters

4.3.5.1 Process parameter development

Based on the interpretation of the DOE results, fewer cracks were observed for:

- high laser powers,
- slow scanning speeds,
- large laser spot diameters
- Low deposit dilution.

In order to validate this observation, two blocks were deposited using the parameters from the extremes of the DOE experiment range.

Table 4-19 - Deposition parameters developed for DOE "optimised" validation blocks

Process parameter	Value	Units
Laser Power	1000	W
Scanning speed	5	mm/s
Laser spot diameter	3	mm
Deposit dilution	1.5	
Powder feed rate	6.5	g/min
Track spacing	1.8	mm
Z increment	0.55	mm

Using the processes established previously, single tracks were deposited at different powder feed rates (Figure 4-56) from which a value was calculated that produced a dilution of 1.5 (Figure 4-58). Deposit widths from the single track trials were used to calculate the 30% overlap spacing, and a single layer deposited (Figure 4-59) that allowed the Z-increment to be calculated.

Using these relationships, parameters were developed for the deposition of a pair of validation blocks (Table 4-19, Figure 4-60). One block was sectioned longitudinally (Figure 4-61) and the other block was sectioned transversely into four equal pieces (Figure 4-62) for crack measurement.

Figure 4-56 - Single tracks deposited at 1000W, 5mm/s, 3mm laser spot diameter, and varying powder feed rates

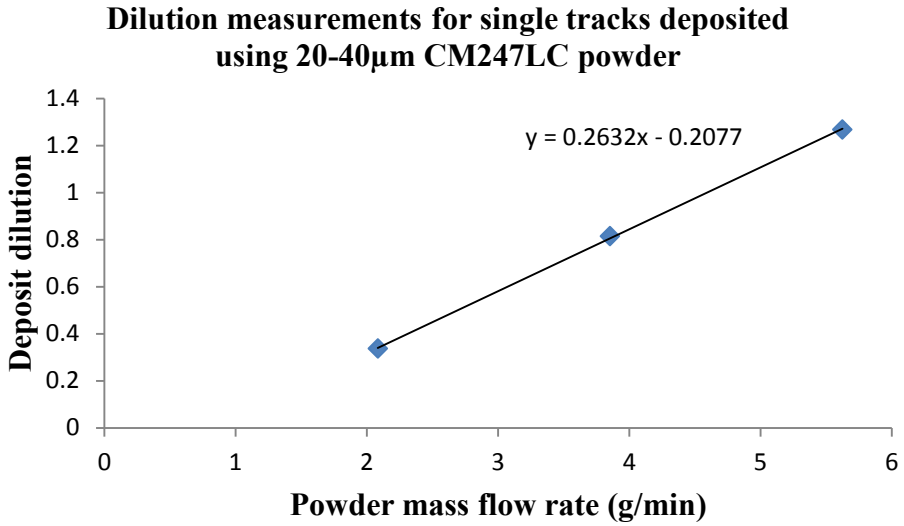

Figure 4-57 - Calculation of deposit dilution as a function of powder mass flow rate for DOE optimised block

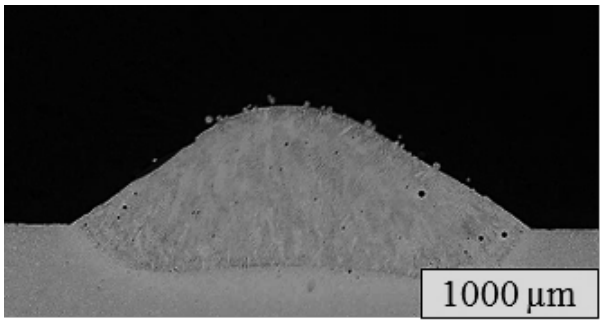

Figure 4-58 - Single track deposited using calculated powder feed rate to produce deposit dilution of 1.5

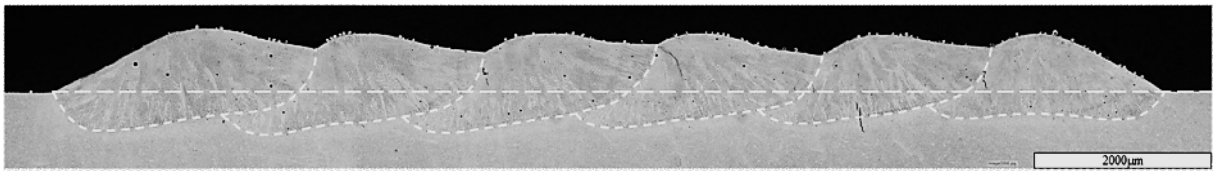

Figure 4-59 - Overlapping tracks deposited using 30% overlap condition (1.8mm), used to calculate Z-increment for the DOE "optimised" block

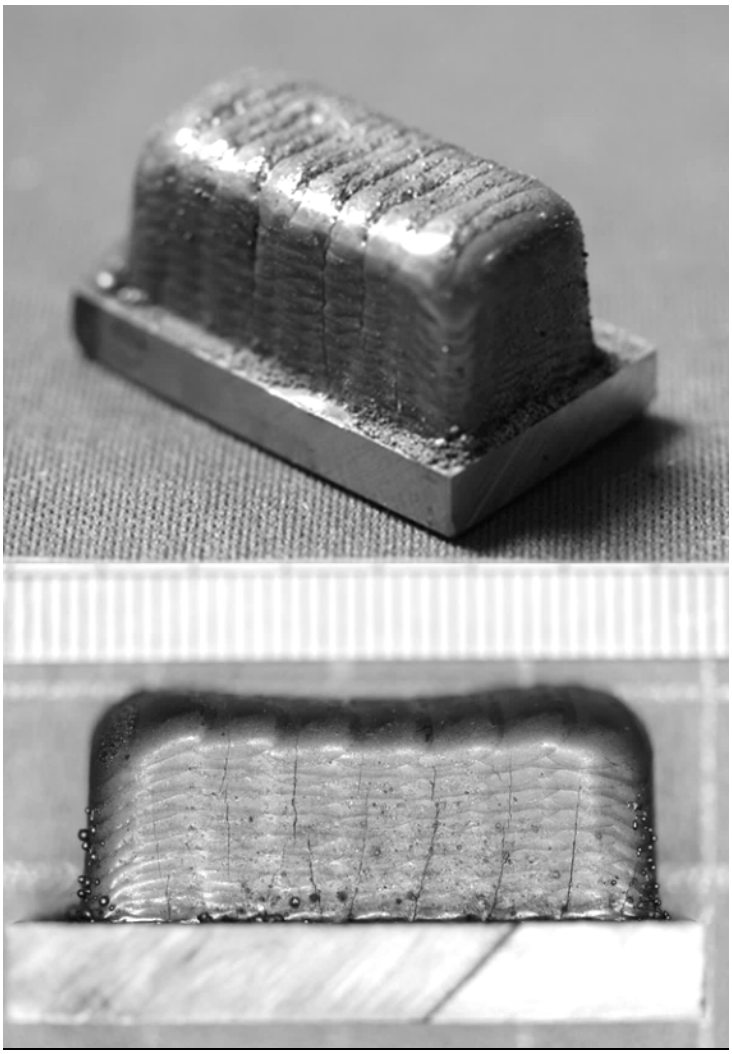

Figure 4-60 - Blocks deposited using "optimised" DOE parameters

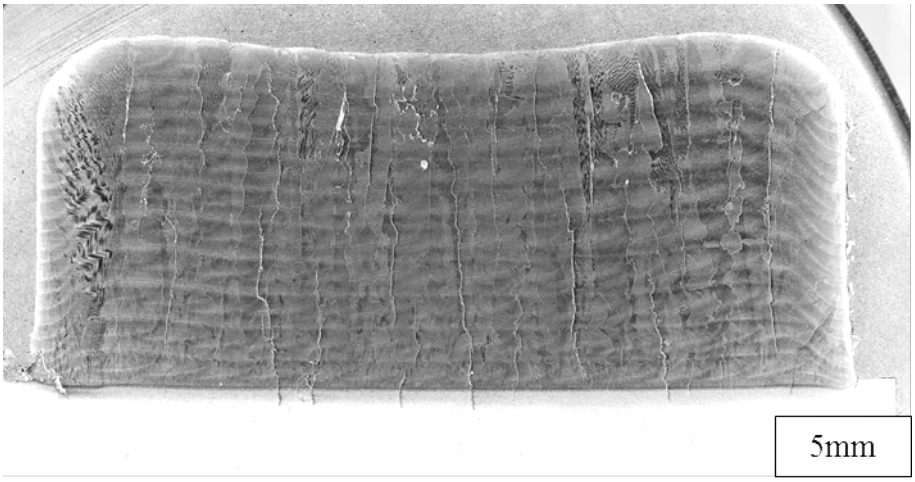

Figure 4-61 - macrograph of DOE optimised block, viewed along the X axis

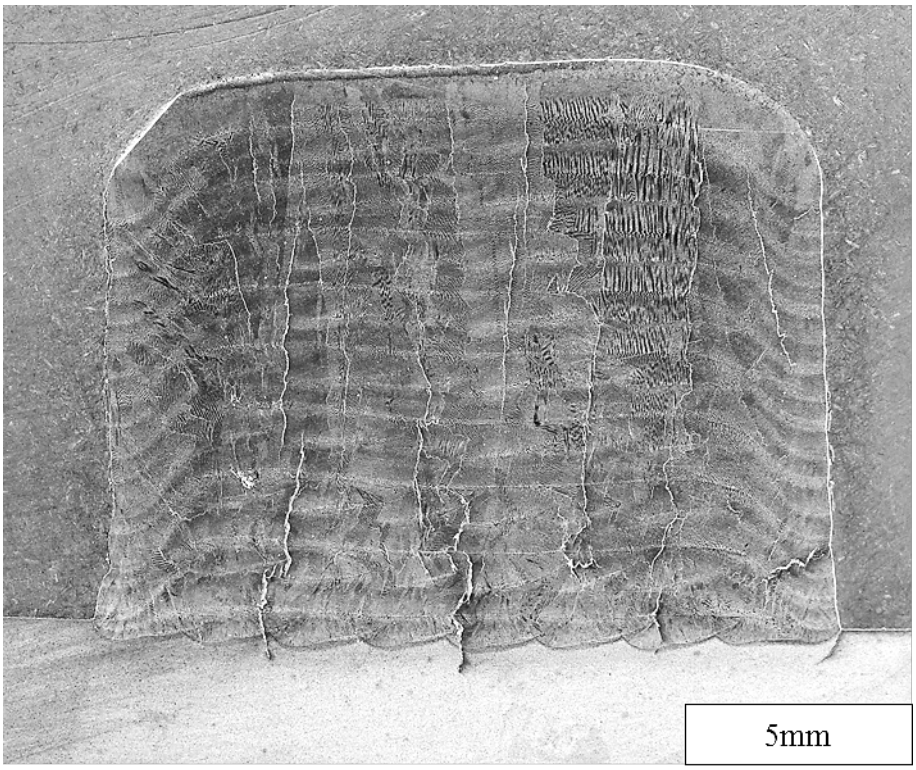

Figure 4-62 - macrograph of DOE optimised block, viewed along the Y axis

Crack density measurements were recorded from the transversely sectioned block, using the procedure described in section 3.3.3. Comparison of the DOE optimised block crack density with the 30 blocks produced for the DOE experiment showed that the crack density was 15% lower than the next lowest crack measurement (Table 4-20, Figure 4-63).

Table 4-20 - Graph illustrating crack density results for all blocks in the DOE test matrix, as well as for the DOE "optimised" block

Run	Laser power (W)	Laser spot diameter (mm)	Scanning speed (mm/s)	Dilution	Energy density (J/mm2)	crack density (µm/µm^2)
1	600	1.75	15	1.5	22.86	0.001388637
2	400	1.38	11.88	1.75	24.40	0.001700638
3	600	1.75	8.75	1.5	39.18	0.001454782
4	400	1.38	5.63	1.25	51.48	0.001533545
5	600	1	8.75	1.5	68.57	0.001481374
6	600	2.5	8.75	1.5	27.43	0.001248434
7	800	2.13	5.63	1.25	66.71	0.001297756
8	800	2.13	11.88	1.75	31.62	0.001296582
9	800	1.38	5.63	1.25	102.97	0.001260089
10	600	1.75	8.75	1.5	39.18	0.001360578
11	400	2.13	11.88	1.75	15.81	0.001524705
12	400	2.13	5.63	1.75	33.36	0.001301179
13	400	2.13	5.63	1.25	33.36	0.001367651
14	600	1.75	8.75	1.5	39.18	0.001400425
15	1000	1.75	8.75	1.5	65.31	0.001188662
16	400	1.38	5.63	1.75	51.48	0.001369582
17	400	2.13	11.88	1.25	15.81	0.001591938
18	800	2.13	11.88	1.25	31.62	0.001488507
19	800	1.38	5.63	1.75	102.97	0.001481374
20	800	2.13	5.63	1.75	66.71	0.001285128
21	600	1.75	8.75	1.5	39.18	0.001423929
22	200	1.75	8.75	1.5	13.06	0.00219571
23	600	1.75	8.75	1	39.18	0.001481374
24	600	1.75	8.75	2	39.18	0.00144701
25	600	1.75	8.75	1.5	39.18	0.001536952
26	800	1.38	11.88	1.75	48.80	0.001362048
27	800	1.38	11.88	1.25	48.80	0.001523107
28	600	1.75	2.5	1.5	137.14	0.001421065
29	600	1.75	8.75	1.5	39.18	0.001539024
30	400	1.38	11.88	1.25	24.40	0.001748725
DOE Opt	**1000**	**3**	**5**	**1.5**	**66.67**	**0.001006865**

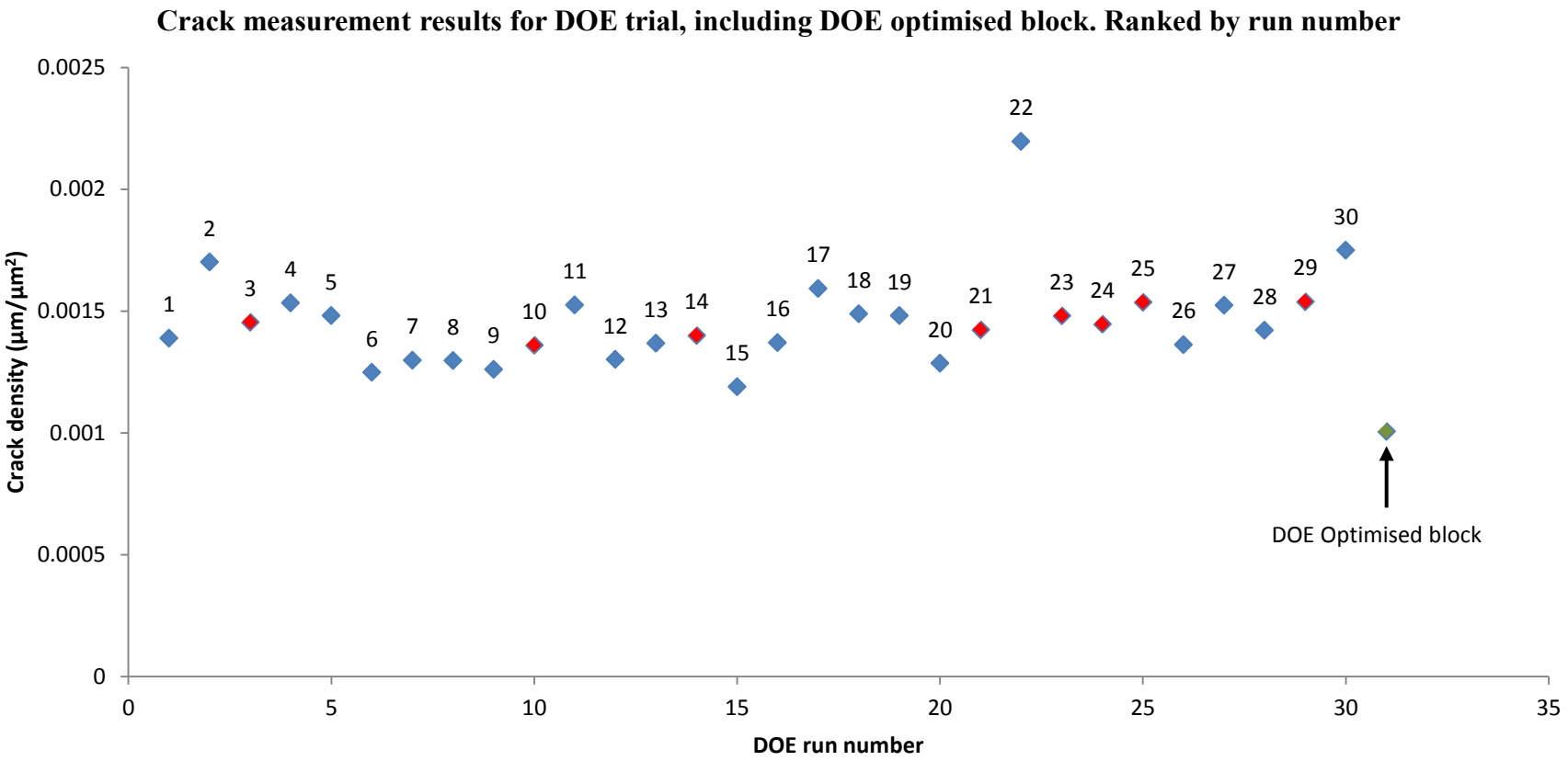

Figure 4-63 - Graph illustrating crack density measurements for DOE trials, including the measurements taken for the DOE optimised block. Red points indicate DOE centre point repetitions, Green point indicates result for DOE optimised block

4.3.5.1.1 Hardness measurements For DOE optimised block

Measurements were recorded in along the centreline of the deposit cross section, going from the bottom of the substrate to the top layer (cap) of the deposit. Measurements were taken at shorter intervals close to the fusion zone (Figure 4-64)

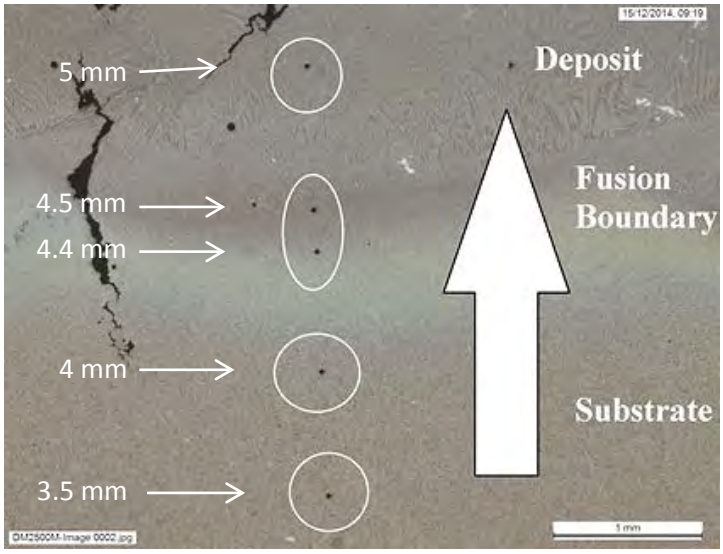

Figure 4-64 - Hardness measurement positions relative to fusion zone

Hardness measurements taken from the substrate, some distance from the HAZ show that the base hardness of the HIP consolidated CM247LC material is 430 H_v. As the measurements get closer to the fusion boundary with the deposit, the hardness is observed to increase sharply to an observed maximum of 510 H_v at a distance 0.5mm from the fusion boundary (4.4mm). At a position immediately below (4.5mm) and above (5mm) the fusion boundary, the hardness is measured to be 465 H_v, dropping down to 371 H_v at the deposit cap.

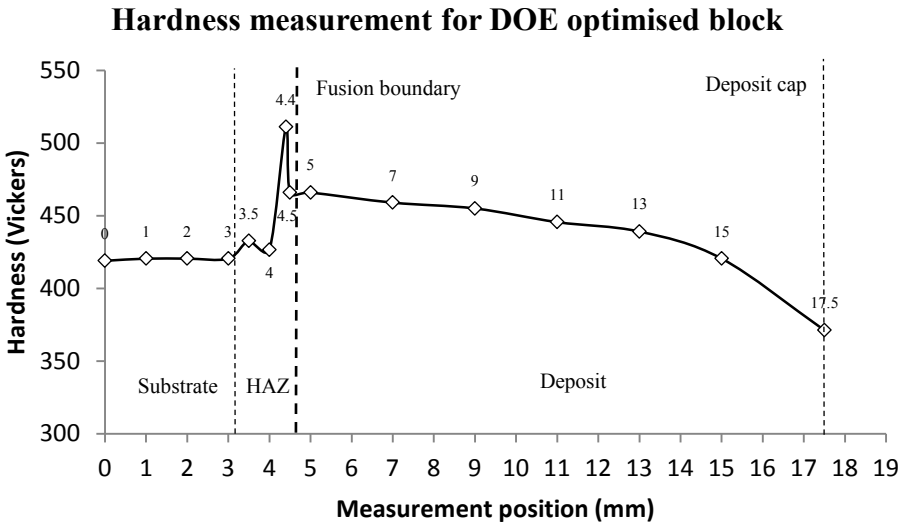

Figure 4-65 - Vickers hardness measurement locations for DOE optimised block, measured from transverse section, vertically through the block.

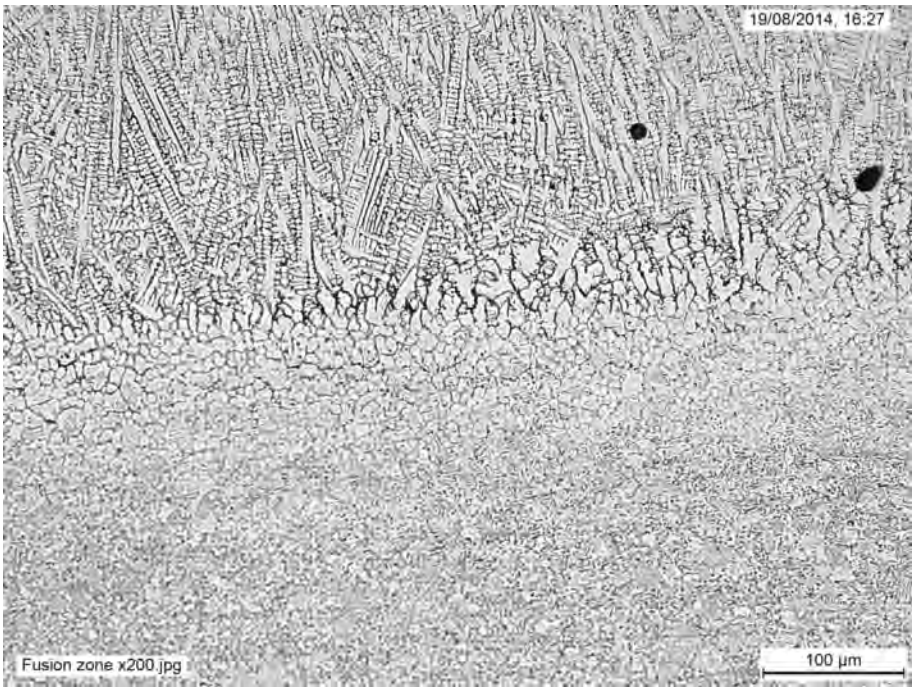

Figure 4-66 - 200x optical micrograph of DOE optimised block deposit fusion zone, showing the transition between microstructures

4.4 Discussion

4.4.1 Powder and substrate analysis

Although the nominal size range of the as received powder was stated as 0-150µm, particle size analysis revealed the presence of artefacts up to 280µm in length. This is most likely due to the formation of elongated particles during the atomisation process, which slipped lengthways through the mesh during sieving. These long particles are generally made up from two or more particles that have welded together during atomisation, or may be formed from liquid metal that has streaked on the sidewall of the atomisation chamber, forming needle like artefacts.

These elongated powder particles are generally detrimental to the flow characteristics of the powder, and can lead to melt pool instability, uneven powder flow to the nozzle, and poor powder focus. Optimisation of the spray conditions used for atomisation can reduce the presence of these artefacts, while secondary processing such as mechanical milling can also be used to improve the powder morphology [2,24,25].

Particles above nominal size range for the 20-40µm and 40-100µm powder samples were also observed, which is indicated by a skewing of the measurement to higher particle sizes (Figure 4-7). This is also observed in SEM and optical microscopy of the powder cross sections (Figure 4-11, Figure 4-12), which also reveals the presence of fused particles.

It was noted that the larger particles had a sharply defined cellular morphology (Figure 4-9, Figure 4-67), which arises during constitutional super-cooling of the molten droplets. This occurs when a solid freezes with a composition that is different to that of the liquid. At the solid-liquid interface, the liquid contains an excess concentration of solute, which creates a region ahead of the solidification front that has a temperature lower than the freezing point [26].

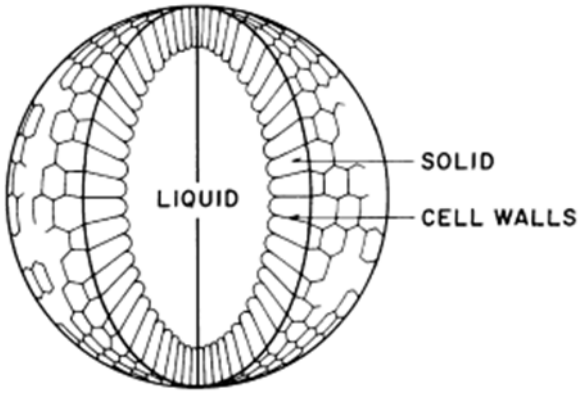

Figure 4-67 - cellular structure formation during constitutional super-cooling [26]

QBSD SEM analysis of the cross sectioned powder particles appears to show the microstructure to be cellular rather than dendritic (Figure 4-13), with what appears to be carbide precipitation along the cellular boundaries. QBSD SEM images of the powder particle surface (Figure 4-10) reveals the presence of nano-scale particles on the powder surface, with particles located primarily at the surface connected cellular boundaries. Although these particles were not conclusively identified, they are thought to be MC type carbides, which are known to form both within the bulk of the powder particles and also on the surface [22,27-30]. Another possibility is that these precipitates may have formed due to oxidation during atomisation, which may lead to the formation of deleterious prior particle boundary (PPB) phases [31] within the HIP'd material.

During deposition, the majority of these powder particles will be melted, and so the micro-segregation observed within the powder particles is expected to have little effect on the microstructure of the deposit bulk. However, examination of the upper layer of deposited blocks has shown where powder particles that have entered the melt pool, but have not fully melted. These solid particles act as nucleation points for crystallisation, with dendrites growing out radially from them until they impinge on adjacent grain boundaries (Figure 4-68). It is unclear what effect this would have on the mechanical properties of a deposited part, as subsequent layers would essentially re-melt this microstructural artefact.

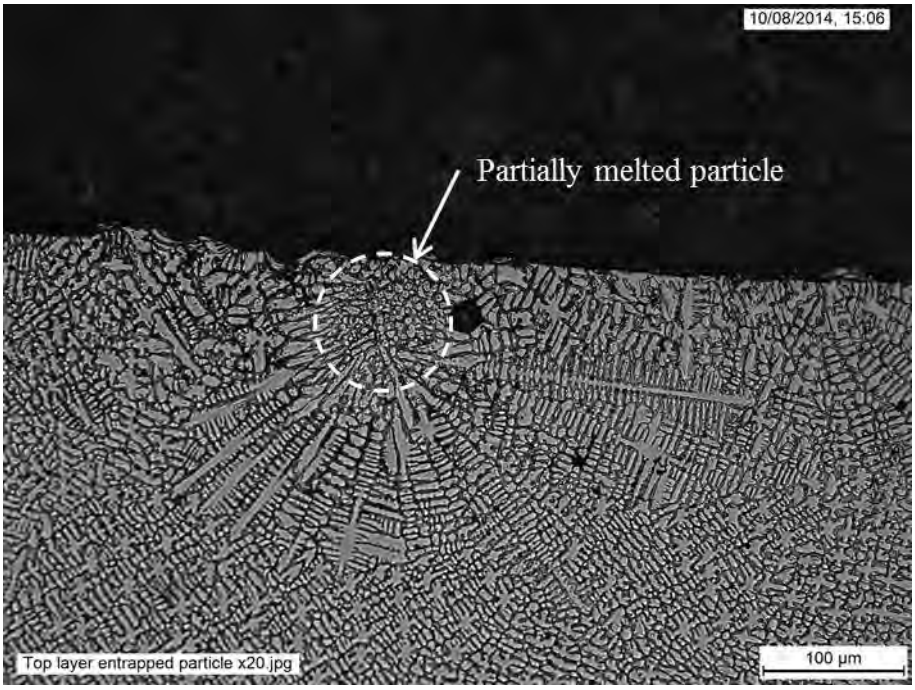

Figure 4-68 - Partially melted powder particle that has formed a nucleation site within the cooling melt pool

SEM examination of the γ' distribution within the substrate material, showed what appears to be coalescence of γ' particles, into bands measuring approximately 10µm long and 1µm wide (Figure 4-16). There is also evidence of a retained powder microstructure in some regions of the HIP'd material, in which circular patterns approximately 20-40µm in diameter are evident (Figure 4-15), with the majority of the coalesced bands of γ' being located within or close to the retained powder particle. This is believed to be a remnant of the original cellular microstructure of the larger particles.

During atomisation, elemental segregation occurs within the powder, causing elements such as titanium and carbon to become segregated to the cellular boundaries, making them preferential locations for the precipitation of γ' and carbides. During the HIP process, the γ' grows and coalesces under the high temperature and Isostatic pressure [22], in a mechanism similar to rafting. Rafting of γ' is commonly observed in turbine blades that have been subjected to long exposures at high temperatures and stresses, with the γ' aligning perpendicular to a tensile stress or parallel to a compressive stress. However, the time,

temperature and stress directions in HIP are much different, and so true rafting is not observed.

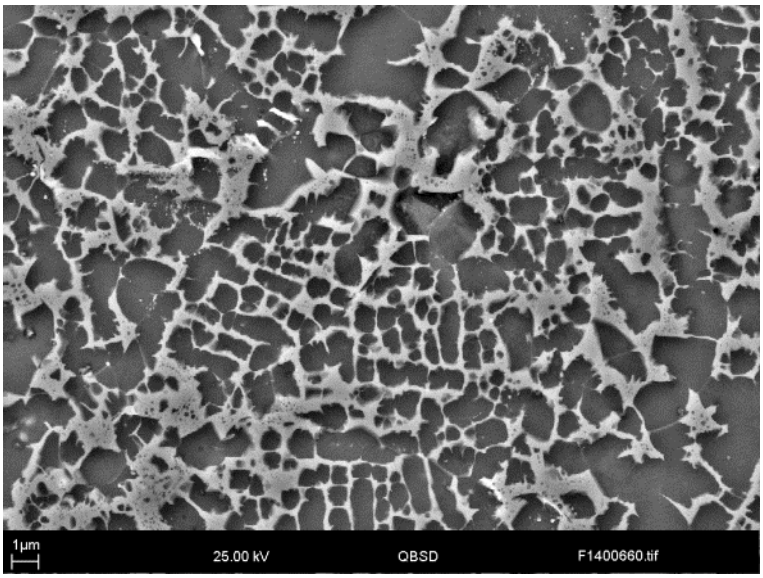

Figure 4- 69 - QBSD SEM micrograph of HIP'd substrate.

While the size and shape of the γ grains and prior particles were not resolvable by optical microscopy or SEM, examination of the HAZ near to a deposit fusion boundary shows the inter-particle boundary (IPB) quite clearly (Figure 4-66). This would suggest that the HIP consolidated substrate material possesses a fine equiaxed grain structure, with the size of the γ grains being approximately 5-20µm in diameter. These fine equiaxed grains are thought to be from the solidification microstructure of the powder, as they are of comparable size. The HIP temperature of 1160°C was below the γ' solvus temperature (determined through DSC of the CM247LC powder - Figure 4-14), meaning that the γ' did not go into solution during HIP, preventing the γ grains from coarsening and retaining the fine equiaxed microstructure [32].

4.4.2 Process parameter development trials

As previously stated in section 4.2.3, it was necessary to establish processing rules that could be applied to all DOE runs, in order to limit the amount of uncontrolled variation between DOE runs. Although the DOE states the specific laser power, scanning speed, laser spot size and deposit shape that each run must be conducted at, it did not define other critical parameters such as track overlap, powder feed rate and Z increment and so experiments were conducted that established rules for how these would be calculated.

4.4.2.1 Dilution calibration

Single tracks were deposited using the DOE defined laser power, scanning speed and spot size, using varying powder feed rates (Figure 4-17 - Figure 4-19), from which the dilution was measured using optical microscopy of the track cross sections.

It should be noted that during this work, carrier gas flow rate and nozzle shielding gas flow rate remained fixed at 6 l/min and 20 l/min respectively. Work done by Pinkerton et al [12] has shown that these gas flow rates can have some small effect on the size and shape of the deposit, but for the purposes of this work it was decided that it would not be necessary to include these variables in the test matrix.

Optical microscopy dilution measurements showed that as powder feed rate increases, the deposit dilution changes in an approximately linear fashion, with deposit volume (A_c) increasing and melt pool volume (A_m) decreasing. This is a fairly common observation for the laser deposition process, and is in agreement with work published by other authors [12-14].

An increase in A_c is directly related to the rate at which powder enters and is assimilated into the melt pool, whereas the size and shape of the melt pool is governed more by the thermodynamics of the process.

For a fixed laser power, spot size and scanning speed:

- low powder feed rates require less heat energy to cause full melting and assimilation, meaning there is more energy reaching the substrate and the melt pool can reach a higher temperature, resulting in a broader and deeper pool [7,8,10,33].
- High powder feed rates have the effect of shielding the substrate from the laser, resulting in a lower energy input into the melt pool [24,33,35]. Introducing more material into the melt pool also requires more energy to cause full melting, further reducing the amount of energy available [8].

This effect was observed during the deposition of single tracks, in which it was noted that as powder feed rate increased, A_c increased, A_m decreased, and track width (W) decreased, resulting in a dilution measurement that scaled linearly with powder feed rate. This relationship cannot be extrapolated indefinitely however, as there is a limit to the amount of powder the melt pool can capture in a given amount of time, and excessive powder feed rates can result in deposits with high wetting angles, which can result in lack of fusion defects due to the undercut being shielded from the laser [36].

One observation for the single track deposition, was that higher powder feed rates can change the shape of the fusion boundary of the melt pool. For some tracks, the fusion boundary has a smooth hemispherical shape, but an increase in the powder feed rate causes the fusion boundary to take on a “W” shape.

This is a direct result of the higher powder feed rate shielding the substrate from the laser. When the powder stream comes to a focus, the particle density across the focal spot has a near bell shaped profile. When this profile gets in the way of the laser beam, it absorbs more energy from the centre of the beam, which is the region of highest intensity. This results in a less intense heating effect in the centre of the melt pool, and shallower penetration. This effect was not observed for all samples, suggesting that it is also influenced by the laser power, scanning speed and spot size to some extent.

Although a fairly linear relationship can be established from two measurement points using this method, greater accuracy and repeatability can be achieved by depositing a greater number of tracks at different powder feed rates.

4.4.2.2 Track overlap spacing

The deposition of overlapping samples showed that different overlap percentages have an impact not only on the surface flatness and regularity of the coating, but also affect the degree of cracking that is observed [37].

From the analysis of samples produced in section 4.2.3.2, it was found that for this particular material, a higher percentage of overlap (>30%) is detrimental for two reasons:

1) Uneven layer thickness due to deposit pile-up
2) Increased formation of cracks both within the deposit and within the HAZ.

4.4.2.2.1 Effect of track spacing on deposit pile-up in overlap trials

Deposit pile up occurs when the track spacing is too low. This has the effect of creating an uneven layer thickness, as the tracks begin to pile up on top of one another, meaning the clad layer will be thicker at the end than at the start. Depending on the application, this may not be a problem, for example, if the process was being used to clad a large area with a single layer (e.g. repairing a worn shaft), the layer would increase in thickness with each pass until it reaches a steady state, and then it would not get any thicker. However, if the process is being used for additive manufacture or repair, surface regularity it quite important.

Uneven layer thickness is detrimental to the quality of the process, because as subsequent layers are added, the differences in thickness become more pronounced and the process becomes unstable as the powder focus and laser spot move across the uneven deposit surface [38]. Scanning a laser beam across an uneven surface has the effect of making the laser spot

smaller or larger, which increases and decreases the energy density respectively, leading to variations in track width and penetration. As subsequent layers are added, the effect becomes more pronounced and the quality of the component rapidly declines.

Similarly, using too small an overlap may also lead to poor surface regularity, as the overlap regions form peaks and troughs that can form lack of fusion defects under certain conditions.

At overlap ratios greater than 30%, deposit pile up was observed for both dilution conditions. Below 30% overlap spacing there was very little improvement in deposit flatness, as the tracks were sufficiently far apart that they had relatively little interaction. This agrees well with other published work on laser cladding, with a 1/3rd track overlap spacing being quite commonly used [6,8,37].

Zhang et al [39] developed a relationship for optimal track spacing condition, which relates the width and height of a hemispherical track to the track spacing, in order to produce a track of the best surface flatness and regularity. This may be a useful approach for producing smooth layers, such as for repair or coating applications, but as mentioned in the introduction to this chapter, it is the presence of cracks that is the limiting factor when depositing CM247LC, and the condition that produces the best surface finish would not necessarily yield the lowest cracking response.

4.4.2.2.2 Effect of track overlap on crack formation in overlap trials

For this particular alloy, a larger overlap between tracks was observed to produce a greater degree of cracking than for those that were spaced further apart, as illustrated in Figure 4-22.

Analysis of overlap deposit micrographs showed that cracks are generally found within the overlap region, penetrating downwards some distance into the HAZ of the substrate and upwards into the uppermost track, as illustrated in Figure 4-70.

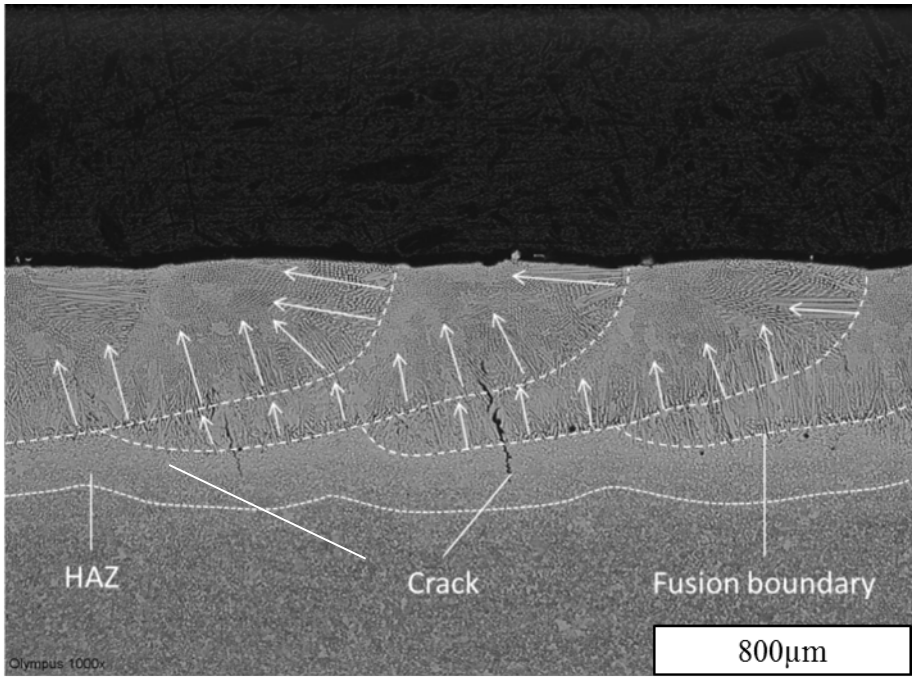

Figure 4-70 - 50x optical micrograph of sample PM-EngD-041 deposited using 50% overlap condition

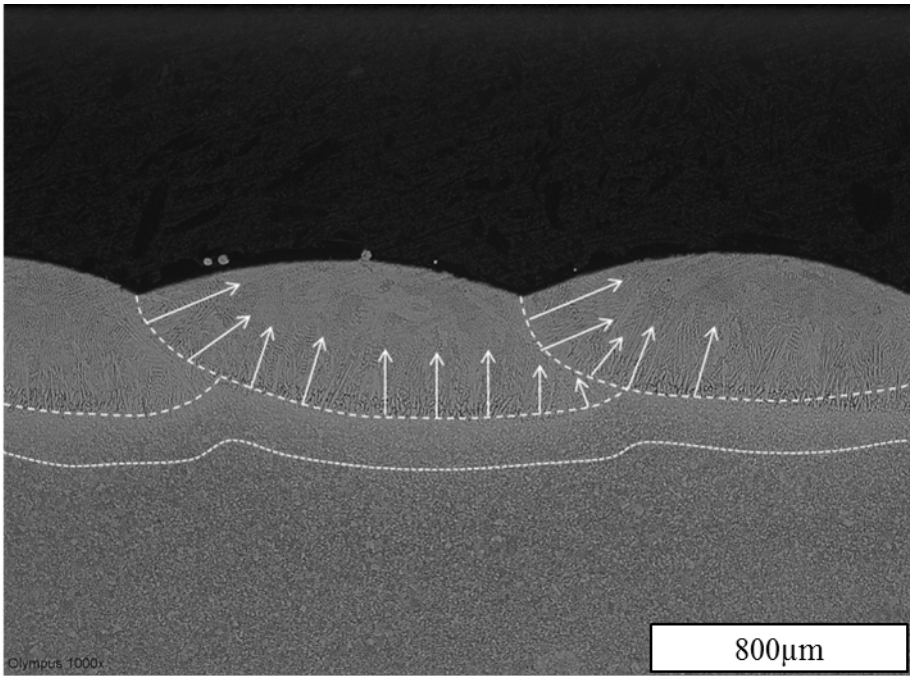

Figure 4-71 - 50x optical micrograph of sample PM-EngD-045, deposited using 20% overlap condition.

This localisation of cracking may be due to a combination of:

1. grain boundary liquation due to re-melting of previous tracks
2. Undesirable alignment of deposit microstructure with localised solidification stresses
3. Formation of annealed bands within the HAZ of the substrate

During deposition of overlapping tracks, a degree of re-melting of the adjacent tracks occurs. For materials that exhibit a relatively broad melting temperature range, such as CM247LC (Figure 4-14), this re-melting on the underlying track can lead to the liquation of low melting point phases at the solidification boundaries and inter-dendritic regions of the previously deposited material, creating a liquid film that separates under an applied stress to create a crack [40].

If we consider a two-track condition, where one track is overlapped by another, the first deposited track has already solidified, with a dendritic microstructure normal to the fusion boundary, approximately aligned along the direction of maximum heat flow. When the second track is deposited, the overlap region will re-melt a portion of the first track, which will then re-solidify with a crystallographic orientation that is influenced by both the direction of heat flow and the crystallographic orientation of the underlying material [41,42], which may lead to epitaxial dendrite growth across the fusion boundary. This is illustrated in Figure 4-70 and Figure 4-71, in which the dendrite growth directions have been highlighted with arrows.

Within the overlapping region in Figure 4-70, there is a point that is both normal to the fusion boundary and also aligned to the dendrites of the underlying track. This region is more likely to allow epitaxial growth of the dendrite of the underlying layer across the fusion boundary.

As discussed in section 2.4.5.3, during solidification of the melt pool, tensile stresses are created in the surface of the deposit due to the high thermal gradients between the melt pool and the surrounding material, as well as the contraction of the melt during solidification (Section 2.4.5.3).

These tensile stresses are perpendicular to the dendrite growth direction, increasing the chance of cracks forming along the elongated liquated dendrite boundaries.

The reduction in cracking for tracks that have a lower overlap can be explained by the misorientation of the dendrite growth directions between the different areas of the track. Figure 4-71 illustrates how smaller overlaps are observed to increase the misorientation angle of the dendrites, reducing the chance of them growing epitaxially into the overlying track as there is no easy propagation pathway.

SEM analysis of the cracks within the HAZ of the substrate shows that there is no evidence of any re-solidified material along the crack edge, and the shape of the crack suggests that cracking occurred in the solid state, most likely along the prior particle boundaries. Other authors have reported on the liquation of γ' and MC carbides within the grain boundaries of the HAZ during welding [43-45], but there was no microstructural evidence that this was the case for this material. Also, much of the reported work on HAZ cracking was conducted on cast material, rather than HIP'd material. Liquation cracking in cast material is far more likely, due to the greater elemental segregation that occurs upon solidification leading to grain boundary phases of suppressed melting temperature. HIP'd material is far more chemically homogenous; meaning liquation cracking is less likely to occur.

However, SEM analysis of CM247LC powder did reveal the presence of microsegregation within the particles (Figure 4-13) which led to the formation of an intercellular carbide phase. Small discrete particles were also observed on the surface of powder particles (Figure 4-10), which may have formed as a result of segregation of solutes elements to the free surface during particle solidification [26,46]. HIP consolidation of these powders may have led to the formation of Prior Particle Boundary (PPB) regions, which would reduce the strength of the material in the HAZ and allow cracks to form.

Another possible explanation for the formation of the HAZ cracks, is a result of the formation of annealed bands that form within the HAZ of the substrate, directly under the overlap region [8] as shown in Figure 4-72. This would agree somewhat with the location of cracks observed in the overlap trials, but the hardness measurement results obtained for the HAZ region (Figure 4-23) were inconclusive. The hardness of the CM247LC substrate, measured away from the HAZ, is found to be 430 Hv, with regions of the HAZ tending to vary between 299 and 352 Hv, suggesting that annealing is occurring, but without any observable trend. Better results may have been obtained from a sample with a smaller overlap percentage, as the overlap regions would be spaced further apart and the differences in hardness may be more pronounced.

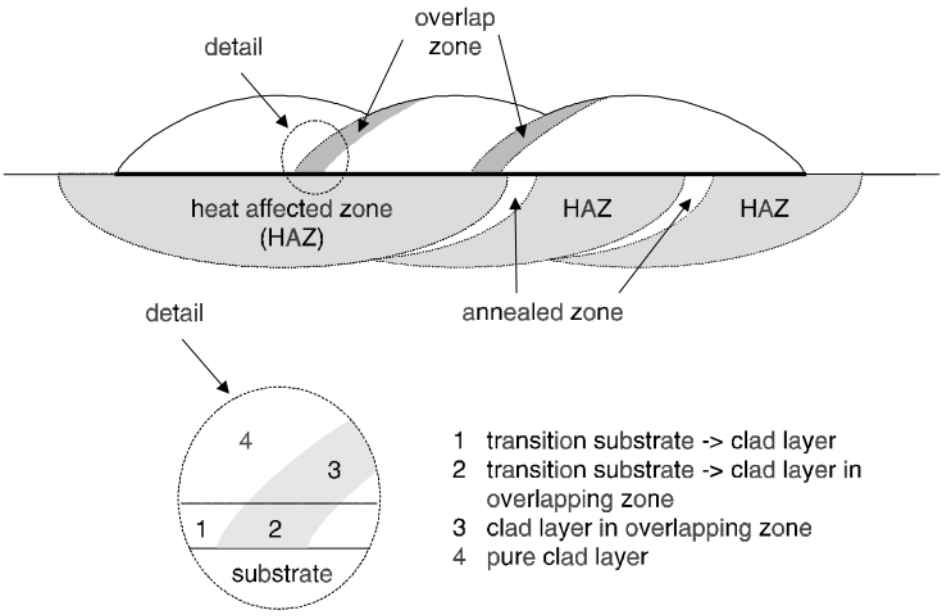

Figure 4-72 - Schematic illustration of overlapping tracks (Schneider 1998)

4.4.2.3 Z-increment condition

Similarly to the trials investing overlap condition, blocks were deposited using varying Z-increment values in order to establish a processing rule that could be applied across all DOE runs. The Z-increment values were calculated as a percentage of the measured layer thickness of a single deposited layer, which was deposited using the 30% overlap condition established in section 4.2.3.2. Blocks were deposited using Z increment values between 70% and 100% of the measured layer thickness. Values greater than 100% were not examined, as the material would not build up as fast as the nozzle pulls away.

Cross sections of these blocks were analysed using optical microscopy, which showed that an 85% Z-increment produced blocks that produced the least difference between the calculated build height and the actual build height (lowest deviation).

The reason for this is that during deposition, as the block gets taller, the thermal conduction pathway into the substrate becomes longer, leading to an accumulation of heat in the deposit. If the laser power, scanning speed and laser spot size remain constant during deposition, this leads to the formation of broader and deeper melt pools (Am increases) as the laser does not have to work as hard to melt the material. As the volume of the melt pool is increasing, but the mass of the powder being delivered is remaining constant, the deposits will become flatter, and the vertical build rate decreases, causing the nozzle to pull away faster than the layers build up.

This effect is more noticeable when depositing thin walls, as the thin deposit wall cannot conduct heat away from the melt pool fast enough, leading to a wall that is wider at the top than at the bottom [47].

If the nozzle is retracting at a fixed rate between deposit layers, this can result in the focal point of the powder drawing away from the melt pool. This leads to loss of powder capture

efficiency by the melt pool, even further reductions in build rate and a rapid deterioration of the deposit quality and surface finish [48].

Modern LMD systems can account for this by means of sophisticated closed loop control mechanisms, which adjust the laser power, scanning speed and laser spot size on the fly to maintain a consistent melt pool temperature and size[18,42,49-54]. However, the equipment used for this work did not have any means of controlling the laser power in this way, requiring an open-loop approach be developed.

By setting the Z increment slightly lower than the build height per layer, the process is effectively throttling the mass of material that is entering the melt pool and controlling its build rate. This prevents the nozzle from pulling away from the surface of the deposit, and by keeping the focal point of the powder below the surface of the deposit the process maintains a relatively consistent nozzle gap, as illustrated in Figure 4-73.

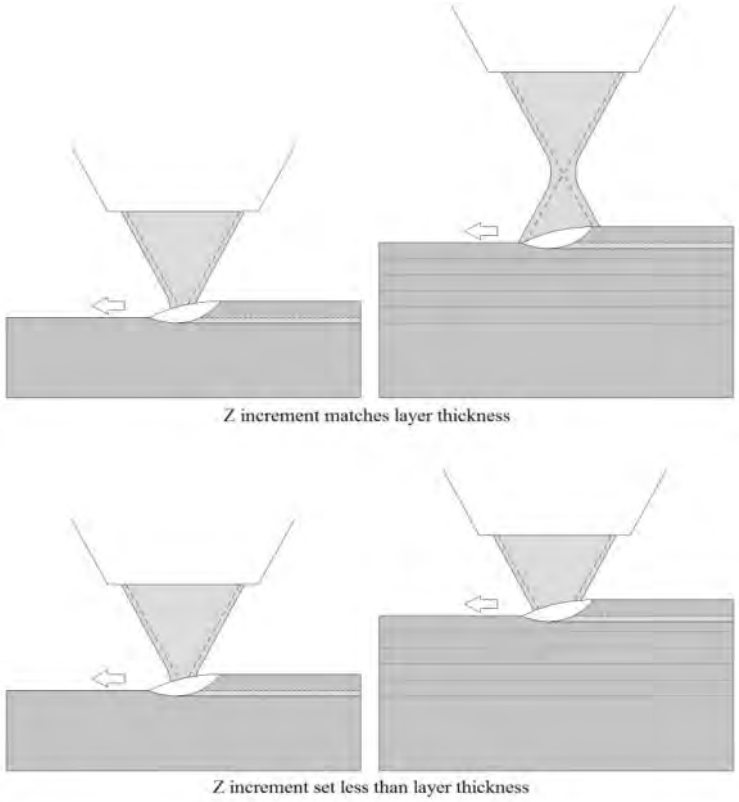

Figure 4-73 - Schematic illustration of the effect of Z increment on nozzle standoff distance.

Application of the 85% Z-increment condition to tracks with dilutions of 1.0 and 1.5 to build blocks 30 layers in height showed that the height of the block after deposition was within 1% of the predicted height (Figure 4-26, Table 4-15). While this method is somewhat crude, it does allow blocks of predictable size and shape to be deposited.

4.4.3 Deposition of test blocks and DOE analysis

As mentioned previously, deposited blocks were sectioned into four equal pieces, transverse to the long axis. Three of the pieces from each block were metallographically mounted, ground and polished to reveal the fine cracks within. Non-overlapping optical micrographs of the deposit cross section at 50x magnification were taken, resulting in approximately 36 images per sample. This resulted in approximately 3240 images being generated from the DOE test blocks.

The crack length and measurement area for each micrograph was manually measured using ImageJ® software, as described in section 3.3.3.1 and a measurement of crack length per unit area calculated for each DOE run. The results were fed back into the DOE software, which applied linear regression methods to determine the interrelationship between the observed crack densities and the process factors used.

General trends were observed for each of the factors (Figure 4-34 - Figure 4-36) and the results were found to have a normal distribution (Figure 4-37). From these results, the DOE software generated a response surface, analysis of which showed that lower crack densities were predicted for blocks that were deposited using:

- High laser powers
- Slow scanning speed
- Large laser spot diameters
- Low dilution

However, the DOE response surface does not indicate a minima value, as the surface is planar and is presumed to extend past the factor limits of the experiment (Figure 4-38). While it was not able to identify a plateau or optimum condition, the response surface was very useful in identify trends in parameter relationships that would help to reduce cracking.

Using the information obtained, a block was deposited using the DOE "optimised" parameters, by which it is meant that the process parameters used lie at the extreme end of the experiment range. This block was deposited using the parameters listed in Table 4-19, using the process rules developed in the previous sections to calculate powder feed rate, track spacing and z-increment.

Crack quantification of the DOE optimised block showed that it contained a crack density approximately 15% lower than the best DOE test block (Figure 4-63), showing that the trend predicted by the response surface does improve the cracking response somewhat. However, the deposited block still contained a large number of cracks, some of which are relatively small and fine scaled, while others are long, surface connected cracks that penetrate through many deposit layers.

4.4.4 Microstructure of deposited blocks and significance to observed cracking

Cross sectioned blocks were metallographically prepared using the methods described in section 3.3 in order to reveal the internal microstructure.

Optical microscopy of the 30 DOE test blocks shows that the microstructure consists of large columnar grains of dendritic composition, which have grown normal to the substrate surface, epitaxially through multiple deposit layers. This is illustrated in Figure 4-40 and Figure 4-41, which shows two blocks (DOE run 22 and 15 respectively), which have been deposited at relatively low heat input (200W) and relatively high heat input (1000W). The large surface connected cracks that are observed in both samples are oriented normal to the substrate

surface, and appear to propagate along the grain boundaries and inter-dendritic pathways, as shown in Figure 4-42).

EDX and QBSD SEM analysis of the solidification boundaries and interdendritic regions showed them to be enriched with W, Hf, Ta, Ti and C (Figure 4-52, Figure 4-53) which are rejected by the dendrites during solidification to create a microstructure of γ/γ' eutectic, primary γ' and cuboidal carbides (Figure 4-49, Figure 4-51). Based on the composition of the region measured using EDX and taking into account the thermal history of the deposit, these are thought to be MC type carbides. The alloying elements Hf, Ti and Ta are known MC type carbide formers, so based on the size, shape and apparent composition of these particles; it would be fair to assume that the observed particles are MC type, as there has not been sufficient time for them to decompose to other stoichiometries.

The γ/γ' eutectic phase that forms during solidification has a lower melting temperature than the γ phase, which means that upon cooling the grain boundaries and dendrites are wetted by a low melting point liquid, decreasing the materials ability to withstand the solidification stresses and resulting in the semi-solid material being pulled apart and forming cracks that propagate along the solidification boundaries. The presence of a low melting point phase was confirmed through DSC analysis of the powder, which showed that the material had a solidification temperature range of 42°C (Figure 4-14) with a liquidus temperature measured to be 1373°C and a solidus temperature measured to be 1331°C.

The evidence of solidification cracking is found in the microstructural and topographical analysis of the deposited blocks. QBSD SEM micrographs of crack edges reveal the presence of a retained eutectic phase along the crack edge (Figure 4-50), while topographical analysis of the crack surfaces shows a dendritic morphology, indicating that the material was not fully solidified when the crack formed (Figure 4-54, Figure 4-55).

Based on this evidence, it is believed that the cracking mechanism at work in laser deposited CM247LC is a solidification cracking, which is exacerbated by the epitaxial growth of dendrites across fusion boundaries that allows the cracks to propagate across deposit layers. Re-melting of previously deposited material would have the effect of melting the low melting point phases first, with the liquated regions penetrating below the solid/liquid interface of the melt pool.

With this interpretation of how the cracks form within the DOE blocks, we can begin to interpret the results of the DOE response surface, which show that high laser power, large laser spot diameter, slow scanning speed and low deposit dilution produce fewer cracks than the other DOE runs.

Although the convention regarding reduction of solidification cracking during welding implies that low heat input is the best approach [55], it was found that in this case the opposite appears to be true, with blocks deposited with higher heat inputs showing the lowest amount of cracking. This observation is in agreement with work conducted by Montazeri [56], which also observed that for nickel superalloys welded with an energy density greater than 25 J/mm^2, although grain boundary liquation was still occurring, cracks were not formed, as the higher energy input pre-heats the material, lowering the cooling rate and the magnitude of the tensile stresses [57-59] that are generated upon solidification and cooling.

4.4.5 Influence of processing parameters on cracking response

4.4.5.1 Effect of laser power and spot size on the cracking response

Work has been reported previously that relates the cracking response of various alloys to the energy density, or specific energy of the process, measured in J/mm^2. This is calculated as a function of laser power, scanning speed and laser spot diameter [60].

$$E = \frac{P}{D.V}$$

From this equation we can see that high energy densities (E = J/mm^2) are achieved by increasing the laser power (P = Watts), and increasing the spot diameter (D = mm) and velocity (V = mm/s). When the specific energy is calculated for each DOE run, and the crack density plotted against it (Figure 4-33), we can see that the low specific energies result in slightly higher crack densities than those for high specific energies, but the relationship is very weak. For example, the deposit with the highest specific energy is DOE run 28, with 137 J/mm2, yet this block contained 13% more cracks than the DOE run 6, which had a specific energy value of just 27.43 J/mm2. This would suggest that there are more factors at play than just specific energy and heat input when it comes to the cracking response.

When we consider the size of the laser spot, and that the DOE response surface indicates that a bigger spot diameter is preferable, then we must consider how the laser spot is affecting the size and shape of the melt pool. For a fixed laser power and scanning speed, a large spot will produce a melt pool that is broad, yet shallow, while a narrow spot diameter will create a melt pool that is narrow and deep (Figure 2-14).

Work conducted by Rush [61] investigated the role of melt pool size during welding, and observed that reductions in solidification cracking occurs at low power when a small melt pool (≈1mm diameter) is used, and at high powers when the melt pool was between 2.5mm and 3mm in diameter, which agrees with the observations of this work. However, work conducted by Dye et al [62] in numerical modelling of the Weldability of superalloys actually suggests that low scanning speeds and large laser powers are *more* likely to increase the solidification cracking response due to the generation of undesirable tensile stress fields transverse to the scanning direction. This is based around the Weldability diagram illustrated in Figure 4-47, which shows the regions predicted to produce solidification cracks.

However this work was based on single track welds onto a room temperature substrate, whereas the stresses that are being generated during multi-directional laser metal deposition are considerably more complex and difficult to predict.

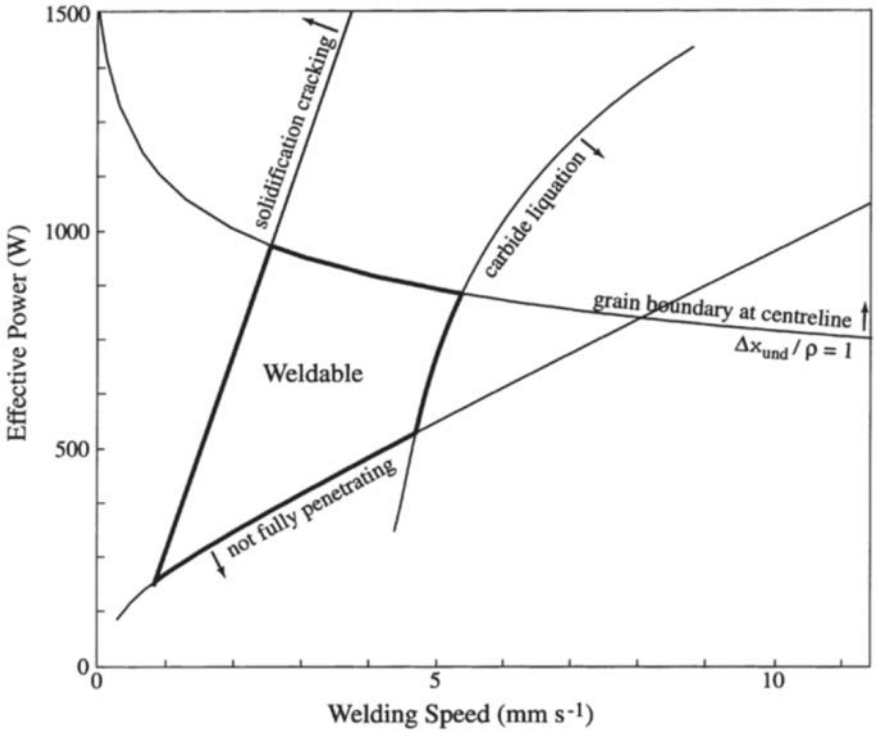

Figure 4-74 – Weldability map illustrating the weldable regime formed by excluding regions where 1) full penetration of the weld bead does not occur 2) A centreline grain boundary is predicted 3) Liquation occurs around carbides in the heat affected zone 4) solidification cracking is predicted [0]

4.4.5.2 Effect of scanning speed on substrate pre-heating

As the laser moves along its toolpath, thermal conduction of heat from the fusion zone increases the temperature of the material ahead of the laser, lowering the temperature difference between the melt pool and the surrounding substrate. This has the effect of reducing the thermal stresses that are generated during solidification, and reducing the driving force for crack formation [63-65]. By using a slow scanning speed, there is more laser power being delivered per unit line length, and thermal conduction from the melt pool allows the surrounding material to reach a higher temperature. Using a fast scanning speed reduces the interaction time between the laser and the substrate, and decreases the amount of time available for thermal conduction.

Liquation cracks form due to non-equilibrium heating conditions, in which secondary phases at the solidification boundaries, such as MC carbides and γ/γ' eutectic, dissolve at a lower temperature than the matrix, wetting the grain boundaries of the material below the fusion zone, and allowing cracks form under an applied stress [66,67].

Fast heating rates have been shown to increase this constitutional liquation effect, as the secondary phases melt below the solidus temperature of the bulk, while slower heating rates allow the bulk and the secondary phases to melt under equilibrium conditions, reducing the wetting of grain boundaries [68,69]. By using a combination of high laser power, large spot size and slow scanning speed, this is helping to reduce the localised heating rate surrounding the fusion zone.

4.4.5.3 Effect of scanning speed on melt pool shape

Slow scanning speeds result in circular melt pools, which are less prone to the formation of deposit centreline cracks. Centreline cracks are a common defect observed in welds, and may form as a result of excessive power and processing speed, resulting in the formation of a teardrop shaped melt pool [70,71]. As the melt pool begins to solidify, the dendrites grow inwards from the tapered edges of the receding side of the melt pool, where they impinge along the centreline forming a continuous grain boundary [72]. Segregation of alloying elements during solidification leads to the formation of a solute enriched region along the centre, which is not sufficiently strong to withstand the tensile stresses being generated transverse to the deposit during cooling, leading to the formation of centreline crack. Welding literature suggests that centreline cracking may be exacerbated by heavy restraints, excessive penetration, insufficient bead size and contamination of the weld [73,74].

This would agree with the work conducted, which showed that slow scanning speeds produced less cracking, but without a means to monitor the shape of the melt pool it was not possible to see what effect the speed had. Generally, excessive scanning speeds can be visually identified from the shape of the surface of the deposited tracks, with chevron patterns indicating that the melt pool have become elongated due to inappropriate speeds. This can also have the effect of creating an undercut, where the liquid in the melt pool is drawn towards the centre, so that upon solidification the edge of the melt track is below the surface of the substrate. However, none of these effects were observed for any of the deposits produced as part of this work.

4.4.5.4 Effect of deposit shape and dilution on cracking response

High laser power, large spot size, slow scanning speed and low dilution produces tracks that can be quite large, meaning fewer of them are required to fill a given volume. Fewer tracks means there are fewer track overlaps, fewer layers and fewer opportunities for cracks to form. From the work conducted investigating the track overlap conditions, it was observed that cracks had a higher tendency to form in the region where two tracks overlap. By producing tracks that are broad and tall, the process is simply reducing the number of these interactions.

Taking for example DOE run 22, which exhibited by far the highest crack density of all the DOE blocks. This run was produced using a laser power of 200W, with a track offset of 0.5mm and a Z increment of 0.14mm. This means that in order to build a block measuring 30x15x10mm, approximately 32142 mm of deposit length is required over 72 individual layers. Compare this to the DOE optimised block, which was deposited at 1000W with a track offset of 1.8mm and a Z increment of 0.4mm, which would only require approximately 6750mm of deposit length over 25 layers to build a block of equivalent size. DOE block 22 has twice the crack density and nearly 5 times the total length of deposit.

Low dilution deposits showed a reduction in cracks, which may be due to two factors.

1) The low dilution results in less re-melting of the underlying layers, meaning less opportunity for the liquation of previously solidified grain boundaries.

2) Low dilution results in large Ac values, meaning the average deposit layer thickness can be larger, resulting in fewer layers required to fill a volume. Fewer layers mean fewer opportunities for cracks to form.

4.5 Conclusions

In this chapter, a DOE approach was used to create an experiment matrix for the deposition of CM247LC blocks, so that the influence of various key processing variables on the cracking response could be investigated and better understood. An experiment matrix was constructed using the DOE software, for which 30 blocks were deposited at different laser powers, scanning speeds, laser spot diameters and dilution ratios.

Through the use of the methodology outlined in section 4.2.3, it was possible to establish processing rules that produced blocks of equivalent shape, size and exterior quality, so that the relationship between the laser power, scanning speed, laser spot diameter and deposit dilution could be examined with the minimum degree of variation, that may have influenced the cracking response and the statistical scatter of the results.

The method used to determine the mass flow rate required to produce a specific dilution worked relatively well, although more accurate results could have achieved if a greater number of tracks were deposited for each condition, however, the shortage of substrate material required that the scale of this trial be limited.

Track overlap trials showed that CM247LC cracks, even when depositing a single layer of overlapping tracks, with the cracks forming mainly in, or near to, the overlap regions of the deposit. This cracking effect was reduced when smaller overlaps were used, as it created a condition where epitaxial growth between adjacent tracks was difficult, reducing the length of the propagation pathways through which the cracks could travel.

All blocks that were deposited as part of the DOE trial contained a large number of cracks of various shapes and sizes. Large surface connected cracks were observed in all deposits, which travel nearly the full height of the deposit, as well as micro-cracks that form within the interdendritic regions and solidification boundaries, as well as within the HAZ region of the substrate. SEM analysis of the cracks located within the deposit revealed that they form

during solidification, due to the presence of low melting point γ/γ' eutectic phases that formed from the terminal liquid due to elemental segregation.

These low melting point phases were found to be rich in Hf, Ta, W, C, Al and Ti, which contributed to the formation of cuboidal MC type carbides and γ/γ' eutectic phase. During melt pool solidification, dendrite growth partitions these elements into the liquid, which creates a eutectic pools and liquid films along the interdenritic regions and grain boundaries. Thermal stresses generated during deposition act to pull these apart, forming cracks that travel very easily along the long, straight dendrites. This type of cracking is characteristic of materials with broad melting temperature ranges.

Crack quantification was conducted manually using optical micrographs, and by this method a measurement of crack length per unit area was determined for each DOE test block. These results were interpreted by the DOE software, and a response surface produced that showed that cracking is reduced when a high laser power, slow scanning speed, large laser spot diameter and low deposit dilution are used. Laser power and scanning speed produced the strongest response, followed by deposit dilution and laser spot diameter.

The lower cracking response for these conditions are believed to be due to the high heat input pre-heating the surrounding material and lowering the thermal mismatch, which would result in lower solidification stresses and less driving force for crack formation and growth. However, the lower cracking response may also be a result of fewer tracks being required to make up a given volume.

Cracking within the HAZ is believed to be due to incipient liquation melting along the prior particle boundaries and intercellular regions of the powder, which act to weaken the material to a point where it cannot withstand the stresses being generated within the material.

4.6 Chapter 4 - List of figures

4.7 Chapter 4 - List of tables

4.8 Chapter 4 - References

1. Tillack, D.J., Welding superalloys for aerospace applications. WELDING JOURNAL-NEW YORK-, 2007. 86(1): p. 28.

2. Carroll, P., et al., The effect of powder recycling in direct metal laser deposition on powder and manufactured part characteristics. 2006.

3. Bodhmage, A., Correlation between physical properties and flowability indicators for fine powders. 2006, University of Saskatchewan.

4. Khan, A.A., E.Y.T. Adesta, and M.Y. Ali, Formation of micro-cracks and recast layer during EDM of mild steel using copper electrodes, in Advanced machining process. 2012, IIUM press: International Islamic University Malaysia.

5. Newton, T.R., et al., Investigation of the effect of process parameters on the formation and characteristics of recast layer in wire-EDM of Inconel 718. Materials Science and Engineering: A, 2009. 513–514(0): p. 208-215.

6. Costa, L. and R. Vilar, Laser powder deposition. Rapid Prototyping Journal, 2009. 15(4): p. 264-279.

7. Kim, J.-D. and Y. Peng, Melt pool shape and dilution of laser cladding with wire feeding. Journal of Materials Processing Technology, 2000. 104(3): p. 284-293.

8. Schneider, M.F., Laser cladding with powder, effect of some machining parameters on clad properties. 1998: Universiteit Twente.

9. Kovaleva, I., et al., Numerical Simulation and Comparison of Powder Jet Profiles for Different Types of Coaxial Nozzles in Direct Material Deposition. Physics Procedia, 2013. 41(0): p. 870-872.

10. Shukla, M., et al., Effect of Laser Power and Powder Flow Rate on Properties of Laser Metal Deposited Ti6Al4V.

11. Fearon, E. and K. Watkins. Optimization of layer height control in direct laser deposition. in 23rd International Congress on Application of Laser & Electro-Optics (ICALEO 2004) Paper. 2004.

12. Shah, K., et al., Effects of melt pool variables and process parameters in laser direct metal deposition of aerospace alloys. Materials and manufacturing processes, 2010. 25(12): p. 1372-1380.

13. Unocic, R. and J. DuPont, Process efficiency measurements in the laser engineered net shaping process. Metallurgical and Materials Transactions B, 2004. 35(1): p. 143-152.

14. Huang, Y., Characterization of dilution action in laser-induction hybrid cladding. Optics & Laser Technology, 2011. 43(5): p. 965-973.

15. Paulo Jorge da Silva Bartolo, A.C.S.d.L., Antonio Mario Henriques Pereira, Artur Jorge Dos Santos Mateus, Catarina Ramos, Cyril Dos Santos, David Oliveira, Elodie

Pinto, Flavio Craveiro, Helena Maria Coelho da Rocha Terreiro Galha Bartolo, Henrique de Amorim Almeida, Ines Sousa, Joao Manuel Matias, Lina Durao, Miguel Gaspar, Nuno Manuel Fernandes Alves, Pedro Carreira, Telma Ferreira, Tiago Marques. High Value Manufacturing: Advanced Research in Virtual and Rapid Prototyping: . in 6th International Conference on Advanced Research in Virtual and Rapid Prototyping. 2013. Leira, Portugal.

16. Zhu, G., et al., The influence of laser and powder defocusing characteristics on the surface quality in laser direct metal deposition. Optics & Laser Technology, 2012. 44(2): p. 349-356.

17. Heralić, A., et al., Increased stability in laser metal wire deposition through feedback from optical measurements. Optics and lasers in engineering, 2010. 48(4): p. 478-485.

18. Mazumder, J., et al., Closed loop direct metal deposition: art to part. Optics and Lasers in Engineering, 2000. 34(4–6): p. 397-414.

19. Qi, H., M. Azer, and P. Singh, Adaptive toolpath deposition method for laser net shape manufacturing and repair of turbine compressor airfoils. The International Journal of Advanced Manufacturing Technology, 2010. 48(1-4): p. 121-131.

20. Toyserkani, E. and A. Khajepour, A mechatronics approach to laser powder deposition process. Mechatronics, 2006. 16(10): p. 631-641.

21. CM-247LC for turbine blades and vanes. Available from: http://www.c-mgroup.com/spec_sheets/CM_247.htm.

22. Donachie, M.J. and S.J. Donachie, Superalloys - A technical guide. second edition ed. 2002: ASM international.

23. Harris, K., G. Erickson, and R. Schwer. MAR M 247 Derivations—CM 247 LC DS Alloy, CMSX® Single Crystal Alloys, Properties and Performance. in 5th Int. Symp. 1984.

24. Boisselier, D. and S. Sankaré, Influence of Powder Characteristics in Laser Direct Metal Deposition of SS316L for Metallic Parts Manufacturing. Physics Procedia, 2012. 39(0): p. 455-463.

25. Pinkerton, A.J. and L. Li, Multiple-layer laser deposition of steel components using gas and water-atomised powders: the differences and the mechanisms leading to them. Applied Surface Science, 2005. 247: p. 175-181.

26. Gessinger, G.H., Powder metallurgy of superalloys. 1984: Butterworths.

27. Tien, J.K., et al., Superalloys 1980. American Society for Metals, 1980, 1980. 1980.

28. Chen, J., et al., MC carbide formation in directionally solidified MAR-M247 LC superalloy. Materials Science and Engineering: A, 1998. 247(1–2): p. 113-125.

29. Szczotok, A. and K. Rodak. Microstructural studies of carbides in MAR-M247 nickel-based superalloy. in IOP Conference Series: Materials Science and Engineering. 2012. IOP Publishing.

30. Yu, Z.-h., et al., Effect of solidification rate on MC-type carbide morphology in single crystal Ni-base superalloy AM3. Transactions of Nonferrous Metals Society of China, 2010. 20(10): p. 1835-1840

31. Wanhong, Y., et al., Effects of heat treatment on prior particle boundary precipitation in a powder metallurgy nickel base superalloy. Advanced Performance Materials, 1995. 2(3): p. 269-279.

32. Maurer, G.E., et al., Development of HIP consolidated P/M superalloys for conventional forging to gas turbine engine components. KISSINGER RD, DEYE DJ, ANTON DL, CETEL AD, NATHAL MV, POLLOCK TM, WOODFORD DA. Superalloys, 1996: p. 645-652.

33. Yan-lu, H., et al., Effects of powder feeding rate on interaction between laser beam and powder streamin laser cladding process. Journal of Wuhan University of Technology-Mater. Sci. Ed., 2004. 19(4): p. 69-72.

34. Pinkerton, A.J. and L. Li, Modelling the geometry of a moving laser melt pool and deposition track via energy and mass balances. Journal of Physics D: Applied Physics, 2004. 37(14): p. 1885.

35. Ahsan, M.N., et al., A comparative study of laser direct metal deposition characteristics using gas and plasma-atomized Ti–6Al–4V powders. Materials Science and Engineering: A, 2011. 528(25–26): p. 7648-7657.

36. Jang, J.-H., et al., Characterization of deposited layer fabricated by direct laser melting process. Metals and Materials International, 2013. 19(3): p. 497-506.

37. Peng, L., et al., Direct laser fabrication of nickel alloy samples. International Journal of Machine Tools and Manufacture, 2005. 45(11): p. 1288-1294.

38. L. COsta, T.R., A. M. Deus, R. Vilar, Simulation of layer overlap tempering kinetics in steel parts deposited by laser cladding, in 2002 International conference on metal powder deposition for rapid manufacture. 2002: San Antonio, Texas.

39. Zhang, K., W. Liu, and X. Shang, Research on the processing experiments of laser metal deposition shaping. Optics & Laser Technology, 2007. 39(3): p. 549-557.

40. Andersson, J., Weldability of precipitation hardening superalloys–influence of microstructure. 2011: Chalmers University of Technology.

41. Bansal, R., et al. Experimental and Theoretical Analysis of Scanning Laser Epitaxy Applied to Nickel-Based Superalloys. in Solid Freeform Fabrication Symposium, at University of Texas at Austin, TX. 2011.

42. Kirka, M., R. Bansal, and S. Das, Recent Progress on Scanning Laser Epitaxy: A New Technique for Growing Single Crystal Superalloys.

43. Lin, W., J. Lippold, and W. Baeslack III, An evaluation of heat-affected zone liquation cracking susceptibility, Part I: Development of a method for quantification. WELDING JOURNAL-NEW YORK-, 1993. 72: p. 135-s.

44. Ojo, O., N. Richards, and M. Chaturvedi, Contribution of constitutional liquation of gamma prime precipitate to weld HAZ cracking of cast Inconel 738 superalloy. Scripta materialia, 2004. 50(5): p. 641-646.

45. Ojo, O.A., Y.L. Wang, and M.C. Chaturvedi, Heat affected zone liquation cracking in electron beam welded third generation nickel base superalloys. Materials Science and Engineering: A, 2008. 476(1–2): p. 217-223.

46. Kear, B.H., M. Cohen, and R. Mehrabian, Rapid Solidification Processing: Principles and Technologies. 1978: Claitor's.

47. Dinda, G., A. Dasgupta, and J. Mazumder, Laser aided direct metal deposition of Inconel 625 superalloy: microstructural evolution and thermal stability. Materials Science and Engineering: A, 2009. 509(1): p. 98-104.

48. Bi, G., et al., Investigation on the direct laser metallic powder deposition process via temperature measurement. Applied Surface Science, 2006. 253(3): p. 1411-1416

49. Beyer, E. New Industrial Systems & Concepts for Highest Laser Cladding Efficiency. 2011; Available from: http://www.laserstoday.com/2011/05/high-performance-laser-cladding/.

50. Beaman, J.J., et al., Additive/subtractive manufacturing research and development in Europe. 2004, DTIC Document.

51. Bourell, D.L., M.C. Leu, and D.W. Rosen. Roadmap for additive manufacturing: Identifying the future of freeform processing. 2009.

52. Groth, A., C. Walz, and S. Naegeler. New innovations in diode laser cladding. in International congress on applications of lasers and electro optics (ICALEO). 2002. Scottsdale Arizona.

53. Levy, G.N., R. Schindel, and J.-P. Kruth, Rapid manufacturing and rapid tooling with layer manufacturing (LM) technologies, state of the art and future perspectives. CIRP Annals-Manufacturing Technology, 2003. 52(2): p. 589-609.

54. Bi, G. and A. Gasser, Restoration of Nickel-Base Turbine Blade Knife-Edges with Controlled Laser Aided Additive Manufacturing. Physics Procedia, 2011. 12, Part A(0): p. 402-409.

55. Zhong, M., et al., Boundary liquation and interface cracking characterization in laser deposition of Inconel 738 on directionally solidified Ni-based superalloy. Scripta materialia, 2005. 53(2): p. 159-164.

56. Montazeri, M., F. Malek Ghaini, and A. Ojo O, Heat Input and the Liquation Cracking of Laser Welded IN738LC Superalloy. Welding journal, 2013. 92(9)

57. Idowu, O., O. Ojo, and M. Chaturvedi, Effect of heat input on heat affected zone cracking in laser welded ATI Allvac 718Plus superalloy. Materials Science and Engineering: A, 2007. 454: p. 389-397.

58. Min, D., et al., Effects of heat input on the low power Nd: YAG pulse laser conduction weldability of magnesium alloy AZ61. Optics and Lasers in Engineering, 2011. 49(1): p. 89-96.

59. Malek Ghaini, F., et al., Weld metal microstructural characteristics in pulsed Nd: YAG laser welding. Scripta Materialia, 2007. 56(11): p. 955-958.

60. Steen, W.M., Laser Material Processing. 1996.

61. Rush, M.T., et al., An investigation into cracking in nickel-base superalloy repair welds. Advanced Materials Research, 2010. 89: p. 467-472.

62. Dye, D., O. Hunziker, and R. Reed, Numerical analysis of the weldability of superalloys. Acta materialia, 2001. 49(4): p. 683-697.

63. Rangaswamy, P., et al., Residual stresses in LENS® components using neutron diffraction and contour method. Materials Science and Engineering: A, 2005. 399(1–2): p. 72-83.

64. Zhou, S., et al., Analysis of crack behavior for Ni-based WC composite coatings by laser cladding and crack-free realization. Applied Surface Science, 2008. 255(5, Part 1): p. 1646-1653.

65. Gooch, T. and J. Honeycombe, Welding variables and microfissuring in austenitic stainless steel weld metal. Welding Journal, 1980. 59(8): p. 233.

66. Rush, M.T., et al., Liquation and post-weld heat treatment cracking in Rene 80 laser repair welds. Journal of Materials Processing Technology, 2012. 212(1): p. 188-197.

67. Ojo, O.A. and M.C. Chaturvedi, On the role of Y' precipitates in weld heat affected zone microfissuring of a nickel-based superalloy. Materials Science and Engineering: A, 2005. 403: p. 77-86.

68. Radhakrishnan, B. and R.G. Thompson, A quantitative microstructural study of intergranular liquation and its relationship to hot cracking. Metallography, 1988. 21(4): p. 453-471.

69. Baeslack Iii, W.A. and D.E. Nelson, Morphology of weld heat-affected zone liquation in cast alloy 718. Metallography, 1986. 19(3): p. 371-379

70. Henderson, M., et al., Nickel based superalloy welding practices for industrial gas turbine applications. Science and Technology of Welding & Joining, 2004. 9(1): p. 13-21.

71. Kamara, A., et al., Modelling of the melt pool geometry in the laser deposition of nickel alloys using the anisotropic enhanced thermal conductivity approach. Proceedings of the Institution of Mechanical Engineers, Part B: Journal of Engineering Manufacture, 2011. 225(1): p. 87-99.

72. Hunziker, O., D. Dye, and R.C. Reed, On the formation of a centreline grain boundary during fusion welding. Acta Materialia, 2000. 48(17): p. 4191-4201.

73. Cheng, B. and K. Chou, MELT POOL GEOMETRY SIMULATIONS FOR POWDER-BASED ELECTRON BEAM ADDITIVE MANUFACTURING

74. Lippold, J., Centerline cracking in deep penetration electron beam welds in Type 304L stainless steel. Welding Journal, 1985. 64(5): p. 127s-136s

Chapter 5

Experimental approaches to mitigate cracking in laser deposited CM247LC

5 Chapter 5 - Experimental approaches to mitigate cracking in laser deposited CM247LC

5.1 Introduction

In the previous chapter, a Design of Experiments (DOE) approach was used to evaluate the influence of various processing variables on the cracking response of laser deposited CM247LC blocks.

From this experiment, it was learned that the degree of cracking is influenced most significantly by the laser power and scanning speed of the process, and to a lesser extent by the laser spot size and deposit dilution. Lowest crack densities were obtained for high laser power, slow scanning speed, large laser spot diameter and low deposit dilution.

Through metallographic analysis of the deposited samples, it was determined that cracks formed during solidification, with elemental micro-segregation leading to the formation of an inter-granular microstructure consisting of primary MC type carbides and γ/γ' eutectic. During melt pool solidification, the intergranular eutectic liquid persists to lower temperatures, forming pools of γ/γ' and continuous liquid films along the grain boundaries and interdendritic regions, which separates under the solidification stresses to form cracks.

In this chapter, three approaches were applied in order to investigate the influence that they have on reducing the cracking response of laser deposited CM247LC. Through the application and analysis of these methods, it is hoped that a strategy for reducing or eliminating cracking in laser deposited CM-247LC may be formed.

1. The influence of powder particle size range on the cracking response
2. The influence of toolpath scanning strategy on the cracking response
3. The influence of induction pre-heating of the substrate on the cracking response

5.2 Experimental approach

5.2.1 Equipment and materials

5.2.1.1 Laser deposition equipment

Work was conducted at TWI Ltd Sheffield, using the laser deposition equipment as described in section 3.1. As for the previous work, all deposition trials were conducted within a sealed and argon purged chamber to minimise the formation of deleterious oxide phases that may otherwise influence the cracking response (Figure 5-1A).

Figure 5-1 - A) Laser deposition processing chamber based at TWI Sheffield B) three beam coaxial nozzle used for deposition trials

Due to the relatively high laser powers and temperatures involved in this work, the three beam coaxial nozzle was used for all deposition trials (Figure 5-1B). This nozzle was successfully used in the previous chapter for the deposition of the DOE optimised blocks, due to its rugged construction and effective water cooling.

5.2.1.2 CM247LC Substrate and powder

The CM247LC powder and substrate material used for these trials, are the same as that used in chapter 4. Powder was supplied in the size range 0-150, which was then sieved into 20-40µm and 40-100µm size ranges. Chemical, morphological and microstructural analysis of the materials used can be found in section 4.3.1

5.2.1.3 Induction heating apparatus

A full description of the induction heating equipment used for the work presented in this chapter, along with the setup and calibration methods used, may be found in sections 3.1.7 and 3.2.5. This consisted of a Cheltenham TR1 induction heater, bespoke induction coil and work-holding jig (Figure 5-2).

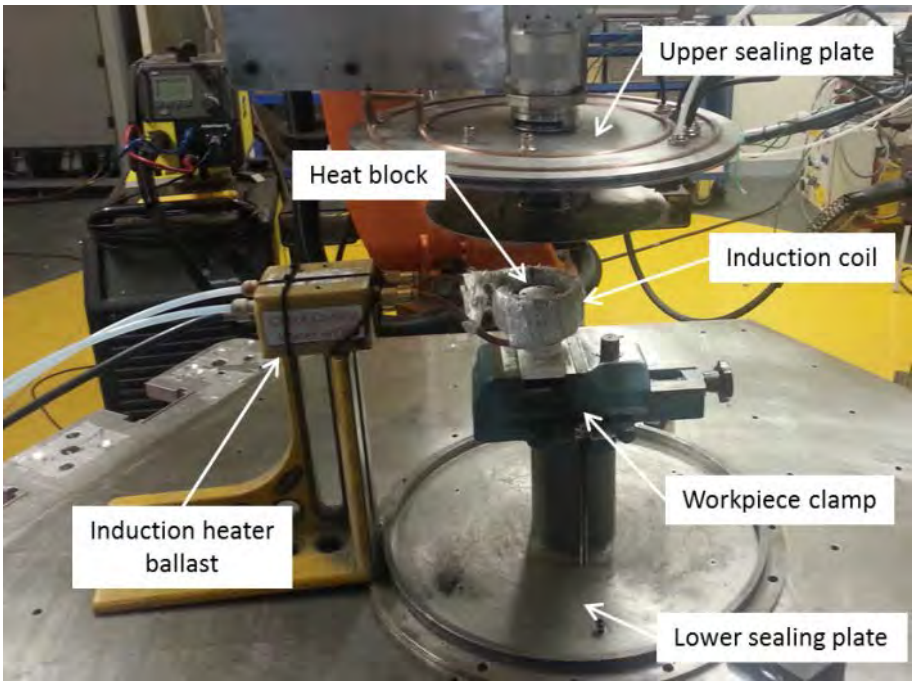

Figure 5-2 - Induction heating deposition apparatus without the sealing bag fitted.

5.2.2 Experiment 1 – The effect of particle size on deposit quality

The work presented in this chapter seeks to investigate what effect, if any, that the powder size range has on the cracking response of laser deposited CM247LC. This will involve direct comparison of samples deposited using the 20-40µm and 40-100µm CM247LC powders.

The effect of powder size on the surface roughness and deposition efficiency of the laser metal deposition process has been investigated by other authors [1], and it has been shown that differences in powder size and morphology have an influence on the amount of laser energy that is absorbed by the powder, and the convection currents within the melt pool [2]. These influences affect the solidification microstructure, and by extension the mechanical properties of the deposited part, although to date no work could be found that related the particle size range to the cracking response.

Test blocks measuring 15x30x15mm were deposited onto CM247LC substrate, using the parameters developed for the DOE optimised block from section 4.3.5 (Table 5-1), which allows for a direct comparison of results without the introduction of additional variables that may otherwise influence the results.

Since the DOE optimised block in section 4.3.5 was deposited using the 40-100µm powder, it is first necessary to calibrate the mass flow rate of the 20-40µm powder so that deposits of the same size, shape and dilution are obtained.

Table 5-1 - Deposition parameters used for deposition of DOE optimised test block

Process parameter	Value	Units
Laser Power	1000	W
Scanning speed	5	mm/s
Laser spot diameter	3	mm
Deposit dilution	1.5	
Powder feed rate	6.5	g/min
Track spacing	1.8	mm
Z increment	0.55	mm

5.2.2.1 Calibrating powder feed rate against dilution for 20-40µm CM247LC powder

Fine particles have a higher packing density than coarse powder, meaning for a given volume, the finer size range will possess a greater mass. This was demonstrated in section 3.2.4 during powder feed rate calibration (Figure 5-3), which showed that the 20-40µm powder delivered 22% more mass per dosing speed (rpm) than the 40-100µm powder.

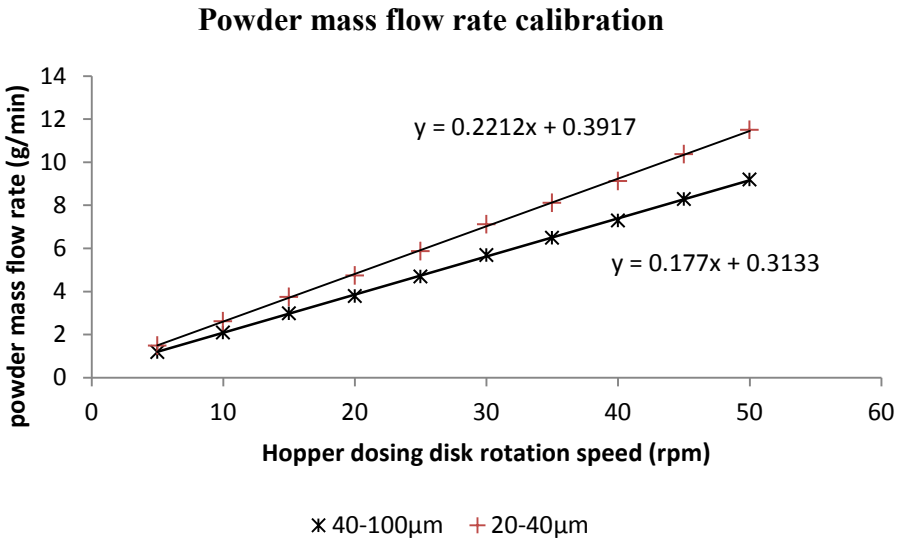

Figure 5-3 - Powder mass flow calibration results for 20-40µm and 40-100µm cm247LC powder

Using the method for calibration of deposit dilution against powder mass flow rate described in section 4.2.2.1, a series of single tracks measuring 30mm in length were deposited onto CM247LC substrate, using the parameters listed in Table 5-2. These were then cross sectioned transversely to the deposition direction, and the track width and dilution measured using the methods described in Section 3.3.

A graph of powder mass feed rate vs deposit dilution was plotted, and a value of powder feed rate calculated that produces the desired dilution of 1.5 (Figure 5-7). Track width measurements were used to calculate the track offset value (ΔX) based on the 30% overlap value established in section 4.3.2.2. These values were compared to those determined in section 4.2.4.2 to ensure that the values are consistent.

Table 5-2 - Parameters used for deposition of single tracks for dilution calibration

Laser power	Scanning speed	Laser spot diameter	Powder feed rate	Desired dilution
W	mm/s	mm	g/min	Ac/Am
1000	5	3	2.6	1.5
			4.8	
			7	

5.2.2.2 Deposition of overlap track to determine Z increment

Using a powder feed rate of 6.1 g/min, a single layer of overlapping tracks were deposited, measuring 30mm in length, 6 tracks in width and using an overlap condition of 30% (1.8mm). This was sectioned, and the layer height measured using the methods described in section 4.2.2.3.

From the measured layer thickness, a Z-increment value was calculated that is 85% of the thickness of the single layer. This was compared to the results obtained for the 40-100µm powder used in section 4.3.5.1 (Table 5-1) to ensure the parameters are consistent

5.2.2.3 Deposition of test blocks using 20-40µm powder

Through application of the process rules developed in section 4.2.2, a set of parameters were defined for the deposition of a pair of blocks, using the 20-40µm CM247LC powder (Table 5-3). The blocks were deposited under an inert argon atmosphere within the processing chamber, before being allowed to cool naturally to ambient temperature for analysis.

Blocks were metallographically sectioned longitudinally and transversely, as illustrated in section 3.3.3, and prepared for optical microscopy and crack quantification using method E described in section 3.3.1.1.

Crack density measurements were recorded using the methods described in section 3.3.3.1, as well as measurements of secondary dendrite arm spacing at various points within the deposit. These results were then compared with those obtained for the DOE test block deposited in section 4.3.5

Table 5-3 - Deposition parameters for 20-40µm CM247LC block

Process parameter	20-40µm powder	40-100µm powder	Units
Laser Power	1000	1000	W
Scanning speed	5	5	mm/s
Laser spot diameter	3	3	mm
Deposit dilution	1.5	1.5	
Powder dosing speed	31	35	rpm
Powder feed rate	6.1	6.5	g/min
Track spacing	1.8	1.8	mm
Z increment	0.55	0.55	mm

5.2.3 Experiment 2 - The effect of toolpath on crack formation

Work conducted in chapter 4 focused on the production of test blocks, in which the only variables were the laser power, scanning speed, laser spot diameter and deposit dilution.

In order to reduce the variation between blocks, which may have influenced the cracking response and introduced unwanted scatter in the results, process variables such as track overlap and z-increment were standardised relative to the geometry of single tracks and overlapping single layers. This also required that a single toolpath pattern be used for all deposited blocks.

All the previous work conducted in this study has been performed using a cross hatch pattern, as it produces blocks of relatively good shape and surface finish over a wide range of processing parameters. However, it is not yet known what effect this toolpath had on the cracking response of the deposits, and whether or not it is the optimal scanning pattern for the reduction in cracking.

Different toolpath patterns will generate different heating and cooling profiles during deposition, which in turn have an effect on the microstructure of the deposited material and the cracking response [3-5]. This section investigates this influence, by testing out various toolpaths, measuring the cracking response and evaluating the effect it has had on the microstructure.

Two blocks were deposited using each toolpath pattern, which were then cross sectioned longitudinally and transversely for crack density measurement and microstructural investigation. Secondary dendrite arm spacing measurements (λ_2) were recorded for each toolpath from different points within the block using optical microscopy, and temperature profiles were recorded during deposition using a type K thermocouple welded to the substrate, adjacent to the first clad track.

5.2.3.1 Deposition of test block using various toolpath patterns for 40-100µm CM247LC powder

The toolpaths used for this section are illustrated schematically in Figure 5-4 and Figure 5-5. Toolpaths were design to minimise the time spent transitioning between layers, in order to minimise the cooling of the deposit.

5.2.3.1.1 Toolpath 1 – Short raster

The short raster toolpath comprises of a repeating structure of four distinct layers (A,B,C,D), as illustrated in Figure 5-4. Each layer is offset by a half track spacing in the Y-axis, so that the tracks do not lie directly on top of each other, and the laser is on continuously for the deposition of each layer. Layer A and C consists of 17 tracks, Layer B and D consists of 16 tracks. The endpoint for layer D is directly beneath the start point for layer A, minimising the transition time between layers.

5.2.3.1.2 Toolpath 2 – Long raster

The long raster toolpath is identical to the short raster toolpath, except that the X and Y axis are flipped (Figure 5-4), so that the tracks are deposited along the Y-axis and the track separation movements are performed in the X-axis. This toolpath consists of a repeating structure of 4 distinct layers, with the endpoint of each layer nearly directly below the start point of the following layer, in order to reduce the amount of time the laser is not emitting during transition between layers. Layers A and C consist of 9 tracks, Layers B and D consist of 8 tracks.

5.2.3.1.3 Toolpath 3 – Cross hatch

The cross hatch toolpath, as described in section 4.2.2.3, consists of a repeating structure of 2 layers, A and B which are deposited at 90° to each other (Figure 5-5). Layer A is a raster pattern deposited along the Y-axis, with track separation movements along the X-axis. Layer B is a raster pattern deposited along the X-axis, with track separation movements along the Y-axis. Layer A consists of 9 tracks, Layer B consists of 17 tracks. Track lengths were calculated to be divisible by the track offset of 1.8mm, so that the start point and end point of each layer do not come out of alignment during deposition.

5.2.3.1.4 Toolpath 4 – Unidirectional

The unidirectional toolpath (Figure 5-5) consists of parallel tracks measuring 30mm in length, deposited in the +Y direction only, with layers A and B offset by half a track width. Layer A consists of 9 tracks, layer B consists of 8 tracks. At the end of each deposited track, the laser emission is interrupted, and the tool performs a diagonal movement to the start point of the adjacent track.

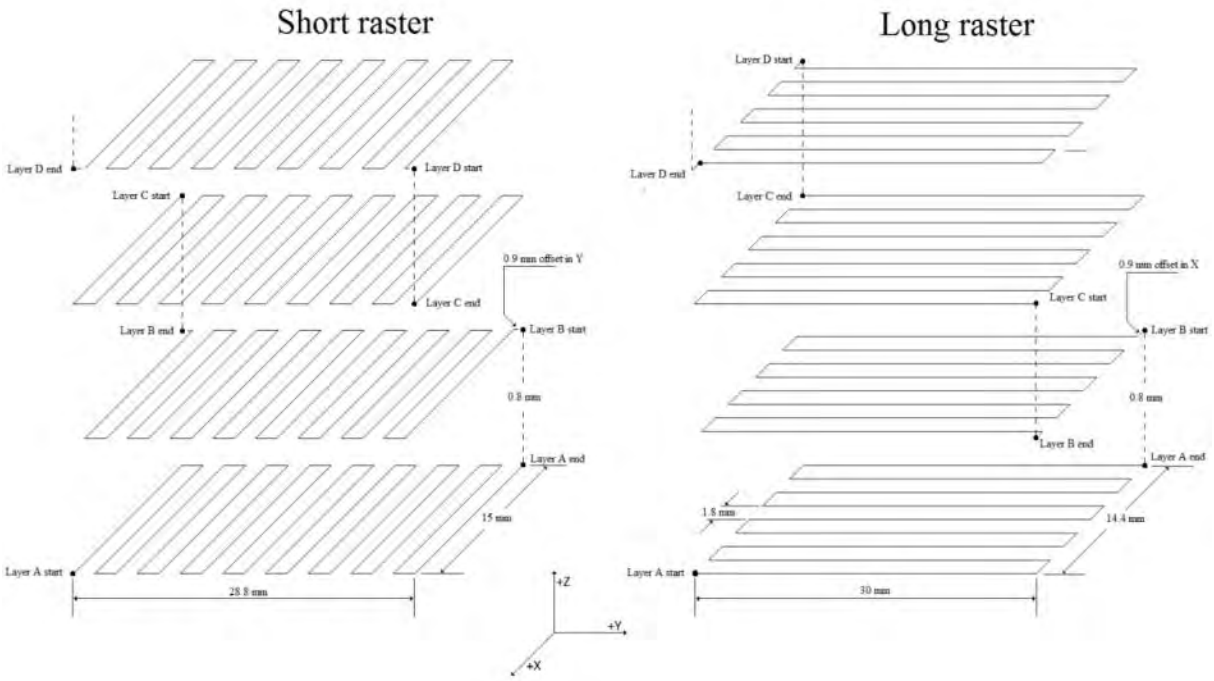

Figure 5-4 - Short and long raster toolpath patterns used for deposition of test blocks

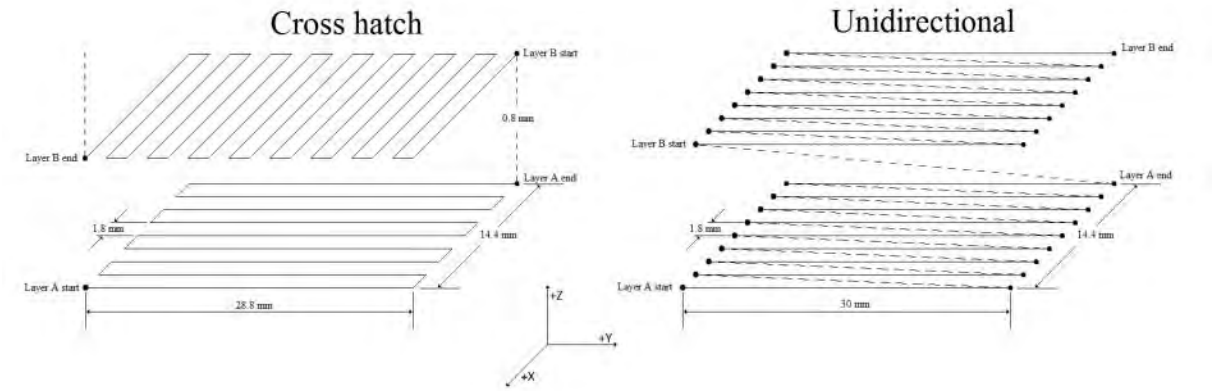

Figure 5-5 - Cross hatch and unidirectional toolpaths used for deposition of test block

5.2.4 Experiment 3 - The effect of pre-heating on crack formation

In chapter 4, DOE analysis of crack density with respect to the processing variables showed that cracking was reduced when laser power and laser spot size was increased, and scanning speed and deposit dilution were decreased. It was also noted that the density of cracks in laser deposited CM247LC blocks decrease the higher up the block the measurements are taken.

This response was believed to be due to the accumulation of heat within the deposit, lowering the thermal mismatch between the molten pool produced by the laser and the surrounding solid material. Lower thermal mismatch leads to reduced cooling rates, lower thermal strain, and less driving force to separate the wetted grains during solidification [6]. Higher temperatures also allow the melt pool to stay liquid for longer, decreasing the rate at which grain growth occurs and allowing backfilling of cracks with residual liquid [7], although no evidence of crack backfilling was observed in chapter 4.

As discussed in section 2.4.5.3, the residual stress in a cladding consists of the thermal stress, the phase transformation stress and structural stress. The thermal stress can be expressed as follows [8]

$$\sigma = \frac{E_C(a_c - a_m)(T_c - T_{mO})}{1 - \varepsilon}$$

- σ - Thermal stress
- E_c - Elastic modulus
- a_c - Thermal expansion coefficient of coating
- a_m - Thermal expansion coefficient of substrate
- T_c - melting point of clad coating
- T_m - Initial temperature before cladding
- E - Poisson ratio of cladding coating

From this equation, it can be seen that as the initial substrate temperature before cladding approaches the melting point of the clad coating, that the stresses are reduced. Therefore

preheating the substrate has the effect of reducing the thermal stress, and reducing the driving force for solidification crack formation.

5.2.4.1 Development of deposition parameters

The increased temperature of the substrate will mean that the size and shape of the deposit will be different to that obtained in sections 4.3.5 or 5.2.2.3, requiring that a series of trials be conducted in order to develop the processing parameters according to the rules established in section 4.3.2. This consists of the following steps:

1. Deposition of single tracks at varying powder feed rates onto preheated substrate, to calculate powder feed rate required to produce a desired dilution of 1.5
2. Measurement of single track width and calculation of track spacing to give 30% track overlap
3. Deposition of a single layer using the calculated powder feed rate and track overlap spacing
4. Measurement of single layer thickness and calculation of Z increment
5. Deposition of test block

5.2.4.2 Deposition of test block at 800°C, using 650°C induction preheat and laser assistance

Using the induction heater calibration voltages obtained in section 3.2.5, the induction heater was set to heat the substrate to a stable 650°C. Although the induction heater was found to be capable of achieving temperatures up to 800°C, the relatively low power of the unit would often cause the thermal overload switch to randomly shut the heater off when voltages greater than 175V were used. In order to increase the temperature of the substrate further, laser preheating was also employed.

Using a laser spot defocused to Ø10mm to avoid melting the substrate, the beam was scanned across the substrate using the cross hatch toolpath, with one scan being performed in the longitudinal direction and another scan being performed in the transverse direction. Laser power and scanning speed were 1000W and 5mm/s respectively.

Three tracks were deposited onto the preheated CM247LC substrate, preheated to 800°C, using the parameters listed in Table 5-4. These were then sectioned and analysed using optical microscopy to determine the dilution and width for each track, as per the established method.

Table 5-4 - deposition parameters for single tracks onto 650°C preheated substrate

Laser power	Scanning speed	Laser spot diameter	Powder feed rate	Desired dilution
W	mm/s	mm	g/min	Ac/Am
1000	5	3	3.9	1.5
			5.6	
			7.4	

A graph of dilution vs powder feed rate was plotted (Figure 5-7), which was used to calculate the powder feed rate required to produce a dilution of 1.5, while track width measurements were used to calculate the track overlap spacing.

Using the powder feed rate and ΔX values calculated, a single layer of overlapping tracks was deposited onto an 800°C preheated CM247LC substrate. This was cross sectioned and optical microscopy methods used to measure the individual layer thickness, from which the ΔZ value was calculated.

Using the parameters listed in Table 5-5, a single block was deposited using a cross hatch toolpath onto a CM247LC substrate, which was preheated to 800°C using combined laser and induction preheating. The block was allowed to cool naturally to ambient temperature under argon shielding over approximately 1 hour before being removed for analysis.

Table 5-5 - Deposition parameters used for induction preheated deposition trial block

Process parameter	Value	Units
Laser Power	1000	W
Scanning speed	5	mm/s
Laser spot diameter	3	mm
Deposit dilution	1.5	
Powder dosing speed	48	rpm
Powder feed rate	8.77	g/min
Track spacing	2.8	mm
Z increment	0.95	mm
Induction heater voltage	175	V

5.3 Results

5.3.1 Experiment 1 – The effect of particle size on deposit quality

5.3.1.1 Parameter development trials

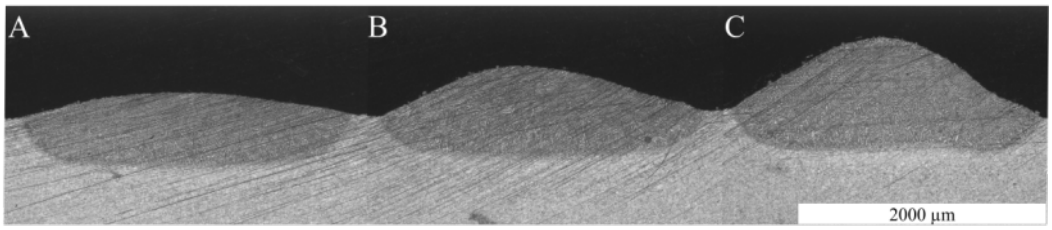

Figure 5-6 - Single tracks deposited using 20-40µm powder for dilution calibration A) 2.6 g/min B) 4.8 g/min C) 7 g/min

Table 5-6 - Dilution and track width measurements for 20-40µm powder parameter development trials

Laser power	Scanning speed	Laser spot diameter	Powder feed rate	Measured dilution	Track width
W	mm/s	mm	g/min		(mm)
1000	5	3	2.6	0.3788	2.67
			4.8	0.8383	2.62
			7	1.4698	2.518

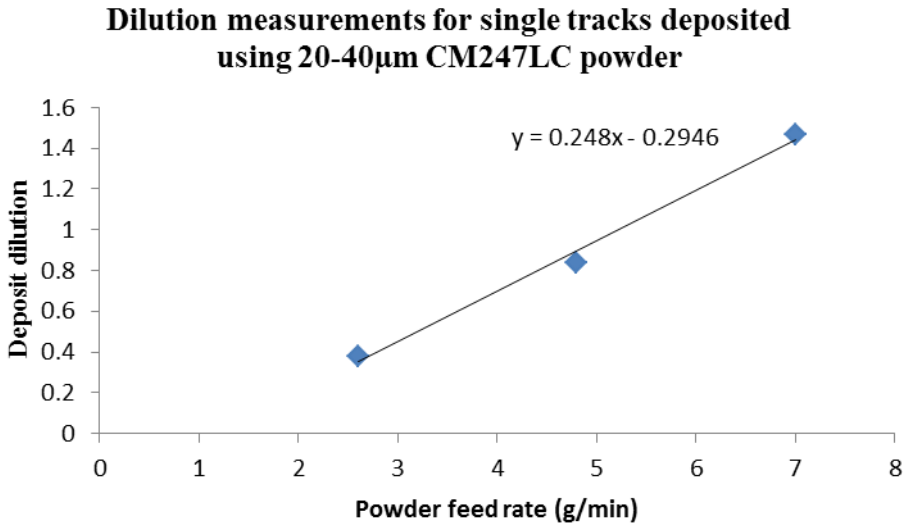

Figure 5-7 - Dilution calibration results for 20-40µm powder

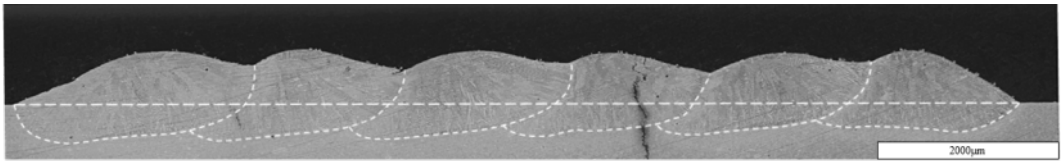

Figure 5-8 - Overlap trial for 20-40µm powder

From the results presented in Table 5-6, a graph was plotted (Figure 5-7) and a powder feed calculated that would produce a dilution of 1.5. This showed that in order to produce the desired dilution, a powder feed rate of 6.1 g/min was required, which produces a track with a width of 2.52mm.

Using the 30% track overlap condition, a single layer of overlapping tracks was deposited (Figure 5-8), with a measured layer thickness of 0.65mm, which is consistent with that produced using the 40-100µm powder. From this layer thickness measurement, a ΔZ value of 0.55mm was calculated.

5.3.1.2 Test block deposition and visual examination

Visual examination of the external surface of the blocks deposited using the 20-40µm powder displayed very good surface finish, with extremely clean, straight sided walls and very few satellite particles, either on the sidewall or at the junction between the deposit and the substrate Figure 5-9B. Surface connected cracks were observed, both on the sidewalls and top surface, similar to those observed for the DOE test blocks deposited in section 4 (Figure 5-10), with cracks running perpendicular to the substrate Figure 5-9A.

5.3.1.3 Microstructural evaluation and crack density measurement

Optical microscopy of the cross sectioned, polished and etched blocks showed a large number of cracks that penetrate through multiple layers in the same way observed in the DOE optimised deposit from chapter 4.3.5.1. (Figure 5-15, Figure 5-16).

Crack density measurements were conducted for the 20-40µm block using the established methods, and the results compared with the DOE optimised block deposited in section 4.3.5.1. This showed that the block deposited using the 20-40µm powder contains 6% more cracks per unit area than the block deposited using the 40-100µm powder (Figure 5-11).

Comparison of the crack morphology between the 20-40µm and 40-100µm blocks showed that the average crack length is 544µm for the 20-40µm powder, and 890µm for the 40-100µm powder (Figure 5-12). As with many of the other blocks, the crack density was observed to decrease, the further away from the substrate the measurement is taken (Figure 5-13).

Secondary dendrite arm spacing measured at the points illustrated in Figure 5-9D and Figure 5-10D, were found to decrease the further away from the substrate the measurements were taken, with the 20-40µm block exhibiting a shorter λ_2 length than the 40-100µm block when measured near to the substrate, and halfway up the block. λ_2 length measurements from the top layer of the deposit were found to be equivalent for both the 20-40µm and 40-100µm blocks (Figure 5-14).

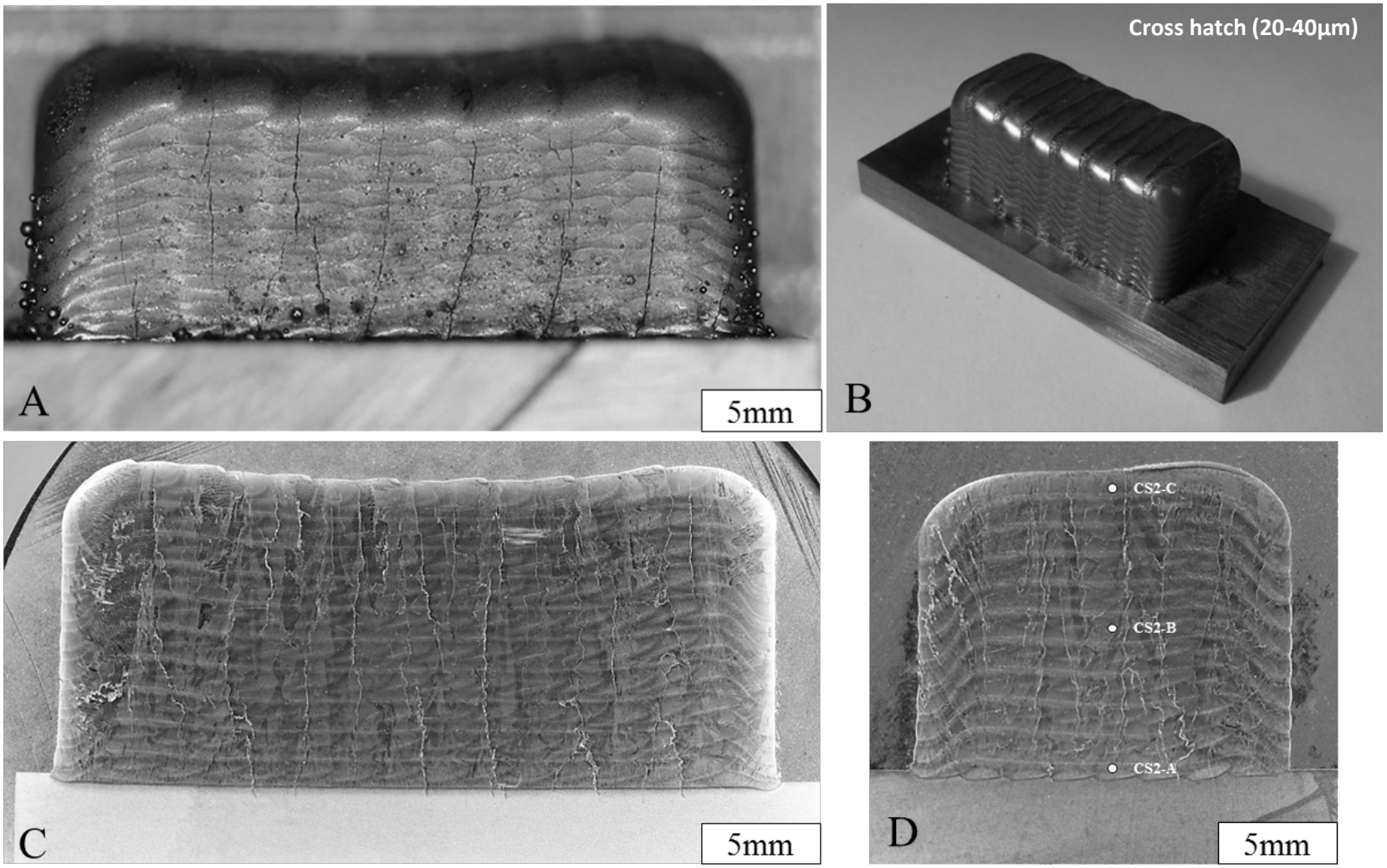

Figure 5-9 - Cross hatch toolpath test block deposited from 20-40µm CM247LC A) external side view B) external isometric view C) longitudinal cross section D) Transverse section

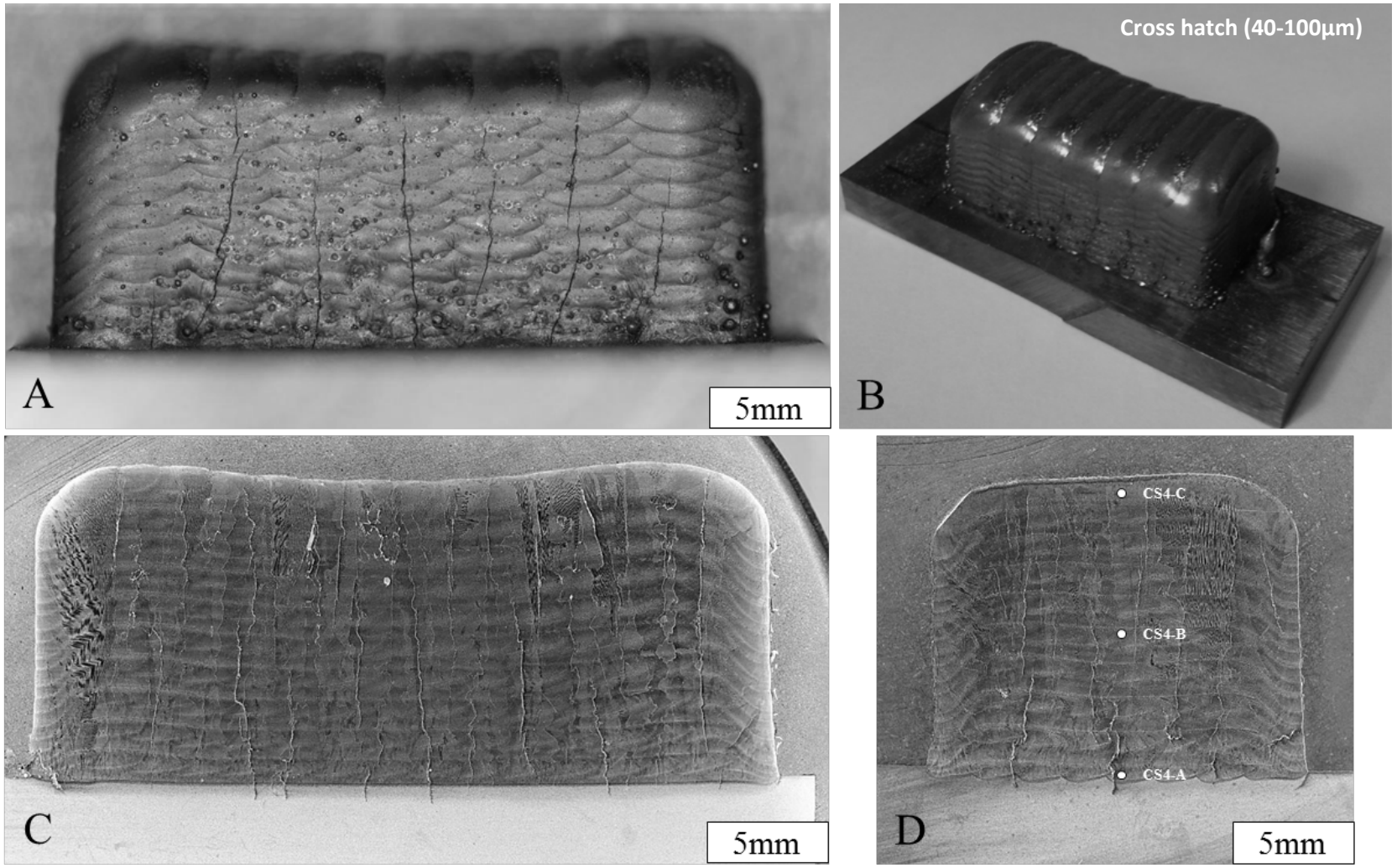

Figure 5-10 - Cross hatch toolpath test block deposited from 40-100µm CM247LC A) External side view B) External isometric C) Longitudinal section D) Transverse section (including SDAS measurements)

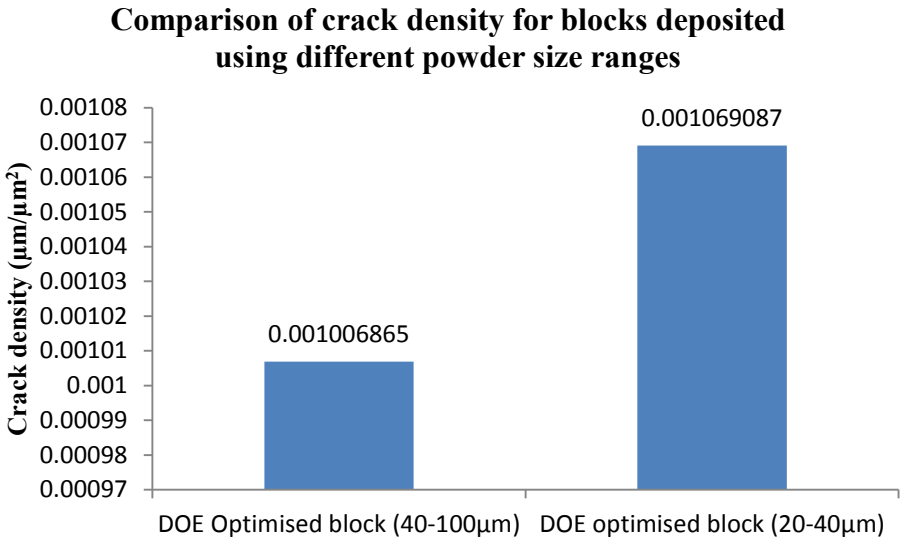

Figure 5-11 - Crack measurement results for blocks deposited using the DOE optimised parameters, using the 20-40µm and 40-100µm powders

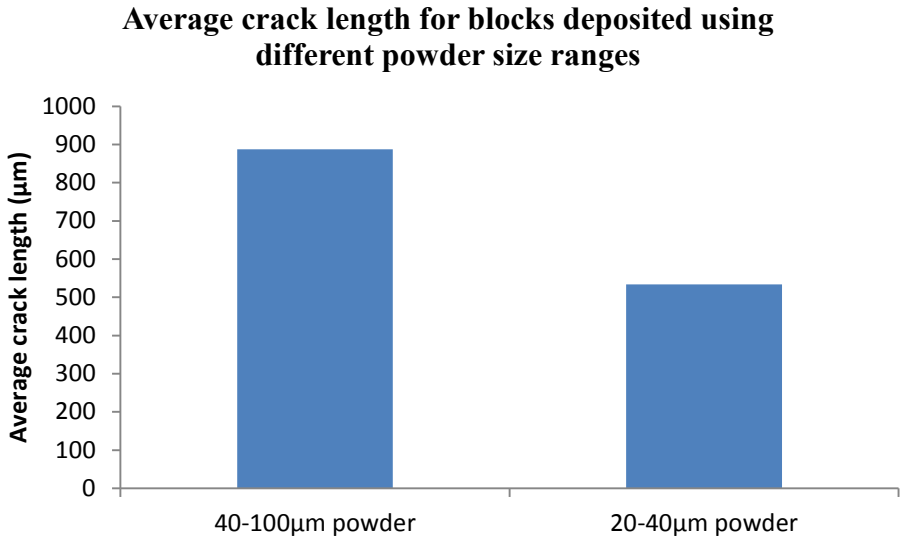

Figure 5-12 - Graph illustrating average crack lengths for blocks deposited using 20-40µm and 40-100µm powder

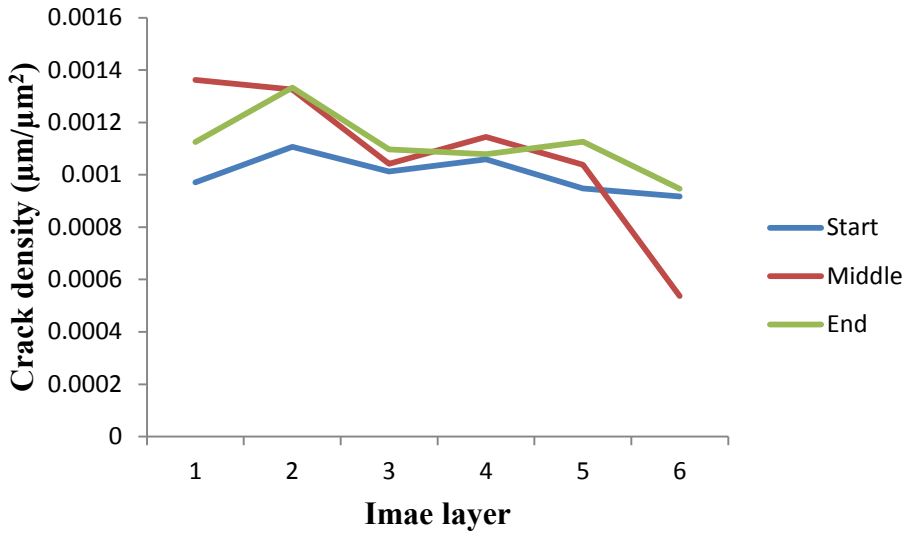

Figure 5-13 - Graph illustrating crack density as a function of deposit height, for cross hatch toolpath deposited using 20-40µm powder

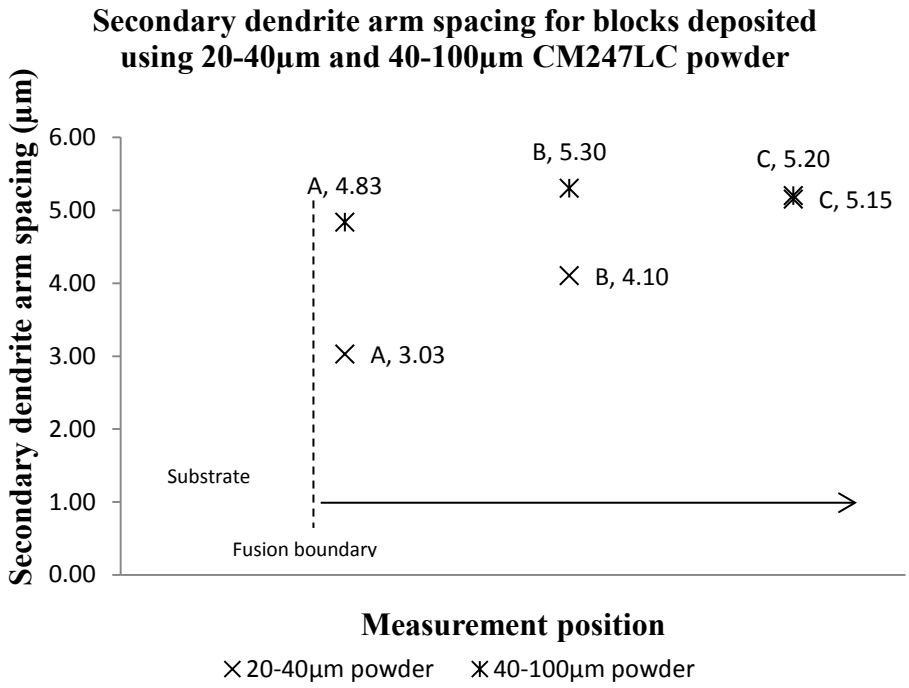

Figure 5-14 - SDAS measurement comparison for cross hatch toolpath blocks deposited using 20-40µm (Figure 5-9D) and 40-100µm (Figure 5-10D) CM247LC powder

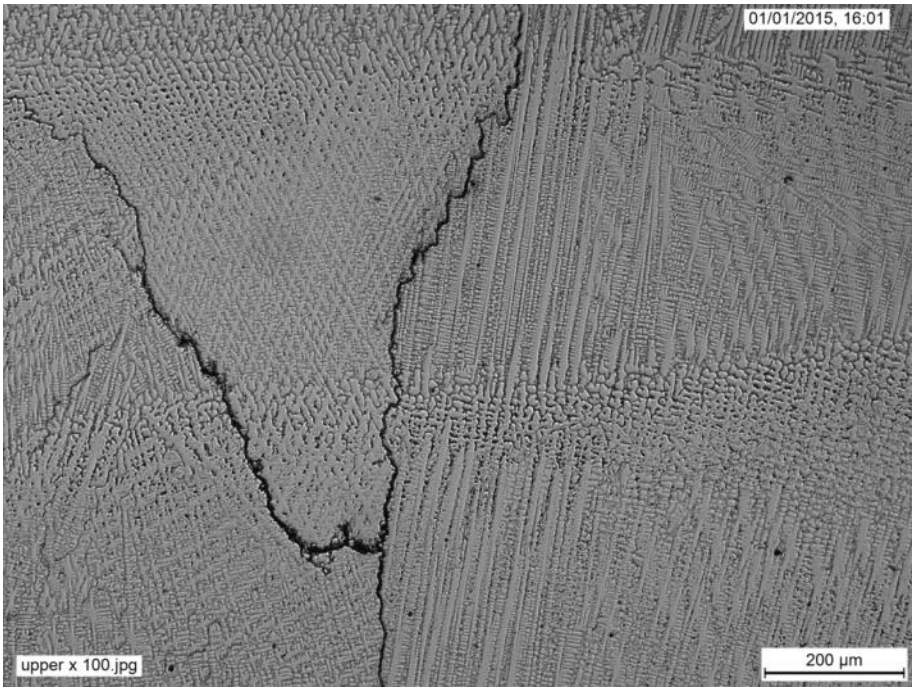

Figure 5-15 - Optical micrograph from 20-40µm deposited block, taken from the upper region

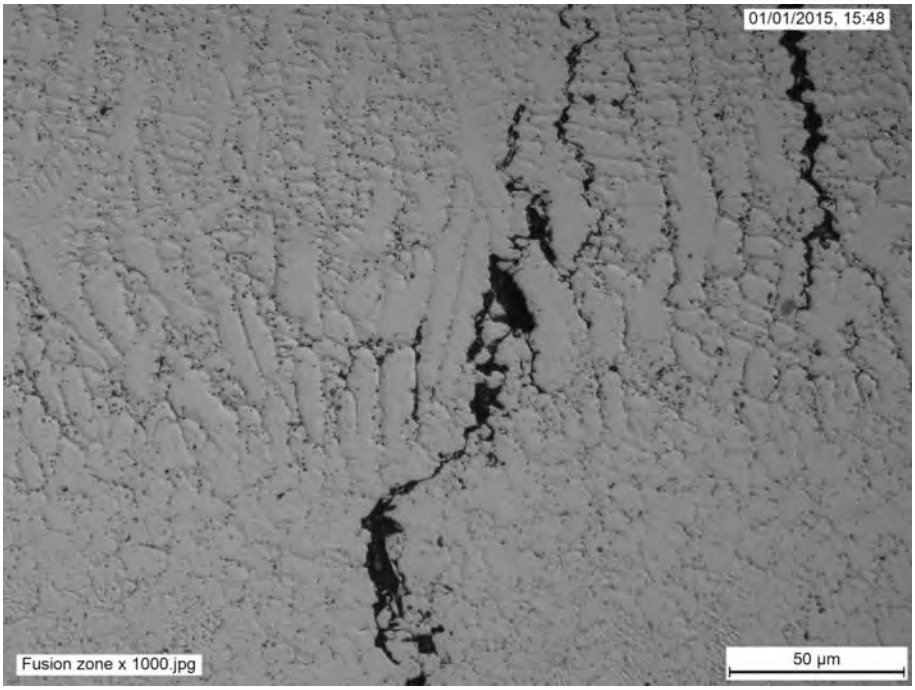

Figure 5-16 - 1000x optical micrograph of deposit fusion zone (20-40µm)

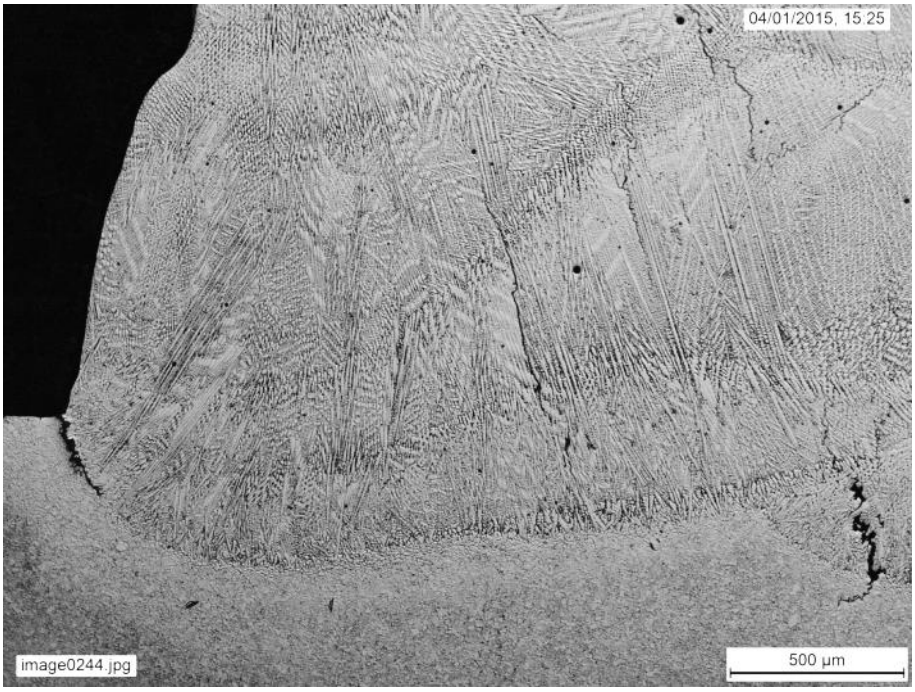

Figure 5-17 - 40-100µm block fusion boundary, showing "toe crack" and interdenritic cracks

5.3.2 Experiment 2 - The effect of toolpath on crack formation

5.3.2.1 Test block deposition and visual examination

Visual examination of the deposited blocks showed that the majority of the samples had a relatively good shape and surface finish, with square side walls and few satellite particles adhering to the outer surfaces (Figure 5-18). All blocks exhibited some degree of surface connected cracking, predominantly along the sidewall of the long axis, with cracks appearing to travel perpendicular to the substrate.

The blocks deposited using the unidirectional toolpath however exhibited poorer deposit geometry than the other blocks, with more sloping side wall, more pronounced surface cracks and a greater degree of satellite particles adhered to the sidewall and substrate interface.

5.3.2.2 Microstructural evaluation and crack density measurements

Blocks from each toolpath were cross sectioned both longitudinally and transversely, and then metallographically prepared for optical microscopy using method E described in section 3.3.1.1. Crack density measurements were performed using the method described in section 3.3.3 for both sections of each block, in order to determine if the crack density was equal along each axis, or if the cracking response is anisotropic. Secondary dendrite arm spacing measurements were also recorded at different points within the deposit for each toolpath.

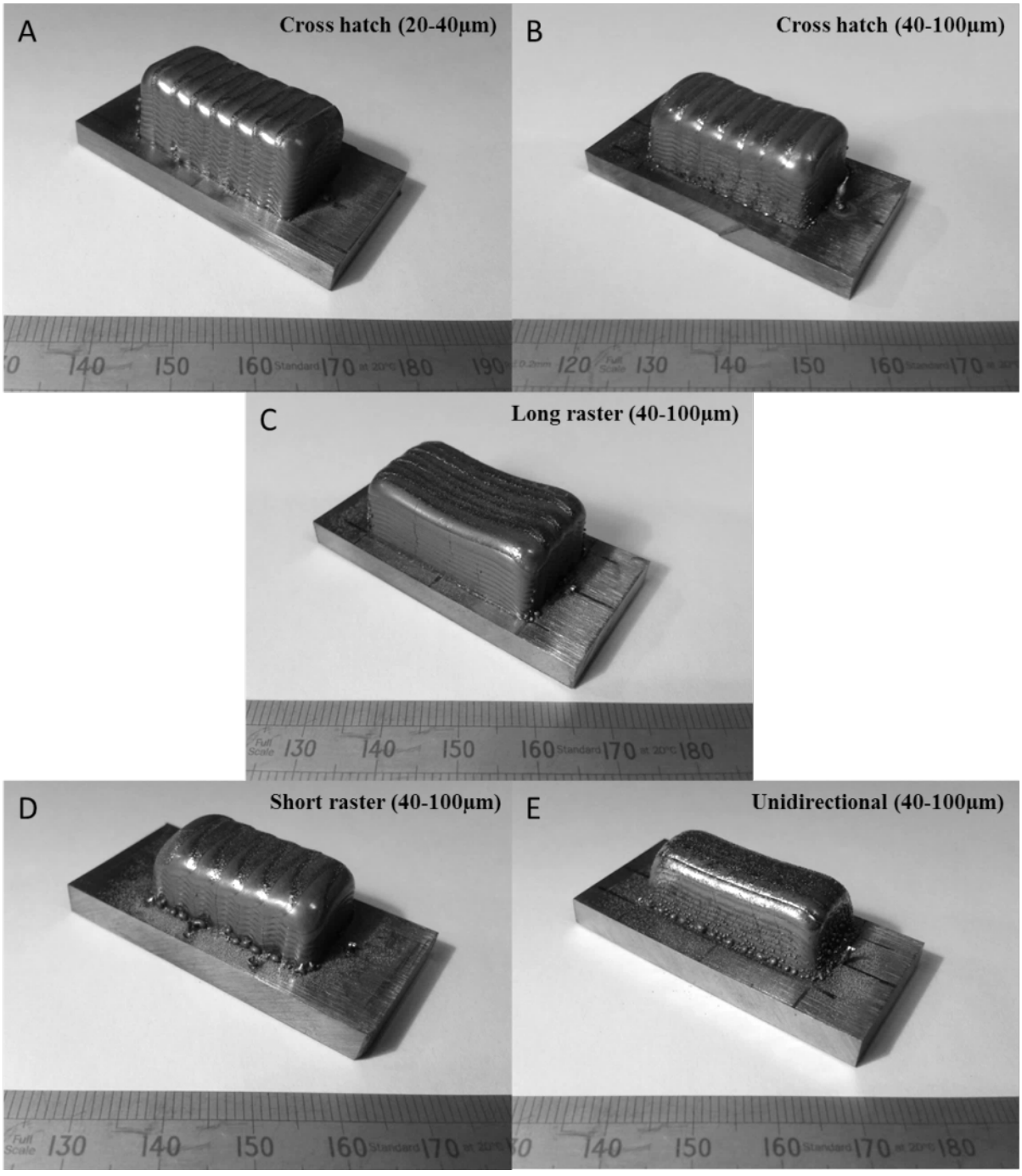

Figure 5-18 - Test blocks deposited using various toolpath patterns.

5.3.2.2.1 Cross hatch toolpath (40-100µm)

The cross hatch toolpath used for this study is the same block that was deposited to validate the DOE response surface in section 4.3.5, also used for comparison with the block deposited using the 20-40µm powder size range in section 5.3.1.

Crack density measurement results for the longitudinal and transverse sections (Figure 5-19) showed that the cracking response was approximately 40% higher when measured in the longitudinal section (Figure 5-10C) than it was for the transverse section (Figure 5-10D), with the crack density remaining relatively constant across the build height, except for the upper layers which decreased significantly (Figure 5-20).

Secondary dendrite arm spacing measurements for the 40-100µm block were recorded in section 5.3.1.3 (Figure 5-14), which shows that the λ_2 length remains relatively consistent between the bottom and the top of the deposit, varying between 4.83µm and 5.2µm respectively.

Temperature measurements for the cross hatch toolpath (Figure 5-21) showed that the deposit temperature increased relatively slowly over the deposition period, achieving a peak temperature of approximately 320°C by the last layer (with temperature measured in the substrate).

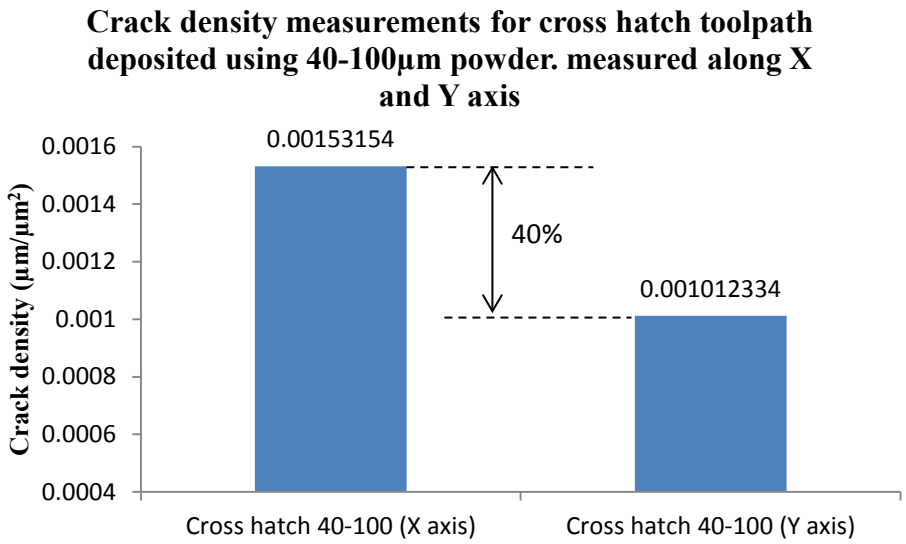

Figure 5-19 - Crack density measurements for cross hatch toolpath, measured along X and Y axis

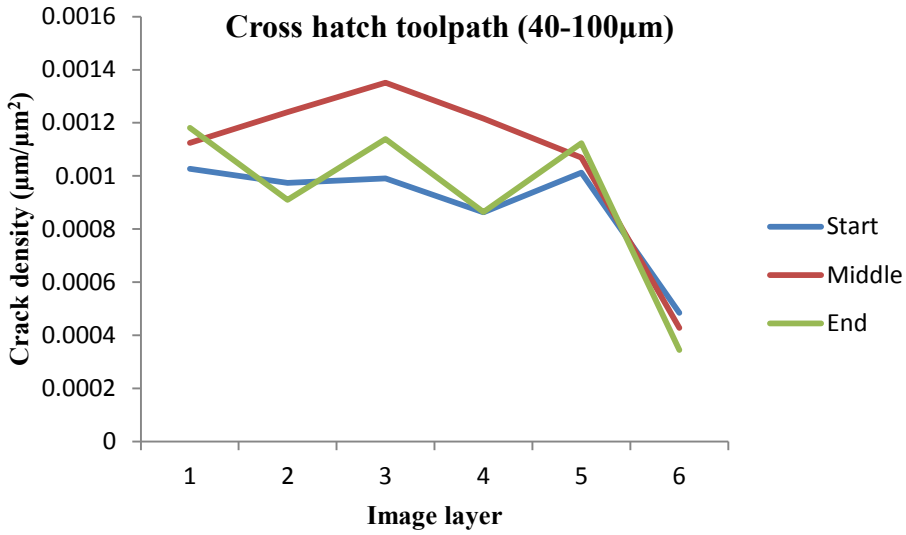

Figure 5-20 - Crack density measurements as a function of deposit height for cross hatch toolpath

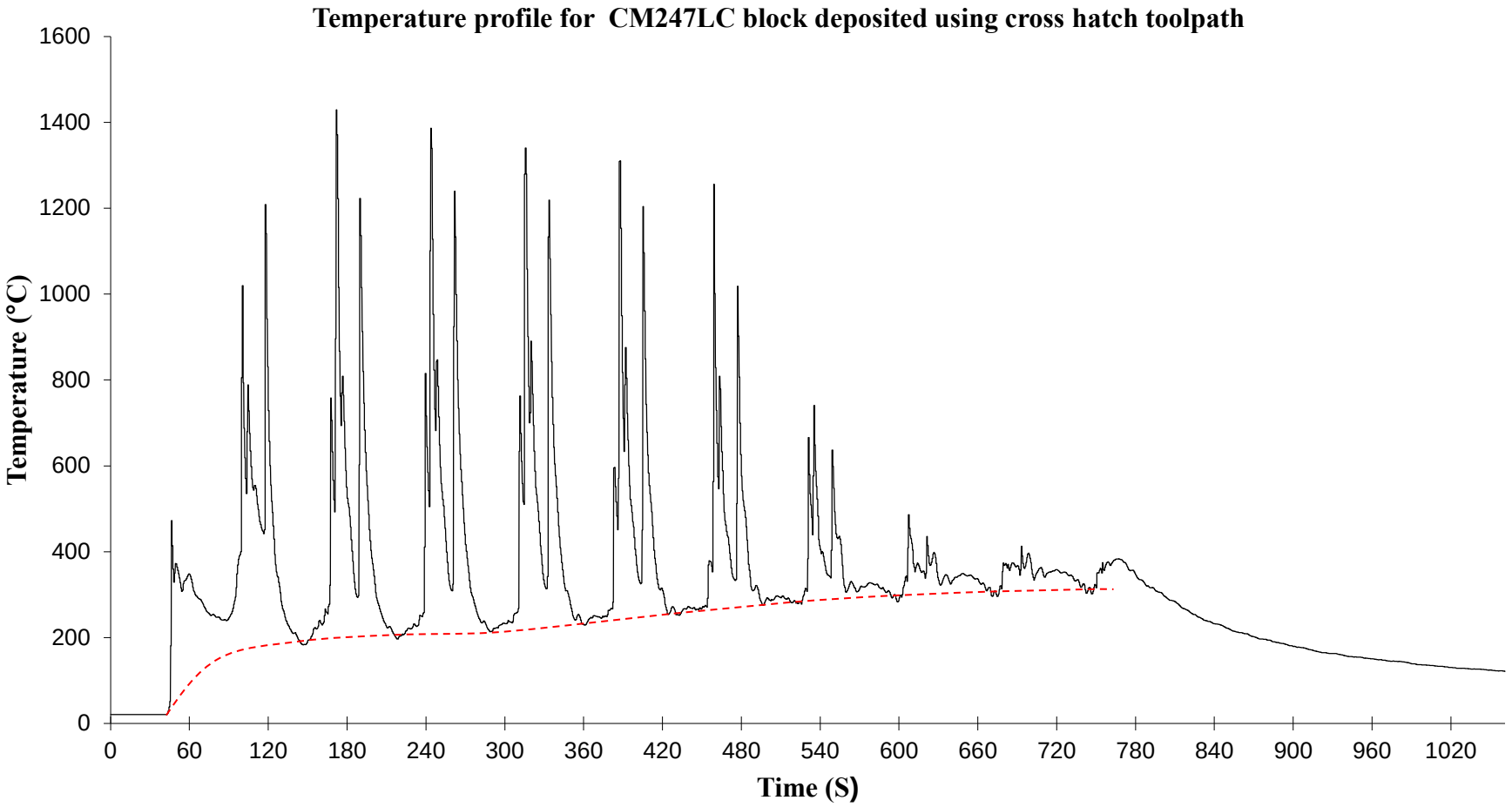

Figure 5-21 - Temperature measurement profile for block deposited using cross hatch toolpath (40-100µm powder)

5.3.2.2.2 Long raster toolpath

Optical microscopy of the block deposited using the long raster toolpath, revealed an anisotropic microstructure (Figure 5-23), comprising of long columnar grains when viewed in the longitudinal section, which are tilted to an angle of approximately 72° to the substrate (Figure 5-22C). When viewed transversely (Figure 5-22D), the microstructure is more random, with more tortuous grain boundaries that change directions frequently, with subsequent zig-zag cracks formed along the boundaries (Figure 5-25).

Cracks of various lengths and size were observed to follow the long grain boundaries, as well as penetrating through the interdendritic regions of the grain interiors in much the same way observed in previous deposits. Micro-cracks were also observed in large quantities (Figure 5-24).

Crack density measurements showed that the cracking response was 14% higher when viewed along the x-axis, than when viewed along the Y axis (Figure 5-26), with a crack density that gradually decreased towards the upper regions of the block (Figure 5-27).

Secondary dendrite arm spacing measurement recorded at different points within the cross section (Figure 5-22D) showed that SDAS varied between 3.3μm near to the bottom of the deposit to 4.7μm in the upper layer (Figure 5-28).

Temperature measurements of the deposited block showed that the substrate temperature reached a maximum of 540°C, but due to malfunction of the data logging equipment the temperature records are incomplete (Figure 5-29).

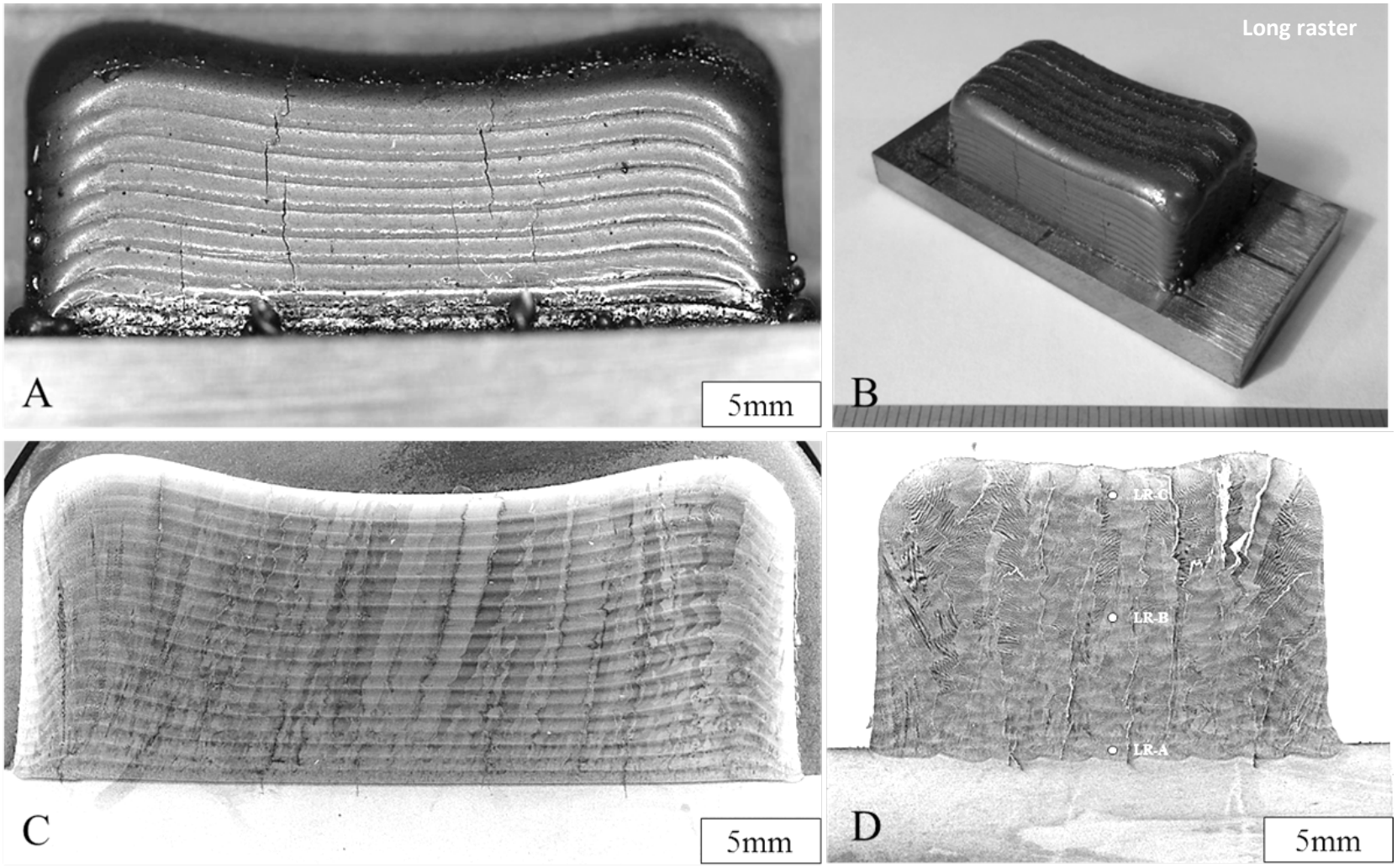

Figure 5-22 - Long raster toolpath test block deposited from 40-100µm CM247LC A) External side view B) External isometric C) Longitudinal section D) Transverse section

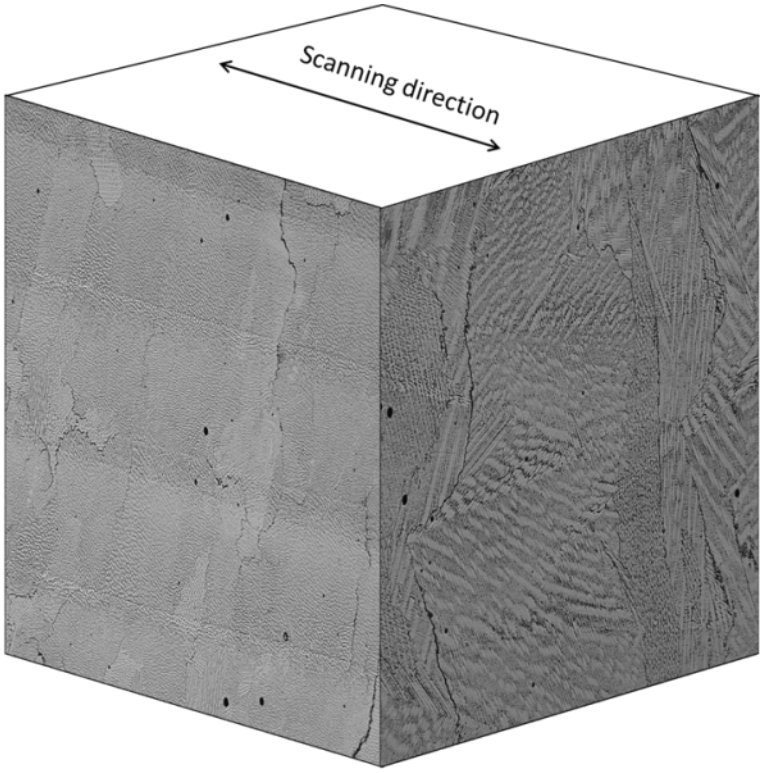

Figure 5-23 – Block deposited using long raster pattern

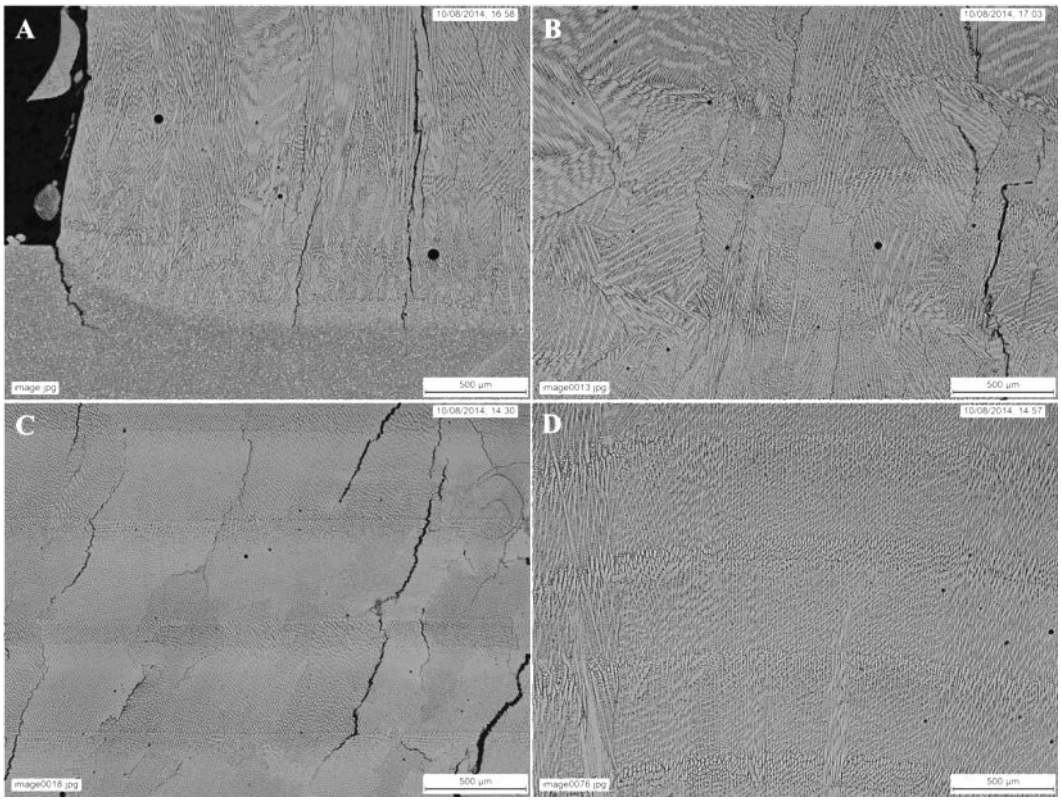

Figure 5-24 - Long raster toolpath, A) End on B) End on C) Side on D) Side on (upper)

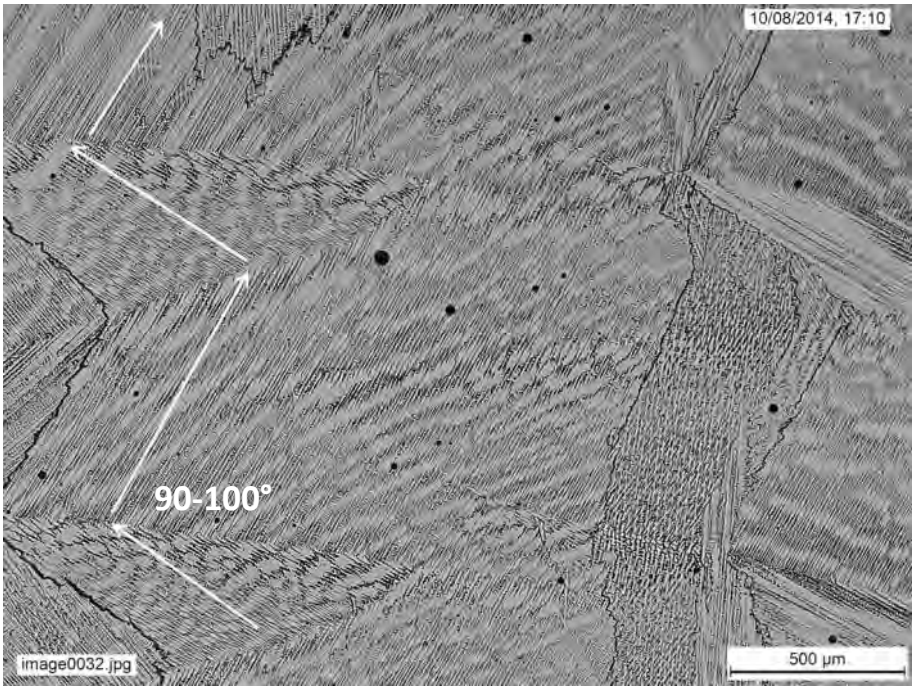

Figure 5-25 - 50x optical micrograph from long raster toolpath, viewed along Y-axis, showing alternating direction of dendrite growth between deposit layers

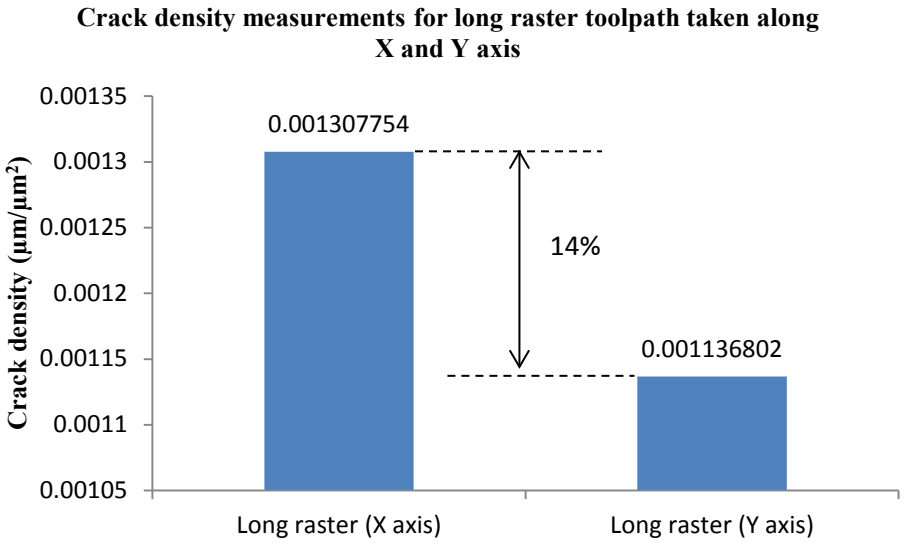

Figure 5-26 - Crack density measurements for block deposited using long raster toolpath, comparing the results found for the X and Y measurement axis.

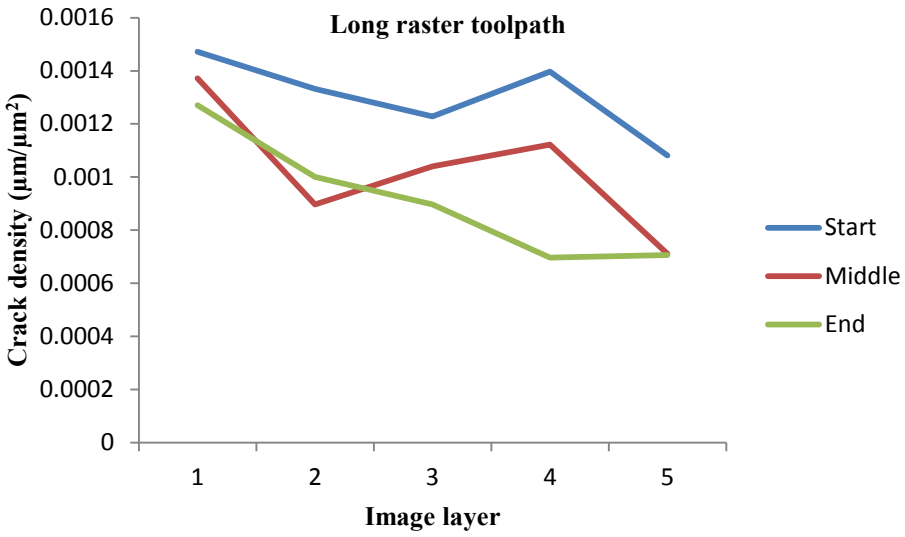

Figure 5-27 - Graph illustrating crack density as a function of deposit height for long raster toolpath

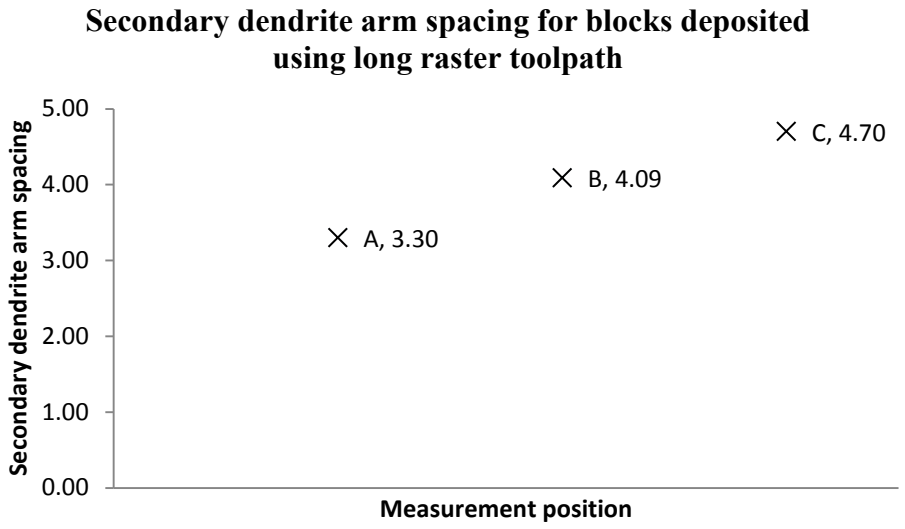

Figure 5-28 - SDAS measurements for block deposited using long raster toolpath

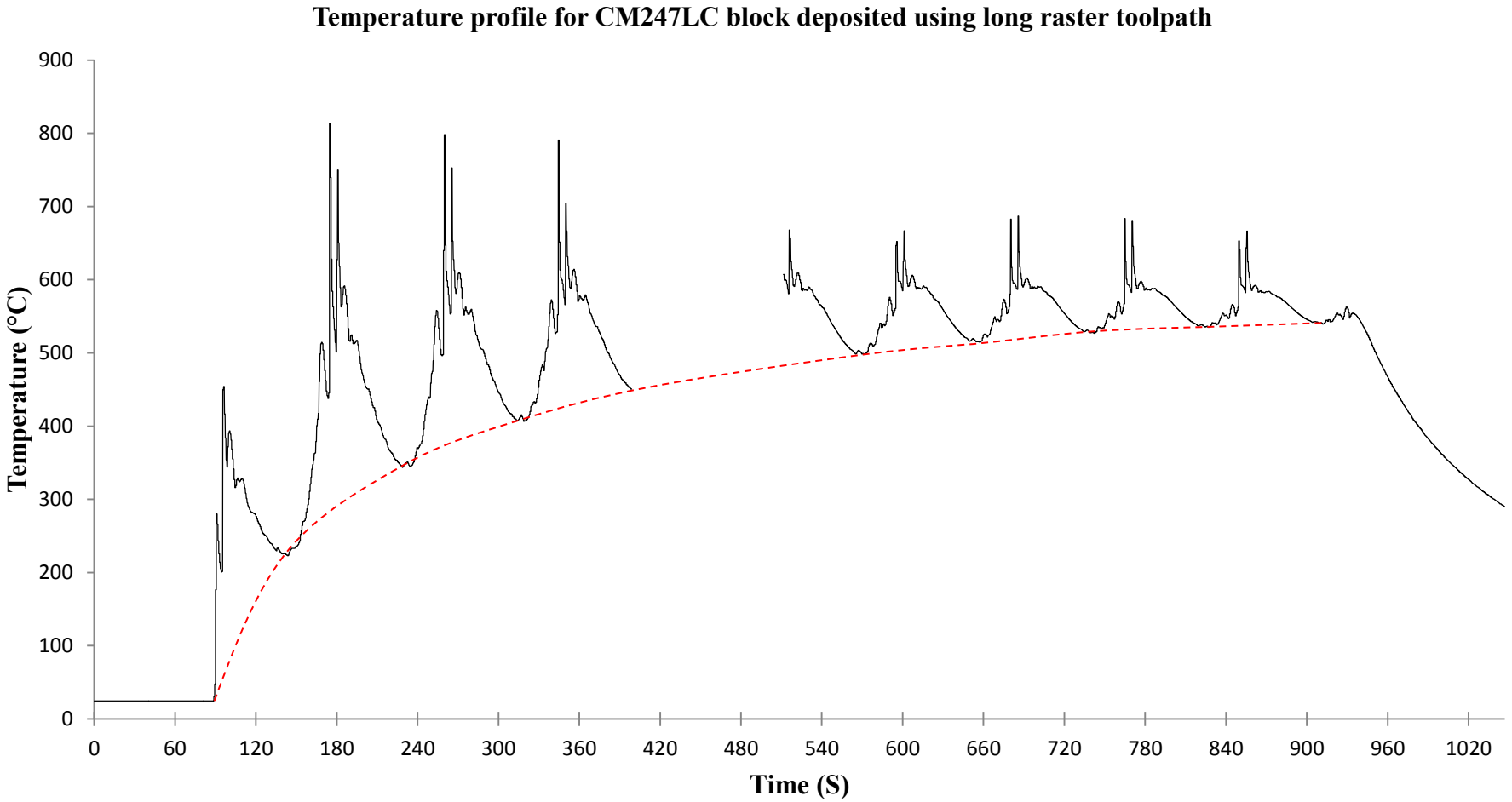

Figure 5-29 - Temperature profile for long raster toolpath (Data missing due to software malfunction)

5.3.2.2.3 Short raster toolpath

Optical microscopy of the block deposited using the short raster toolpath, when viewed transversely, show a microstructure comprising of columnar dendritic grains, with clearly visible inter-layer fusion lines and large cracks that form along the solidification boundaries (Figure 5-30D).

When viewed longitudinally, the microstructure consists of shorter, more randomised grains (Figure 5-30C), with a large number of cracks along the solidification boundaries and interdendritic regions (Figure 5-31-Figure 5-32). Comparison of crack density measurements along different direction showed that there are 54% more cracks in the longitudinal section than there are in the transverse section (Figure 5-33), with a reduction in crack density in the upper layers (Figure 5-34).

Secondary dendrite arm spacing measurements were conducted at various positions in the transverse section (Figure 5-30D) to examine the change in λ_2 with deposit height, but were also measured longitudinally along the bottom layer, to examine how λ_2 changes within the first layer due to heat accumulation. Transverse measurements (Figure 5-30D) showed that λ_2 varied between 3.5µm in the bottom layer and 5.8µm in the top layer (Figure 5-35), while longitudinal measurements (Figure 5-30C) varied between 2.9µm and 4.3µm for the first layer (Figure 5-36).

Temperature measurement during deposition (Figure 5-37) showed that the block reached a temperature of approximately 540°C by the end of deposition, although a software malfunction produced incomplete data.

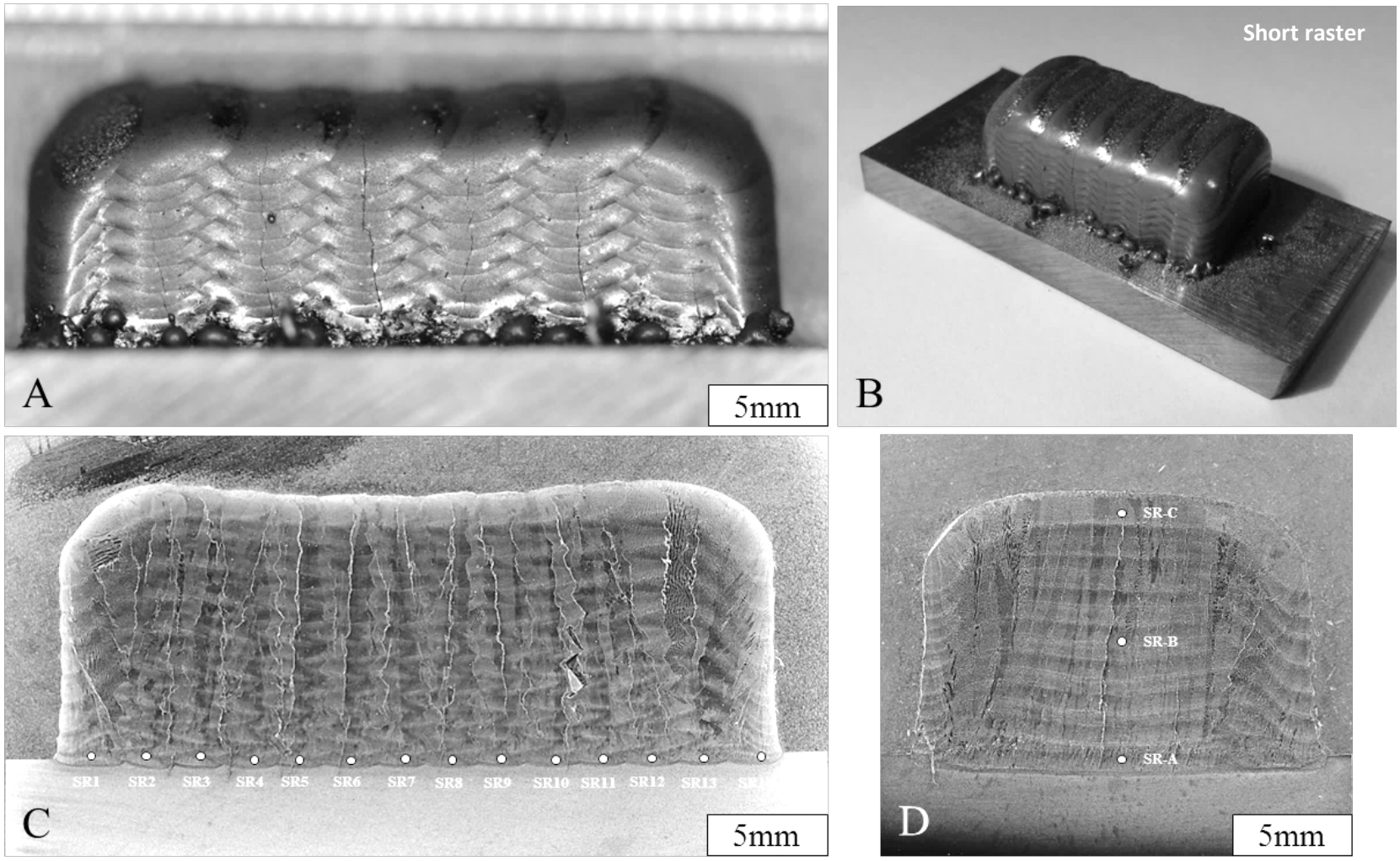

Figure 5-30 - Short raster toolpath test block deposited from 40-100µm CM247LC A) External side view B) External isometric C) Longitudinal section D) Transverse section

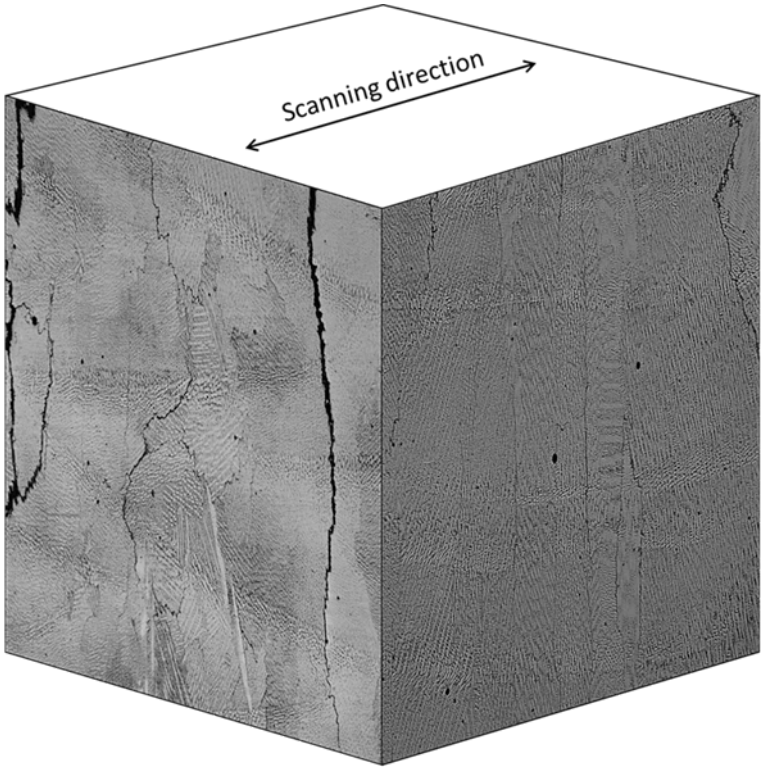

Figure 5-31 - 50x optical micrographs taken along X and Y axis for short raster toolpath

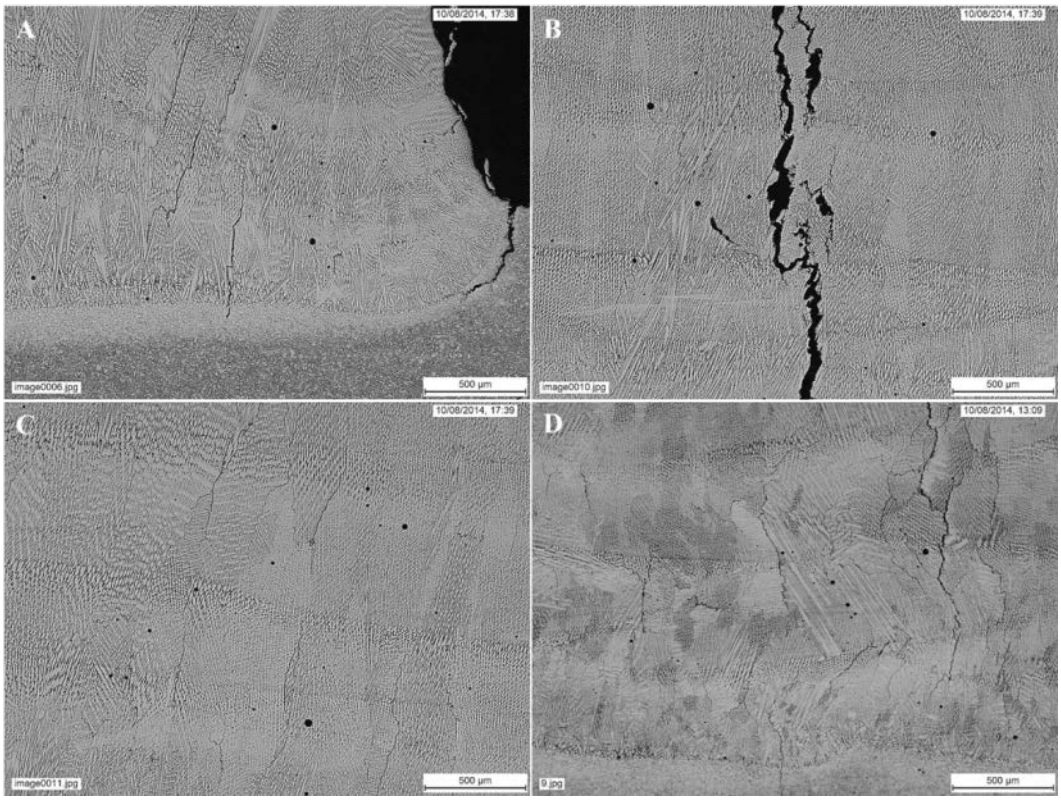

Figure 5-32 - Short raster toolpath A) End on B) End on C) side on D) Side on

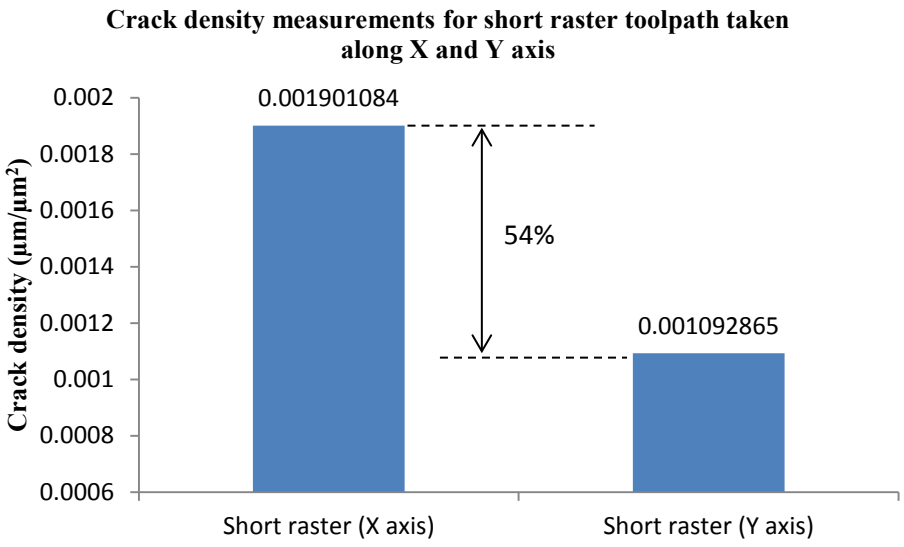

Figure 5-33 - Crack density measurements for block deposited using short raster toolpath, comparing the results found for the X and Y measurement axis.

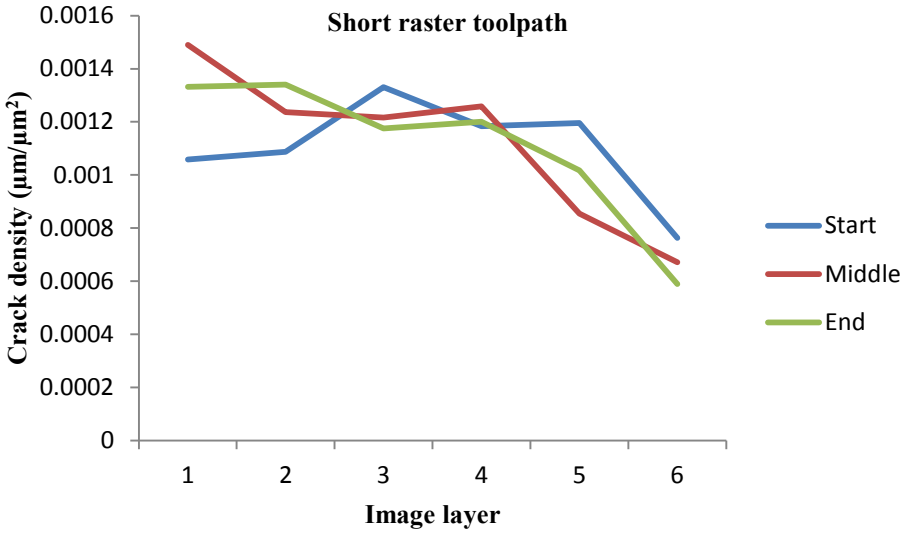

Figure 5-34 - Graph illustrating crack density as a function of deposit thickness for short raster toolpath

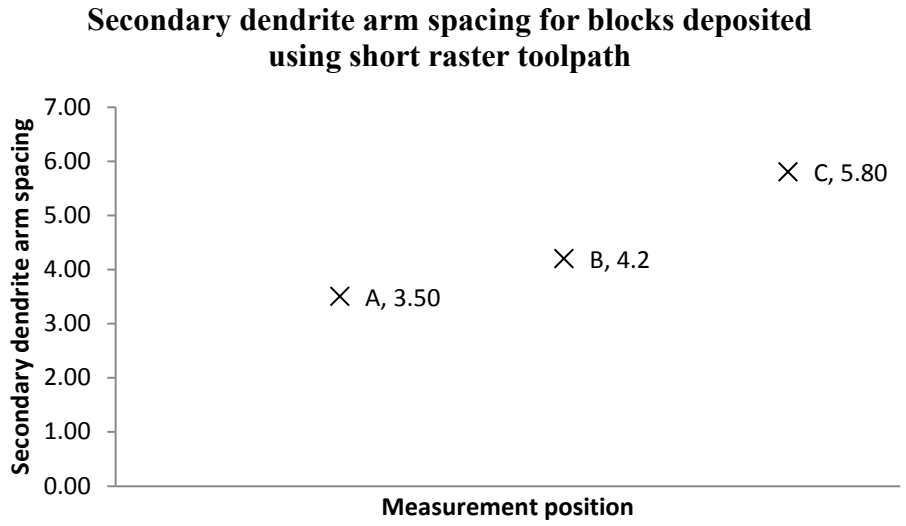

Figure 5-35 - SDAS measurements for block deposited using the short raster toolpath

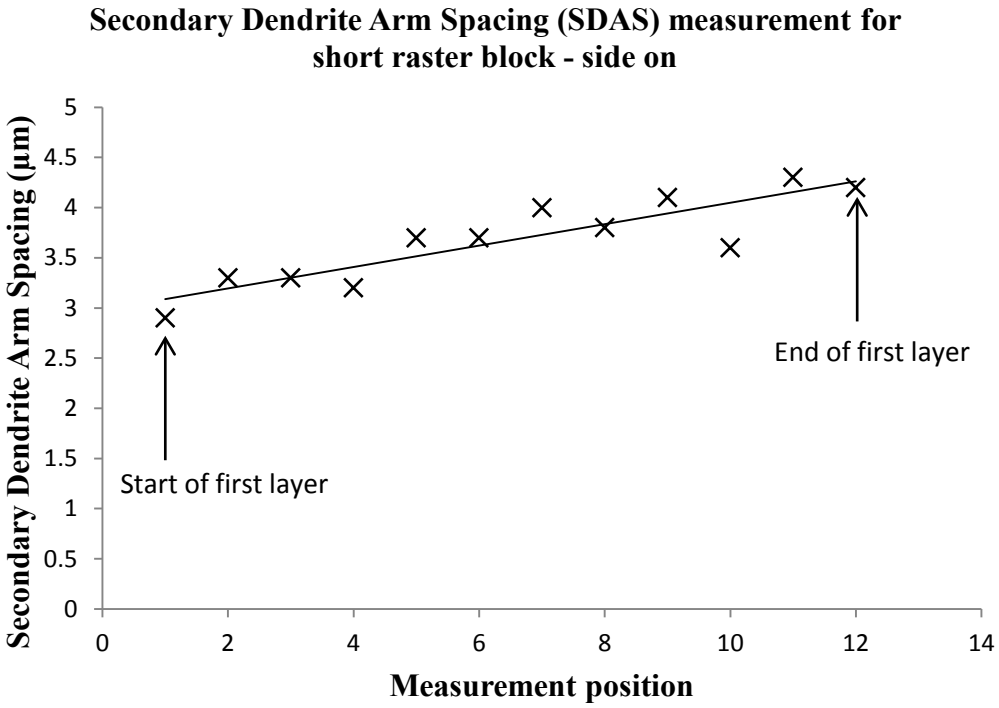

Figure 5-36 - SDAS measurements recorded across the bottom layer of the short raster toolpath (Figure 5-30C)

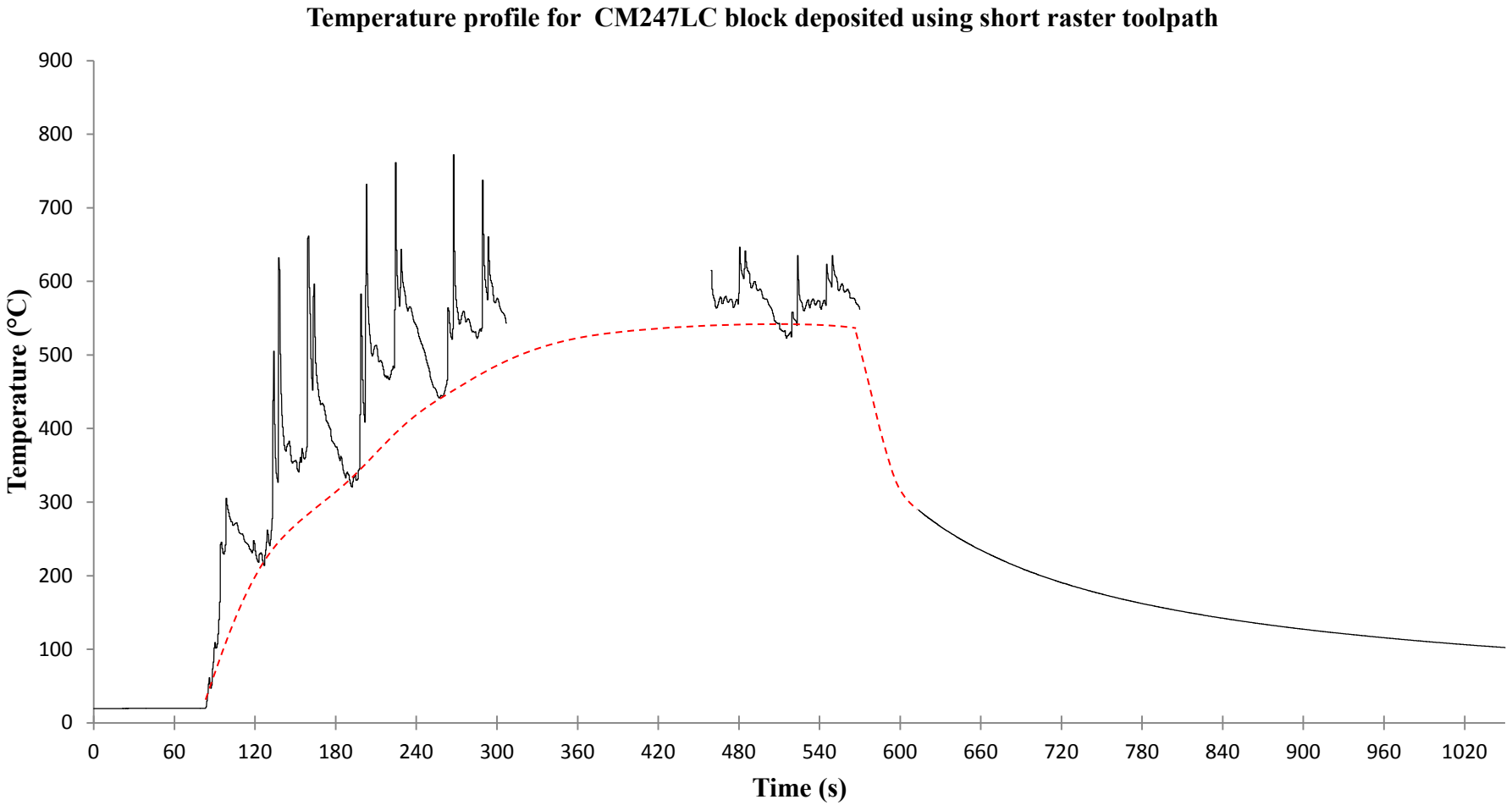

Figure 5-37 - Temperature profile for short raster toolpath – Data missing due to software malfunction

5.3.2.2.4 Unidirectional toolpath

Visual examination of the unidirectional block shows that it has a relatively poor surface finish and shape, with trapezoidal transverse cross section and rounded surfaces (Figure 5-38D). This block also exhibited a greater number of satellite particles, particularly around the toe of the deposit (Figure 5-38B), with surface connected cracks that were tilted along the deposition direction at approximately 65° (Figure 5-38A,C).

Longitudinal section shows that there is a strong metallographic texture of columnar grains tilted along the deposition direction (Figure 5-38C), with long cracks travelling along the columnar grain boundaries (Figure 5-39, Figure 5-40C,D). Viewing the deposit transversely reveals a more randomised microstructure (Figure 5-38D, Figure 5-40A,B) with large cracks propagating horizontally, as well as vertically, although the randomised grain structure limited the crack length somewhat Figure 5-41.

Comparison of crack density between longitudinal and transverse sections shows that there are approximately 72% more cracks in the longitudinal direction (Figure 5-43), with crack density changing very little across the height of the deposit (Figure 5-44).

Secondary dendrite arm spacing measurements show that the λ_2 distance is 3.3µm for the first layer, then 3.7µ for the middle and top layers (Figure 5-45). Temperature measurements during deposition showed that the block remained relatively cool throughout, reaching a temperature of approximately 205°C by the end of deposition (Figure 5-46).

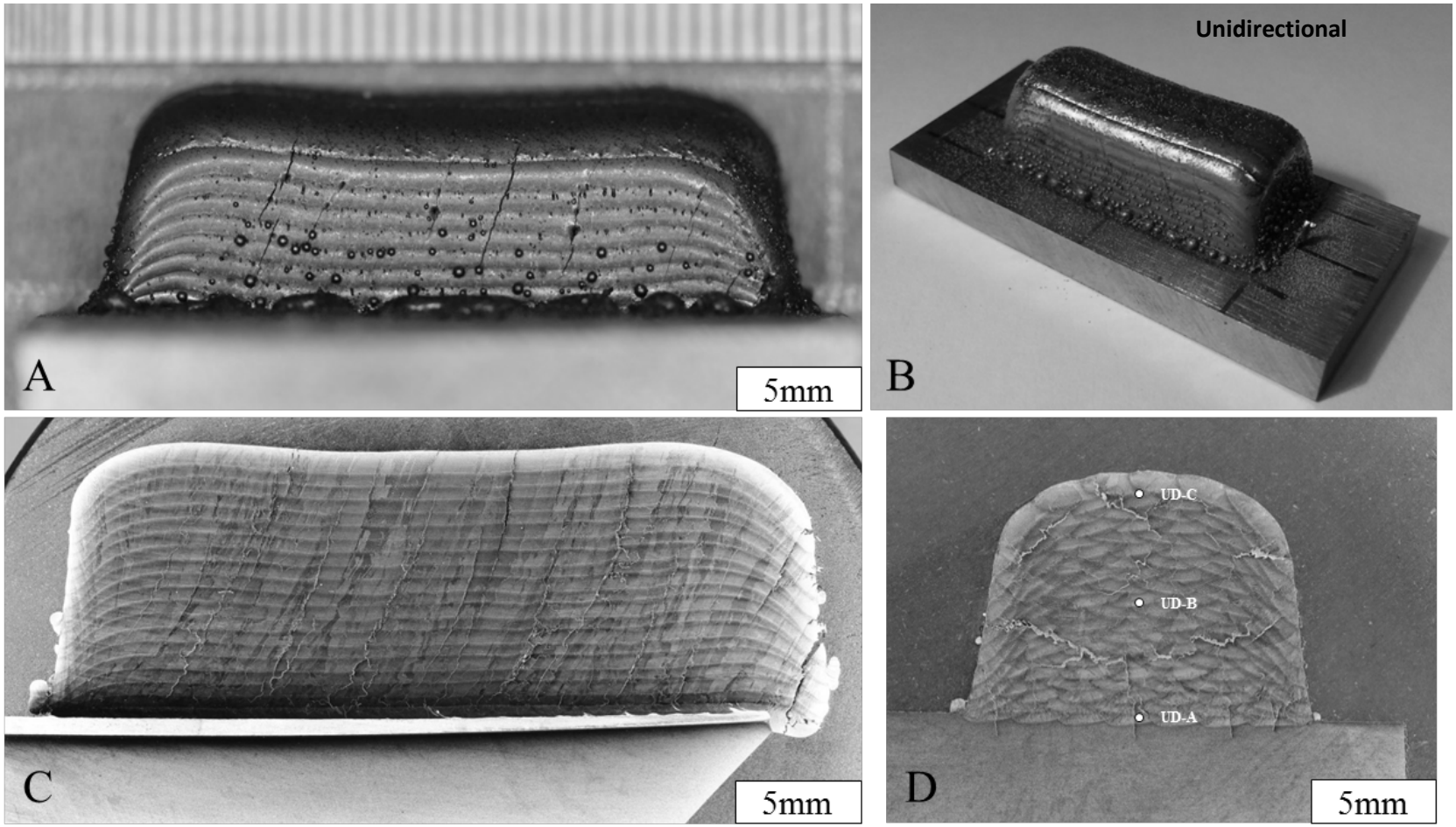

Figure 5-38 - Unidirectional toolpath test block deposited from 40-100µm CM247LC A) External side view B) External isometric C) Longitudinal section D) Transverse section

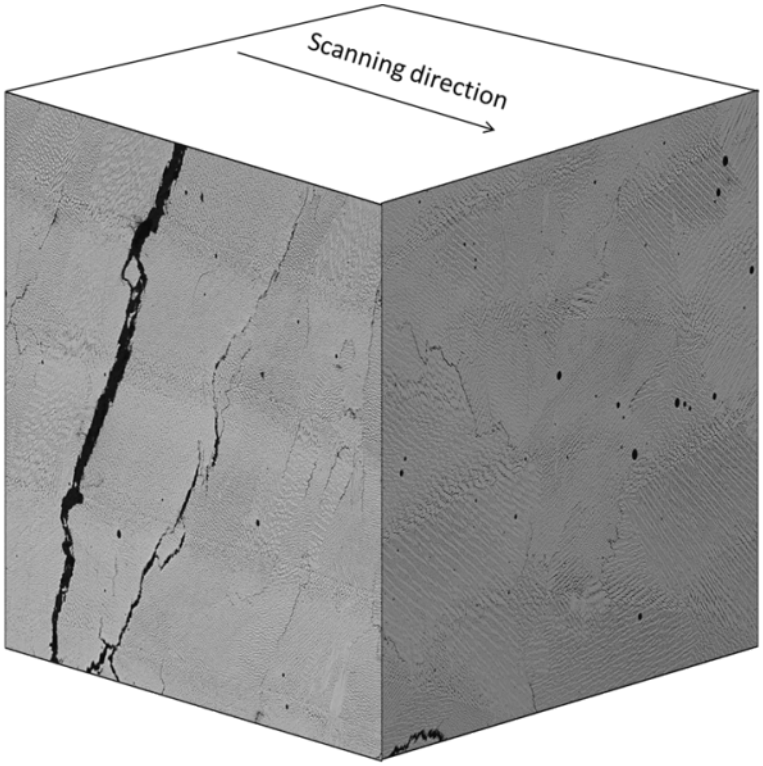

Figure 5-39 - Unidirectional block viewed along the X and Y axis

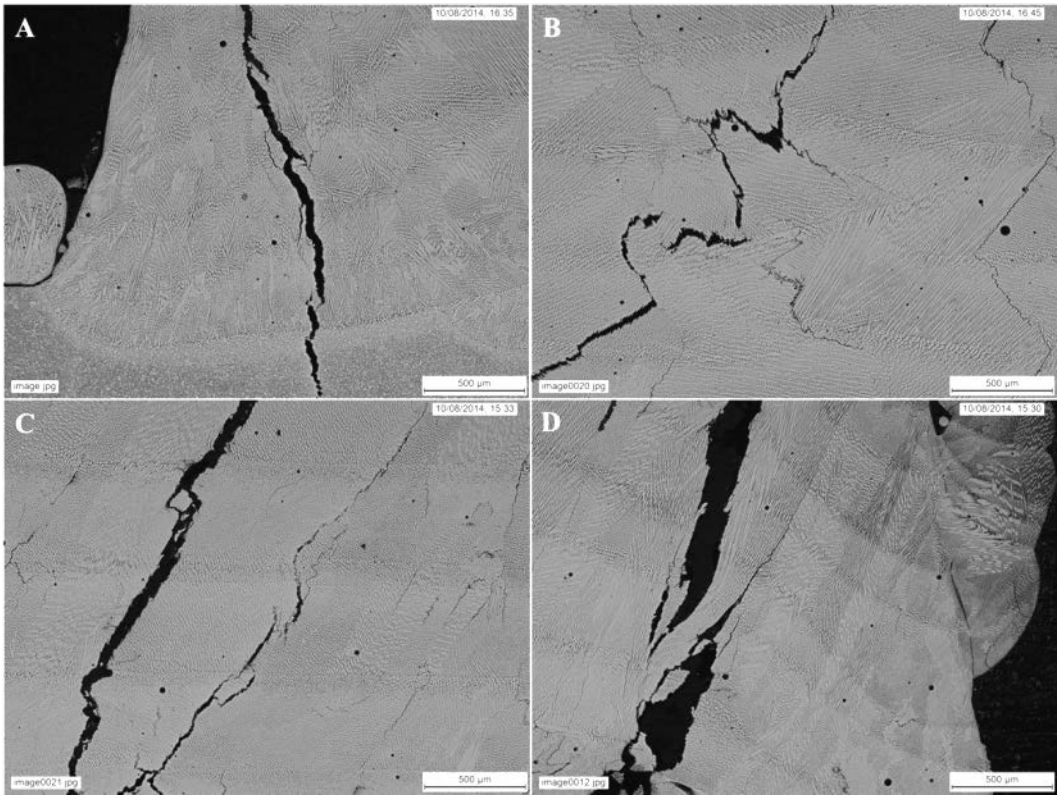

Figure 5-40 – Optical micrographs of unidirectional block A) Deposit toe (transverse) B) transverse showing tortuous grain boundary C) Longitudinal showing columnar grain and crack D) Longitudinal at deposit end.

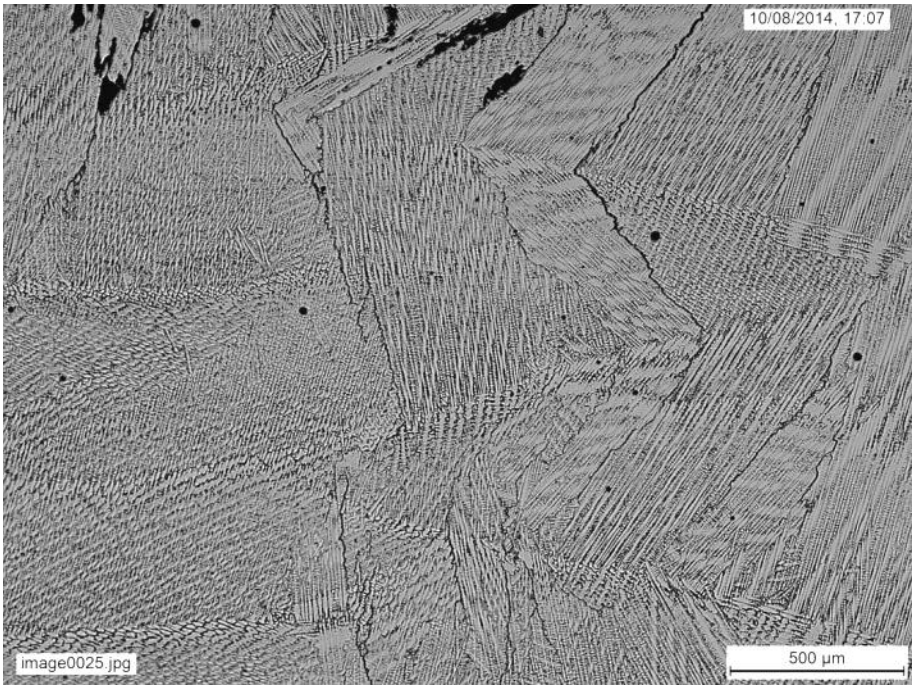

Figure 5-41 - Transverse section of unidirectional toolpath

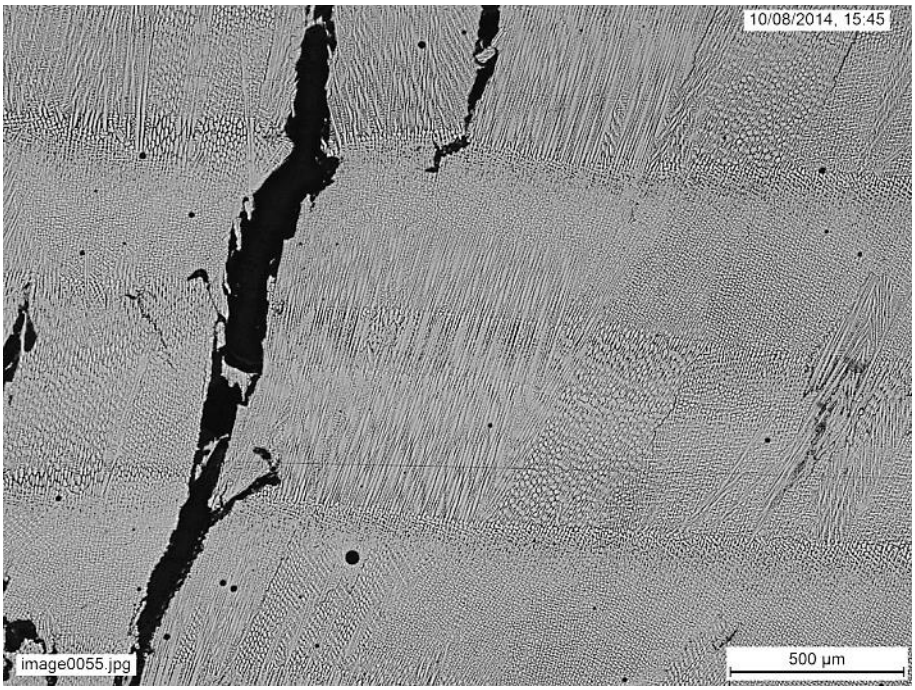

Figure 5-42 - Longitudinal section of unidirectional toolpath

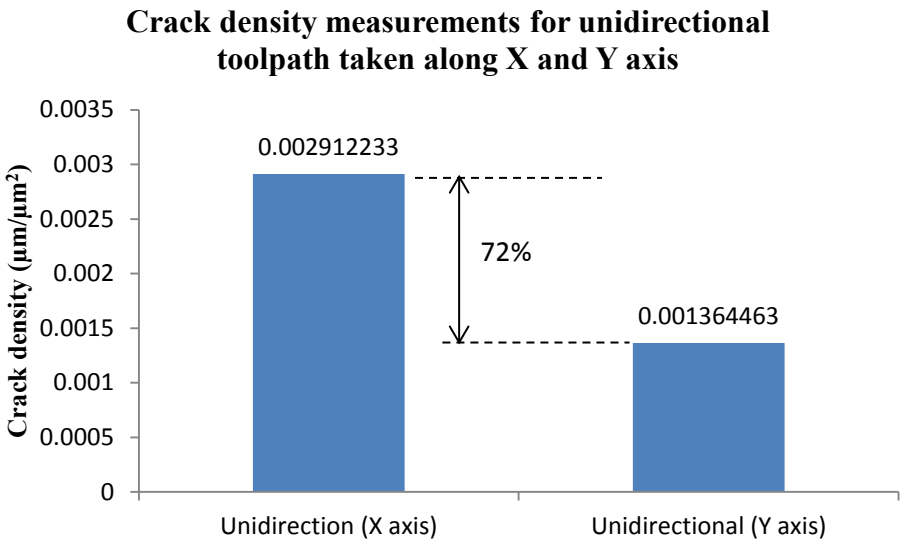

Figure 5-43 - Crack density measurements for block deposited using unidirectional toolpath, comparing the results found for the X and Y measurement axis.

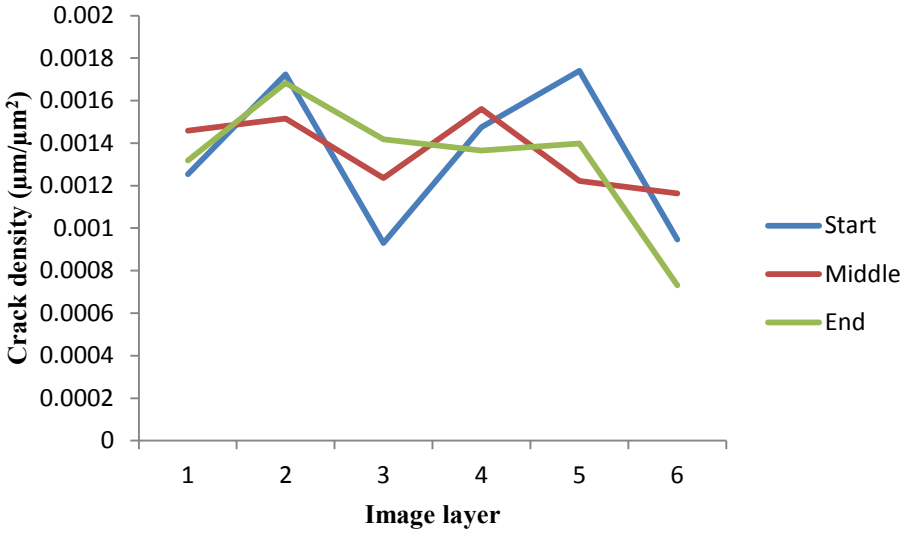

Figure 5-44 - Graph illustrating crack density as a function of deposit thickness for unidirectional toolpath

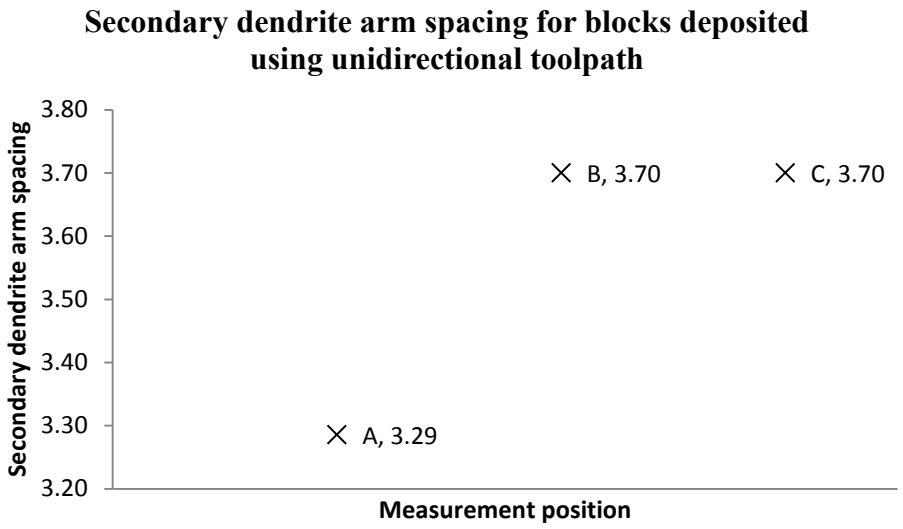

Figure 5-45 - SDAS measurements for block deposited using the short raster toolpath

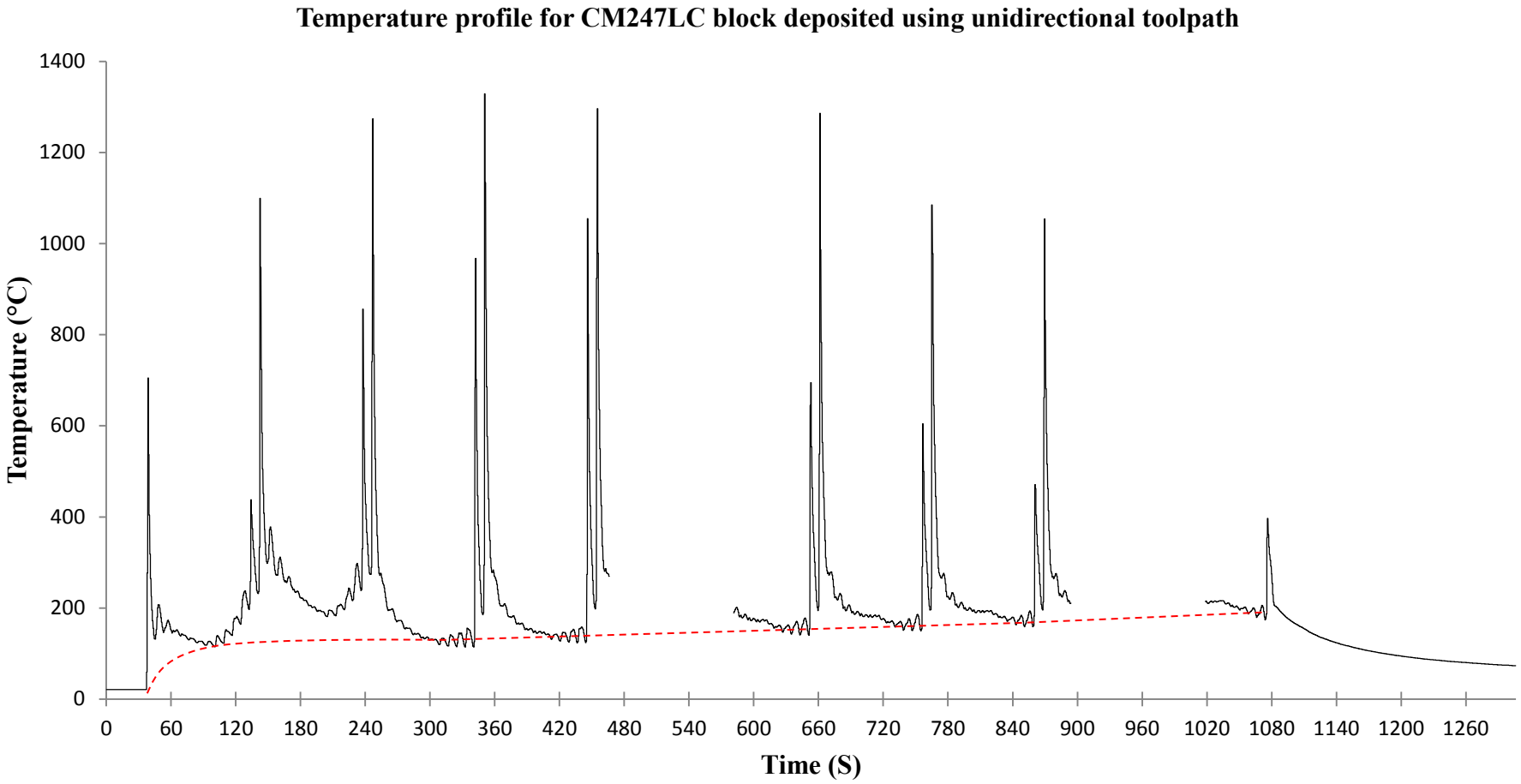

Figure 5-46 - Temperature profile for CM247LC block deposited using unidirectional toolpath

5.3.2.3 Results summary

5.3.2.3.1 Comparison of secondary dendrite arm spacing measurements

Table 5-7 - SDAS measurement results for blocks deposited using different approaches

	20-40µm cross hatch block (µm)	40-100µm cross hatch block (µm)	Long raster block (µm)	Short raster block (µm)	unidirectional block (µm)
Bottom	3.03	4.83	3.30	3.50	3.29
middle	4.10	5.30	4.09	4.2	3.70
top	5.15	5.20	4.70	5.80	3.70

5.3.2.3.2 Comparison of crack density measurements

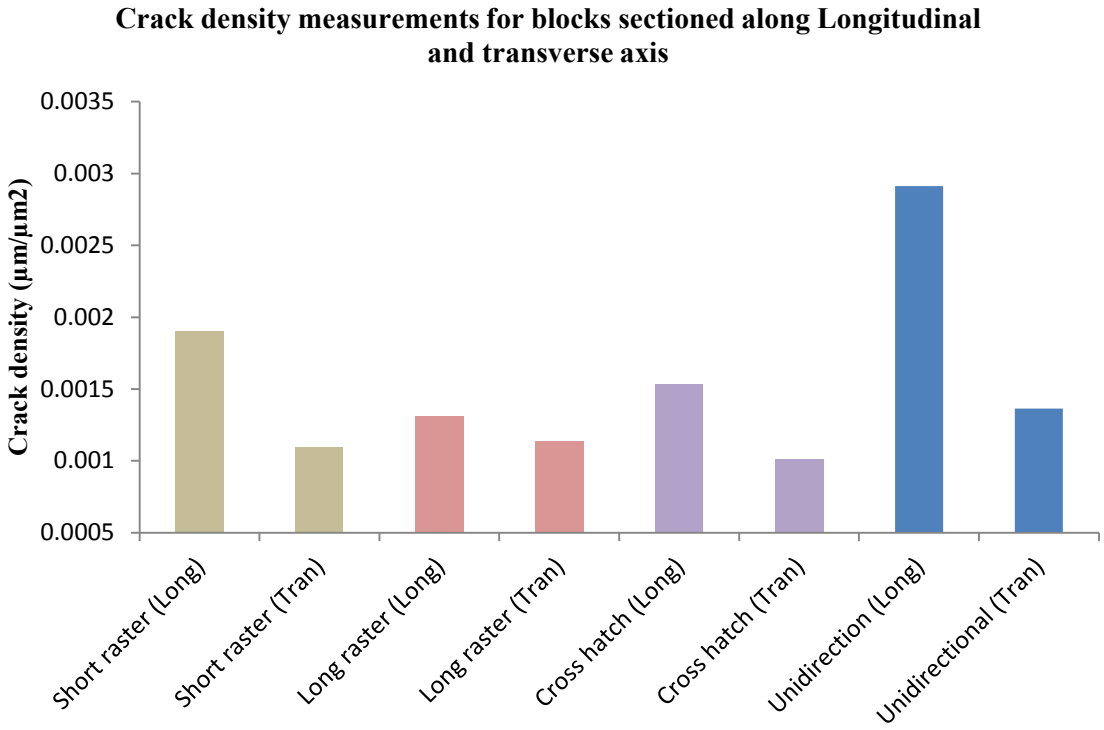

Figure 5-47 - Graph illustrating crack density measurements for different toolpaths when viewed along longitudinal and transverse axis.

5.3.3 Experiment 3 - The effect of pre-heating on crack formation

5.3.3.1 Parameter development trials

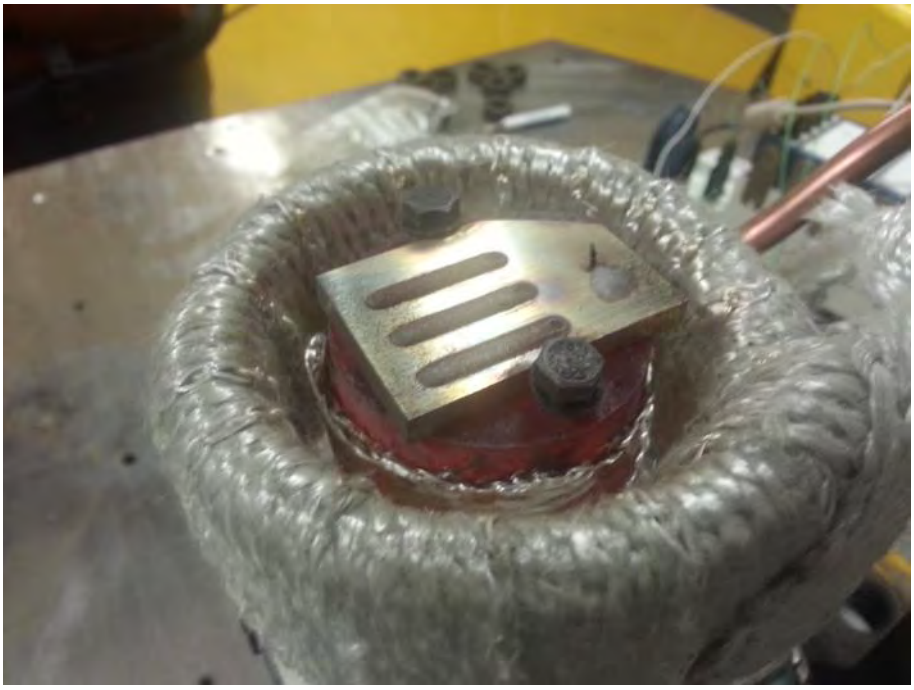

Figure 5-48 - Dilution calibration trial onto preheated CM247LC substrate

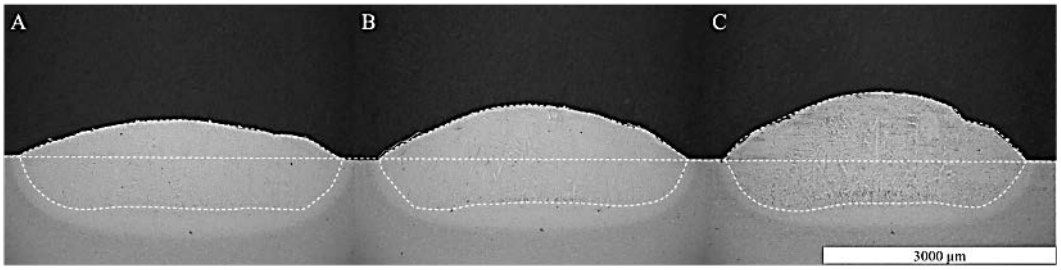

Figure 5-49 - Single tracks deposited at A) 2.6 g/min B) 4.8 g/min C) 7 g/min powder feed rate, using 40-100µm CM247LC powder onto substrate preheated to 800°C using combined laser + induction preheating

Table 5-8 - Dilution and track width measurements for single tracks deposited onto 800°C preheated substrate

Laser power	Scanning speed	Laser spot diameter	Powder feed rate	Measured dilution	Track width
W	mm/s	mm	g/min		(mm)
1000	5	3	2.6	0.552	4.37
			4.8	0.903	4.15
			7	1.227	4.04

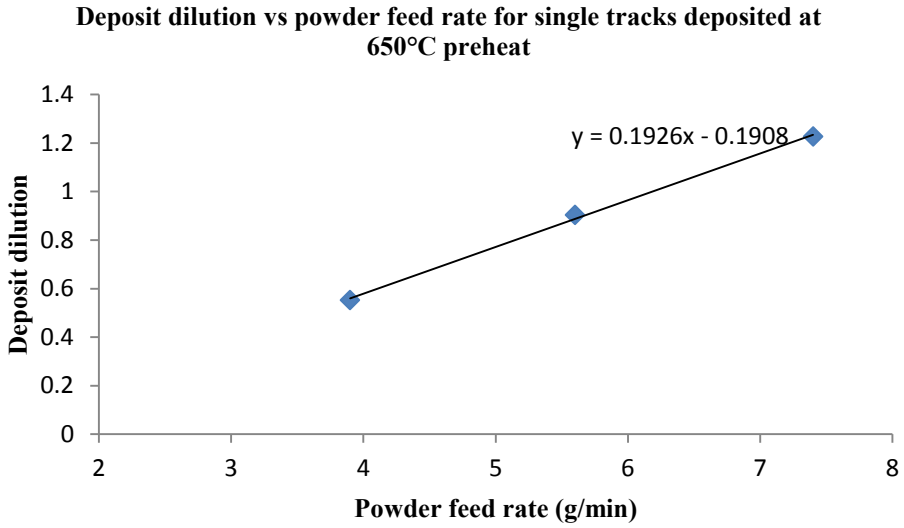

Figure 5-50 - Dilution measurement results for single tracks deposited using increasing powder feed rates for 650°C preheated substrate

Single track dilution trials conducted on an 800°C preheated substrate (Figure 5-48) produced tracks that were significantly broader than those produced previously (Figure 5-49). Cross sectioned tracks were measured for dilution and track width (Table 5-8) and the results used to calculate the powder feed rate and track separation required to produce a dilution of 1.5 and an overlap of 30% (Figure 5-50).

Using the calculated track separation and powder feed rate, a single layer of 6 overlapping tracks were deposited using the same preheat condition, which was then used to calculate the z-increment for block deposition.

Using the developed parameters (Table 5-5), a block was deposited onto a preheated substrate, using a combination of induction heating and laser preheating to raise the temperature to 800°C prior to deposition (Figure 5-51A). Induction heating was active during deposition to maintain a high temperature, which were recorded during pre-heat and deposition (Figure 5-69 Figure 5-70).

5.2.3.2 Deposition and analysis of test block

Visual examination of the deposited block showed a relatively well formed block, with rounded upper surface and smooth surface finish, with very few satellite particles on the sidewall or deposit toe (Figure 5-51B). No surface connected cracks were observed either on the sidewall or upper surface, but the substrate had suffered some distortion along the long and short axis, causing the ends to curl upwards.

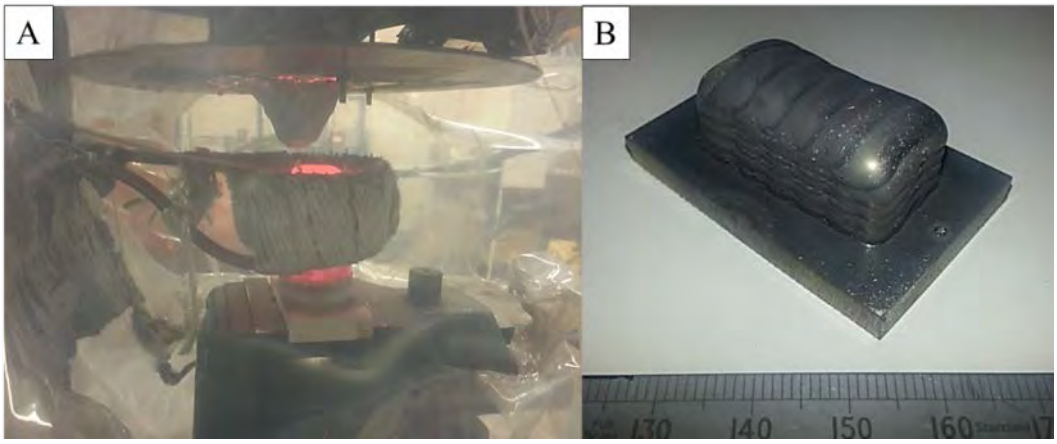

Figure 5-51 - CM247LC block deposited at 800°C substrate preheat temperature with laser assistance – 10 layers thick

Transverse cross sections of the block were prepared for optical microscopy using the established methods, so that measurements of crack density and secondary dendrite arm spacing could be recorded (Figure 5-52).

Microstructural analysis of the transverse cross sections of the block showed a dendritic microstructure similar to that observed for other blocks deposited using the cross hatch toolpath, with randomly oriented short and long columnar grains, and evidence of epitaxial growth across inter-track fusion boundaries (Figure 5-55, Figure 5-56).

Cracking was observed to be greatly reduced for the preheated deposit, but not entirely eliminated. No cracks were observed penetrating into the HAZ, either from the toe of the deposit (Figure 5-53) or the fusion boundary (Figure 5-54). Cracks were still present, but they

were greatly reduced in number and size, mostly being confined to individual deposit layers and residing at the grain boundaries and interdendritic regions (Figure 5-55, Figure 5-57).

Secondary dendrite arm spacing measurements conducted using optical microscopy (Figure 5-52) showed that λ_2 was much larger than previously observed in the earlier trials (Table 5-7), with a λ_2 distance between 9.6µm and 11.3µm (Figure 5-58).

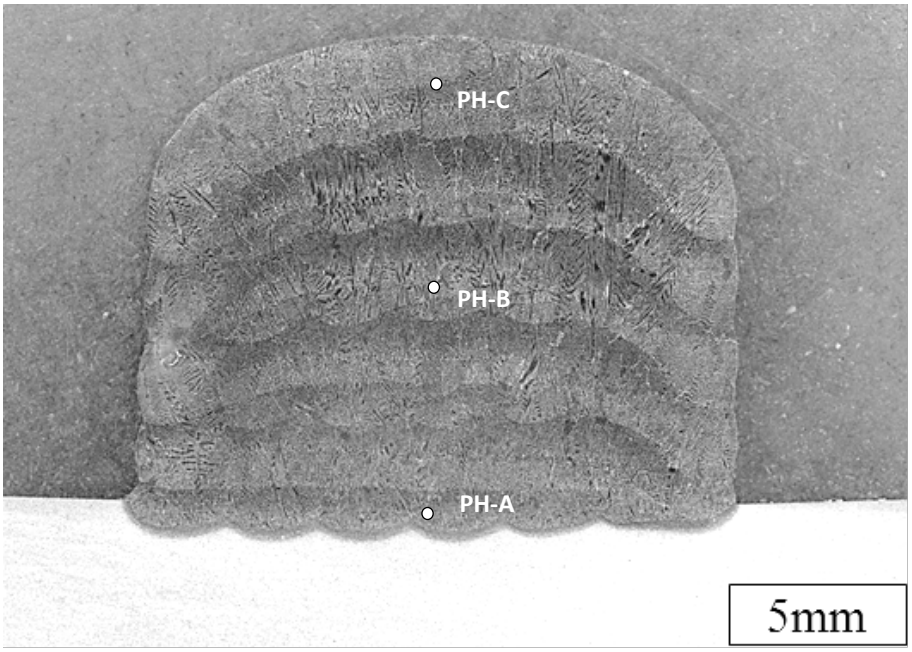

Figure 5-52 - Optical macrograph of block deposited at 800°C preheat, showing position of SDAS measurements (PH-A-C)

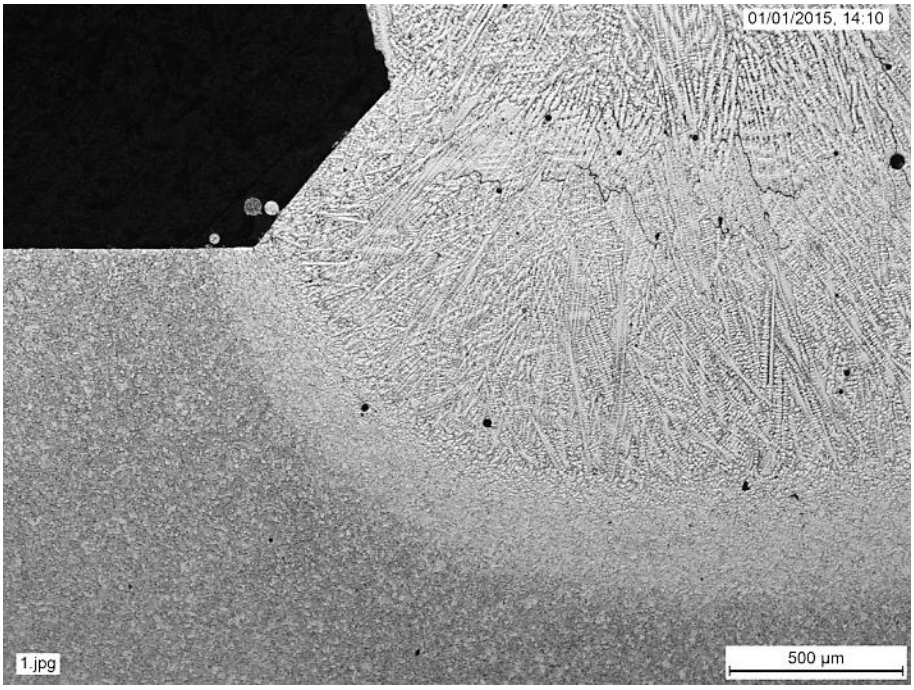

Figure 5-53 - 50x optical micrograph of deposit toe for block deposited using 800°C induction preheat, showing absence of toe cracks, as were observed in blocks deposited without preheat (Figure 5-17)

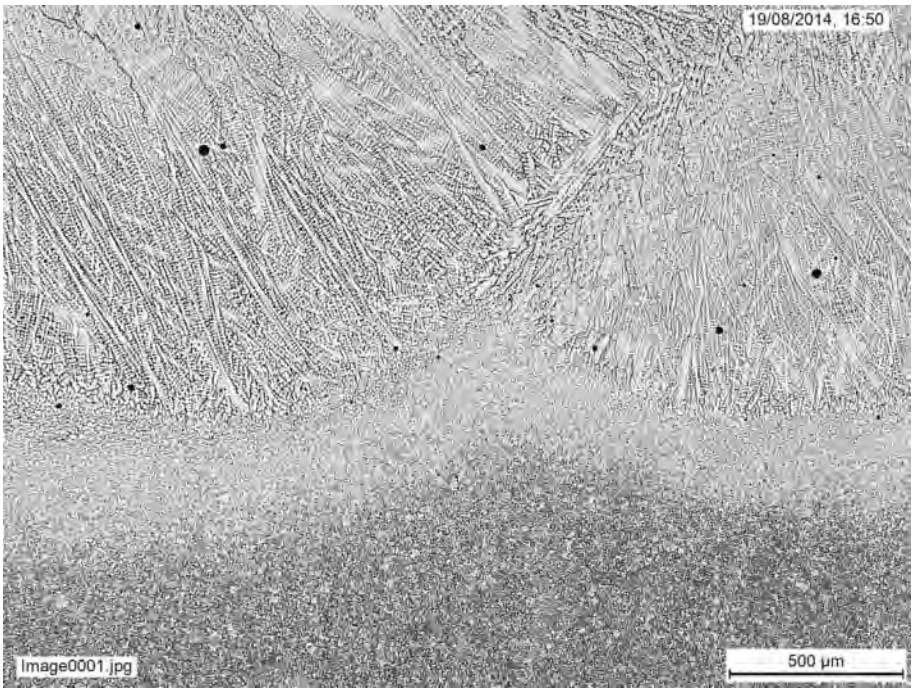

Figure 5-54 - 50x optical micrograph of deposit fusion boundary with substrate for block deposited using 800°C induction preheat

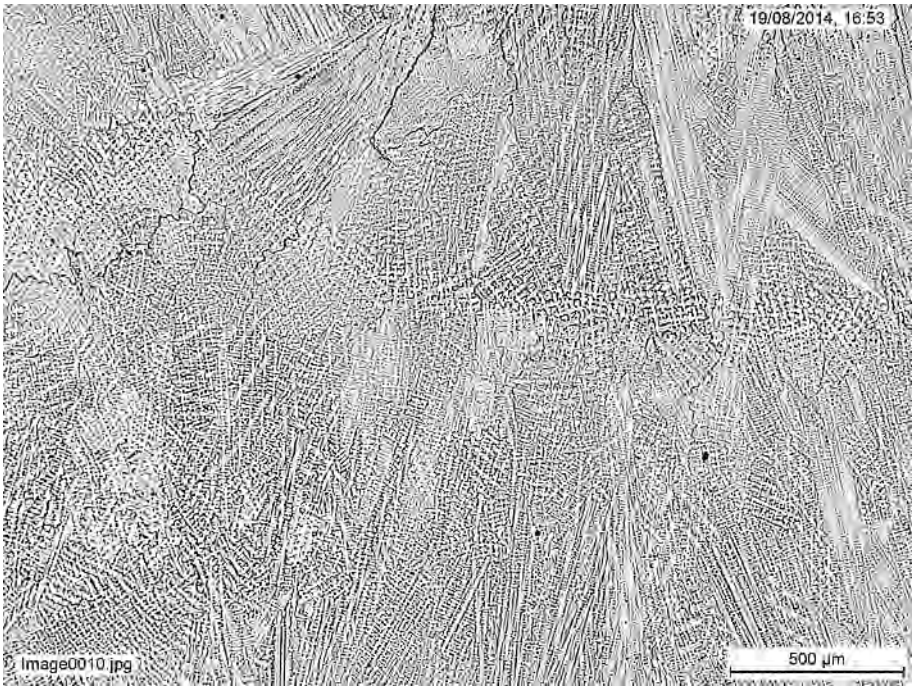

Figure 5-55 - 50x optical micrograph taken from lower region of deposited block, showing presence of fine scale intergranular cracking

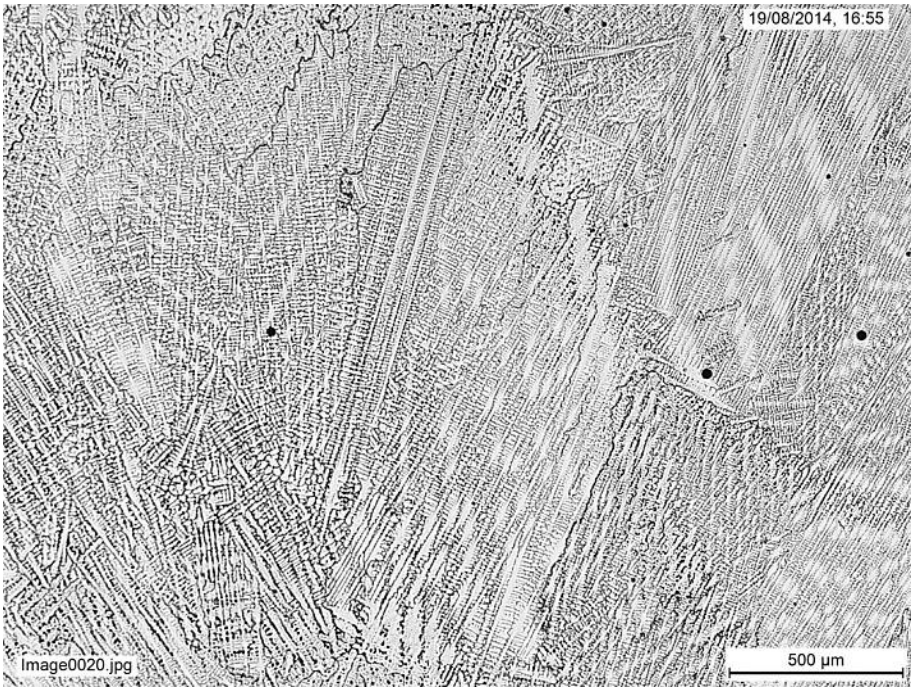

Figure 5-56 - 50x optical micrograph taken from middle of block deposited using 800°C preheat

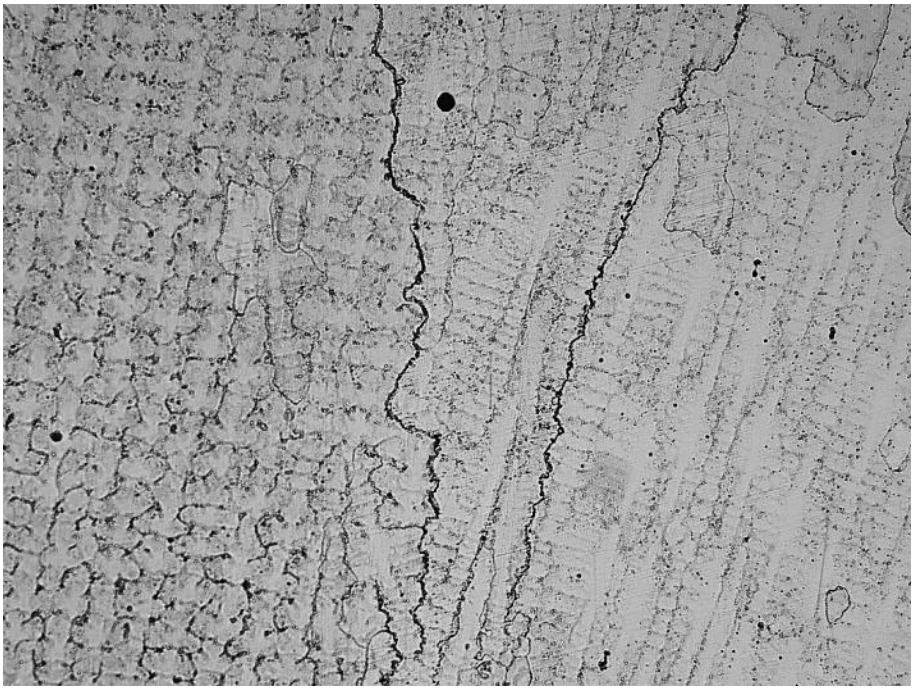

Figure 5-57 - 500x optical micrograph of fine scale inter-dendritic cracking in block deposited using 800°C preheat

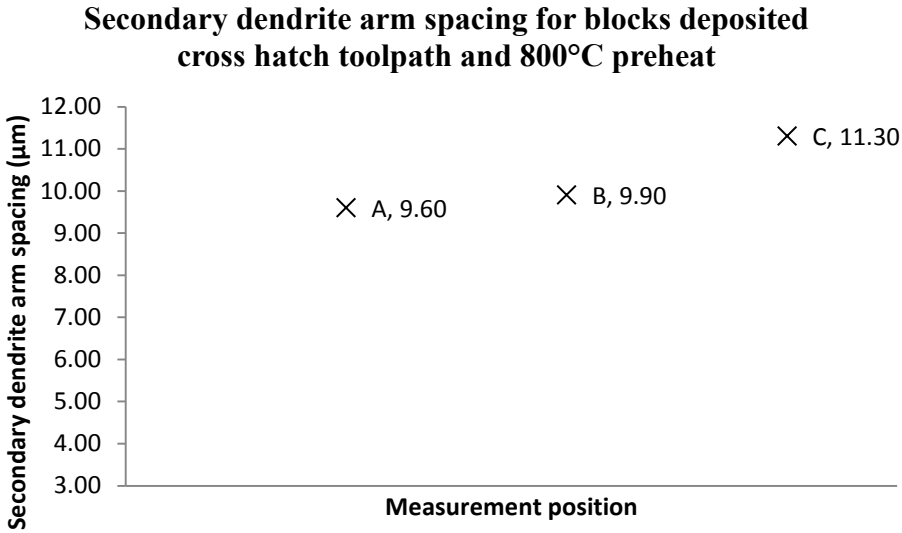

Figure 5-58 - SDAS measurements for block deposited using 800°C preheat

5.3.3.3 SEM characterisation of preheated deposit

SEM micrographs taken at different locations within the substrate and deposit revealed a dendritic microstructure, with intergranular and interdendritic carbides, γ/γ' eutectic and MC type carbides, similar to the observations made in chapter 4 (Figure 5-60, Figure 5-62).

While cracks were still evident within the block, mainly at the solidification boundaries, it was noted that the quantity was greatly reduced. SEM analysis of the interdendritic regions showed the presence of solidification voids, which are generally located within the grain boundaries and interdendritic regions, at pockets of γ/γ' eutectic (Figure 5-59 - Figure 5-62). This type of void formation was not observed quite so much in previously deposited samples.

The size and morphology of the γ' precipitated within the preheated deposit was also observed through QBSD SEM, which showed that in the lower regions of the deposit, the secondary γ' was more developed, with a cuboidal morphology, between 50nm and 200nm in width. By comparison the SEM micrograph taken from the middle of the deposit showed that the γ' was slightly less developed, with a globular morphology and a diameter of between 50-100nm (Figure 5-62).

Comparison of SEM micrographs taken from the lower (Figure 5-59, Figure 5-60) and middle regions of the block (Figure 5-61, Figure 5-62) appeared to show an absence of primary carbides in the latter. Closer examination of the carbide site revealed what appears to be a straight edged socket, similar in shape to cuboidal MC carbide, measuring approximately 1μm in width (Figure 5-62) with a region of lighter contrast surrounding the socket when viewed using the backscattered detector.

By comparison, the lower region of the deposit has a fine dispersion of discrete carbides along the interdendritic regions, with carbides measuring approximately 0.5μm in width, and no difference in contrast around the edges, as was observed for Figure 5-62.

Examination of the HIP'd CM247LC substrate away from the HAZ showed that the γ' developed during heat consolidation and heat treatment remained relatively unchanged, but small unidentified voids started to appear, close to the γ/γ' interfaces (Figure 5-63, Figure 5-64).

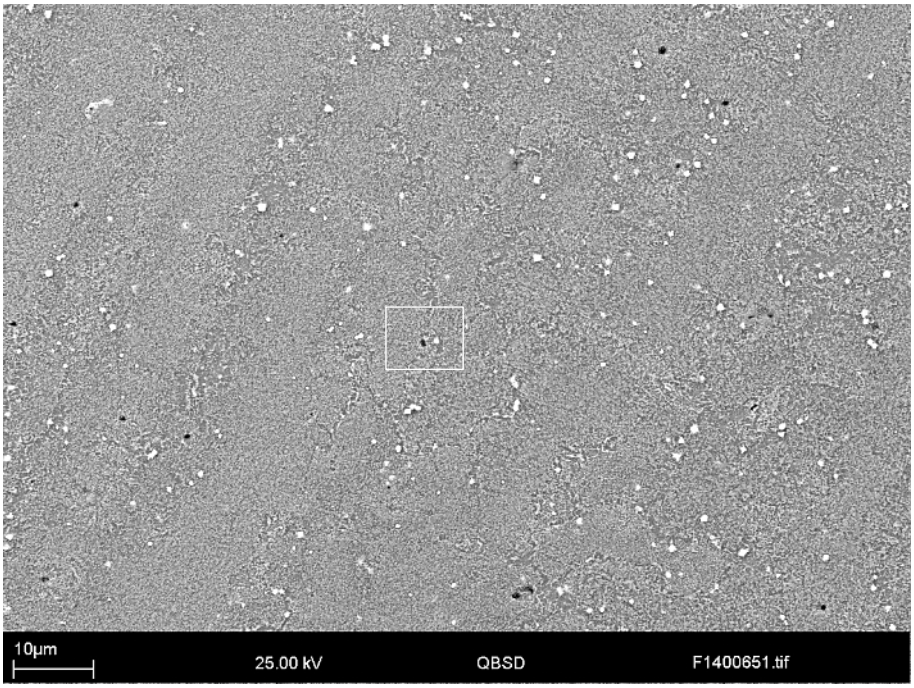

Figure 5-59 - QBSD SEM micrograph of lower region of deposit , showing presence of sub-micron precipitates within the interdenritic regions.

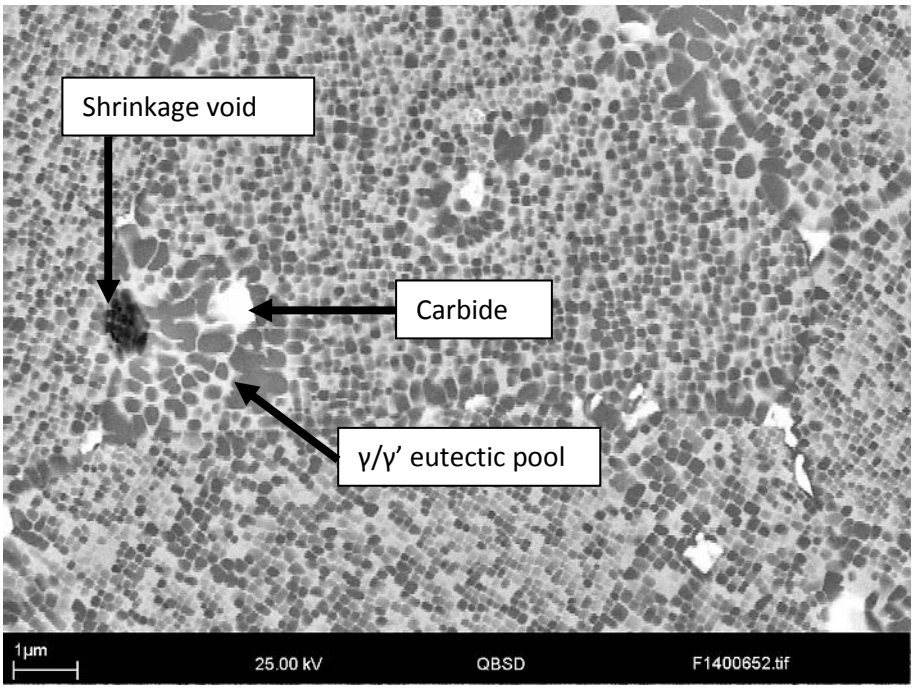

Figure 5-60 - QBSD SEM micrograph of region highlighted in Figure 5-59, showing presence of sub-micron void, γ/γ' eutectic, and cuboidal γ'.

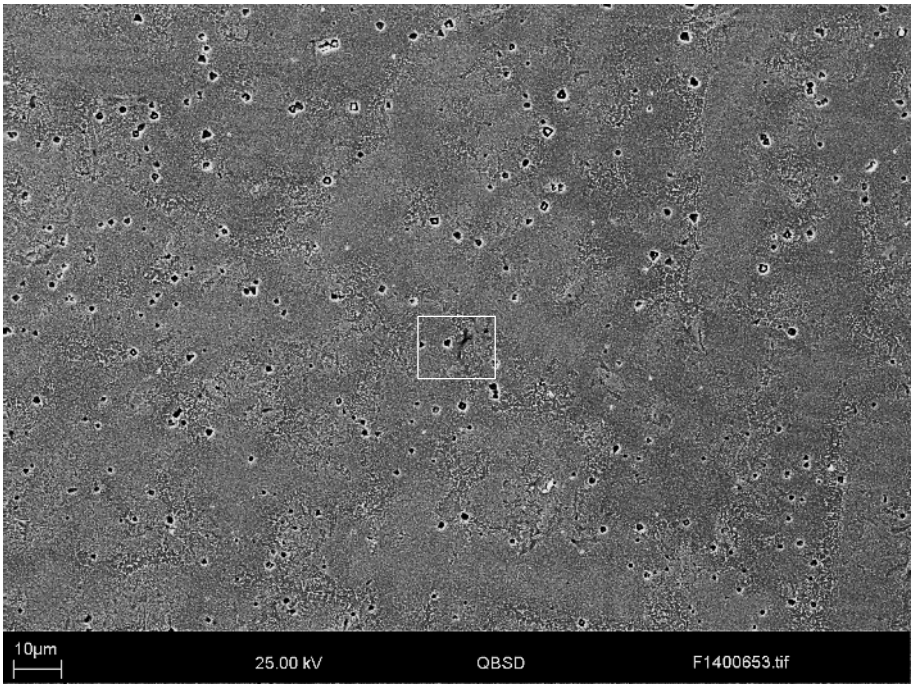

Figure 5-61 - QBSD SEM micrograph taken from near middle of deposit

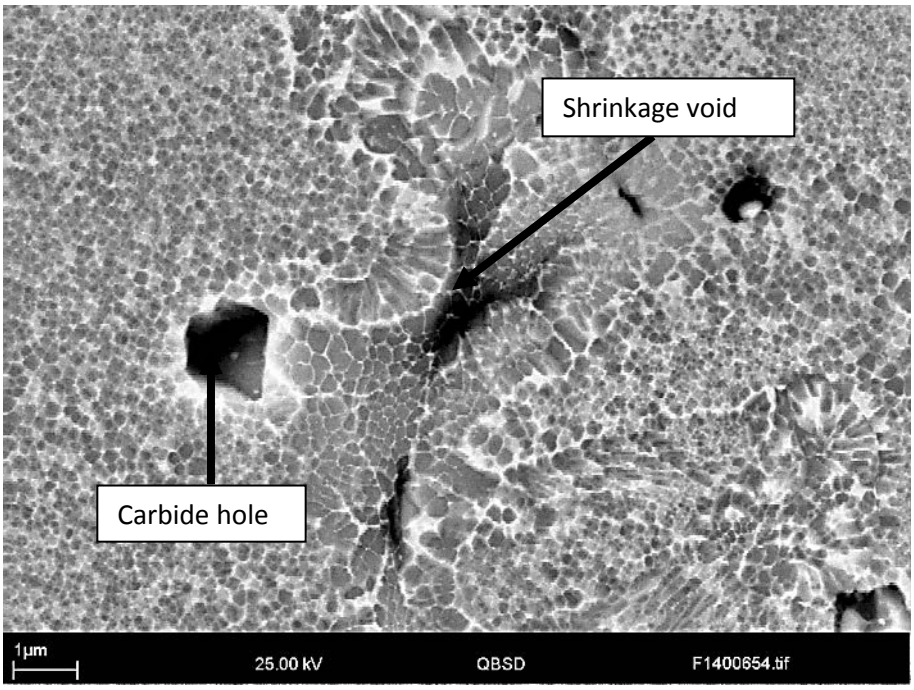

Figure 5-62 - QBSD SEM micrograph of region highlighted in Figure 5-61, showing void formation within 800°C preheated deposit and carbide shaped hole.

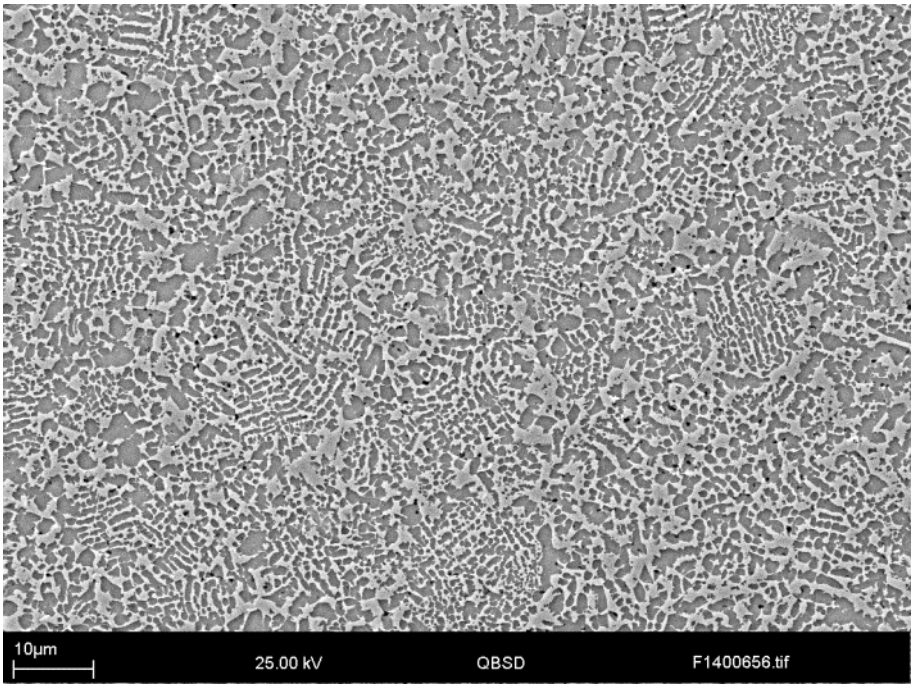

Figure 5-63 - Preheated CM247LC substrate, away from HAZ

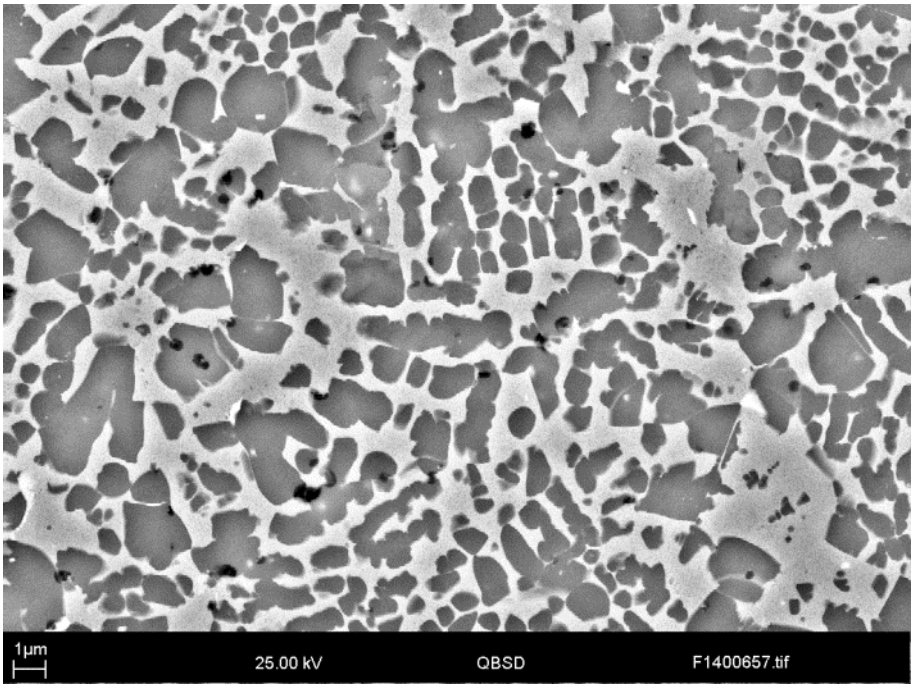

Figure 5-64 - Preheated substrate, away from HAZ

5.3.3.4 Hardness measurements for preheated deposit

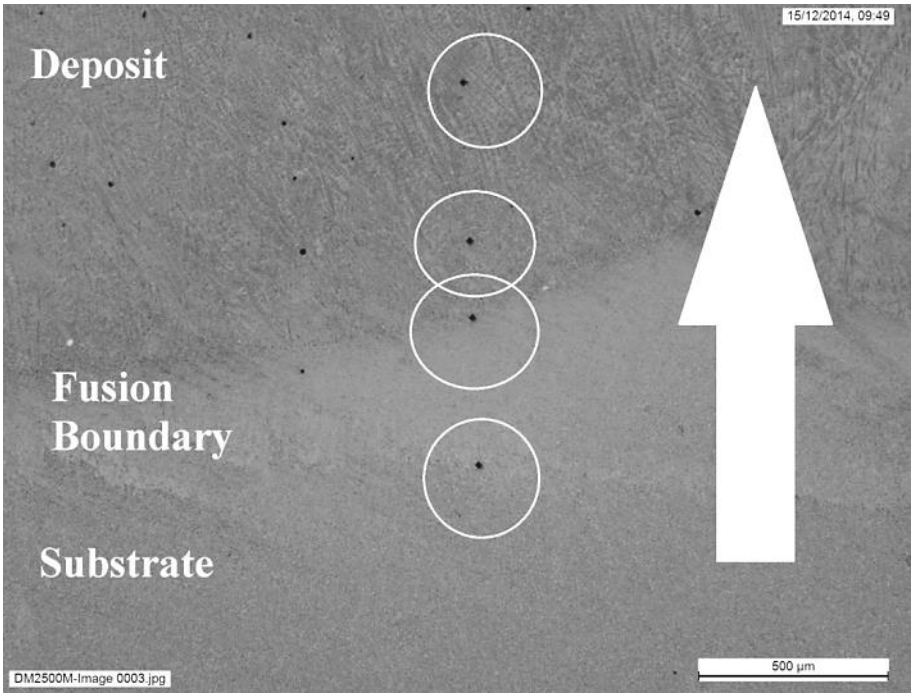

Figure 5-65 - Hardness measurement positions relative to fusion zone

The hardness measurement taken from the bottom edge of the substrate, directly underneath the deposit showed that the substrate had softened somewhat from the 430 H_v value recorded for the HIP'd CM247LC substrate in chapter 4, with the bottom edge of the preheated substrate having a hardness of 391 H_v. The substrate hardness gradually increases until it reaches a maximum of 495H_v, just below the fusion boundary (Figure 5-65).

Immediately above the fusion boundary, there is a dip in the hardness, which then gradually increases until it reaches a maximum value of 495H_v within the deposit, approximately 4.5 mm from the fusion boundary. Hardness drops off again gradually the higher up the deposit the measurements are taken, with the top layer of the deposit having a much lower hardness value of 338 Hv (Figure 5-66).

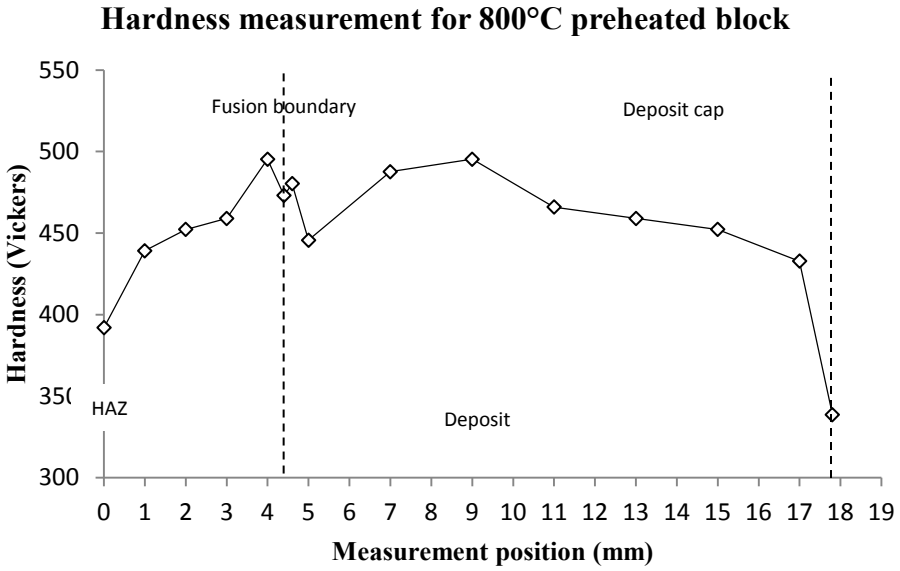

Figure 5-66 - Hardness profile for block deposited using induction preheating

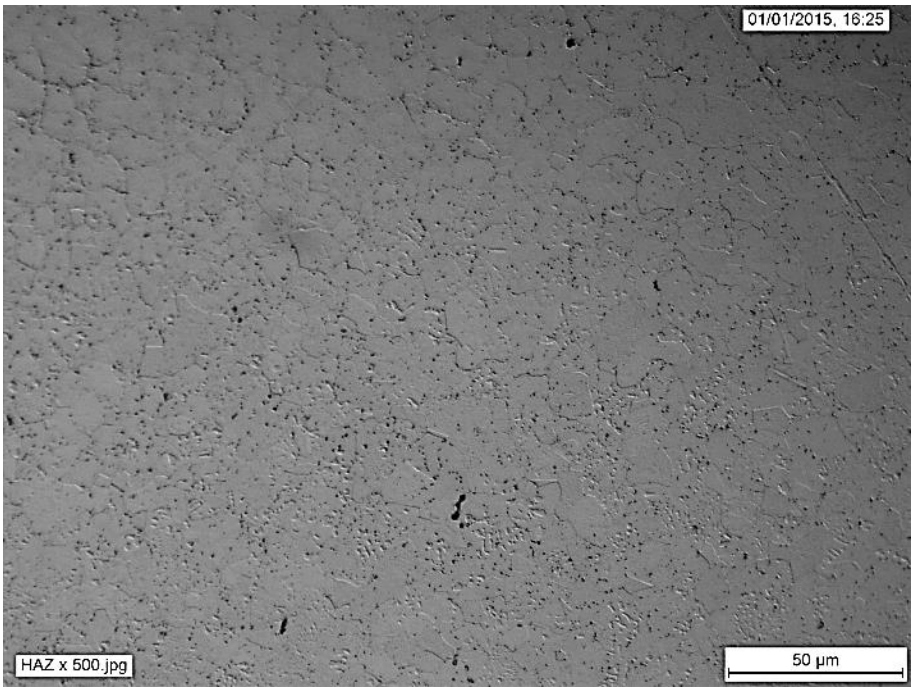

Figure 5-67 - 500x optical micrograph of HIP'd CM247LC substrate, within the HAZ for sample deposited using 800°C preheat

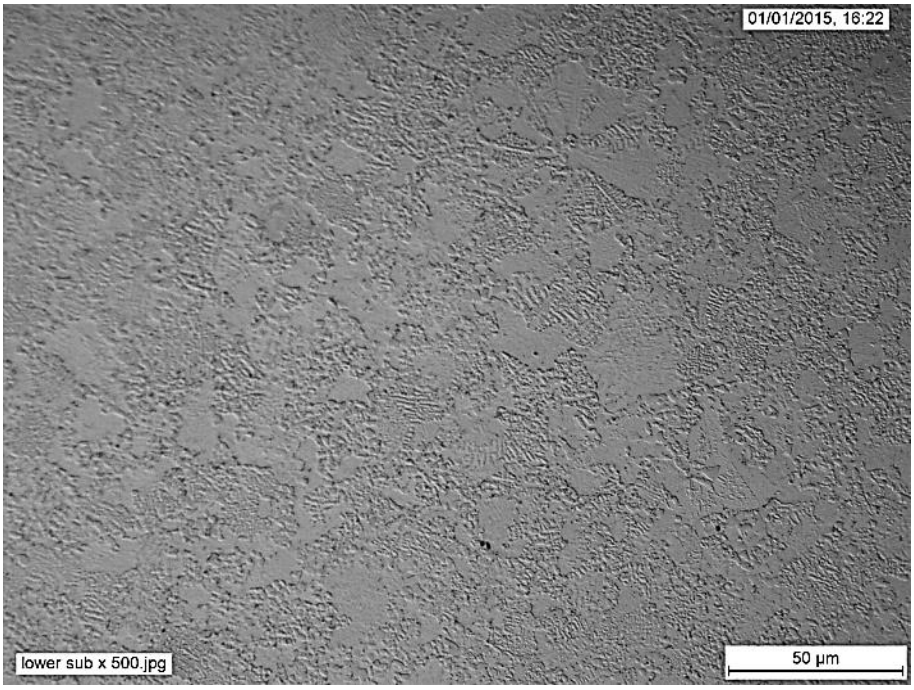

Figure 5-68 - 500x optical micrograph of HIP'd CM247LC substrate, outside of the HAZ for sample deposited at 800°C preheat

5.3.3.5 Temperature measurement during deposition of preheated block

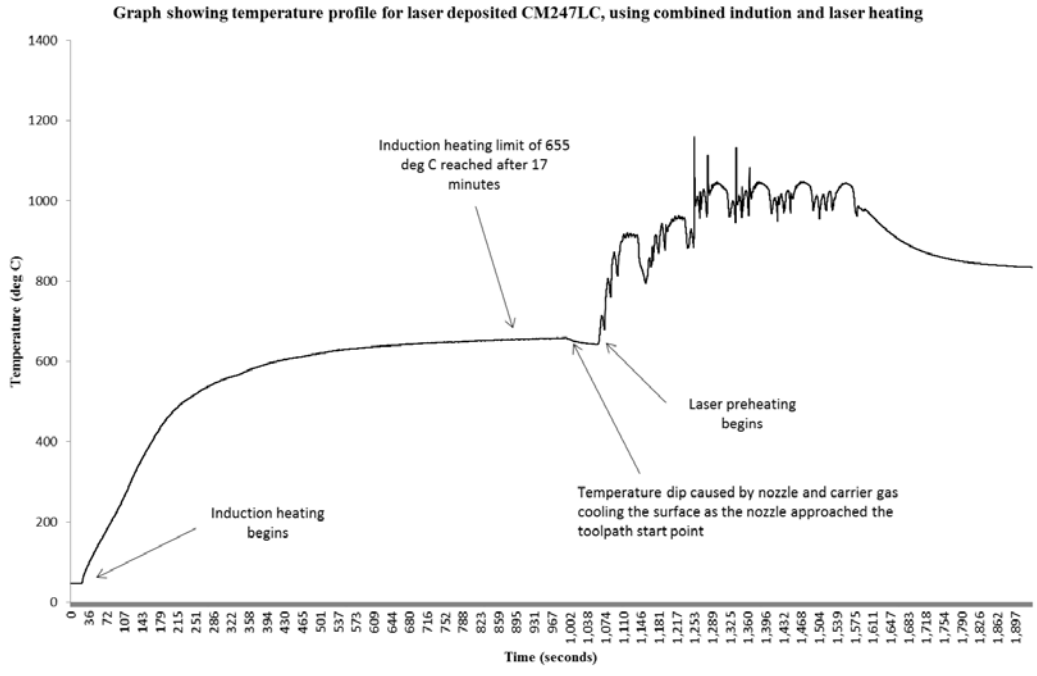

Figure 5-69 - Temperature profile for 800°C preheat, showing heat up time and laser preheating step.

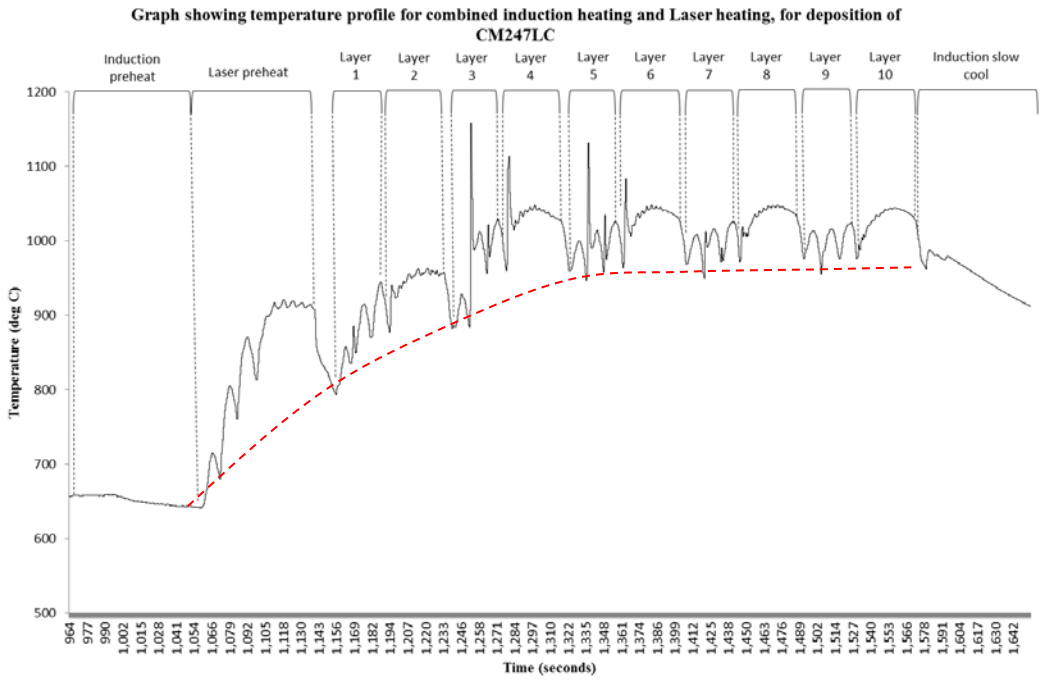

Figure 5-70 - Temperature profile for block deposited using 800°C preheat.

Examination of the thermocouple data gathered during block preheating and block deposition shows that the induction heater raises the temperature of the substrate slowly over a period of 17 minutes, until the temperature plateaus at approximately 650°C (Figure 5-69). As the cladding head approaches the surface to begin the laser assistive preheating, the flow of shielding argon from the nozzle causes a slight cooling effect on the substrate, as illustrated in Figure 5-69. Laser heating of the substrate prior to deposition raises the substrate temperature to 900°C, but then cools to 800°C before the deposition process could be begin.

10 layers of deposit were built up onto the substrate using the cross hatch toolpath, raising the substrate temperature to approximately 960°C by the 5th layer, after which the temperature at the substrate remains fairly constant until deposition was complete (Figure 5-70).

Following deposition of the block, the sample remained in the fixture under induction heating, maintaining the temperature at 820°C for approximately 10 minutes before allowing the deposit to cool down slowly to ambient temperature over the course of an hour.

5.3.3.6 Crack density measurement for preheated block

Using the methodology described in section 3.3.3, the crack density of the preheated deposited block was measured using optical microscopy. Results show that the crack density is greatly reduced compared to the other blocks deposited previously (Figure 5-71).

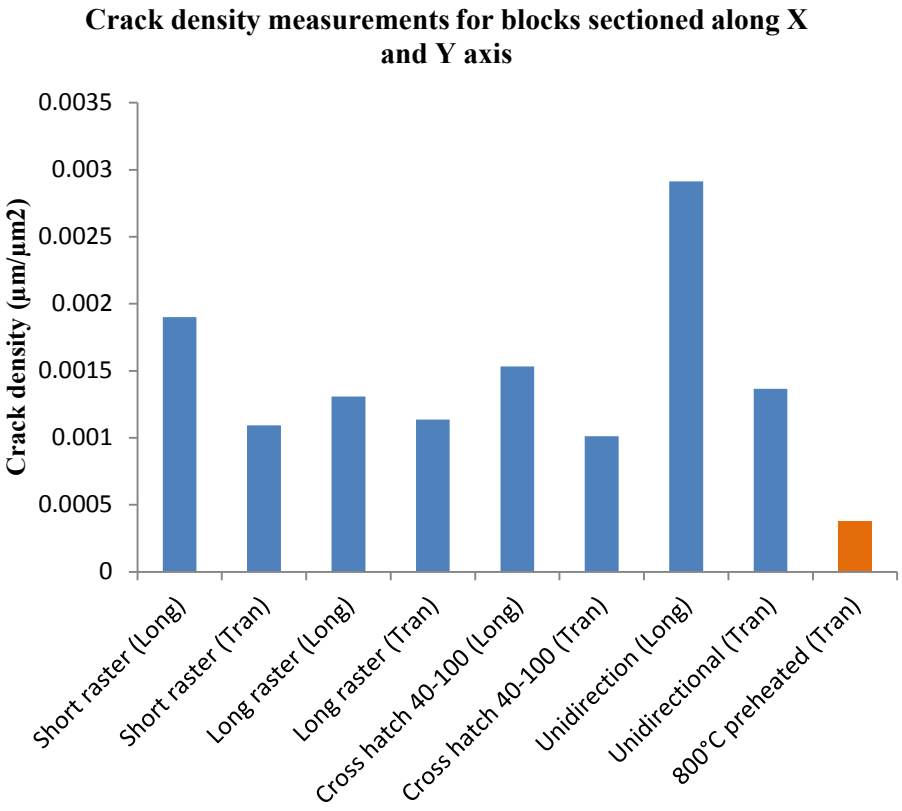

Figure 5-71 - Crack measurement results for deposited blocks, including block deposited at 800°C preheat

5.4 Discussion

5.4.1 Experiment 1 - The effect of particle size on deposit quality

Process development trials conducted in section 5.2.2.1 showed that the 20-40µm CM247LC powder had a greater density per unit volume than the 40-100µm powder, as evidenced by the comparative mass flow rate measurements (Figure 5-3). Work presented by other authors have demonstrated that finer powder particle size ranges are beneficial for laser metal deposition, as they flow better within the nozzle and allow improved focusability of the powder stream [1,9-11], which leads to improved process efficiency as a greater fraction of the powder is captured by the melt pool.

This effect can be observed in Table 5-3, which lists the parameters used for the deposition of blocks using the 20-40 and 40-100µm powders. Comparison of the mass flow rates required to produce a dilution of 1.5, showed that the 20-40µm powder required only 6.1 g/min, while the 40-100µm powder required 6.5g/min. This difference of 6.5% is attributable to the decreased focusability of the coarser powder, which resulted in more powder particles missing the melt pool and impacting on the sidewall and deposit surfaces where they adhered as satellite particles [12-15]. By comparison, the 20-40µm block displayed a very clean surface, with very few satellite particles adhered to the surface. This is an important consideration for applications that require a high standard of surface finish and material efficiency.

Poor nozzle flow optimisation can also greatly affect the deposit quality. In order for a nozzle to produce a tightly focused stream of powder particles for maximum deposition efficiency, the gas flow properties of the critical nozzle surfaces must be smooth and laminar [16,17], with no turbulence. Turbulence of gas flow leads to loss of powder focus, and can be caused by poor nozzle design, or damage to the tip of the nozzle as a result of clogging due to spatter contamination or impact damage. Incorrect nozzle alignment to the melt pool can also seriously affect deposit quality.

Powder size and aspect ratio also plays an important role in ensuring optimal flow. If a fine spherical powder is used, the particles are more easily carried by the gas flow, whereas large irregular shaped particles have a tendency to bounce around the channels as they are delivered through the nozzle. This results in the larger particles exiting the nozzle at stray angles, resulting in poor powder focus [1,13,18,19]. This is an important consideration for process stability and repeatability, as different powder batches will behave in different ways, and produce different results.

Based on the factors involved, it would be reasonable to come to the conclusion that the improved surface finish of the 20-40µm powder is a result of the following contributions:

1. The process uses a laser spot of 3mm, which produces a fairly broad melt pool that effectively captures the majority of particles when using the 3 beam coaxial nozzle. High laser powers and spot sizes result in more energy being available to cause complete melting [20].
2. The tighter particle size range and more regular morphology of the 20-40µm powder results in better flow characteristics in the nozzle, allowing a smaller powder focus spot to be achieved. This results in a higher fraction of particles entering the melt pool and being assimilated into the deposit.
3. The broader particle size range of the 40-100µm powder contains a higher number of irregular shaped particles, which are not conducive to laminar flow through the nozzle. This results in poor powder focus, low capture efficiency and the adherence of these particles to the deposit surface, forming the satellite particles observed.

5.4.1.1 Effect of particle size on cracking response and microstructure

Metallographic analysis of the two blocks deposited using 20-40µm and 40-100µm powder revealed similar microstructures, with cracks forming along the grain boundaries and interdendritic regions. This is consistent with the observations made in chapter 4, in which segregation of Hf, W, Ta, Ti and C to the interdendritic regions led to the formation of a eutectic composition liquid that persists below the solidus temperature of the alloy. As the

interdendritic region has a higher concentration of alloying elements, these regions form γ' preferentially over the dendrite core, and primary MC carbides are often located between the dendrites and at solidification grain boundaries. These primary MC carbides decompose over time at high temperature, providing carbon for the precipitation of secondary carbide phases along the grain boundaries, such as $M_{23}C_6$ and M_6C [21].

Within the 20-40µm block, the cracks appear shorter in length than for the 40-100µm block, but they occur at a greater frequency. This observation was confirmed through comparative crack density measurements, which showed the 20-40µm block to have a crack density 6% higher than that measured for the 40-100µm block (Figure 5-11), with an average crack length that is nearly 50% shorter (Figure 5-12). These measurements of crack length are quite subjective however, as it was not always possible to measure the *true* length of a crack using the microscopy method, because it spanned several micrographs. However, the difference in crack length between these two samples was significant enough to be considered relevant.

The difference in specific surface area (m^3/g) of the two powders may be a contributing factor to this difference in cracking response, with the 20-40µm and 40-100µm powder exhibiting a specific surface area of $0.155m^3/g$ and $0.0692m^3/g$ respectively (Section 4.3.1.1). High specific surface area powder creates a greater number of nucleation sites within the melt pool [22-24] and encourages melt pool mixing. These two factors both contribute to an increase in the solidification rate and a reduction in the columnar grain size [14,25,26]. This effect can be illustrated schematically through the influence of the temperature gradient (G) and the solidification rate (R) in Figure 5-73. Increased solidification rate results in the microstructure moving from the columnar dendritic phase field to the Equiaxed dendritic phase field [20].

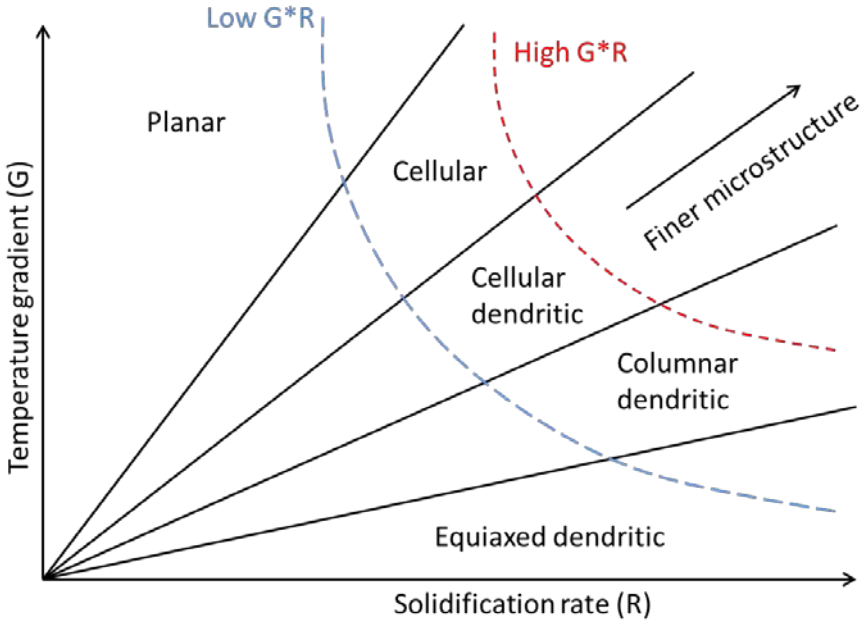

Figure 5-72 - Schematic illustration of the influence of solidification rate and temperature gradient on the microstructure [20]

Shorter columnar grains reduce the tendency of the deposit to form very long cracks between multiple deposition layers, as the propagation pathway along the grain boundaries are more convoluted and the crack would need to change direction multiple times [27]. However, reduced grain size increases the total grain boundary area within the deposit, creating a greater number of solid/liquid interfaces that are oriented transverse to the solidification stresses, meaning cracks are more likely to form during solidification, but be confined to smaller areas due to the difficulties in propagation.

Comparison of the secondary dendrite arms spacing between the 20-40µm and 40-100µm blocks (Figure 5-73) revealed that the SDAS length is affected both by the location within the deposit, and by the size of the powder particles. This is evidenced by comparison of SDAS measurements taken at equivalent positions within each block (Figure 5-9D, Figure 5-10D).

The first layer of deposit, forming the fusion boundary with the substrate (Point A) has a SDAS value of 3.03µm for the 20-40µm powder, and 4.83µm for the 40-100µm powder, indicating that the solidification rate of the first layer is higher for the finer powder.

This scale of SDAS is typical of the Laser Metal Deposition (LMD) process, with cooling rates between 10^2–10^3 K s^{-1} being typical [28]. In comparison, a cast microstructure could have a SDAS of 10-40µm [24], due to much slower cooling rates.

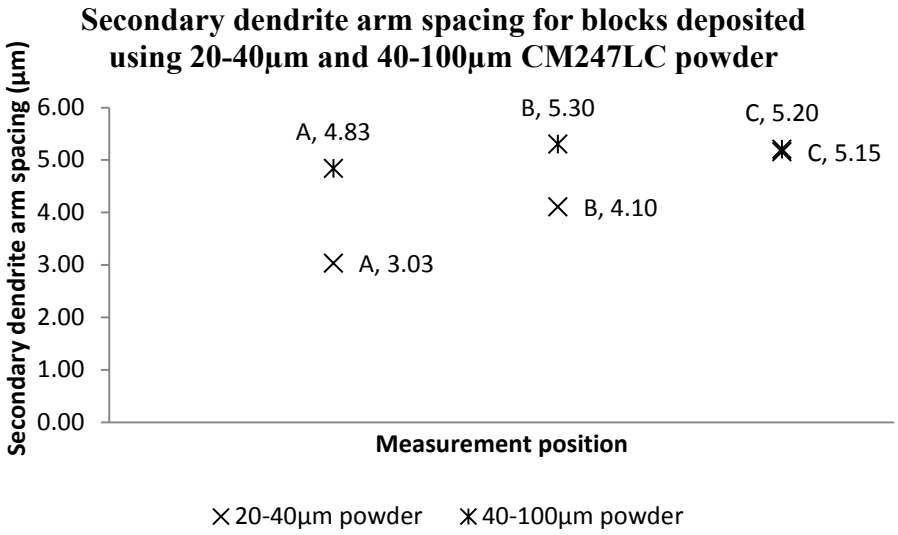

Figure 5-73 - SDAS measurement comparison for cross hatch toolpath blocks deposited using 20-40µm and 40-100µm CM247LC powder

Towards the centre of the blocks, the SDAS is slightly higher for each powder, and by the final layer the SDAS values are almost identical. This would mean that as the temperature of the substrate increases due to temperature accumulation and a longer thermal conduction pathway into the substrate, the cooling rate begins to decrease and the influence of the powder particle size become less pronounced.

Comparing the SDAS measurement positions for these two blocks to the crack density measurements recorded from equivalent areas (Figure 5-13), shows that the regions which experienced more rapid cooling, also exhibit the highest density of cracks. While fast cooling rates are beneficial to a reduction in micro-segregation (Due to the reduced time for back diffusion of alloying elements), it also causes an increase in strain rate, which is a major contributing factor to the formation of solidification cracks [29-31].

5.4.2 Experiment 2 - The effect of toolpath on cracking response

Visual examination of the deposited blocks indicated that all samples contain a significant degree of cracking, evidenced by the presence of surface connected cracks on the side walls and upper surfaces. Most blocks had reasonably good shape, with square sides and low quantities of satellite particles, with the exception of the unidirectional block, which exhibited a trapezoidal cross section, and quite heavily rounded edges (Figure 5-38).

Blocks were cross sectioned longitudinally and transversely, so that the microstructure could be evaluated along both the X and Y axis, and to allow crack density measurements to be recorded for each direction.

5.4.2.1 Cross hatch pattern

Microstructural analysis of the blocks deposited using the cross hatch toolpath revealed a grain structure comprised of columnar grains growing perpendicular to the substrate surface, with a fairly random texture (Figure 5-10C,D) . Long cracks were observed penetrating from the substrate all the way to the deposit cap, propagating along the columnar grain boundaries, changing direction frequently and joining up with adjacent cracks (Figure 5-15). A large number of smaller cracks were also evident at both the grain boundaries and interdendritic regions (Figure 5-16).

This fairly random texture is a result of the alternating scanning path, which first deposits a layer lengthways (Layer A), then deposits the following layer crosswise (Layer B). As the melt pool starts to solidify, the dendrites will grow at an angle that is influenced by the underlying crystallographic orientation, angle of the melt pool fusion boundary and by the direction of maximum heat flow, which is usually normal to the melt pool fusion boundary (Figure 5-74). By alternating the scanning path by 90° between layers, the direction of heat flux is also changed, leading to complex isotherm patterns and crystallographic textures being formed that

inhibit the growth of large columnar grains [32], such as those observed in the long raster, short raster and unidirectional toolpaths.

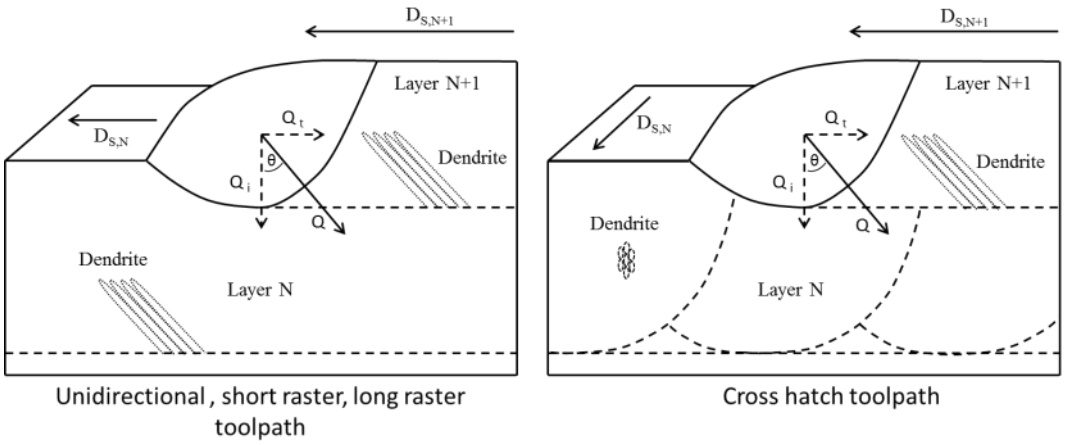

Figure 5-74 - Effect of scanning direction on dendrite growth orientation. Q = heat flux, D_s = scanning direction. Source Liu et al 2008 [32]

Examination of crack density measurements conducted for the cross hatch toolpath showed that, when viewed longitudinally the cross hatch toolpath had the lowest crack density of all the toolpath patterns used (when deposited with the 40-100µm powder). However, when viewed transversely the crack density was 40% higher (Figure 5-19). While both orientations had similar microstructures, it would appear that the magnitude of the thermal stresses along the long axis of the block were greater than those in the transverse axis [33], causing a greater number of solid/liquid interfaces to become separated and form cracks.

The relatively constant SDAS values obtained for the cross hatch block deposited using 40-100µm powder (Figure 5-14) indicated that cooling rate was fairly constant across the build height, which would agree with the temperature profile obtained (Figure 5-21). Thermocouple measurements of the block during deposition showed that the temperature increased to 270°C for the first layer (Layer A), then by the end of the second layer (Layer B), the temperature reached 460°C. By the start of the third layer, the temperature of the substrate had fallen to 203°C, before gradually increasing to 324°C by the end of deposition.

Because the temperature of the deposit only varied by approximately 120°C across the build height, the cooling rate of the melt pool would remain relatively consistent, which would explain the flat SDAS results illustrated in Figure 5-14. However, comparison of the SDAS values obtained for the cross hatch block with those obtained for the short raster block (Table 5-7), which achieved a much higher deposit temperature (Figure 5-37) of 540°C by the final layer, showed that the SDAS was larger for the cross hatch block, which is contrary to the expected result.

Fourier's law of heat conduction shows that the rate of heat transfer into the surrounding material is proportional to the thermal conductivity of the material (k), the area over which conduction occurs (A) and the thermal gradient (dT/dX).

$$q = -kA\frac{dT}{dX}$$

Larger temperature gradients will result in higher heat transfer rates and faster cooling of the melt pool. As described in section 5.4.1.1, the secondary dendrite arm spacing can be used as an indication of the cooling rate or solidification rate, with finer SDAS being indicative of fast cooling rates and high temperature gradients.

Temperatures were measured using a K-type thermocouple welded to the substrate, halfway along the long edge of the block, approximately 1mm away from the fusion boundary. As such it was not possible to achieve a precise measurement of the peak melt pool temperature, from which cooling rates could be accurately calculated. Because the junction of the thermocouple is welded to the upper surface of the substrate, reflected laser light may cause a heating effect that gives a false temperature measurement.

One possible explanation for the lower crack density within the cross hatch block, is that the alternating scanning directions created competing stress fields that negate some of the tensile

stress experienced by the deposit [34]. This would have the effect of lowering the driving force for crack growth, as the solid/liquid interfaces are under less tension.

This behaviour has been utilised by SLM equipment manufacturer concept laser, in which each layer is divided into smaller segments, which are melted at different orientations to each other (Figure 5-62). By randomising the order in which these islands are deposited, it is possible to minimise the net tensile stress generated by the deposition process, producing competing stress fields that act to lower the overall distortion of the part [35]

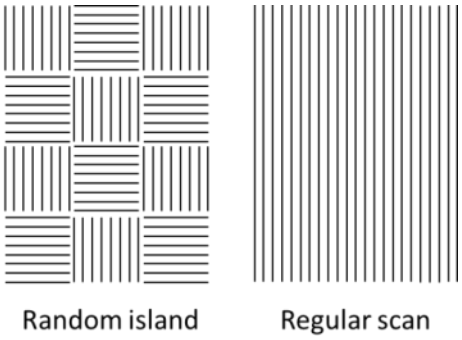

Figure 5-75 - Random island scan pattern and regular scan pattern used in SLM processing

5.4.2.2 Long raster toolpath

Optical microscopy of the block deposited using the long raster toolpath revealed a microstructure comprising of long columnar grains when viewed along the longitudinal axis, and randomly oriented dendritic grains when viewed along the transverse direction. Columnar grains are oriented at various angles along the length of the deposit, from 90° to 72°, whereas closer to the end of the deposit the microstructure becomes more randomised, with zig-zag shaped grain boundaries and cracks observed (Figure 5-25).

Epitaxial columnar growth of dendrites across the fusion boundaries occurs as a product of the direction of heat flux into the substrate, and by the crystallographic orientation of the underlying layers. In Figure 5-22A, the long columnar grains are formed of dendrites that have grown preferentially along the <001> cubic direction of the γ phase. In areas where the grain boundaries have taken on a zig-zag pattern, this occurs because the thermal flux from the melt pool created a situation where it was more favourable for precipitation at the fusion boundary to be seeded by the secondary dendrite arm from the underlying layer, rather than the primary dendrite arm. The result is that dendrite growth direction of the first layer is at 90° to the dendrite growth direction of the second layer. This change of direction occurs at the inter-layer fusion boundary, as illustrated in Figure 5-25.

Cracks of various lengths and size were observed to follow the long grain boundaries, as well as penetrating through the interdendritic regions of the grain interiors in much the same way observed in previous deposits. Micro-cracks were observed in large quantities (Figure 5-23 - Figure 5-25).

Temperature measurements of the deposited block showed that the substrate temperature reached a maximum of 540°C, but due to malfunction of the data logging equipment the temperature records are incomplete (Figure 5-29).

Secondary dendrite arm spacing measurement recorded at different points within the cross section (Figure 26D) showed that SDAS varied between 3.3µm near to the bottom of the deposit and 4.7µm at the upper layer, indicating that as the deposit grew larger the thermal accumulation resulted in a decreased cooling rate.

It is interesting that the long raster toolpath achieved a higher temperature than the cross hatch toolpath, despite using the same laser power and scanning speed. One possible explanation is that the long raster pattern only scans in the Y direction, so the isotherms are being pushed ahead of the fusion boundary as a near planar front, giving the deposit little time to cool. With the cross hatch toolpath, the alternation between longitudinal scanning and transverse scanning layers resulted in parts of the block being allowed to cool down before the laser scanning path reaches it again.

Crack density measurements showed that the cracking response was 14% higher when viewed along the longitudinal direction, than when viewed along the transverse direction (Figure 5-26), with a crack density that decreased in the upper regions of the block (Figure 5-27).

The difference in crack density between the longitudinal and transverse direction is still significant, but it is much lower than that observed for the cross hatch pattern, which displayed a 40% increase in cracking along the X-axis. The reason for this is thought to be due to the orientation of the scanning path, relative to the longitudinal tensile stresses that are generated during deposition. As the laser only scans along the Y direction, there are relatively few fusion boundaries that are perpendicular to the longitudinal axis, which act as initiation points for crack formation. When viewed along the X axis, there are numerous columnar grain boundaries that act as easy propagation pathways for crack growth, but when these cracks form, it is believed that they act to reduce the net tensile stress in the deposit, although additional work would be required in order to verify this, which may involve neutron diffraction measurement of regions surrounding cracks in order to evaluate the difference in residual stress.

5.4.2.3 Short raster toolpath

The block deposited using the short raster toolpath, when viewed in the transverse direction, exhibited a microstructure of long columnar grains (Figure 5-30D) that grow epitaxially through multiple deposit layers. When viewed longitudinally, the microstructure is far more random (Figure 5-30C), with a dendritic columnar structure that changes direction frequently at fusion boundaries, or grows epitaxially across the boundary (Figure 5-31, Figure 5-32). This is similar to that observed for the long raster toolpath, but the long columnar grains observed in the short raster block were not tilted along the scanning direction, as observed for the long raster toolpath (Figure 5-22).

Comparison of crack density measurements obtained for the longitudinal and transverse cross sections showed that the crack density was measured to be 54% higher in the longitudinal direction. This difference is significantly higher than that observed for the cross hatch (40% difference) and long raster (14% difference) toolpaths.

As discussed in section 4.4.2.2.2, the overlapping regions between adjacent tracks are easy initiation points for the formation of cracks, particularly when epitaxial dendrites growth across the fusion boundary occurs. This aligns the weakest orientation of the deposit along the axis with the greatest tensile stress, making cracks far more likely to form. Studies into solidification cracking susceptibility have shown that large columnar grains have a greater tendency to form solidification cracks [36], which is in agreement with the observations made so far, in which the largest cracks are located at the columnar grain boundaries.

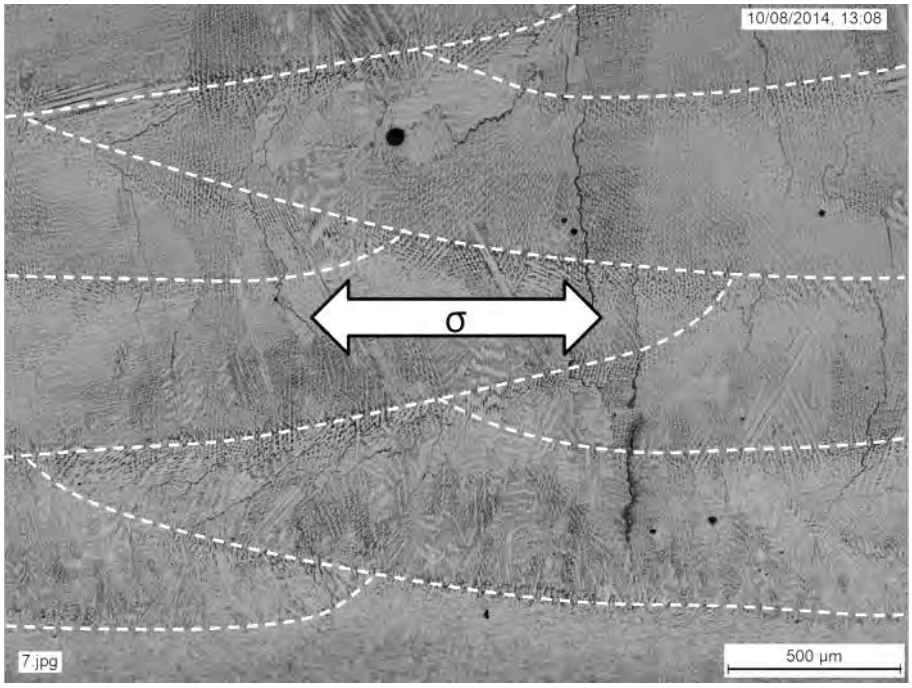

Figure 5-76 - Longitudinal section of short raster block, with scalloped fusion boundaries highlighted and axis of tensile stress indicated

Examination of the temperature profile showed that the short raster pattern reached the highest temperature of all of the deposits, with a maximum temperature of 540°C by the end of deposition.

While the higher deposition temperature achieved for the short raster toolpath will have influenced the cracking response by lowering the solidification stresses, the orientation of the tracks relative to the long axis of the block presented a great number of fusion boundaries to the axis of maximum tensile stress, which resulted in a larger number of cracks forming along the longitudinal axis.

Examination of the secondary dendrite arm spacing showed that the λ_2 distances varied between 3.5 and 5.8µm (Figure 5-35) over the height of the deposit, which is slightly larger than those obtained for the other toolpaths, reflecting the slower cooling rate due to the higher deposit temperature.

Measurements were also recorded of the λ_2 distances for the first layer of deposit, when viewed along the longitudinal axis (Figure 5-30C), which showed that λ_2 increases gradually between 3µm and 4µm, when measuring from the first track to the last track on the first layer (Figure 5-36).

During laser deposition using the short raster pattern, the temperature isotherms are expected to move as an almost planar front, based on the work conducted by Carter [5], as the scan length is relatively small and the tracks don't have a lot sufficient time to cool down before the laser scans back again. Comparing this to the long raster toolpath, which has a similar scan pattern, but along different direction, the laser takes longer to traverse from one end of the block to the other, meaning the ends of the block experience heating every twelve seconds, whereas the centre of the block is heated every 6 seconds. In comparison, the short raster toolpath takes 2 seconds to deposit each track, so the heating events occur much closer together, meaning heating is more gradual and the thermal gradients between the melt pool and the substrate are reduced.

Jendrzejewski et al [37] used a combination of finite element analysis and deposition trials, which showed that as preheat temperature increases, the stress field is decreased and fewer cracks were formed within Stellite laser deposits, but also found that longer dwell times between deposit layers also increased the stress field and introduced more cracks. This would agree with the results of the DOE conducted in section 4.4.5.1, in which high laser powers and slow scanning speeds were found to decrease the cracking response in laser deposited CM247LC, as conduction of heat into material ahead of the melt pool was effectively preheating it.

5.4.2.4 Unidirectional toolpath

The strong metallographic texture observed for the unidirectional toolpath is formed as a result of a consistent scanning direction, which allows epitaxial growth of dendrites through multiple

deposit layers, as the dendrites of the clad layer are aligned along the same direction as the underlying layer. When viewed transversely, the fusion boundaries form the characteristic scallop shapes, with dendrite growth changing direction frequently at the fusion boundaries, as illustrated in Figure 5-41.

Optical microscopy of the transverse and longitudinal sections shows that cracks are long and wide, indicating that they were under significant stress during crack formation, causing them to open up, as illustrated in Figure 5-42.

The texture of the deposit has essentially placed a large number of columnar grain boundaries normal to the axis of highest stress, so that the columnar grains form long cracks (Figure 5-38, Figure 5-39) that penetrate through multiple deposit layers. As these columnar grains are tilted along the deposition direction at an angle of approximately 65°, transverse sections of the deposit will reveal a greater number of cracks that are parallel to the substrate, as they are presenting cracks that are located on the front or back face of the columnar grain boundary. This effect can be observed in the transverse cross sections of the unidirectional block (Figure 5-38D), which is illustrate schematically in Figure 5-77.

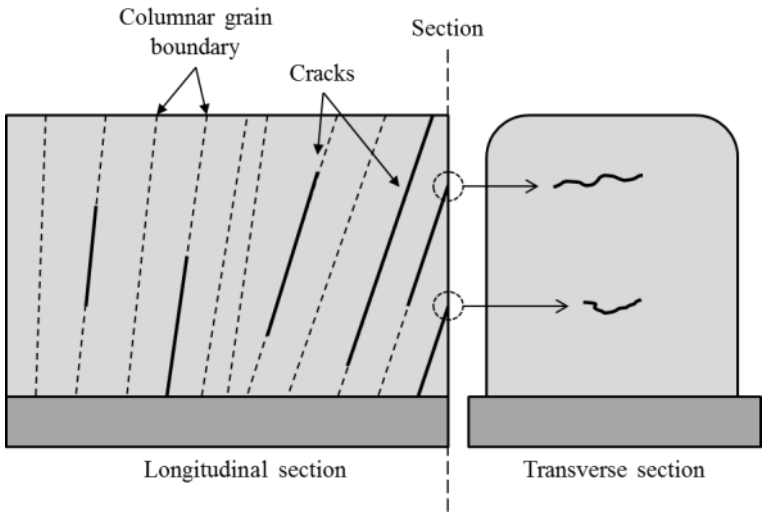

Figure 5-77 – Formation of non-vertical cracks in uni-directionally deposited samples

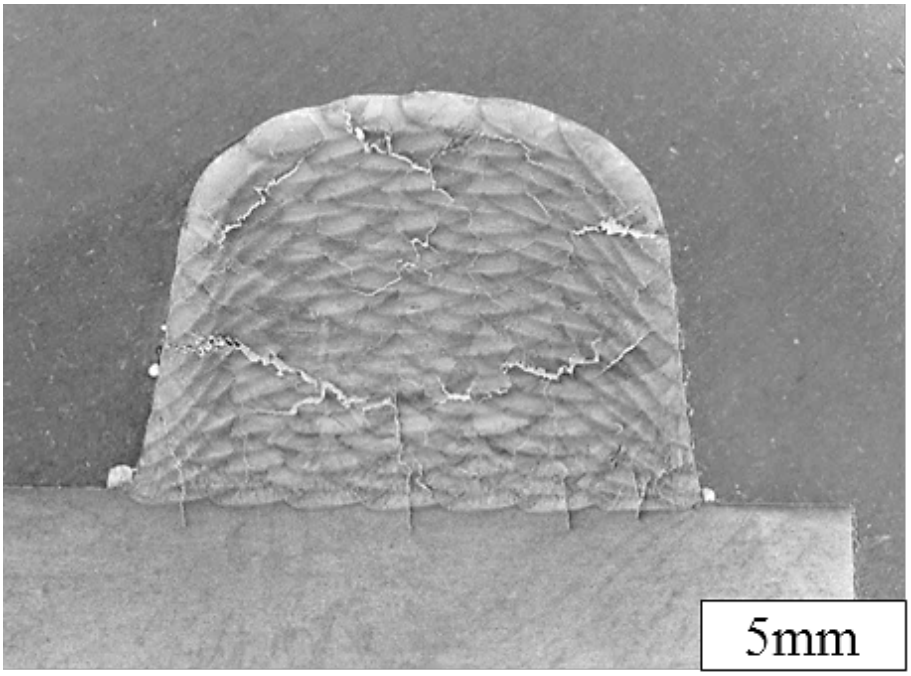

Figure 5-78 - Transverse section of unidirectional test block, showing presence of non-vertical cracks

A high quantity of small and large cracks were also observed propagating along various directions as for the other toolpaths, but it was only the unidirectional block that exhibited the characteristic horizontal cracks. Although the scanning pattern used for this toolpath is similar to that used for the longitudinal raster, the heating profile was very different. The long raster toolpath also exhibiting a strong metallographic texture in the form of long columnar grains, but the cracks observed in the transverse section were between 45° and 90° to the substrate.

At the end of each deposited track, the laser beam is interrupted so that the cladding head can make the lateral movement to the start of the next track. This results in the laser being off for approximately half of the processing time, allowing the block to conduct heat away from the deposit and into the substrate, lowering the net temperature. Thermocouple data for the unidirectional block showed that the temperature reaches approximately 200°C by the end of deposition (Figure 5-46).

As mentioned previously, lower substrate temperatures result in high heating and cooling rates, which are a known cause of constitutional liquation of grain boundary phases, meaning non-equilibrium heating of the previously deposited material can cause the eutectic and carbide phases located at the solidification boundaries to melt at a lower temperature than it could under equilibrium conditions. Added to this effect, that high heating and cooling rates introduce a greater amount of residual stress into the component, which acts to pull the liquid/solid interfaces apart and form cracks, as the magnitude of the stress depends on the sharpness of the thermal gradients [38].

5.4.2.5 Anisotropy of cracking response

All deposited blocks exhibited a higher degree of cracking when viewed longitudinally than when viewed transversely. All toolpaths were deposited under identical conditions, and so the degree of cracking that is observed in the longitudinal direction can be attributed to the scanning strategy used.

While the cross hatch toolpath produced the lowest cracking response when viewed transversely, approximately 40% more cracks were visible when viewed longitudinally. This is thought to be due to a combination of the somewhat random texture generated during deposition, with the cross-wise scanning strategy aiding to reduce the net tensile stress in the depositing by creating competing stress fields [33]. The higher number of cracks in the longitudinal direction may be a result of half of the deposited tracks being deposited perpendicular to the long axis, which are intrinsically more prone to solidification crack formation than tracks that are deposited parallel to the long axis, as demonstrated in section 4.3.2.2, where overlapping tracks were found to crack due to a combination of solidification stress and dendrites that grew epitaxially through the overlap fusion boundaries

This can be observed when comparing the longitudinal crack density results for the short raster and long raster toolpaths. The short raster toolpath had the second lowest crack density when

viewed transversely, but contained 54% more cracks when viewed longitudinally. Compare this to the longitudinal raster toolpath, in which the tracks are parallel to the long axis of the block, which only had a 12% difference in crack density between longitudinal and transverse sections, despite possessing a columnar texture in the longitudinal section, similar to the unidirectional block, which possessed the highest crack density, both transversely and longitudinally, believed to be due to the low deposit temperature which was a result of the intermittent laser heating.

5.4.3 Experiment 3 - The effect of preheating on crack formation

5.4.3.1 Microstructure and cracking response

Through the use of active induction heating during deposition, the crack density within the laser deposited CM247LC was reduced by 66% compared to the cross hatch toolpath (Figure 5-71), but was not entirely eliminated.

Optical microscopy of the transverse cross sections showed that while cracks were still evident, the size and scale of the cracks was much reduced, with an average crack length of 465µm, which is lower than that observed for the cross hatch toolpath (Figure 5-12) using either the 20-40µm powder (534µm) or the 40-100µm powder (888µm).

While cracks were still evident, they were mostly confined to single deposit layers, or followed the columnar boundary a short distance across several deposit layers. It was also observed that the cracks were much finer, not having opened up as much under the solidification stresses as was observed for the other deposits.

As discussed previously, raising the temperature of the material decreases the thermal gradient and lowers the amount of residual stress in the deposit, which lowers the driving force for crack growth. This could be observed through electron microscopy of the deposited sample, where the interdendritic regions and grain boundaries were observed to contain a greater amount of micro-voids than were previously observed in other deposits (Figure 5-60, Figure 5-62). These voids were found to be located mainly within the eutectic pools, located in the intergranular and interdendritic regions. As the eutectic pool begins to solidify, it is surrounded by solid material that does not accommodate the volumetric contraction, causing a shrinkage void to form [39]

For deposits such as the cross hatch block deposited without pre-heating, the residual stresses would have caused these micro-voids to become separated, pulling them apart to form cracks

that travelled easily through the mushy intergranular regions where solidification was still incomplete, but this was not observed as much for the preheated block.

By decreasing the thermal gradient between liquid and solid, this causes a reduction in the cooling and solidification rates during deposition. The result of this is that the secondary dendrite arm spacing was almost doubled (Figure 5-58) compared to that measured for the cross hatch toolpath deposited without induction heating (Figure 5-14). Reduction of thermal gradients also increases the tendency to transition from a columnar dendritic grain structure to an equiaxed structure, as there is less directionality to the heat flux which is one of the driving forces for columnar grain growth [40,41]. This effect is illustrated schematically in Figure 5-72.

While slower cooling rates actually increases the amount of micro segregation that occurs during solidification [42], as the dendrites are spaced further apart, this did not detrimentally affect the cracking response, as the lower residual stress did not allow them to become separated quite as much as was observed for other deposits.

5.4.3.2 Carbide distribution and morphology

Comparison of the carbide distribution between the lower and middle regions of the deposit showed an apparent lack of carbides in the latter. As mentioned in section 5.3.3.3, the sites that would normally have contained carbides in the interdendritic regions are mostly empty sockets, with a region of lighter contrast surrounding the edge of the holes, when imaged using the SEM backscattered detector.

This lighter region may be due to diffusion of Ta from the MC carbides that formed upon solidification into the surrounding area (Where M = Ti, Hf and Ta). Ta has an atomic number of 71, which would show up very bright under backscattered SEM in contrast to the γ matrix, so there is a possibility that that observed contrast is due to the decomposition of TaC.

Decomposition of MC carbides is a common reaction during heat treatment and component service, with primary MC carbides acting as a source of carbon for the precipitation of secondary carbides along grain boundaries (such as $M_{23}C_6$), as well as a source of titanium for γ' precipitation. The preferred order of formation (in order of decreasing stability) is HfC, TaC, NbC and TiC [21], which shows that carbide dissolution would preferentially occur in TiC and TaC before HfC.

However, this reaction normally takes place over many hours at high temperatures, and so complete dissolution within the limited timeframe of the deposition process is unlikely, even taking into account the slow cool down post deposition.

Work conducted by Huang et al [43] showed that solution treatments of CM247LC at temperatures of 1220°C for two hours were not sufficient to decompose the MC carbides fully into $M_{23}C_6$ or M_6C, but it was noted that TiC type carbides decomposed to release titanium into the solid solution for γ' formation, due to the lower thermal stability when compared to TaC and HfC. Coutsouradis et al [44] also identified that TaC decomposes to release Ta into the solid solution.

Mehta et al [45] investigated the role of post solutionising cooling rate on the degeneration of primary MC carbides in cast CM247LC, and found that when a relatively rapid (81°C/min) cooling rate was used following a 2 hour solution heat treatment at 1260°C, the MC carbides were found to degenerate in more stable MC and $M_{23}C_6$ forms, such as HfC and $Cr_{23}C_6$.

One explanation may be that charging during SEM examination caused the higher contrast, but that is less likely to occur in QBSE imaging than it would for secondary electron imaging (SEI), which is more sensitive to shape effects. More likely is that during metallographic preparation the carbides were pulled from the matrix by excessive grinding forces, or the etching method used caused a localised attack of the carbide/matrix interface that caused it to

become detached. More analysis is required to determine if this is simply a preparation defect or the result of carbide reactions during deposition at elevated temperatures.

5.4.3.3 Hardness measurements

Hardness measurements taken for the transverse section, along the deposit centreline (Figure 5-66), showed that the substrate had softened somewhat from the $430H_v$ value obtained for the un-heated CM247LC substrate, with hardness in the substrate varying from $390H_v$ at the bottom edge, to $495H_v$ just below the fusion boundary (Figure 5-65). This spike in hardness just below the fusion boundary was also observed for the block deposited using the cross hatch toolpath without preheat in Section 4.3.5.1.1.

Because nickel is a relatively simple face centre cubic material that does not undergo a phase transformation upon cooling, it is not possible to harden the material by applying a rapid cooling rate as would normally be performed for materials such as carbon steel. Hardening of nickel superalloys comes from a combination of solid solution and precipitation strengthening via a solution and ageing heat treatment, with the precipitation of carbide phases and γ' being the most critical.

Within the HAZ, the material experiences high temperatures that can cause the dissolution of precipitated phases back into solution, such as Ti and Al which form the Ni_3Al,Ti phase γ'. By dissolution of these elements back into the FCC γ phase, this creates a solid solution with increased hardness. This can be observed through examination of the substrate microstructure in Figure 5-67, which shows the γ' depleted region in the substrate immediately below the fusion boundary, and Figure 5-68, which show the substrate outside of the HAZ.

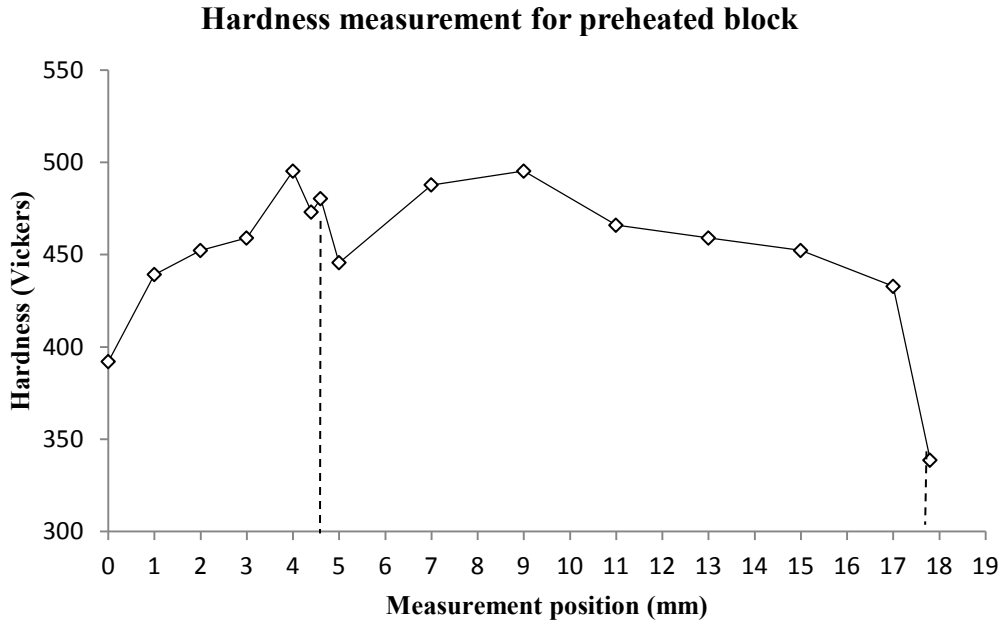

Figure 5-79 – Hardness map for sample deposited at 800°C preheat

Immediately above the fusion boundary, the hardness of the deposit was recorded at approximately 445H_V, rising to 495H_V. The increase in hardness is thought to be due to the high temperatures encouraging the precipitation of a greater volume fraction of the γ' strengthening phase, and the subsequent decrease in hardness is thought to be a result of the limited time available for γ' precipitation and growth. As a result, the γ' located in the lower region of the deposit is more cuboidal than that observed in the upper regions of the block, which is more spherical. The increase in hardness observed may also be a result of carbide dissolution, which would partition elements such as Ta to the matrix, producing a solid solution strengthening effect, however further analysis would be needed to confirm this.

5.5 Conclusions

In this chapter, three approaches were explored in order to determine what effect they had on the cracking response of laser deposited CM247LC. While none of the methods produced blocks that were of satisfactory internal quality, several interesting results were obtained.

While the finer powder particle size used in section 5.2.2 resulted in improved external deposit quality and deposition efficiency, the influence on cracking response was less positive. Finer particle sizes are thought to have contributed to melt pool mixing effects and accelerated melt pool cooling due to the much higher surface area to volume ratio. The result of this is that the solidification rate of the melt pool was increased, leading to the formation of smaller columnar grains. While smaller grains are considered beneficial to solidification cracking resistance, it would appear that in this case the crack density was increased and average crack length was decreased. Accelerated solidification rates are also known to contribute to higher residual stresses in the deposited part, which may have contributed to the separation of the semi-solid grain boundaries and interdendritic regions.

Comparison of toolpaths used to deposit blocks under otherwise identical conditions showed that the cross hatch toolpath produced the lowest crack density when viewed along the transverse axis, but crack density was 40% higher when viewed along the longitudinal axis. Similarly, all other deposited blocks demonstrated this effect, which would suggest that the residual tensile stresses along the long axis are higher than for the transverse axis.

There was a significant difference in cracking response between the short raster and the long raster toolpaths, particularly when viewed in the longitudinal direction. This is believed to be due to the deposited tracks being more susceptible to crack formation when the tensile forces are aligned perpendicular to the deposition direction. As the highest stresses are oriented along the long axis of the block, the short raster toolpath was far more susceptible to crack formation

and growth, as the weak track orientation was perpendicular to the axis of maximum tensile stress.

Transverse tensile stresses also contributed to cracking significantly, as evidenced by the long raster toolpath. This demonstrated a similar microstructure to the short raster toolpath, only in this case the deposition direction as aligned along the long axis of the block, with the transverse tensile stresses acting perpendicular to the scanning direction. The result of this is that the long raster toolpath exhibited the highest transverse crack density of all the toolpaths, but the lowest crack density in the longitudinal direction.

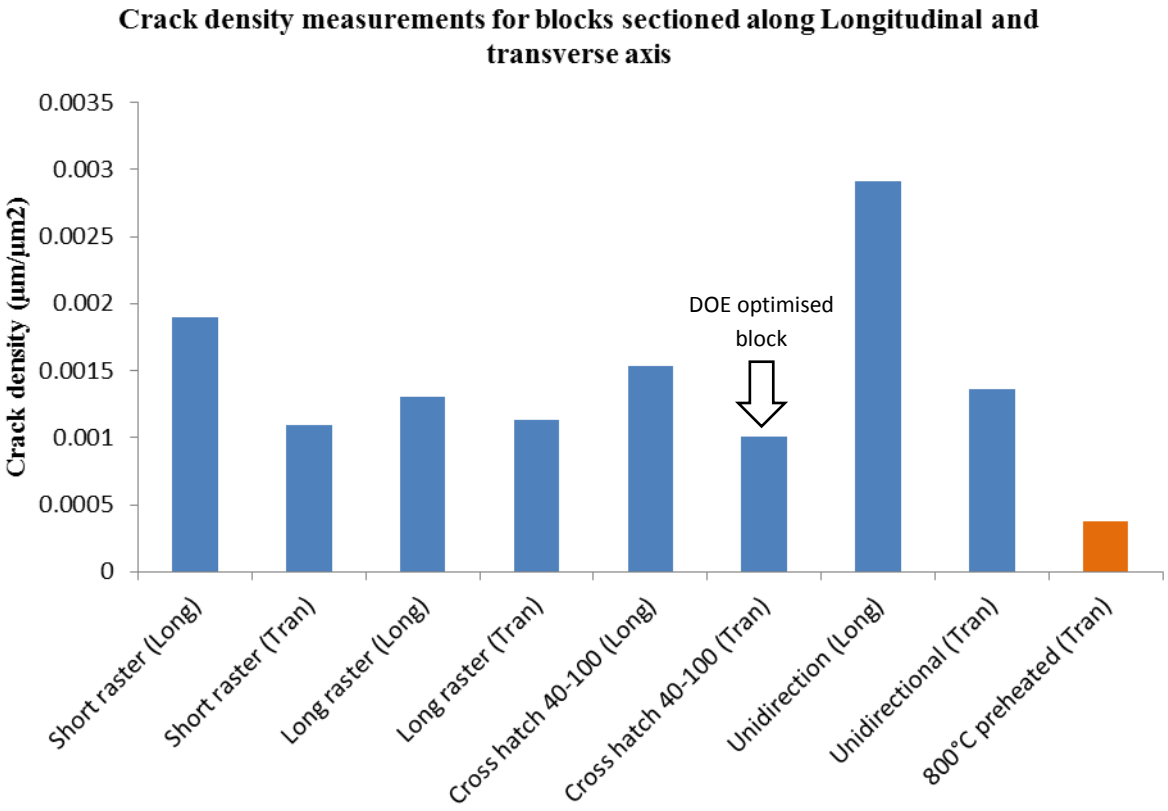

Figure 5-80 - Crack density results for blocks deposited in chapter 5

Blocks deposited using the unidirectional toolpath produced a strong metallographic texture of columnar dendritic grains, angled along the scanning direction. Unlike the long raster toolpath, which was strongest when the cladding direction was parallel to the long axis, the unidirectional toolpath was the weakest, producing very large, long cracks that followed the

long columnar grain boundaries. This is believed to be partially due to the faster cooling rates exhibited by the unidirectional block, which led to a higher residual stress formation.

The role of temperature in the cracking response of CM247LC was investigated in section 5.2.4, in which a block was deposited onto an actively heated substrate. This resulted in a great reduction in crack density, with the cracks being of shorter length and more confined to individual deposit layers. Eutectic pools within the intergranular regions which normally separate under the resultant solidification stresses were observed to be intact, although many exhibited shrinkage voids that form as a result of volumetric contraction during part cooling.

While induction preheating of the deposit resulted in a far superior deposit quality, with regards crack density, there is much work required in order to optimise the process and achieve further reductions in cracking before it can be considered a viable repair or manufacture route for CM247LC.

5.6 Chapter 5 - List of figures

5.7 Chapter 5 - List of tables

5.8 Chapter 5 - References

1. Boisselier, D. and S. Sankaré, Influence of Powder Characteristics in Laser Direct Metal Deposition of SS316L for Metallic Parts Manufacturing. Physics Procedia, 2012. 39(0): p. 455-463.

2. Pinkerton, A.J. and L. Li, Multiple-layer laser deposition of steel components using gas and water-atomised powders: the differences and the mechanisms leading to them. Applied Surface Science, 2005. 247: p. 175-181.

3. Milenkovic, S., I. Sabirov, and J. LLorca, Effect of the cooling rate on microstructure and hardness of MAR-M247 Ni-based superalloy. Materials Letters, 2012. 73: p. 216-219.

4. Ludovico, A.D., A. Angelastro, and S.L. Campanelli, Experimental Analysis of the Direct Laser Metal Deposition Process. 2013.

5. Carter, L.N., et al., The influence of the laser scan strategy on grain structure and cracking behaviour in SLM powder-bed fabricated nickel superalloy. Journal of Alloys and Compounds, 2014. 615(0): p. 338-347.

6. Fallah, V., et al., Impact of localized surface preheating on the microstructure and crack formation in laser direct deposition of Stellite 1 on AISI 4340 steel. Applied Surface Science, 2010. 257(5): p. 1716-1723.

7. Noecker II, F.F. and J.N. DuPont, Microstructural development and solidification cracking susceptibility of Cu deposits on steel: Part I. Journal of materials science, 2007. 42(2): p. 495-509.

8. Huang, Y. and X. Zeng, Investigation on cracking behavior of Ni-based coating by laser-induction hybrid cladding. Applied Surface Science, 2010. 256(20): p. 5985-5992.

9. Mahamood, R.M., et al., Effect of Laser Power on Material Efficiency, Layer Height and Width of Laser Metal Deposited Ti6Al4V. 2012.

10. Bodhmage, A., Correlation between physical properties and flowability indicators for fine powders. 2006, University of Saskatchewan.

11. Schneider, M.F., Laser cladding with powder, effect of some machining parameters on clad properties. 1998: Universiteit Twente.

12. R. M. Mahamood, E.T.A. Effect of laser power on surface finish during laser metal deposition process. in World congress on Engineering and Computer science. 2014. San Francisco.

13. Carroll, P., et al., The effect of powder recycling in direct metal laser deposition on powder and manufactured part characteristics. 2006.

14. Yan-lu, H., et al., Effects of powder feeding rate on interaction between laser beam and powder streamin laser cladding process. Journal of Wuhan University of Technology-Mater. Sci. Ed., 2004. 19(4): p. 69-72.

15. Zhu, G., et al., The influence of laser and powder defocusing characteristics on the surface quality in laser direct metal deposition. Optics & lasers technology, 2012. 44: p. 349-356.

16. Zekovic, S., R. Dwivedi, and R. Kovacevic, An investigation of gas-powder flow in laser-based direct metal deposition. Research Center for Advanced Manufacturing. Reviewed, Accepted September, 2006. 14: p. 558-572.

17. Zekovic, S., R. Dwivedi, and R. Kovacevic, Numerical simulation and experimental investigation of gas–powder flow from radially symmetrical nozzles in laser-based direct metal deposition. International Journal of Machine Tools and Manufacture, 2007. 47(1): p. 112-123.

18. Ahsan, M.N., et al., A comparative study of laser direct metal deposition characteristics using gas and plasma-atomized Ti–6Al–4V powders. Materials Science and Engineering: A, 2011. 528(25–26): p. 7648-7657

19. Kovaleva, I., et al., Numerical Simulation and Comparison of Powder Jet Profiles for Different Types of Coaxial Nozzles in Direct Material Deposition. Physics Procedia, 2013. 41(0): p. 870-872.

20. Lee, Y., et al., Influence of Fluid Convection on Weld Pool Formation in Laser Cladding. Welding Journal, 2014.

21. Donachie, M.J. and S.J. Donachie, Superalloys - A technical guide. second edition ed. 2002: ASM international.

22. Gäumann, M., et al., Epitaxial laser metal forming: analysis of microstructure formation. Materials Science and Engineering: A, 1999. 271(1–2): p. 232-241.

23. Pinkerton, A.J., et al., Thermal and microstructural aspects of the laser direct metal deposition of waspaloy. Journal of laser applications, 2006. 18(3): p. 216-226.

24. Parimi, L.L., D. Clark, and M.M. Attallah, Microstructural and texture development in direct laser fabricated IN718. Materials Characterization, 2014. 89: p. 102-111.

25. Kurz, W., C. Bezencon, and M. Gäumann, *Columnar to equiaxed transition in solidification processing.* Science and Technology of advanced materials, 2001. **2**(1): p. 185-191.

26. Tyrer, M.G.R.H.J. and M. Blackmur, *THE CONTROL OF GRAIN SIZE DURING WELDING AND DIRECT METAL DEPOSITION USING THREE DIMENSIONAL TIME-TEMPERATURE CONTROL PROVIDED BY HOLOGRAPHIC BEAM SHAPING.*

27. Shinozaki, K., et al., *Effect of Grain Size on Solidification Cracking Susceptibility of Type 347 Stainless Steel during Laser Welding.* QUARTERLY JOURNAL OF THE JAPAN WELDING SOCIETY, 2011. **29**(3): p. 90s-94s.

28. Hofmeister, W., et al., *Investigation of solidification in the laser engineered net shaping (LENSTM) process.* JOM, 1999. **51**(7): p. 1-6.

29. Kou, S., *Solidification and liquation cracking issues in welding.* JOM, 2003. **55**(6): p. 37-42.

30. Pellini, W.S., *Strain theory of hot tearing* Foundry, 1952. **80**: p. 125.

31. Kou, S., *Welding metallurgy*. 2nd ed. 2003: John Wiley and sons.

32. Liu, F., et al., *The effect of laser scanning path on microstructures and mechanical properties of laser solid formed nickel-base superalloy Inconel 718.* Journal of Alloys and Compounds, 2011. **509**(13): p. 4505-4509.

33. Moat, R., et al., *Residual stresses in laser direct metal deposited Waspaloy.* Materials Science and Engineering: A, 2011. **528**(6): p. 2288-2298.

34. Liu, F., et al., *Microstructure and residual stress of laser rapid formed Inconel 718 nickel-base superalloy.* Optics & laser technology, 2011. **43**(1): p. 208-213.

35. Fessler, J., et al. *Laser deposition of metals for shape deposition manufacturing*. in *Proceedings of the solid freeform fabrication symposium*. 1996. University of Texas at Austin.

36. Shinozaki, K., et al., *Effect of grain size on solidification cracking susceptibility of type 347 stainless steel during laser welding.* 2010.

37. Jendrzejewski, R. and G. Śliwiński, *Investigation of temperature and stress fields in laser cladded coatings.* Applied Surface Science, 2007. **254**(4): p. 921-925.

38. Montazeri, M., F. Malek Ghaini, and A. Ojo O, *Heat Input and the Liquation Cracking of Laser Welded IN738LC Superalloy.* Welding journal, 2013. **92**(9).

39. Cheng, J.M.-L., *Transient Liquid Phase bonding in the nickel base superalloy CM 247 LC*. 2005, University of British Columbia.

40. Zhang, C.S., L. Li, and A. Deceuster, *Thermomechanical analysis of multi-bead pulsed laser powder deposition of a nickel-based superalloy.* Journal of Materials Processing Technology, 2011. **211**(9): p. 1478-1487

41. Griffith, M.L., et al., *Understanding the Microstructure and Properties of Components Fabricated by Laser Engineered Net Shaping (LENS).* MRS Online Proceedings Library, 2000. **625**: p. null-null.

42. Davis, J.R. and A.S.M.I.H. Committee, *ASM Specialty Handbook: Heat-Resistant Materials*. 1997: ASM International.

43. Huang, H.-E. and C.-H. Koo, *Characteristics and mechanical properties of polycrystalline CM 247 LC superalloy casting.* Materials Transactions, 2004. **45**(2): p. 562-568.

44. Coutsouradis, D., *Materials for Advanced Power Engineering 1994: Proceedings of a Conference Held in Liège, Belgium, 3-6 October 1994*. 1994: Kluwer Academic

45. Mehta, K.K., R. Mitra, and S. Chawla, *Effect of post-solutionizing cooling rate on microstructure and low cycle fatigue behavior of a cast nickel based superalloy.* Materials Science and Engineering: A, 2014. **611**(0): p. 280-289.

Chapter 6

General Summary and conclusions

6 Chapter 6 – General summary and conclusions

6.1 Conclusions

The aim of this body of work was to investigate the cracking behaviour of nickel superalloy CM247LC during laser deposition, in an effort to develop a process that would yield fully dense and crack free deposits that would be suitable for the repair and manufacture of components.

While none of the experiments conducted were successful in achieving this goal, a great deal was learned regarding how various laser deposition processing variables affect the cracking response of this material, such as laser power, scanning speed, laser spot diameter, deposit dilution, powder particle size range and substrate temperature.

Through a series of process development trials, general rules were developed that standardised the relationship between powder feed rate and deposit dilution, track width and overlap percentage, layer thickness and Z-increment. These rules proved effective for standardising various process parameters required to deposit blocks of acceptable shape and external quality, so the cracking response could be evaluated without the introduction of additional variables that may alter the results.

Through the use of Design of Experiments methodology, an experiment plan was created that investigate how laser power, scanning speed, laser spot diameter and deposit dilution affected the crack density of laser deposited blocks. Through the deposition and analysis of 30 test blocks, it was determined that cracking was most significantly influenced by laser power and scanning speed, and to a lesser extent by laser spot diameter and deposit dilution. These conditions correlate to high heat input, and so a test block was deposited using 1000W laser power, 5mm/sec scanning speed, 3mm laser spot diameter and dilution of 1.5, which showed that cracking was reduced.

Microstructural analysis of the cracking mechanisms showed that solidification cracking was occurring during deposition, due to the presence of a low melting point phase that wets the grain boundaries and interdendritic pathways. During melt pool solidification, the semi-solid region is pulled apart by the solidification stresses, leading to the formation of cracks that follow the dendrite growth axis and columnar grain boundaries.

Work conducted attempting to reduce the cracking effect further involved altering the particle size range, using different toolpath patterns, and raising the temperature of the substrate via induction preheating.

Particle size was shown to have a significant effect on the cracking density, with finer particles creating a greater number of shorter cracks per unit area. This is thought to be a result of melt pool mixing and melt pool chilling, leading to an accelerated solidification rate, higher residual stress, and shorter columnar grains.

Of the toolpaths investigated, the cross hatch pattern was the most successful in reducing the cracking in the transverse axis, while the long raster toolpath produced the lowest crack density in the longitudinal axis. The anisotropy of cracking response along different axis is believed to be due to the long axis of the block experiencing a significantly higher residual tensile stress, which magnifies the cracking response along the long axis.

The best improvement in deposit quality was obtained by increasing the substrate temperature to 800°C by a combination of induction and laser preheating. This produced a block with a greatly reduced crack density, with cracks being confined to individual deposit layers, rather than penetrating through them.

While cracking was still evident, it was of a finer scale, and not surface connected. This raises the possibility that parts deposited using active preheating may be suitable for post deposition HIP processing to heal the internal cracks, but further work would be required in order to

develop this process to a point where it could be considered an appropriate repair and manufacture method for CM247LC.

6.2 Recommendations for further work

- Deposition of CM247LC at temperatures exceeding the 800°C used for this study, using FEA methodology to calculate heating and cooling rates
- Laser deposition onto cryogenically cooled substrate, to maximise the cooling rate and reduce the effect of elemental segregation and eutectic liquid formation as much as possible.
- Vibratory agitation of the melt pool as a method to reduce residual stress and encourage crack healing